Controlling Growth of Metals and Semiconductors for Optoelectronic and Photonic Device Application

by

Yong-Bum Park

Doctoral Committee:

Professor L. Jay Guo, Chair
Associate Professor Emmanouil Kioupakis
Professor Jamie Phillips
Associate Professor Zhaohui Zhong

Yong-Bum Park

ybpark@umich.edu

ORCID iD: 0000-0001-5317-7975

Dedication

To my wife, two adorable daughters,

And my parents.

"In all your ways acknowledge Him and He shall direct your paths"

Proverbs 3:

Acknowledgements

First and foremost, I would like to sincerely express my gratitude to my faculty advisor Professor L. Jay Guo, for being such a great mentor. It was his unfathomable scientific curiosity that leads students to think and understand better of their research. Personally, I find this as the greatest privilege of my PhD journey because through him I learned what research is really about. It was his questions and advices that led me to think deeper about my research and how I can better convey my idea. His questions can be extremely keen, often nailing down the core of the problem. Also, his insightful suggestions guided me to think “out-of-the-box”. Along with supervising my research, he gave me an opportunity in transforming our research into a commercial technology. This was a great experience for me as a researcher trying to think my research in the context of its practical impact. In sum, My PhD years with Professor Guo has been a great learning experience where I was able to truly enjoy myself as a researcher.

Secondly, I would like to truthfully thank my committee members, Prof. Zhaohui Zhong, Prof. Jamie Phillips, and Prof. Emmanouil Kioupakis. During my thesis proposal meeting, they gave me constructive feedbacks to better convey my research and verify important scientific assumptions. I am grateful that Prof. Zhong gave me comments regarding the theoretical limit of metal film-based transparent conductor’s figure-of-merit compared to state-of-the-art technology. This opened up an opportunity for me to better convey my technology in context of theory which enabled the delivery of future potential impact that our technology holds. Also, I am thankful that

I acquired a strong fundamental in solid state physics through his EECS 521. I thank Prof. Jamie Phillips for his intuitive questions during our proposal discussion. In fact, he also served as a committee for my qualifying exam where I still remember visiting his office and being asked a question about dopant activation in semiconductors, the very beginning of my qual exam. I also thank Prof. Emmanouil Kioupakis for his sharp question on asking about the assumptions of parameters used on percolation threshold model. During our joint project on low-emissive window, I was fascinated by his theoretical approach of associating optical and electrical properties of metal film.

I would like to thank all the Guo group members as it had been a great pleasure working with all of them. First, I have to truly thank Changyeong Jeong for many of the collaborative works we did together. I can remember days and nights of discussion with him regarding our research which gave me a true joy in doing research. I am grateful for I met a person like him who has a true appreciation for unraveling underlying physical phenomenon despite how trivial it may seem. I would like to thank Saurabh Acharya. I was fortunate to be given a chance to work with Saurabh. We spent significant amount of time in the cleanroom working on amorphous silicon photodetectors as well as transparent conductor works. He is very experienced and knowledgeable in many things, and it was a joy working with an intelligent person like him. I thank Chengang Ji for his help on teaching me how to perform film analysis techniques as well as inspirations on the subject of metal-based transparent conductor. I also appreciate Sangeon Lee for giving me insight on the analysis of mechanical flexibility of metal-film based transparent conductor. I also thank Sunghyun Nam for his wonderful work on polymer materials and how these can be applied for electronic device applications. Also, it was great time with Suneel Joglekar, Kaito Yamada, Weijie Feng, Yichun Zhang, Boonjae Jang, Jennie, and many more students from Guo group.

I also thank my collaborators from other research groups. I truly thank Michael J. Waters for his fabulous work on using non-linear optimization to solve multi-layer optical stack problems for collaborative work on low-emissive coating project. With his help, I was also able to apply his code to solve challenging problems in metal-film based transparent conductors. I also thank my collaborator Benjamin Derby from Professor Amit Misra's group with his help on electron microscope analysis on meta-material layer for low-emissive coating. I also acknowledge my collaborator Tae Cho from Professor Neil Dascupta's group for his assistance on providing atomic layer deposition film of aluminum-zinc oxide films for passivation purpose. Finally, I would like to show my appreciation to Lurie Nanofabrication Facility staff members. It was through their support and help that I was able to make it through the end. Thank you all!

Table of Contents

Dedication **ii**

Acknowledgements **iii**

List of Tables **ix**

List of Figures **x**

Abstract **xxvi**

Chapter 1 Introduction **1**

Chapter 2 Controlling Growth of Ultrathin Ag Film and Its Electrical/Optical Property **8**

- 2.1 Introduction 8
- 2.2 Selection Criteria of Seed-Layer 10
- 2.3 Experimental Result of Seed Layer Comparison 11
- 2.4 Optimization of Cu and Ge Seed Layer 18
- 2.5 Modeling of Electron Conduction in Thin Films 20
  - 2.5.1 Introduction 20
  - 2.5.2 Experimental Properties of Ag Film 25
  - 2.5.3 Modeling by Classical Size Effect Model 28
  - 2.5.4 Modeling by Mean-field Theories 36
- 2.6 Verification and Implication of Model 44
  - 2.6.1 Dielectric function of inhomogeneous medium 44
  - 2.6.2 Implication of critical thickness in $\boldsymbol{\rho ext.\ GEM}$ 46
- 2.7 Conclusion 54

Chapter 3 Flexible Transparent Conductor for Organic Light Emitting Device **56**

3.1 Introduction 56

3.2. Figure of Merit and Anti-reflective Effect of Ag Film inside OLED 58

  3.2.1 Ag Film’s Electrical and Optical Properties versus d_{Film} 58

  3.2.2 Theoretical Calculation of Sheet Resistance 60

  3.2.3 Optical Simulation 61

  3.2.4 Figure-of-Merit Comparison and Anti-reflective Effect 62

3.3. Ag Diffusion Inhibition by AZO 64

3.4. Device Performance of OLED with Cu-Ag Anode 66

  3.4.1 Modal Power Dissipation Analysis 66

  3.4.2 Fabricated Device EQE Comparison 70

  3.4.3 Experimental Observation of Waveguide Mode Elimination 72

3.5. Conclusion 75

Chapter 4 Metal-based Transparent Conductor's Optical Property and Environmental Stability 76

4.1 Introduction 76

4.2 Criteria for Anti-reflective coating 78

4.3 Issue with reducing color contrast 85

4.4 Non-linear Optimization to Minimize Color Contrast 90

  4.4.1 Optimization Method 90

  4.4.2 Optimization of 3-layered stack 92

  4.4.3 Optimization of 4-layered stack 93

4.5 Metal-Dielectric Photonic Crystal for Low Resistance FTC 95

  4.5.1 1-dimensional photonic crystal structure 95

  4.5.2 Colored-Transparent Antenna 98

4.6 DMD for Highly Efficient OLED 99

4.7 Stability of transparent conductor 104

  4.7.1 Stability Issue of Ag-based Transparent Conductor 104

  4.7.2 NiCr for Ag Atom Diffusion Barrier and Self-Assembled-Monolayer (SAM) for Humidity Resistance 105

  4.7.3 Electrochemical Evaluation of Passivation Dielectric Layer 109

4.8 Conclusion 118

Chapter 5 Thin Film-Based Photodetector for Optical Fingerprint Sensor 119

5.1 Introduction 119

5.2 Leakage in a-Si Heterojunction Photodiode Device 121
5.3 Thickness Choice of a-Si Layer 127
5.4 Process Optimization to Suppress Leakage 130
5.5 Array Level for Fingerprint Detection and Potential of Cu-Ag Anode 136
5.6 Conclusion 137

Chapter 6 Silver Nanoparticle to Tailor Sunlight for Low-e Application 139

6.1 Introduction 139
6.2 Fabrication of Meta-Material 143
  6.2.1 Cr-TiO_2 Meta-Material 143
  6.2.2 Ag-Si_3N_4 Meta-Material 144
6.3 Optical Properties of Meta-Material 149
6.4. Application of Meta-Material on Commercial Low-e Stack 150
6.5 Conclusion 156

Chapter 7 Growth and Characterization of Single Crystalline III-V Nanostructure for Solar Energy Harvesting Application 157

7.1 Introduction 157
7.2 Fabrication/Growth of InGaN Nanoridge 159
7.3 Growth Morphology and Photoluminescence 163
7.4 Transmission Electron Microscopy of InGaN Nanoridge 170
7.5 InGaN Nanoridge for Solar Energy Conversion Application 172
  7.5.1. III-nitride for Solar Energy Conversion 172
  7.5.2. Photoelectrochemical Cell Measurement 172
  7.5.3. Photoelectrochemical Performance Comparison 175
7.6 Conclusion 179

Chapter 8 Conclusion and Outlook 180

Bibliography 184

List of Tables

Table 2.1 Binding strength energy of seed layer atoms with -O or -Ag 11

Table 2.2 Ag film’s thickness, RMS roughness, and density extracted from XRR data in comparison with those from Ellipsometer and AFM. 16

Table 4.1 General guide on *ΔE* table with respect to human eye perception. 87

Table 4.2 Types of passivation dielectrics used for experiment. 112

Table 4.3 Comparison table of calculated and extracted C_{coat}. 115

Table 4.4 Corrosion parameters extracted from polarization curve of Cu-Ag and Cu-Ag-SAM. 117

Table 5.1 Deposition condition of conventional and optimized a-Si material 125

Table 7.1 MBE growth condition for InGaN nanoridge. 161

List of Figures

Figure 1.1 Cross-sectional schematic of three different modes of thin film growth: (a) Volmer-Weber (island-like), (b) Stranski-Krastanov (layer-plus-island), and (c) Frank-van der Merwe (layer-by-layer). Each mode is shown for several different amounts of surface coverage, Q [K. Oura, V. G; et al. SurfaceScience: An Introduction, Springer, Berlin 2003.]. 2

Figure 1.2 High-level summary of the work discussed in this dissertation. 3

Figure 2.1 Standard electrode potential of various atoms including Al, Ge, and Cu. 11

Figure 2.2 AFM surface image and RMS surface roughness (Ra) of Ag film with (a) Al, (b) Ge, and (c) Cu as a seed layer. (d) Absolute transmittance and (e) resistivity of 8 nm Ag films with 1 nm Al, Ge, and Cu seed layers.). 12

Figure 2.3 (a) Absolute transmittance (including substrate) and (b) resistivity of 8 nm Ag films with 1 nm Al, Ge, and Cu seed layers.). 13

Figure 2.4 (a)-(c) AFM images 4nm of Ag film with seed layer of Al, Ge, and Cu, respectively. 13

Figure 2.5 Top-down scanning electron microscopy (SEM) images of Al-Ag, Ge-Ag, and Cu-Ag films for seed layer only film or those with various thickness of Ag films. 14

Figure 2.6 X-ray Reflectivity data for Ag thin film with (a) Al, (b) Ge, and (c) Cu as a seed layer plotting measured data (black line) and fitted simulation data (red symbol). 15

Figure 2.7 Measured Qs for (a) LSPR and (b) SPPs of 9 nm of Al-Ag, Ge-Ag, and Cu-Ag films. 16

Figure 2.8 (a)-(c) Relative transmittance and (d)-(f) Sheet resistance (RSh) of Al, Ge, or Cu seeded Ag films over a span of time exposed in air, respectively. Arrows in the relative transmittance curves indicate time evolution. 17

Figure 2.9 (a) Sheet resistance (Rs) and average Transmittance (T%), (b) RMS roughness of 4nm Ag thin film with varing Ge or Cu seed layer. Photographic (top) and AFM images (bottom) of 4nm Ag thin film with different seed layers for (c) Ge and (d) Cu where seed layer thickness is specified. 19

Figure 2.10 Resistivity ρ of (a) Cu, (b) Ge, or (c) no-seeded Ag films as a function of film thickness d plotted in log-log scale. The open symbols are the measured data while dotted lines extrapolating double-slope behavior of resistivity scaling are not based on any physical model. 27

Figure 2.11 Ag (Cu) film's (a) RMS surface roughness values as a function of $deff$. (b) XRD intensity curve over 2- theta for different film thickness. (c) Extracted film's crystallite grain size as a function of $deff$ showing linear relationship. Inset figure is TEM image of the film with 10 nm of thickness, which show approximate grain sizes in the range of D ~ 10 nm. Top-down TEM images of Ag (Cu) film with effective thickness of (d) 8.5 nm, (e) 5.5 nm, (f) 4.1 nm, (g) 2.7 nm, and (h) 2.0 nm. All images have scale bar of 50 nm. Inset of (f) is the STEM image taken as an example where black dots show void areas. 28

Figure 2.12 Theoretically calculated ρ - d plot in (a) linear-linear and (b) log-log scale of Ag (Cu) thin film using surface (F-S) or grain boundary (M-S) scattering models each model with varying specularity parameter p and reflection coefficient R, respectively. The open symbols are the measured data. F-S and M-S models are plotted in dotted-black and red-solid lines, respectively. Theoretical values calculated for sweeping parameters where arrows indicate the direction of parameters (with ranges $0 \leq p \leq 1$ and $0 < R < 1$) in decreasing order.................................. 31

Figure 2.13 Schematic chart describing theoretical models of electron transport in thin metal film. 33

Figure 2.14 (a) Colormap of deviation (*eq 2.7*) in theoretical model (Namba [*eq 2.3*] + M-S [*eq 2.4*] models) from experimental data involving two parameters, p and R where optimum point is at p = 0.1 and R = 0.2. Colormap scale is plotted in log scale. (b) Comparison of resistivity data predicted by all the combinations of surface or grain boundary models. Data in symbol is measured data while that in lines are calculated from a single or sets of models. 35

Figure 2.15 (a) Log plot of normalized resistivity $\rho/\rho 0$ as a function of metal fraction for measured and theory. Percolation theory of conductivity with $\rho/\rho 0 = (\phi - \phi c) - t$ for $\phi > \phi c$ and $\rho/\rho 1 = (\phi c - \phi)s$ for $\phi < \phi c$ was used as a model for theoretical calculation. Percolation threshold ϕc of 0.59 (indicated as dotted line), critical exponent values of t and s of 3.06 and 1.0, respectively, metal-insulator resistivity ratio of $\rho 0/\rho 1 = 10^8$ was used where resistivity scaling factors $\rho 0$ and $\rho 1$ are the resistivity of metal and insulator, respectively. Inset graph shows a plot of $\rho/\rho 0$ as a function of $(\phi - \phi c)/1 - \phi c$ in log-log scale where the negative of the slope Δ represent t found here as 3.06 ± 0.2. (b) The measured metal fraction ϕ of Ag (Cu) film as a function of film's effective thickness $deff$ shown as a symbol. Its empirical relationship was extracted using logic function plotted in dotted line where its equation is in the inset. 38

Figure 2.16 (a) Real part $\varepsilon 1$ and (b) imaginary part $\varepsilon 2$ of Ag (Cu) film's dielectric function for different film thickness $deff$. Black arrows indicate the curve change behavior as decreasing $deff$. (c) Measured $\varepsilon 1$ (in symbol) at wavelength of 1500 nm as a function of film's metal fraction ϕ, where ϕ for a given film thickness was obtained from empirical relationship in Figure 2.15b. Modeled $\varepsilon 1$ (dashed line) using percolation model [M. Hovel et al. Phys. Rev. B 81, 035402].

Percolation threshold ϕc of 0.59 is indicated in vertical black dotted line. ϕc coincide with the metal fraction at which $\varepsilon 1$ crosses 0 indicative of metal-insulator transition.............................. 39

Figure 2.17 Resistivity ρ of Ag (Cu) film as a function of film's effective thickness $deff$. The open symbols are experimental resistivity values and lines are calculated values from the theoretical models based on size effect ($\rho size$ [*eq 2.6*], black solid line), GEM (ρGEM [*eq 2.8*], blue dotted line), extended GEM ($\rho ext.GEM$ [*eq 2.8* with replacing $\sigma 0$ with $\sigma size = 1/\rho size$], red dashed line), or applying Matthiessen's rule ($\Delta\rho GEM+\rho size$ [*eq 2.6* and *eq 2.8*], green dashed-dot line). Thickness that corresponds to the percolation threshold ϕc is shown as vertical grey dashed line for reference. 41

Figure 2.18 $\rho - deff$ plot from theory by percolation model [$\rho percolation$, *eq 2.10*], Landauer model [ρEMA, *eq 2.11*], GEM model [ρGEM, *eq 2.8*] and extended GEM model [$\rho ext.GEM$, *eq 2.8* with $\rho 0 = \rho size$]. Grey horizontal line indicates resistivity scaling factor (or baseline resistivity) of $\rho 0$ = 7.66 Ωcm. Experimental resistivity values are plotted in symbol for reference. 43

Figure 2.19 Ag (Cu) film's real part of dielectric function $\varepsilon 1$ as a function of wavelength for different air fraction. Solid lines are the measured $\varepsilon 1$ for varying projected air fraction ϕair. Dashed curves are $\varepsilon 1$ (real part of εeff) calculated from BEMT model (*eq 2.12*) for varying volumetric air fraction $fair$. For each curve, corresponding film thickness $deff$ are noted as well. The curves show a trend of increase in $\varepsilon 1$ for entire wavelength range as air fraction increases. 45

Figure 2.20 (a) Ag (Cu) film's total resistivity $\rho total$ (= $\rho ext.GEM$, dashed black line) on the left axis and contribution of size effect model over total resistivity, $\rho size/\rho total$ (dashed-dot red line) on the right axis both as a function of film thickness $deff$. Symbols on left axis are measured experimental resistivity values. (b) Experimental (symbol) and theoretical (from $\rho ext.GEM$, dashed line) scattering time τ of Ag (Cu) film as a function of $deff$. Inset figure plots the film's predicted effective mean free path l (symbol) as a function of $deff$ where proportionality relation of grain size D with $deff$ is plotted (red dashed line). (c) Film's measured average transmission (T_{AVE}) and absorption (A_{AVE}) over visible wavelength (380 – 780 nm) plotted as a function of $deff$. (d) Haacke's figure-of-merit ϕTC (= $T10Rs$) of Ag (Cu) film as a function of $deff$ where T is transmission at 550 nm wavelength and Rs is sheet resistance. Symbols and dotted line are experimental and modelled ϕTC, respectively. For the modelling of ϕTC, Rs was calculated from extended GEM model and T is calculated from measured Ag (Cu) film's optical constants using transfer-matrix method. In all four figures, Ag (Cu) film's critical thickness dc (= 5nm) is indicated as a vertical solid line. 47

Figure 2.21 Ag (Cu) film's (a) mobility μ, carrier concentration Nc, (b) scattering time τ, and $\rho \times deff$ plotted as functions of film's effective thickness $deff$. Solid black lines in each figure indicates the critical thickness dc. Dashed line in (b) shows theoretical τ calculated from extended GEM model (*eq 2.8*). 48

Figure 2.22 Comparison of Ag (Cu) film's optical (black circle) and electrical (red square) scattering time τ as a function of $deff$. 50

Figure 2.23 Film's predicted effective mean free path l (symbol) as a function of $deff$ where proportionality relation of grain size D with $deff$ (red dashed line) is plotted as well. The figure is identical to the inset figure of Figure 2.20b but with top-down schematic view to illustrate the film's morphology in relation with the l and D under the presence of electric field (E). 51

Figure 2.24 Change in resistivity $\Delta\rho$ of Ag (Cu) film for different $deff$ after exposure in air for 30 days. 53

Figure 3.1 (a) Sheet resistance R_{Sh}, average optical (λ = 380 - 780 nm) transmission T_{AVE}, and (b) root-mean-square (RMS) surface roughness of 5 nm Ag film with varied Cu seed layer thickness. Inset in (b) is AFM image of Ag film with 5 Å Cu-seed. (c) R_{Sh} of Cu-Ag and Ag-only films as functions of film thickness d_{Film}. Average optical (d) transmittance T_{AVE}, (e) reflectance R_{AVE}, and (f) absorbance A_{AVE} as a function of film thickness d_{Film} for Cu-Ag and Ag-only films. Experimental data (in symbol) and simulated data (dotted line) of Ag-only film (black) and Cu-Ag film (red) are plotted together. 60

Figure 3.2 Theoretically calculated sheet resistance R_{Sh} as functions of film thickness d_{Film} for (a) ideal Ag film with F-S model (*eq 3.1*) and (b) ITO film (*eq 3.1*). Right axis of (a) and (b) shows simulated average optical transmittance T_{AVE} for ideal Ag film and ITO film, respectively........ 62

Figure 3.3 (a) Haacke's figure-of-merit ϕ_{TC} as a function of film thickness for Cu-Ag, Ag-only, and ITO based transparent conductors. Experimental data (in symbol) and simulated data (dotted line) of Ag-only film (black) and Cu-Ag film (red) are plotted together. Theoretical ϕ_{TC} of ideal Ag film is also plotted (blue dotted line) as a reference to show the potential of metal-film based TCE. Reference for ITO values used are Ref1 [107], Ref2 [108], and Ref3 [109]. (b) Measured (black solid line) and simulated (black dashed line) transmittance (T) and reflectance (R) of Cu-Ag films in air. Simulated T and R of Cu-Ag films inside an OLED structure is plotted (red dashed line) as well showing enhancement of transmittance owing to AR effect of HTL layer. Schematics of simulated optical stacks for each case are illustrated in inset for each curves. 63

Figure 3.4 Schematic image illustrating the Ag migration process in organic light emitting device (OLED) under operation (presence of high electric field). 64

Figure 3.5 (a) Constant voltage stress test (10V) with measured current as a function of time for Ag anode OLED devices without passivation, with ZnO or AZO passivation. (b) Current density versus voltage characteristic curve of OLED without any passivation or with 2 nm of ZnO or AZO passivation layer. After several cycles of voltage scan, ZnO-passivated Ag anode results in Ag migration thereby increasing the subthreshold current. AZO-passivated Ag anode device shows stable operation even after multiple voltage scans. Inset picture shows stable device operation with strong illumination for AZO-Ag anode device. 66

Figure 3.6 (a) Green OLED device structure. Dispersion relation from modal power distribution analysis of (b) ITO and (c) Cu-Ag device. (d) Spectrum of green emission material. Light intensity distribution from modal power distribution integrated over green emission material spectrum. . 67

Figure 3.7 Simulated OLED device structure (a) with and (e) without Cu-Ag anode. Modal power distribution map with total thickness of (b) 100 nm, (c) 200 nm, and (d) 300 nm for OLED with Cu-Ag and (f) 100 nm, (g) 200 nm, and (h) 250 nm for OLED without Cu-Ag. 68

Figure 3.8 Dissipated modal power in each modes as a function of wavelength for (a) ITO and (b) Cu-Ag devices, respectively. (c) Fraction of each mode's modal power integrated over wavelength range for ITO and Cu-Ag devices. 70

Figure 3.9 Device performances of ITO and Cu-Ag devices. (a) EQE and (b) current density - voltage characteristics (*J*-*V*) of ITO and Cu-Ag devices with and without IMF. IMF is used to extract light trapped in the substrate. 72

Figure 3.10 Experimental investigation of waveguide mode elimination. (a) Top-down and cross-sectional views of experiment setup in schematic. The sample was placed on top of holders with a small gap away from the prism. The gap was filled with IMF to remove substrate mode from the sample. The fabricated waveguide in this experiment consists of organic and anode layers used in OLEDs without the top cathode. (b) Measured intensities of waveguide and substrate modes as a function of excitation intensity. The Cu-Ag waveguide with IMF showed negligible measured light intensities that was similar to the noise level, indicating no optical energy in the form of waveguide mode. (c) Photographs of the Cu-Ag and ITO waveguide samples. *i*) Side-view image of the sample under ambient light. Photographs of *ii*) the ITO and *iii*) the Cu-Ag waveguide samples without IMF. Photographs of *iv*) the ITO and *v*) the Cu-Ag waveguide samples with IMF. The waveguide mode was observed in the ITO sample but completely disappeared in the Cu-Ag sample. 74

Figure 4.1 Technology roadmap of display industry including that from LG. 77

Figure 4.2 (a) $T_{ave}\%$ as a function of dielectric thickness for different bottom dielectric materials. Inset shows the DMD structure with bottom dielectric as a variable for simulation. (b) $T_{ave}\%$ - wavelength spectra for selected oxide materials each with optimum thickness. (c) $T_{ave}\%$ and (d) optimum bottom dielectric as a function of average index. 81

Figure 4.3 (a) $T_{ave}\%$ as a function of dielectric thickness for different top dielectric materials. Inset shows the DMD structure with top dielectric as a variable for simulation. (b) $T_{ave}\%$ - wavelength spectra for selected oxide materials each with optimum thickness. (c) $T_{ave}\%$ and (d) optimum top dielectric as a function of average index. 83

Figure 4.4 Effect of anti-reflection coating in a DMD structure on PET substrate. 84

Figure 4.5 (a) CIE XYZ standard observer color matching functions and (b) c-white light spectra. 86

Figure 4.6 Calculated ΔE values from transmittance spectra of varying (a) bottom and (b) top dielectrics. 88

Figure 4.7 ΔE from film side reflection for varying (a) bottom and (b) top dielectric layers where black bar represents ΔL^* and red bar represent ΔCab^*. $R_{ave}\%$ and $|Rf\text{-}R_{sub}|\%$ over 400-700nm wavelength for various candidates of (c) bottom and (d) top dielectric materials. 89

Figure 4.8 Optimization process flow of transparent conductor to meet various target specifications. 91

Figure 4.9 T and R spectra for the DMD stack optimized only for $T_{ave}\%$ or for $T_{ave}\%$ and ΔE. 92

Figure 4.10 (a) T and R spectra for the 4-layered stack optimized for high $T_{ave}\%$ and low ΔE. (b) T and R spectra of optimized 4-layered stack with x, y, and z spectra. 94

Figure 4.11 (a) Transmittance spectra of DMD structure with increasing Ag film layer thickness. (b) T_{ave}, R_{ave}, and Y% as a function of Ag film layer thickness. 96

Figure 4.12 (a) Schematic of Ag-AZO based 1-D MDPC structure. (b) Average T% and Y% with respect to the number of Ag layers used in the 1-D MDPC where total thickness of Ag used in each case is fixed to 40nm. (c) Transmittance spectra of 1-D MDPC with varying number of Ag layer thickness. 98

Figure 4.13 Low resistance 1-D MDPC transparent conductor with tunable property. By adjusting the metal and dielectric thickness, the stack can be designed to show bandpass filter properties at (a) blue, (b) green, and (c) red wavelength. Corresponding film-side transmission (Tf) and reflection (Rf) color calculated from the spectral curves are shown to illustrate the color of stack. 99

Figure 4.14 Average *T%* of DMD under (a) air-air medium (b) organic-air medium, and (c) organic-substrate medium. 100

Figure 4.15 (a) Simulated/measured T and R of ITO and DMD. (b) R as a function of angle of incidence. 101

Figure 4.16 (a) External quantum efficiency (EQE) and (b) current density-voltage (J-V) characteristics of ITO and DMD devices with and without index-matching fluid (IMF). (c) DMD device on flexible substrate after bending with 2mm bending radius. 102

Figure 4.17 (a) Angle-dependent EL analysis and (b) polar radiation pattern of ITO and DMD device. 103

Figure 4.18 2D map of DMD optimization for (a) blue and (b) red emission. (c) *T* and *R* spectrum for DMD optimized for green, blue, and red emission. 104

Figure 4.19 (a) and (e) are film stack schematic of Cu-Ag and Cu-Ag-NiCr film, respectively. Top-down SEM image of film surface before ((b) and (f)) and after ((c) and (g)) annealing of Cu-Ag film and Cu-Ag-NiCr film, respectively. (d) and (h) are photograph of sample surface after annealing of Cu-Ag and Cu-Ag-NiCr film, respectively. 106

Figure 4.20 (a) Humidity cycle test result and (b) oxidation effect of NiCr layer on transmittance. 107

Figure 4.21 Change in ΔR of SAM coated Cu-Ag film under DI water immersion test. 109

Figure 4.22 (a) Schematic of experiment for analyzing passivation of Ag film. (b) Equivalent circuit of Ag-film with passivation dielectric immersed in electrolyte solution. 110

Figure 4.23 (a) Nyquist plot and (b) amplitude and (c) phase of Bode plot as a function of frequency for 30nm ITO-coated Cu-Ag film sample immersed under 0.51M NaCl for different time period. 112

Figure 4.24 (a) Bode plot's *Z* magnitude, (b) phase, and (c) extracted *Rs* and R_{coat} for various dielectric layers after 0 hrs of immersion in NaCl. (d) change in Ccoat as a function of immersion time in NaCl. 113

Figure 4.25 (a) Polarization curve and (b) Nyquist plot of Cu-Ag film without and with SAM treatment. 117

Figure 5.1 Technology roadmap of fingerprint sensor in display technology. 120

Figure 5.2 (a) Device structure of top illumination-type a-Si thin film heterojunction photodiode structure. (b) Current-voltage characteristic of conventional a-Si photodiode device under dark or light illumination. (c) Energy level of a-Si heterojunction photodiode with possible leakage paths marked in red arrows. 122

Figure 5.3 (a) Reverse dark current of a-Si heterojunction photodiode with varying trap density for both acceptor and donor traps. The result named “Actual” represents the donor and acceptor defect profiles resembling actual a-Si material used in the literature. (b) Density of state (DOS) profile as a function of energy level respect to the valence band edge of a-Si. Red curve represents acceptor state which includes tail and bump states and black cure represent donor state which also includes tail and bump states. This DOS was used for simulating “Actual” curve in (a). 125

Figure 5.4 Current-voltage characteristic of a-Si photodiodes with varying deposition conditions of a-Si layer (specified in Table 5.1) with and without light response. 126

Figure 5.5 (a) Plot of photogeneration rate and photon absorption rate inside a-Si photodiode. (b) Plot of photon absorption rate as a function of a-Si thickness with respect to the HTL interface. The plot has an overlap of curves for varying a-Si thickness from 150 to 700 nm. 128

Figure 5.6 (a) Simulated and (b) measured dark and light response of a-Si photodiode with different a-Si thickness. 129

Figure 5.7 (a) Simulated and (b) measured capacitance of a-Si photodiode with different a-Si thickness as a function of reverse bias voltage. Applied frequencies are indicated in the figures. 130

Figure 5.8 (a) Current-voltage characteristic of unpatterned and patterned device. Cross-sectional schematic of (b) unpatterned and (c) patterned device with possible leakage paths for each case. 132

Figure 5.9 Schematic showing elimination of (a) "Path 1" via separating TiO_2 and a-Si patterning process and (b) "Path 2" via sputtered MoOx. (c) Current density – voltage characteristic of patterned devices with elimination of "Path 1", "Path 2", or both. (d) Measured EQE of the optimized device as a function of bias voltage. (e) Calculated transit time of the photo-generated hole inside 300 nm of a-Si. (f) Measured EQE – wavelength plot of the device for each applied reverse bias voltage. 133

Figure 5.10 Possible mechanism of carrier transport in a-Si heterojunction photodiode under dark and light condition. 135

Figure 5.11 (a) Photograph of arrays of a-Si photodiode integrated on a TFT pixel circuitry chip for fingerprint detection. (b) Image processed result of the fingerprint mark detected by our a-Si photodiode. (c) Current density – voltage characteristic of dark and light (50 lux) response of a-Si photodiode with Cu-Ag as top transparent anode. 136

Figure 6.1 Schematic illustrating the concept of low-e coating window for cold and warm weather. 140

Figure 6.2 Commercial Ag-based low-e coating with 1, 2, and 3 alternating 1-D MDPC layers case and their *T*, *Rf*, and *Rg* spectra. 141

Figure 6.3 Example of a color-shift with respect to viewing angle in a blue-colored low-emissive window. Plot shows calculated a* b* from a simulated glass-side reflection (Rg) spectrum as a function of viewing angle. 142

Figure 6.4 Simulated refractive index of (a) Cr-TiO_2 and (b) Ag-Si_3N_4 meta-material matrix. 143

Figure 6.5 (a) Fabrication process of Cr-TiO_2 meta-material using lift-off process. Top-down (b) scanning electron microscope (SEM) and (c) atomic force microscope (AFM) images of Cr ND. 144

Figure 6.6 Fabricated nucleation layer assisted Ag NP's (a) AFM and (b) SEM image. (c) *T*, (d) *R*, and (e) *A* spectra of AlAg-Si_3N_4 meta-material matrix various AlAg thickness condition. .. 145

Figure 6.7 Rotation sputtering method for the fabrication of Ag-Si_3N_4 matrix........................ 146

Figure 6.8 HAADF-TEM images of Si/Ag power ratio of (a), (d) 90/10, (b), (e) 80/20, and (c), (f) 70/30. 147

Figure 6.9 EELS spectra from HAADF-TEM for Si/Ag power ratio of (a) 90/10, (b) 80/20, and (c) 70/30. 148

Figure 6.10 (a) *T*, (b) *R*, and (c) *A* spectra of Ag-Si_3N_4 meta-material samples with Si/Ag power ratio of (a) 90/10, (b) 80/20, and (c) 70/30 deposited on fused silica substrate......................... 149

Figure 6.11 Refractive index of (a) Cr-TiO_2 and (b) Ag-Si_3N_4 meta-materials. 150

Figure 6.12 Six major criteria for low-e coating windows and its priority during optimization is shown. The target specifications are not shown for proprietary reasons.................................. 151

Figure 6.13 Plot of a* b* of Rg as a function of viewing angle for low-e coating with various meta-materials. 153

Figure 6.14 *Rg* as a function of angle of incidence (or viewing angle) with respect to normal incidence of low-e stack window of (a) original stack and with (b) Cr-TiO_2 and (c) Ag-Si_3N_4 inserted as a meta-material layer.. 154

Figure 6.15 Low-e coating's *Rg* color as a function of viewing angle (a) 0° – 85° and (b) 50° – 85° for each type. 155

Figure 7.1 Schematic illustration of fabrication process of InGaN nanoridge/nanoprism with integration of top-down and bottom-up approach. Top-down: (a) RIE etching and (b) KOH crystallographic wet etching of GaN nanowall array. Bottom-up: (c) MBE growth of InGaN on GaN nanowall array. (d) Cross-sectional view and (e) Top view illustration of the nanoridge/nanoprism dimension. (f) SEM of cross-section of InGaN nanoridge/nanoprism array. 160

Figure 7.2 SEM images of top view of GaN nanowall after (a) Reactive Ion Etching (RIE) with 500 nm of SiO_2 masking layer and (b) subsequent crystallographic etching using 30 wt% of KOH. 161

Figure 7.3 Bird’s-eye view SEM image of InGaN/GaN structure grown in MBE under (a) Sample A, (c) Sample B, and (e) Sample C condition. The inset shows the cross-sectional schematic illustration of surface roughness after growth. High resolution top-down view of SEM image of InGaN/GaN nanowall grown in MBE under (b) Sample A, (d) Sample B, and (f) Sample C condition. Refer to Table 7.1 for the growth condition of each sample. (g) Room temperature micro-PL emission comparison of InGaN nanowall with Sample A (black solid line), Sample B (red dashed line), Sample C (blue short dash line) conditions, and InGaN planar grown with Sample C condition (green dash dotted line). The peak wavelength is at 468, 452, 545, and 575 nm for InGaN nanowall with Sample A, B, C, and InGaN planar with Sample C condition, respectively. 162

Figure 7.4 Cross-sectional SEM image of single GaN nanowall segment with InGaN growth duration of (a) 0, (b) 2, (c) 4, and (d) 6 hrs. In (b)-(d), InGaN region is shown with arrow to indicate the growth length along c-axis. All scale bars represent 500 nm unless specified. (e) High magnification cross-sectional SEM image of very narrow fin-shaped InGaN nanoridge elongated on top of InGaN nanoprism after 6 hours of growth. (f) Measured InGaN height (black square) and calculated [0001] direction growth rate (red circle) with respect to growth time. 164

Figure 7.5 Cross sectional SEM image of 4 hrs of InGaN nanoridge/nanoprism growth with measured angle between (0001) c-plane and inclined side plane of 63° 165

Figure 7.6 Schematic illustration of growth interface in self-assembled growth (SAG) nanowire and nanoridge/nanoprism representing hexagonal pyramid and prismic shape, respectively, after long time integration showing facetted morphology. The x-axis and y-axis represent the $[11\bar{2}0]$ and $[\bar{1}010]$ direction, respectively. SAG nanowires have 6 equal-sized r-plane facets, whereas nanoridge/nanoprism sample has 6 r-plane facets with elongated $(10\bar{1}0)$ and $(\bar{1}010)$ planes along $[11\bar{2}0]$ direction. The schematic is illustrated only to depict the growth contour over time scale and has been referred to work by V. Jindal et al. 166

Figure 7.7 Room temperature micro-PL of InGaN nanoridge/nanoprism with duration of 0 (black solid line), 2 (red dashed line), 4 (green short dash line), and 6 hrs (blue dash dotted line). The peak wavelength position for duration of 2, 4, and 6 hrs are 540, 560, and 524 nm, respectively. 167

Figure 7.8 (a) Micro-PL of 4 hours of InGaN grown on GaN nanowall with nanowall spacing of 500 (black solid line), 800 (red dashed line), and 1200 nm (blue dotted line). Out of three samples, only the sample with 500 nm spacing showed peak at 540 nm indicating that the emission at this wavelength is coming from the narrow InGaN nanoridge emerging on top as shown in Figure 7.4e. All three samples showed peak in the range of 420-480 nm indicating the emission at this wavelength is coming from the bulk InGaN grown either on top of GaN nanowall or on the bottom in between the nanowall segments. (b) Logarithmic PL intensities of three samples for better intensity comparison. All samples were excited with 405 nm laser source with using 100X objective under room temperature. 169

Figure 7.9 Single crystal 1D InGaN nanoridge grown on GaN nanowall array (a) Side-view SEM (b) HAADF STEM image on cross-sectional fin-shaped InGaN nanoridge from one of the InGaN nanoridge/GaN nanowall array in a and simultaneous STEM EDS spectroscopic mapping showing the grown InGaN tip primarily comprised of Ga (red), In (blue), and N (green). (c) High resolution HAADF STEM on the sharply-faceted InGaN nanoridge in c indicating highly single crystalline. (d) Room temperature micro-PL of InGaN nanoridge (black solid line), planar (red dashed line), and nanowire (blue dotted line) measured with 405 nm laser source. Peak wavelength position and full-width at half maximum (FWHM) values for 6 hrs InGaN nanoridge and InGaN nanowire sample are 40 and 101 nm, respectively. € Atomic resolution HAADF STEM on the termination of the InGaN tip in c indicating the lattice constant that is consistent with InGaN.................... 171

Figure 7.10 (a) Schematic of experimental setup for photoelectrochemical cell under light illumination. (b) Band-diagram of semiconductor-liquid junction illustrating the charge transfer process of photo-generated hole from semiconductor anode to the redox potential of electrolyte. (c) Equivalent circuit representing charge transfer process in semiconductor-liquid junction... 174

Figure 7.11 Current density (*J*) versus voltage (*V*) plot of InGaN photo-anode with nanowire or nanoridge structure under 1-sun illumination with electrolyte being (a) 1M HBr or (b) 0.2M KCl with 0.1M of phosphate buffer (pH7) solution. 175

Figure 7.12 Extracted elements of (a) $\mathrm{R_{trap}}$, (b) $\mathrm{R_{ct,SS}}$, (c) $\mathrm{C_{SS}}$, and (d) τIS of InGaN nanowire (black) and nanowire (red) photo-anode cells under 1-sun illumination with varying voltage. The measurements were done with samples immersed under 0.2M of potassium chloride (KCl) with 0.1 phosphate buffer (pH7) solution. 178

Abstract

For past decades, research on semiconductor/metal thin films and nanostructures have earned a great interest from both scientific and engineering community due to its impact on optoelectronic device application. Ability to precisely control the growth and morphology of these metal/semiconductor thin films and nanostructures can play a key role in enhancing the performance of such device. Various methods like physical vapor depositions (PVD), chemical vapor deposition (CVD), or molecular beam epitaxy (MBE) have been extensively studied to obtain desired semiconductor / thin films and nanostructures. Regardless of the methods, it is difficult to precisely control the growth of nanostructure and thin film as one intended due to various reasons like large surface energy difference or lattice mismatch between the substrate and the film. The aim of this paper is to explore various growth regimes by controlling the growth mode and utilize metal/semiconductor thin films and nanostructures to solve challenging problems in optoelectronic and photonic applications.

The first part of the thesis focuses on controlling the growth of silver (Ag) film by inhibiting de-wetting property to make the film continuous down to extremely thin regime (< 5nm). By controlling the nucleation sites, extremely thin and smooth Ag film is obtained which can be used as a transparent conductor for optoelectronic devices. Detailed study of governing electron transport mechanism in extremely Ag film is discussed and its association with optical properties are discussed. Then, this film is demonstrated as a transparent anode to solve challenging problems

in light emitting devices. Also, methods to further enhance the optical property and environmental stability of Ag film as a transparent conductor for its commercialization is detailed. Additionally, the transparent conductor film is integrated with amorphous silicon thin-film (via CVD) photodiode array to show its potential for in-display optical fingerprint sensor.

The second part of the thesis focuses on taking advantage of de-wetting property of Ag adatom on oxide substrate to create metal-nanocomposite layer having fine-sized Ag nanoparticles embedded into silicon nitride dielectric. This can be done in one-step process by using PVD, a method widely practiced in industry for thin film deposition. This nanocomposite layer is used to enhance the angle-robustness of colored low-emissive coating for window application.

The last part of the thesis focuses on layer-by-layer growth of highly ordered single crystalline InGaN nanostructure with high indium (In) composition by using molecular beam epitaxy (MBE). With the aid of nanopatterning lithography, lattice mismatch between InGaN ternary and GaN binary structure can be efficiently relaxed thereby enabling the growth of single crystalline InGaN semiconductor with high In composition. This semiconductor is used as a photoanode to convert solar energy into chemical energy by splitting water molecules. Detailed study of charge transport from this single-crystalline semiconductor to liquid junction is studied using electrochemical impedance spectroscopy.

Chapter 1 Introduction

Nanoscale thin films and crystals play a significant role in semiconductor optoelectronic devices. Controlling these films/crystals at a nanoscale level to manipulate light-matter interaction in a desired way can make us use of these structures for more efficient optoelectronic devices. For example, ability to control the metal film's thickness down below its optical skin depth allows transmission of optical waves, which can be beneficial for transparent conductor application. Also, by controlling the size of the metal nanoparticle, one can create a composite material that can selectively absorb optical light. In such, having a precise controllability of material growth gives great flexibility in designing optoelectronic and photonic devices with functionalities.

For the past decades, researchers have extensively studied thin films and crystals growth in a nanoscale using deposition methods like physical vapor depositions (PVD), chemical vapor deposition (CVD) including atomic layer deposition (ALD), or molecular beam epitaxy (MBE). Each deposition methods have their own advantage and drawbacks. However, regardless of the deposition method, the problem during these depositions is that it is difficult to control the growth as one intended due to various reasons such as lattice mismatch or the large surface energy difference. As a result, the morphology of film growth can greatly vary depending on deposition type or the condition. As shown in Figure 1.1, such film growths can be categorized into three different growth modes: (a) "island-like" growth named as Volmer – Weber mode, (b) "layer-plus-island" growth known as Stranski-Krastanov mode, or (c) "layer-by-layer" growth called Frank-van der Merwe mode [1].

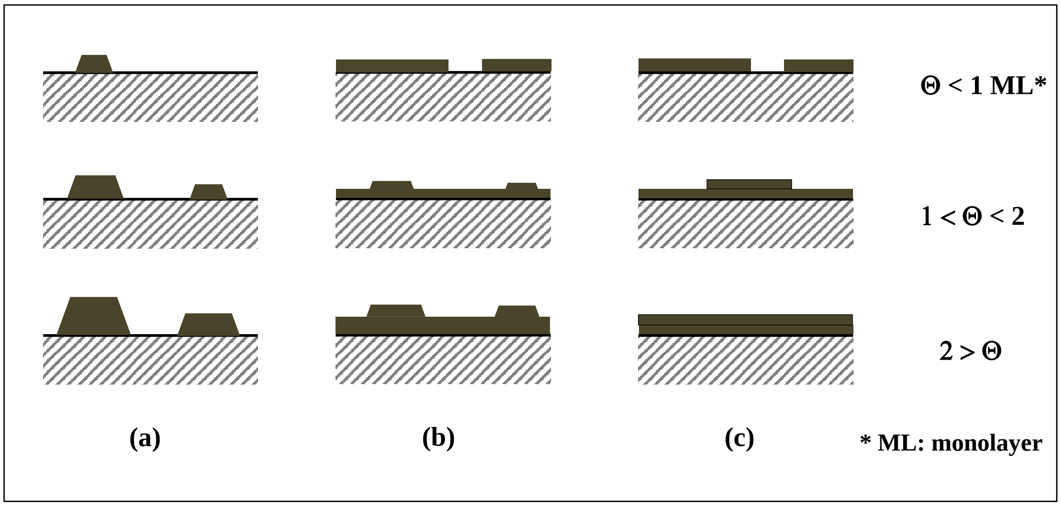

Figure 1.1 Cross-sectional schematic of three different modes of thin film growth: (a) Volmer-Weber (island-like), (b) Stranski-Krastanov (layer-plus-island), and (c) Frank-van der Merwe (layer-by-layer). Each mode is shown for several different amounts of surface coverage, Q [K. Oura, V. G; et al. SurfaceScience: An Introduction, Springer, Berlin 2003.].

As a high-level summary of this thesis, I explored the growth modes of metals or semiconductors by using novel deposition technique, controlling deposition condition, or providing additive methods to the substrate under various deposition methods. As shown in Figure 1.2, I utilized de-wetting property of metal to make metal nanocomposite for low emissive window, used seed-layer to promote layer-plus-island growth to make extremely thin metal films for transparent conductor, or even explore layer-by-layer growth of semiconductor nanocrystals for solar energy harvesting.

Here, I start the discussion by introducing PVD technique, which is widely practiced method for film deposition in the industry. Specifically, the focus will be on the deposition at a room temperature which is compatible with flexible substrates for flexible electronics that requires low temperature process. For a growth system performed at a room temperature via PVD which involves small kinetic energy of adatoms, the interfacial energy difference between the substrate and the film can result in a different film growth mode taking either Volmer – Weber or Stranski – Krastanov modes.

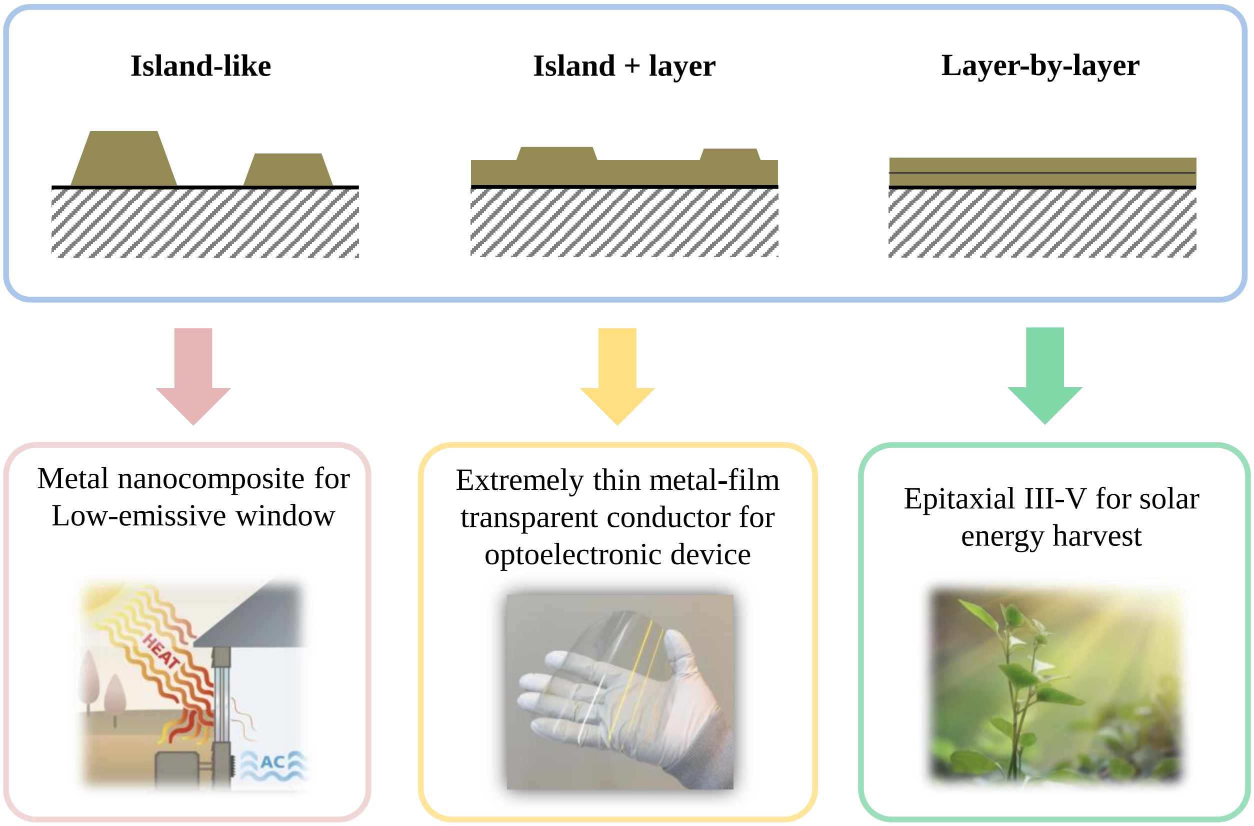

Figure 1.2 High-level summary of the work discussed in this dissertation.

In Chapter 2, I focus on engineering Ag film to grow under Stranski-Krastanov regime. Despite many effort to produce ultrathin and ultra-smooth metal films using silver, gold, or copper, it is difficult to suppress the island-like growth of these films on a widely used oxide based substrates due to a large difference in the surface energy of the host and the incoming material. This creates a large optical loss within the film which makes it difficult to be used for optoelectronic or plasmonic application. Based on the concept of introducing seed-layer which provides dense nucleation sites favorable for the metal adatoms to bind, I have produced a silver-based metal films that is continuous down to extremely thin regime with low optical loss. This ability to grow Ag film under Stranski-Krastanov mode in a PVD system holds enormous potential for its direct use as a transparent conductor (TC) for flexible electronics. Although seed-layer method is practiced by others, the uniqueness of my contribution in this work lies in the systematic approach of selecting the seed-layer. Moreover, in a fundamental aspect, I discuss the electron transport mechanism in this metal films and discuss the governing scattering mechanism at a film thickness range of 10 nm. From this fundamental study, I introduce a model that can fully describe the resistivity scaling of thin metal film down to an extremely thin regime by incorporating size effect theory into general effective medium theory. The novelty of this theoretical work is that this model is the first model that can comprehensively describe the resistivity scaling behavior down to near percolation regime. Then, the term critical thickness at which rapid transition in conduction mechanism occurs is discussed in terms of its scientific and engineering impact. The film's electrical and optical properties are comprehensively discussed at such extremely thin regime by associating it with the film's figure of merit as a TC.

Chapter 3 discusses about utilizing extremely thin silver film as a transparent anode for organic light emitting device (OLED). This chapter presents simulation and experimental results on how optical property of metal-only transparent anode can eliminate the waveguide mode inside OLED. Conventional approaches of mitigating the waveguide mode use gratings or corrugated structures, causing non-planar surfaces which is detrimental for electrical properties. Moreover, these methods involve complex fabrication steps which can increase the cost. With the strategy of using extremely thin silver film as a transparent anode, waveguide mode is not even defined in the device, hence fundamentally different from previous approaches. Although metal film-based transparent conductor for OLED have been demonstrated by others, previous works lacked in thorough studies of the effects of TCs on light outcoupling aspect in OLEDs. The uniqueness of the work presented in this chapter lies in the optical analysis to prove the benefit of using thin metal anode in enhancing outcoupling efficiency in OLEDs. In specific, the concept of waveguide mode removal is demonstrated by optical simulation which is supported by experimental results. In operating silver-film as an electrode, the practical problem of silver migration through the device under the presence of a high electric field during device operation is presented and solutions to solve this problem is suggested. This simple yet novel approach is demonstrated as a solution to better extract light from the OLED which can never be achieved by conventional transparent conductive oxides. Moreover, this approach can be easily integrated into display mass-production lines which makes it far more superior to any other existing methods.

In Chapter 4, I focus more on the practical aspect of using silver-based thin film as a TC application. I introduce criteria to choose anti-reflective coatings for silver-based film by taking so called dielectric-metal-dielectric (DMD) structure to further enhance the transmittance for TC application. Moreover, I discuss ways to minimize the color contrast of this DMD-type TC, which is a crucial factor for touch panel application. The optical multilayer stack strategy of minimizing color contrast without compromising the optical transmittance is presented in this thesis which is never dealt in other literature. I also show that such DMD structure can be tailored to show maximum transmittance at a specific desired range of wavelength giving flexibility in engineering DMD for red, green, and blue emitting devices. Next, methods to improve the stability of silver film is discussed, which is a critical step for its commercial use. As silver film is known to be prone to oxidation at atmospheric environment, I suggest methods that could stabilize this silver based DMD TC from oxidation process and adopt impedance spectroscopy to quantify the efficacy of the coating.

In Chapter 5, I introduce amorphous silicon (a-Si) thin film heterojunction photodiode technology for in-display optical fingerprint detection, which is deposited using low temperature CVD. Owing to its structure involving active layer sandwiched by charge transporting layers, which is analogous to that of OLED, photodiodes can be integrated together with OLED for multi-functional display technology. Also, as the device requires transparent conductor, it can be integrated with the thin Ag film technology mentioned in the previous chapters. First part of this chapter presents simulation and experimental results on identifying the cause of reverse bias current under dark and optimizing a-Si thin film deposition condition to suppress this reverse bias current without compromising other device performance. In the process of scaling up of device into an array for its integration on a display in-cell pixel circuitry, the origin of leakage current path in the patterned device is identified and a solution to solve this issue is suggested. In total, successful demonstration of optical fingerprint detection was achieved after integrating more than 20,000 a-Si photodiodes each onto a sensing circuitry for the detection. Moreover, Cu-Ag film was demonstrated as transparent anode of a-Si photodiode to demonstrate its potential application in flexible display technology.

In Chapter 6, by taking the advantage of the island-like growth nature of silver on a dielectric substrate, metal-nanocomposite layer consisting of silver nanoparticle (Ag-NP) embedded dielectric layer can be fabricated in a one-step process using PVD system. While Ag films are widely used in low emissive (low-e) coatings for windows application, silver as a form of Ag-NP are never been used for such application. The uniqueness of the approach discussed here is using novel process named rotation sputtering method that can create metal-nanocomposite medium in a single step. Moreover, by utilizing the property of light extinction by Ag-NP at specific wavelength, this meta-material layer can enhance the angle-insensitivity in low-e coating allowing it to exhibit its original color for large degree of angle. The approach of using meta-material to hold desired optical properties in multilayer optical stack can be widely used to any optical coatings where absorption at a specific wavelength is beneficial.

Finally, in Chapter 7, I explore the regime of Frank-van der Merwe mode or as known as epitaxial growth where the focus of material will be on a III-V semiconductor. For a growth system like MBE involving large kinetic energy of adatoms that allows epitaxial growth, lattice mismatch between the substrate and the grown film can result in strain in the film causing dislocations and defects within the crystal lattice. For a semiconductor film that is used to absorb light, such behavior is detrimental as dislocation and defect sites can contribute to the non-radiative recombination sites thereby reducing the efficiency of these devices. I use nanolithography technique to grow single-crystalline InGaN nanocrystal with high composition of Indium by effective strain relaxation. I have compared how such a method is beneficial over conventional spontaneous nanowire growth. Then, I used this novel structure as a photoanode to convert solar energy into chemical energy by oxidizing water to hydrogen by splitting water. I use electrochemical impedance spectroscopy to study the charge transport at this semiconductor/electrolyte junction and calculate the surface states at the interface in correlation with water oxidation process. Through this process, I show that highly ordered single-crystalline InGaN is advantageous over conventional nanowire structure in terms of light absorption and solar energy conversion.

Chapter 2 Controlling Growth of Ultrathin Ag Film and Its Electrical/Optical Property

2.1 Introduction

Thin silver (Ag) films have many applications in optoelectronic and plasmonic devices provided that they have excellent conductivity and low optical loss at visible wavelength. The performance of thin Ag films is largely dependent on the thickness and the morphology of the film. If the Ag films' thickness can be reduced below optical skin depth (~ 20 nm for Ag at 530 nm) [2, 3] it can transmit significant portion of light wave. Furthermore, as Ag is known to have lowest loss at a visible wavelength among metals, making it as an excellent candidate for transparent conductor application.

However, it is known that a thin Ag film is prone to grow in 3D island-like (Volmer-Weber) modes on oxide substrates, leading to high electrical resistance and optical scattering loss [4]. A film with such type of growth can induce large extinction coefficient due to scattering of light or LSPR induced absorption reducing the overall transmittance, which is detrimental for transparent conductor application. Researchers have spent much effort to suppress such 3D island growth by introducing inorganic [5-7] or organic [8] seed-layer prior to the Ag growth or co-deposition of alloy during the Ag deposition [9]. Among these approaches, widely practiced method is to use Ge [5] or Cu [7] as a seed-layer, which reduces the surface roughness by an order of magnitude for ultrathin Ag films. Unlike other methods like organic seed-layer or co-deposition of alloy, this approach is simple and compatible with widely used roll-to-roll commercial sputtering tools which is suitable for flexible electronic fabrication process. Therefore, comprehensive study of the inorganic seed-layer is key to obtain high performance Ag film for optoelectronic and plasmonic devices.

Moreover, studying the electron conduction at ultrathin metal film and unraveling the governing scattering mechanism is not only scientifically interesting but can attain important engineering merit. Despite numerous studies were conducted to better understand the conduction mechanism at relatively thicker regime (>20 nm), such studies at ultrathin regime is relatively unexplored. It was only recent that the advent of techniques like engineering nucleation site made it possible to reach film thickness below 10nm which has enormous use for optoelectronic and plasmonic application. By understanding electron transport mechanism in ultrathin film allows us to not only quantify the quality of the film but also allows to design better metal thin films.

In this chapter, various types of inorganic seed-layer (Ge, Cu, Al) will be explored to study the efficacy in terms of growing subsequent Ag layer. This will be investigated in terms of the optical loss, surface roughness, and resistivity. Electrical properties of Ag ultrathin films will be studied in detail by adopting various electron transport models from literature to unravel the governing mechanism. Based on the transport mechanism, I define two distinguishing carrier transport mechanism near the percolation threshold and relate this with the mathematical model of mean-field theory. With introducing a model that can comprehensively describe the resistivity scaling of metal film down to extremely thin regime, I will explore the scientific and engineering implication of the model.

2.2 Selection Criteria of Seed-Layer

Among commonly used inorganic seed layers, Ge, Cu, and Al were selected to compare on its efficacy in obtaining low electrical and optical loss Ag film. When selecting appropriate materials for nucleation site, several criteria needs to be considered: seed layer must have high bond strength energy (BSE) with substrate as well as with Ag atom; atomic diffusion barrier of Ag on the nucleation site should be large in order to prevent Ag from agglomerating with each other; standard electrode potential needs to be low to maintain durability of the film; material should have low optical loss at visible/NIR wavelength.

Table 2.1 shows BSEs of the seed layer atoms with oxygen (-O) and -Ag, which can provide the mechanism of seed site. The seed layer should have high BSEs with Ag atom and underlying oxide substrate to bind well with Ag and oxide atoms, thus preventing Ag agglomeration. However, the BSE of the seed should not be too high since it can alter the film morphology over time due to out-diffusion of atoms toward oxygen-rich environment. In this aspect, all Al, Ge, and Cu atoms show reasonable BSEs.

Also, a seed layer should have high diffusion-barrier for Ag atoms as it should act as an adhesive layer where incoming adatom can adsorb onto the surface. As shown in Table 2.1, activation energies of Ag diffusion on Al, Ge, and Cu surfaces are 1.21, 0.45, and 0.76 eV, respectively [10], which are higher than the glass (0.32 eV) [11] and thus make them an ideal choice for seed layers.

Table 2.1 Binding strength energy of seed layer atoms with -O or -Ag

Seed layer	Binding strength energy [kJ/mol]		Activation energy of Ag diffusion [eV]
	- O	**- Ag**	
Al	512	184	1.21
Ge	657	175	0.45
Cu	343	172	0.76

In terms of the durability aspect, seed layer with higher standard electrode potential will likely go through oxidation process (prone to the environmental effect). In this aspect, Cu or Ge may be preferred over Al when considering the stability of the film, as shown in Figure 2.1. Finally, thickness of the seed layer was engineered to reduce the optical loss induced by it.

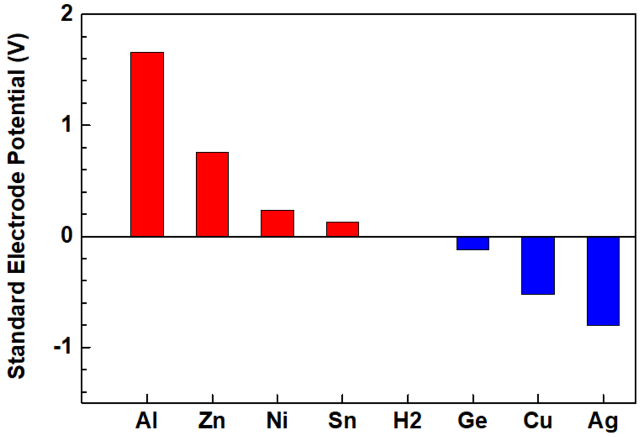

Figure 2.1 Standard electrode potential of various atoms including Al, Ge, and Cu.

2.3 Experimental Result of Seed Layer Comparison

Seed layer effect was experimentally verified by depositing 1 nm Al, Ge, or Cu layers on a silica substrate followed by subsequent deposition of 8 nm Ag. Figures 2.2a-c show the atomic force microscope (AFM) images and root-mean-square surface roughness (R_a) (RMS) values of the Ag films with Al, Ge, and Cu seed layers, respectively. Cu and Ge seed layers suppress R_a of the Ag films below 0.25 nm whereas the Al seed gives R_a = 0.6 nm, indicating better seed characteristic at Cu and Ge than Al.

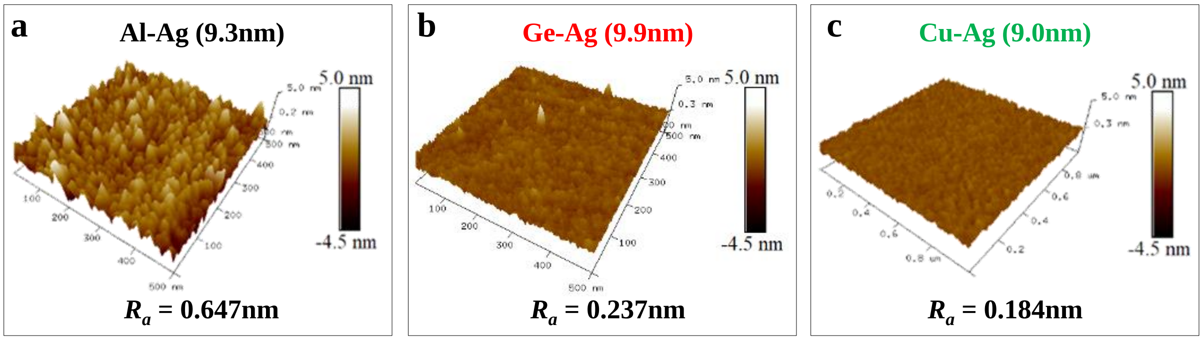

Figure 2.2 AFM surface image and RMS surface roughness (Ra) of Ag film with (a) Al, (b) Ge, and (c) Cu as a seed layer. (d) Absolute transmittance and (e) resistivity of 8 nm Ag films with 1 nm Al, Ge, and Cu seed layers.).

Figure 2.3a shows measured transmittance of the seed-Ag samples, where the transmittance was obtained including the substrate. The Cu-Ag film shows higher transmittance than the Ge-Ag or A-Ag films. Note the Al-Ag film shows the spectral dip around 450 nm which is attributed to localized surface plasmon resonance by quasi-particle behavior of the film. This is consistent with the AFM result of Al-Ag where the surface shows nanoparticle-like clusters of Ag rather than smooth film. Lower transmittance of Ge-Ag film is likely due to large optical loss of Ge at visible wavelength. Electrical resistivity, which is resistance normalized with film thickness, is plotted in Figure 2.3b, and the lowest resistivity was achieved in the Cu-Ag film. Detailed analysis on the resistivity of Ag films will be discussed in the later part of this chapter.

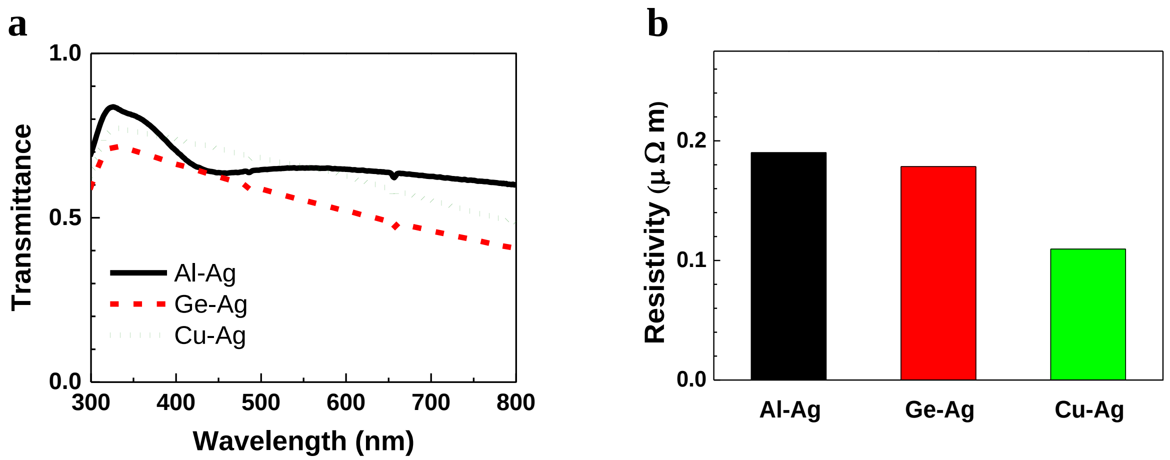

Figure 2.3 (a) Absolute transmittance (including substrate) and (b) resistivity of 8 nm Ag films with 1 nm Al, Ge, and Cu seed layers.).

To verify how low of thickness can continuous Ag-film be formed with the seed layer, total thickness of 'seed layer + Ag film' was kept at around 4nm and the resulting AFM surface analysis were performed as shown in Figure 2.4. It was confirmed that Al-Ag showed discontinuous film behavior where agglomerate of Ag nanoparticles were observed whereas Ge-Ag and Cu-Ag showed a continuous film with RMS surface roughness values kept below 0.3nm for a 4nm thin film. This result indicates that Cu and Ge functions as superior seed layer compared with Al.

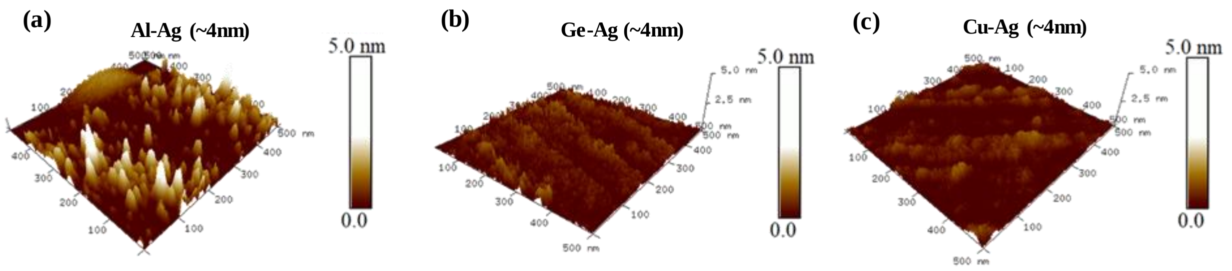

R_a=0.702nm (R_q=0.920nm)

R_a=0.274nm (R_q=0.352nm)

R_a=0.263nm (R_q=0.326nm)

Figure 2.4 (a)-(c) AFM images 4nm of Ag film with seed layer of Al, Ge, and Cu, respectively.

Further studying microscopic evolution of Ag film growth on a seed layer by observing under the top-down view of scanning electron microscopy (SEM) images for Al-Ag, Ge-Ag, and Cu-Ag samples as shown in Figure 2.5 where the images are depicted in a matrix form. It is clearly shown that Al is not as effective as Cu or Ge as a seed layer to grow Ag film.

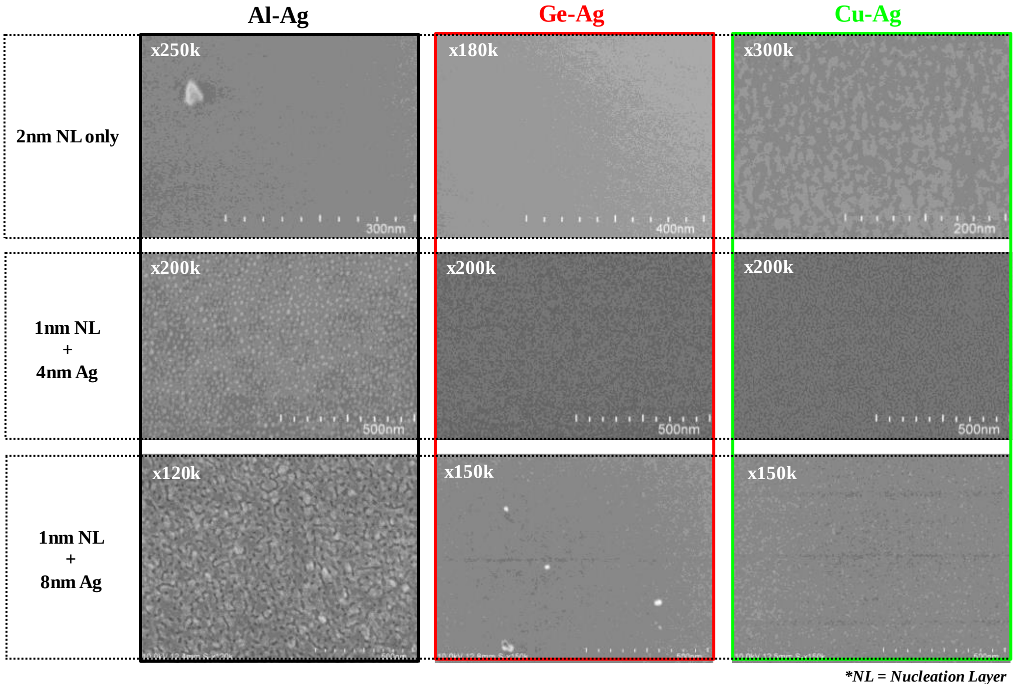

Figure 2.5 Top-down scanning electron microscopy (SEM) images of Al-Ag, Ge-Ag, and Cu-Ag films for seed layer only film or those with various thickness of Ag films.

As the thickness of the films dealt here are extremely thin, it is extremely important to gather accurate information of the thin film. In this aspect, high resolution X-ray Reflectivity (XRR) measurements were acquired because it tells comprehensive information on thin film's thickness, surface roughness, and density. In Figure 2.6, measured and simulated (fitted) XRR spectra for different types of seed layers is plotted. The sharper features and higher modulation of oscillations in the XRR intensity is a characteristic of a smooth film when the film thickness is in a similar range. Also, a rapid decrease of intensity in reciprocal space is observed for a film with greater interfacial roughness. In this respect, Ag film with Al seed layer shows highest roughness followed by that of Cu and Ge. From the simulated (fitted) spectra, Ag-film's thickness, surface roughness, and film density values were extracted and compared with those data measured from ellipsometer and AFM which are summarized in Table 2.2.

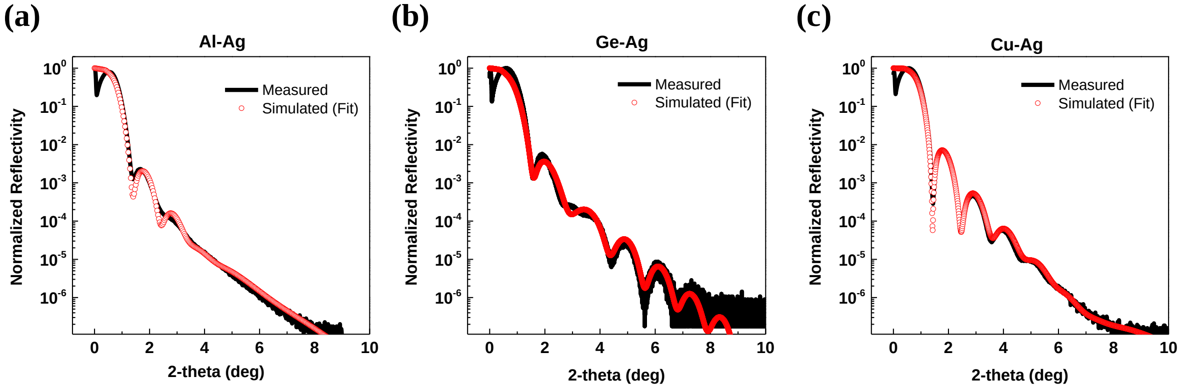

Figure 2.6 X-ray Reflectivity data for Ag thin film with (a) Al, (b) Ge, and (c) Cu as a seed layer plotting measured data (black line) and fitted simulation data (red symbol).

In general, the extracted film thickness and surface roughness from XRR matches well with the data obtained from ellipsometer and AFM with exception to the Ag film with Cu as a seed layer. Slight discrepancy in the data for Ag film with Cu as a seed layer may be attributed to the evolutionary change of film morphology as a result of exposure in air over a span of time before measuring XRR. Further discussion of film stability will be discussed in next chapter. Considering the density of Ag is 10.5 g/cm^3, extracted Ag film's density from XRR spectra can give us information on how porous or densely packed Ag atoms are inside the film. In this aspect, seed layer of Ge can give highest density of Ag film which indicates that this film is densely packed whereas those with Al or Cu shows slightly more porous behavior.

Table 2.2 Ag film's thickness, RMS roughness, and density extracted from XRR data in comparison with those from Ellipsometer and AFM.

Type	**Thickness (nm)**		**RMS Roughness (nm)**		**Ag Density (g/cm^3)**
	Ellipsometer	**XRR**	**AFM**	**XRR**	**XRR**
Al-Ag	9.32	10.91	0.891	1.03	8.29
Ge-Ag	7.44	7.92	0.312	0.335	10.03
Cu-Ag	8.99	7.58	0.233	0.682	8.30

For these layers to be used as a plasmonic device application, quality factor (Qs) is an important criterion to determine the efficiency of the device. Two figures-of-merit plot depicting Qs are plotted in Figure 2.7 for both LSPR in (b) and surface plasmon polaritons (SPPs) in (b). The Qs represents how effective films/particles resonate with the incoming light wave. Therefore, it is beneficial to have ε_1 as large as possible while ε_2 as small as possible. From these aspect, Cu-Ag film shows the highest Qs for both LSPR and SPP followed by Ge-Ag and Al-Ag. This indicate that for designing efficient plasmonic devices, type of seed layer should be chosen carefully.

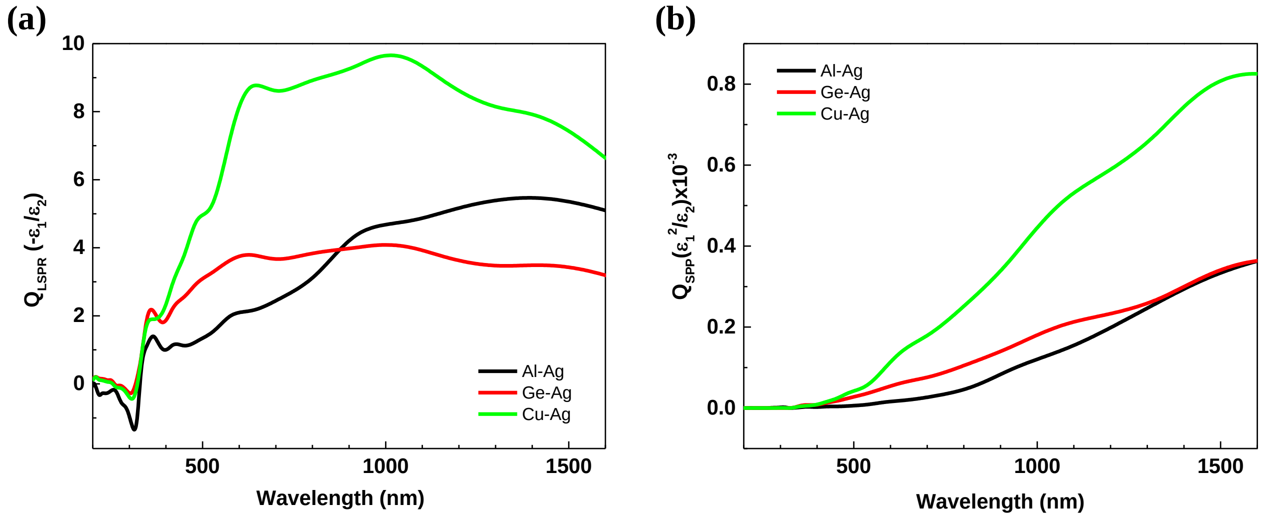

Figure 2.7 Measured Qs for (a) LSPR and (b) SPPs of 9 nm of Al-Ag, Ge-Ag, and Cu-Ag films.

Stability is one of the most important properties for a transparent conductor (TC) application, and a seed layer impacts stability of an Ag film. Film stability can be quantified with standard electrode potential (SEP), with larger SEP indicating higher likelihood of oxidation process. SEPs of Cu, Ge, and Al are -0.52, -0.12, and 1.66 V, respectively, therefore Cu or Ge are preferred as these atoms are less likely to oxidize.

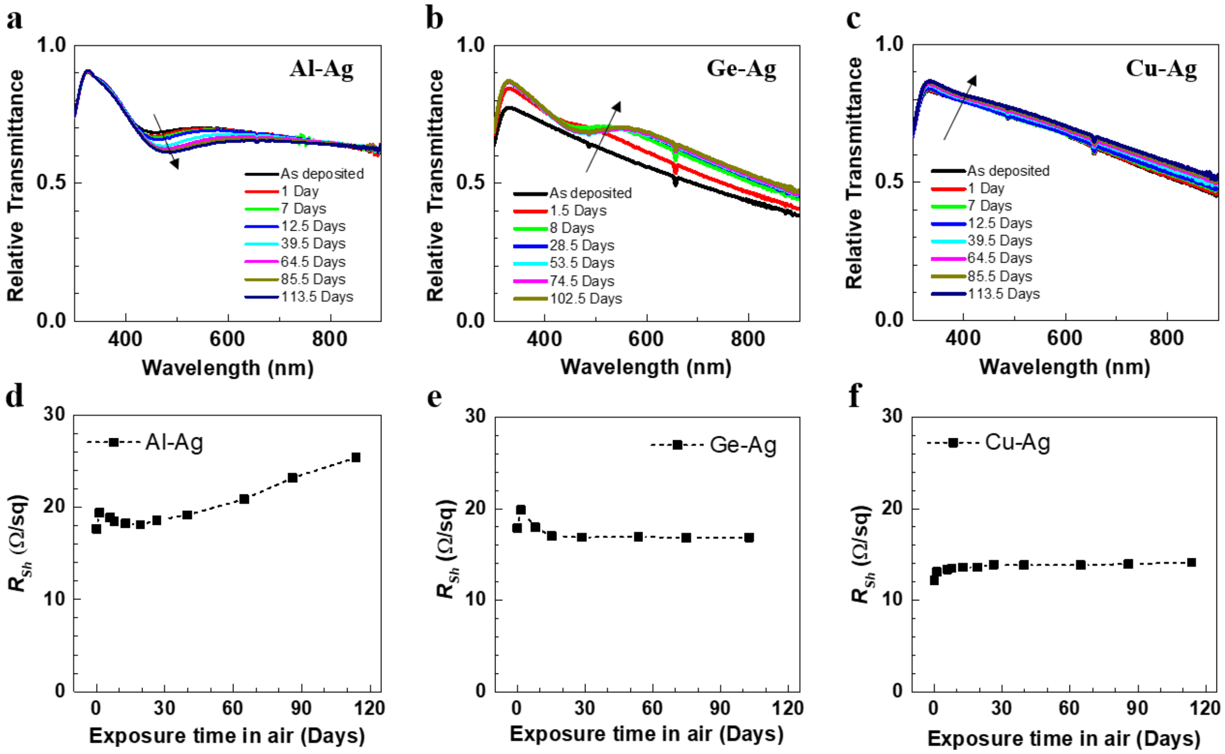

Figure 2.8 (a)-(c) Relative transmittance and (d)-(f) Sheet resistance (RSh) of Al, Ge, or Cu seeded Ag films over a span of time exposed in air, respectively. Arrows in the relative transmittance curves indicate time evolution.

Figures 2.8a - c show relative transmittance, a value normalized over the substrate, of Al-Ag, Ge-Ag, and Cu-Ag films over a span of 113.5 days exposed in air. 1 nm seed layer and 8 nm Ag films were deposited in this experiment for comparison. The transmittance shows noticeable change in Al-Ag and Ge-Ag, whereas Cu-Ag is relatively more stable, meaning that it more immune to the air exposure. The transmittance of Ge-Ag dramatically changes with time due to the migration of Ge atoms toward surface of the Ag film through the grain boundaries [12]. The similar phenomenon in co-sputtered Al-Ag film was reported by Gu et al. that diffusion of Al atoms toward interface with air creates gradient of Al content in a film depth direction [9]. These migration behaviors can be explained by their BSE and SEP. In terms of BSE, both Al and Ge have a strong tendency to bind with oxygen, thus these atoms can migrate toward the outer surface of the Ag films where oxygen is abundant. Cu, on the other hand, has much lower BSE with oxygen and lower SEP which explains lower degradation of the Cu-Ag film over time as shown in Figure 2.8c.

Figures 2.8d - f shows sheet resistance (R_{Sh}) change of the Al-Ag, Ge-Ag, and Cu-Ag films over time, respectively. The Al-Ag film shows the largest increase in R_{Sh} from 17.7 to 25.4 Ω/sq which is 43.5% change from the initial value, but the Ge-Ag and Cu-Ag films show little change in R_{Sh}. Summing up, Cu was chosen to be the most effective seed layer in obtaining highly stable ultra-smooth Ag film with low optical loss and electrical resistance.

2.4 Optimization of Cu and Ge Seed Layer

The thickness of Ge and Cu seed layers were selected and further optimized to maximize the transmittance at a visible wavelength while maintaining the continuous film behavior with minimum surface roughness. Figure 2.9 shows the result of sheet resistance (Rs), average absolute transmittance (T%), and surface roughness values as a function of Ge (black symbol) and Cu (red symbol) seed layer thickness. For all the samples, 4nm of Ag film was subsequently deposited after varying seed layer. Rs values were compared instead of resistivity because these all had same Ag film thickness. As evident in Figure 2.9a, decreasing the seed layer from 20 Å down to 5 Å increases the T% which is expected as Ge or Cu has insignificant optical loss at visible wavelength. Further decreasing it down below 5 Å reduces T% which is due to the discontinuous film behavior where the agglomerate of Ag films scatters/absorbs light and reduces T% due to the insufficient amount of seed layers that can anchor incoming Ag atoms.

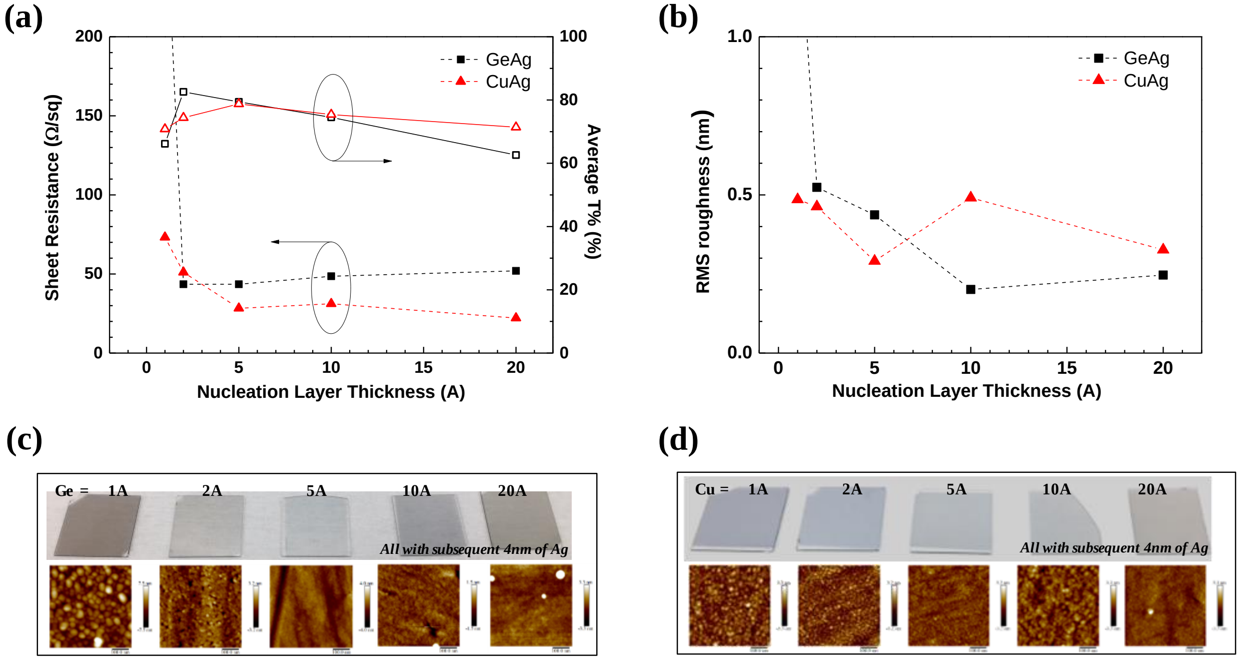

Figure 2.9 (a) Sheet resistance (Rs) and average Transmittance (T%), (b) RMS roughness of 4nm Ag thin film with varing Ge or Cu seed layer. Photographic (top) and AFM images (bottom) of 4nm Ag thin film with different seed layers for (c) Ge and (d) Cu where seed layer thickness is specified.

For the case with Rs, the film showed a constant value with decreasing seed layer thickness down to 2 Å for Ge and 5 Å for Cu. Once it decreases beyond that regime, the film's Rs drastically increases and eventually becomes discontinuous. From these aspects, Ge acts as a more effective seed layer compared to Cu purely in terms of making the subsequent Ag film continuous. RMS surface roughness values of Ge-Ag and Cu-Ag films plotted in Figure 2.9b shows roughening of

Ag film surface as seed layer thickness decreases, which may be expected. Photographic images and AFM images in Figure 2.9c and d further clarify this behavior. One can easily think that there would be a tradeoff between the Rs or T% and the surface roughness especially for this Ag film to be used as a transparent conductor or photonic device application. Based on these parameters, seed layer thickness of 5 Å, which is equivalent to about 1-2 monolayer of seed-layer, was selected as an optimum thickness for subsequent studies.

2.5 Modeling of Electron Conduction in Thin Films

2.5.1 Introduction

Classical resistivity scaling: Understanding and modeling of electron conduction mechanism in thin metal film has great scientific and engineering merit. Models to describe classical size effect of resistivity (surface or grain boundary scattering) as film thickness reduces have been used to identify the governing scattering mechanism in metal films. Active research on this field was carried out providing means to characterize metal film's electrical properties and attaining insight to further improve it for various applications [13-17], although much of these dealt with sufficiently thick films (few tens of nanometers or above).

Advancement of ultrathin film and lack of theoretical framework: More recently, metal film with thickness in the ultrathin (< 10 nm) or even extremely thin (~ 5 nm) scale has caught great interest due to its potential use for various optoelectronic and plasmonic application. For example, metals such as gold or silver (Ag) are known to have excellent optoelectronic or plasmonic property due to their low resistivity and optical loss. In order to obtain continuous and ultrathin films of these metals, efforts were made to lower the percolation thickness of these materials by overcoming their intrinsic de-wetting problem [4, 18, 19]. These efforts enabled numerous applications like transparent conductor [20, 21], EMI shielding [22, 23], or other nanophotonic applications [24-26]. As the resistivity gets more strongly coupled to the film's thickness at this ultrathin regime, understanding the mechanism of electron conduction at such ultrathin regime may provide scientific insight and engineering guidance. Despite its significance, research on ultrathin metal films so far mostly involve experimental observation of resistivity scaling [7, 8, 20] with much less or no emphasis put on the theoretical framework. It is still of a question whether the classical size effect theory can fully describe the conduction mechanism in metal film down to ultrathin or extremely thin regime.

Percolation model: Approaching from the lower thickness limit, metal film is often regarded as an inhomogeneous medium where the film's property is affected by the coalescence of metal clusters. In such a regime the medium can be treated as a metal-insulator composite where the insulator domain is air. Extensive amount of effort was made to formulate electrical conduction of metal-insulator composite medium by using electrical percolation theory [27-31], effective medium theory (EMA) [32-34] or general effective medium (GEM) theory [35] that combines percolation and EMA effect together. Despite these theories provide critical aspect on the transition behavior of the inhomogeneous medium from insulator to conductor state, previous works involving these theories typically involve resistivity modeling in the vicinity of percolation threshold. The composite materials dealt in these studies are closer to the random cluster of conductor networks rather than film-like behavior. Therefore, a closer look is needed on how these theories can interface with classical size effect models or whether these theories are responsible for conduction mechanism at ultrathin metal films.

Lack of theory in ultrathin regime: In metal film with ultrathin or extremely thin regime where its thickness can be slightly above the percolation threshold, the carrier transport mechanism may involve mixture of classical size effect and EMA/percolation effect. Relatively less efforts were put in theoretically describing the conduction mechanism of metal film at ultrathin thickness regime. Despite the values that each work provides in analyzing conduction mechanism, these works each has limitations in providing a comprehensive model that captures all the above-mentioned effects in a physically relevant way, to the best of our knowledge. For example, Vancea et al [36] demonstrated that their experimental resistivity data can be described by Fuch-Namba model down to the onset thickness of 10 nm where film becomes island-like morphology. However, as the model does not include percolation effect nor the effective medium effect, this model cannot fully describe the conduction especially as the thickness further reduces to near percolation threshold. Maaroof et al., on the other hand elegantly elaborated the change in electrical conduction of the film with respect to the critical thickness [37]. Despite the work provides valuable insight on how conduction mechanism evolves as metal film grows, discretizing the transitioning of conduction mechanism from percolation theory to size effect theory is impractical (for the continuous change of film thickness and yet with rapid transitions). As I will elaborate in the next section, it is physically more plausible to think that the effect of size effect does not vanish but is interlinked together with effective medium theory in determining the resistivity even in the vicinity of percolation threshold. Also, as the power-law nature of percolation theory show offset in the resistivity with respect to metal's resistivity as metal fraction reaches unity, their approach of using percolation theory to describe the resistivity transitioning to the size effect theory may show inaccuracy.

More recent results on studying metal film's resistivity scaling at ultrathin regime attempt to conceptually explain the conduction mechanism but deficient in theoretical calculation to verify their hypothesis [7, 38]. For example, Zhang et al. described the film's resistivity showing two different slopes where conduction at thinner region is governed by tunneling mechanism. As the resistivity values calculated from tunneling models are at least few orders of magnitude higher, which is typically used for describing conduction at discontinuous metal films [39-42], Zhang's description of conduction via tunneling can be misleading. Also, it is of a question whether the resistivity in thicker region (stage II) can be described solely by surface scattering (Fuch-Sondhiemer) model. Formica et al. observed the rapid increase in electrical resistivity of ultrathin silver film as thickness shrinks in which they attributed to surface scattering as the dominant mechanism [7]. However, this was not supported by any theoretical calculation and so their basis is unclear. As recent work by Sun et al. showed that contribution of surface scattering portion is insignificant [15] also consistent with calculation in this work, is clearly contradicting assumption made by Formica. Moreover, rapid increase in the resistivity at an extremely low thickness in Formica's work cannot be explained solely by classical size effect theory.

Recent studies on ultrathin metal films involving theoretical frameworks discuss the resistivity behavior only in context to the classical size effect model [43, 44] excluding the percolation effect. For example, Lin et al. used grain boundary scattering model to show that a strong scattering is happening at the boundary in Iridium film down to sub nanometer thickness [43]. However, such analysis of using size effect theory is applicable only for a thickness above which percolation effect no longer plays a role (or for the films free of percolation effect). This is a limitation as the film growth of most metals involve percolation problem. In total, there is an urge for theoretical framework that can comprehensively grasp the entire physical picture of film's resistivity scaling property from classical size effect regime down to near percolation regime.

In this section, I provide a theoretical framework of resistivity scaling in ultrathin or extremely thin metal film to identify the governing conduction mechanism with respect to film thickness. Experimentally, I observe the distinct transition of carrier conduction mechanism from classical size-effect dominated regime to metal-insulator composite medium dominated regime as film thickness reduces to an extremely thin regime. Measured resistivity scaling at ultrathin metal film can be theoretically described only via incorporating size effect model into the GEM theory, a theory which grasps both essence of percolation and EMA models. Bruggeman’s theory is used to model the film’s optical dielectric function near the metal-to-insulator transition regime which optically verifies the film’s transitioning from homogeneous (continuous) to inhomogeneous (quasi-continuous) state. On the verge of this transition, I introduce a critical thickness d_c defined by the onset thickness below which the resistivity contribution due to classical size effect theory rapidly diminishes while effective medium effect starts to dominate. I observe that the meaning and implication of this critical thickness is not only scientifically interesting but also practically beneficial in engineering aspect. First, below this critical thickness, electrical property of the film undergoes a drastic change where carrier's mobility drops, resulting in rapid decrease in scattering time of electrons. Physically, it is the onset point at which the electron mean free path becomes smaller than the film’s size. Second, optical absorption of the film increases while optical transmission reaches a plateau. Finally, when using such extremely thin metal film as a transparent conductor (TC), the film’s maximum figure-of-merit was theoretically determined at its critical thickness using extended GEM model.

I begin the theoretical modeling of the Ag (Cu) thin metal film by first exploring models that describe the resistivity scaling due to size effect. Specifically, I will investigate resistivity contribution due to surface scattering and grain boundary scattering as film’s size reduces and see if these models can describe the empirical data. Then, I will explore percolation model and effective medium models to see how the resistivity data can be analyzed in context to these models.

The aim of this section is to provide a theoretical model that can comprehensively describe the physics of electron conduction in Ag film as thickness shrinks to extremely thin regime.

2.5.2 Experimental Properties of Ag Film

First, Ag film was deposited on a fused silica substrate where 5Å of Cu was used as a seed-layer to promote the wetting of Ag film. This seed approach of Ag (Cu) film enables smooth and continuous Ag film down to extremely thin regime. The optimum thickness of Cu was chosen that guarantees Ag film with low electrical and optical loss with minimum surface roughness. The Ag (Cu) films were deposited using physical vapor deposition under base pressure of 1e-7 Torr at room temperature (Kurt J. Lesker Co, LAB 18 & PVD-75). The film's resistivity was measured using 4-point-probe method (Miller Design & Equipment FPP-5000) and was cross-checked with Hall measurement (Ecopia HMS-3000) where the values were consistent within 10% of range. Minimum of three samples were prepared for a given thickness where the resistivity value of each sample was obtained from the average of five different measurement data. The film's thickness was measured via ellipsometer (Woollam M-2000), which was consistent with the result obtained from calculated thickness extrapolated from deposition rate. The thickness was further verified using X-ray reflectivity (XRR, Rigaku SmartLab) which also showed consistent result with that obtained from ellipsometer. Film's transmission and reflection spectra was obtained using ellipsometer and reflectometer (F20, Filmetrics), respectively. The film's root-mean-square (RMS) surface roughness values were obtained from atomic-force-microscopy (AFM, Bruker ICON) analysis under the tapping mode, in which the extracted film's average RMS roughness value was used as a parameter in surface roughness models. X-ray diffractometer (XRD, Rigaku SmartLab) measurement was performed using Cu-Kα radiation and estimated grain size was extracted using Scherrer equation for varying Ag thickness. Transmission electron microscopy (TEM, JEOL 2010F) and scanning transmission electron microscope (STEM, JEOL 3100) images of Ag (Cu) films were obtained and processed to extract the projected area fraction ratio of metal-insulator composite films for an extremely thin film regime. For each thickness value, images were taken from at least 8 different locations of the film and the area fraction value was averaged over these images.

Thin metal film's resistivity often follows an exponential increase with decreasing film thickness. Figure 2.10a shows the log-log plot of measured Ag (Cu) film's resistivity as a function of average (effective) thickness *d* in open symbol. Note the resistivity shows two distinct linear regimes in a log-log scale (two lines are drawn as a guide only), in which the rapid resistivity scaling at lower thickness can be easily overlooked if plotted under linear scale. This double-sloped behavior is also observed on Ag film with Ge as seed-layer or even without any seed layer (Figure 2.10b and c). In fact, this double-sloped behavior can be found in other literatures for Ag film [45, 46], and in other metal films like Au [19], Cu [47], or NiCr [48]. I aim to understand this behavior, and in particular to elucidate the meaning of the critical thickness at which the transition occurs.

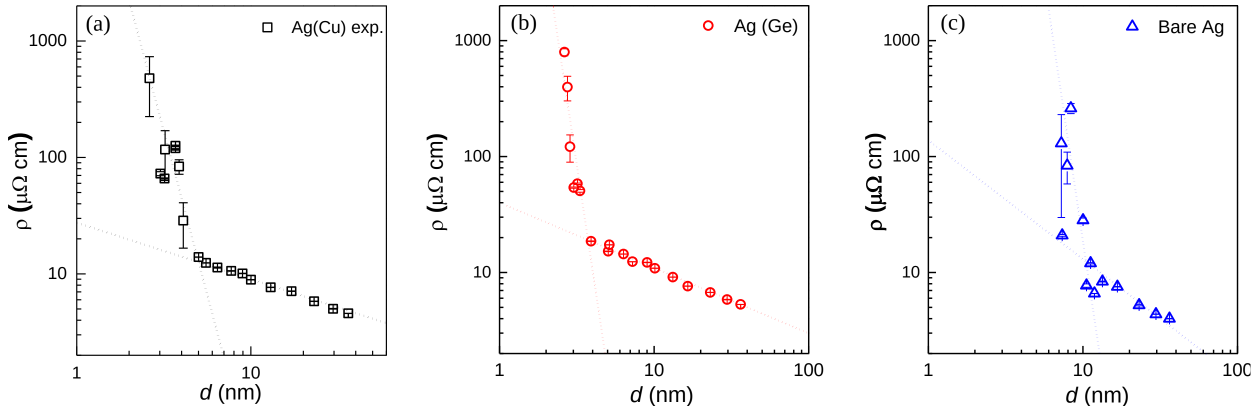

Figure 2.10 Resistivity ρ of (a) Cu, (b) Ge, or (c) no-seeded Ag films as a function of film thickness d plotted in log-log scale. The open symbols are the measured data while dotted lines extrapolating double-slope behavior of resistivity scaling are not based on any physical model.

Ultrathin Ag (Cu) film's physical properties like surface roughness, grain size, and metal fraction of film were extracted from the measured data to be used as physical parameters in size effect model and generalized effective medium model. First, Figure 2.11a is the plot of Ag (Cu) film's root-mean-square (RMS) surface roughness as a function of film's effective thickness d_{eff}. The film maintains a relatively smooth surface for thickness range from 4 to 8 nm but then rapidly increases below 4 nm due to the inhomogeneous film property. In the calculation of size effect models involving surface roughness scattering, film roughness of R_a = 0.263 nm was used which is the average roughness of film with d_{eff} ranging from 5 – 8 nm. Next, Ag (Cu) film's X-ray diffractometer (XRD) analysis was performed, and estimated crystallite grain size D was extracted using Scherrer equation for varying d_{eff} as shown in Figure 2.11b and c. As the crystallite grain size extracted from XRD is only good to show the trend while it may not represent the actual size, $d \sim D$ proportionality relation was used as an approximation in the M-S model. This should be a good approximation as I have confirmed for the case of 10 nm thickness film, grain size was confirmed to be in the range of 10 nm under transmission electron microscopy (TEM) image (inset of Figure 2.11c). Lastly, to extract metal fraction (projected area) ϕ of Ag (Cu) film as a function of film's d_{eff}, multiple of top-down TEM and scanning transmission electron microscope (STEM) images were extracted for each thickness. Figure 2.11d - h shows the selected TEM images for each thickness (d_{eff} from 2.0 - 8.5 nm) after performing image processing to calculate the void area. The region that appear to be bright in TEM images are voids whereas that appear as dark spots in the STEM image (inset of Figure 2.11f) are voids. To reduce the measurement error, ϕ

values were averaged over at least 8 different TEM images from different spots and was cross-checked with that obtained from STEM image for each thickness.

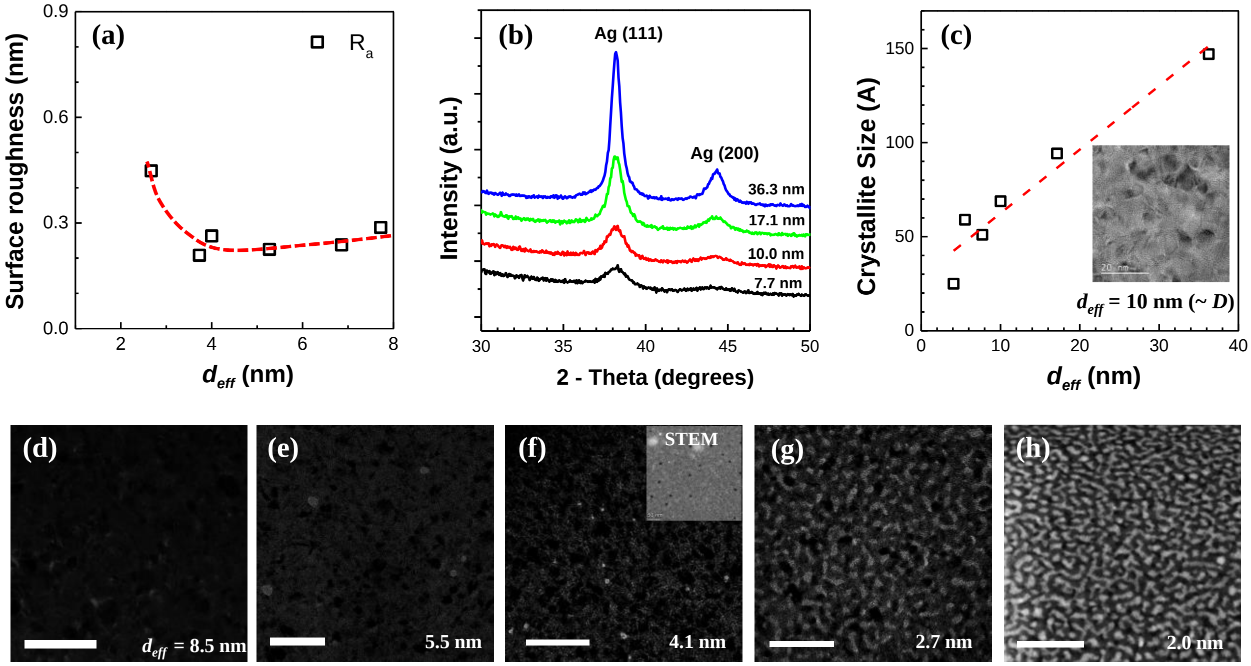

Figure 2.11 Ag (Cu) film's (a) RMS surface roughness values as a function of d_{eff}. (b) XRD intensity curve over 2- theta for different film thickness. (c) Extracted film's crystallite grain size as a function of d_{eff} showing linear relationship. Inset figure is TEM image of the film with 10 nm of thickness, which show approximate grain sizes in the range of *D* ~ 10 nm. Top-down TEM images of Ag (Cu) film with effective thickness of (d) 8.5 nm, (e) 5.5 nm, (f) 4.1 nm, (g) 2.7 nm, and (h) 2.0 nm. All images have scale bar of 50 nm. Inset of (f) is the STEM image taken as an example where black dots show void areas.

2.5.3 Modeling by Classical Size Effect Model

The first comprehensive analysis of size effect in metal thin film was suggested by Fuch, and later known as Fuchs-Sondheimer (F-S) model which takes into account resistivity increase due to surface scattering as film's thickness becomes comparable to the electron mean free path [49]. The resistivity of a thin metal film described by this model is calculated as:

$$\rho_{FS} = \rho_i \left[1 - \left(\frac{3}{2k}\right)(1-p)\int_1^{\infty}\left(\frac{1}{t^3} - \frac{1}{t^5}\right)\frac{1-\exp(-kt)}{1-p\cdot\exp(-kt)}dt\right]^{-1} \tag{2.1}$$

where ρ_i is the bulk resistivity of the metal, $k(=d/l_0)$ is the ratio between the film's average thickness d and the electron's mean free path in bulk l_0, p is the specularity parameter describing the degree of specular reflection at the surface, and t is the integral variable. Although F-S model has been widely used to analyze experimental results, it has few limitations and so is often regarded as a model that underestimates the resistivity increase as thickness shrinks, especially at thinner regime [36]. As one example of limitation, the model considers the degree of surface scattering by using specularity parameter p, but it fails to take into account the effect of surface roughness of the actual deposited films. To better express this surface roughness, Ziman [50] and Soffer [51] improved the model by incorporating surface roughness into specularity parameter so that the value p is based on a physically relevant parameter. This model allows for comparison without needing of fitting parameters when the surface roughness of top r_1 and bottom r_2 interface is known, in which the specularity parameters are given by:

$$p_1(cos\theta) = \exp\left[-\left(\frac{4\pi r_1}{\lambda_F}\right)^2 cos^2\theta\right] \tag{2.2a}$$

$$p_2(cos\theta) = \exp\left[-\left(\frac{4\pi r_2}{\lambda_F}\right)^2 cos^2\theta\right] \tag{2.2b}$$

$$\overline{p(cos\theta)} = \frac{1}{2}\left[p_1(cos\theta) + p_2(cos\theta)\right] \tag{2.2c}$$

where θ is the angle of incidence on electrons to the surface, p_1 and p_2 are specularity parameters for top and bottom surface respectively, the average specularity is $\overline{p(cos\theta)}$, and λ_F is the electron wavelength at a Fermi surface (typically ~ 6Å for Ag). The resulting resistivity by Soffer model is then:

$$\rho_{Soffer} = \rho_i \left[1 - \left(\frac{3}{2k}\right) \int_0^1 \frac{(u-u^3)\left[1-\exp\left(-\frac{k}{u}\right)\right] \left\{1-\bar{p}(u)+[\bar{p}(u)-p_1(u)p_2(u)]\exp\left(-\frac{k}{u}\right)\right\}}{[1-p_1(u)p_2(u)\exp\left(-\frac{2k}{u}\right)} du \right]^{-1} \tag{2.2d}$$

Soffer's model assumes that the scattering at the surface is only attributed to the roughness. The limitation of this model is that the contribution of roughness to resistivity is minute unless roughness r_1 or r_2 is close to λ_F [36].

Later, Namba represented 1-dimentional geometrical roughness using Fourier series has proposed the inclusion of geometrical film cross section due to roughness into F-S model's expression for resistivity [52]. This leads to a stronger increase in resistivity which better estimates experimental resistivity compared to other existing surface scattering models especially at a low thickness regime of 40 nm [41, 53]. The resulting expression for the roughness incorporated thickness $d(x)$ is given as:

$$d(x) = d_0 + h\sin(2\pi x/L) \tag{2.3a}$$

where x is one-dimensional position coordinate, L is sample length, d_0 is average film thickness, and h is a measure of surface roughness. Then the resistivity of the film is:

$$\rho_{Namba} = \rho_i \frac{d_0}{L} \int_0^L \frac{\rho_{FS}[d(x)]}{d(x)} dx \tag{2.3b}$$

where $\rho_{FS}[d(x)]$ is the resistivity according to F-S theory. Despite its limitation that sinusoidal expression of the real film's roughness is an oversimplification of a problem, Namba model gives a strong resistivity scaling with respect to the thickness. In this work, Soffer and Namba's models will be used for surface scattering models.

A typical metal film deposited via commonly used physical vapor deposition will be polycrystalline and have a finite grain size. The effect of grain boundary scattering on the resistivity is well described in Mayadas-Shatzkes (M-S) model [54]. M-S model treats electron as a wave traversing the grain boundary as a periodic potential well, and the probability that electron wave gets reflected is represented by reflection coefficient R. The expression of grain-boundary scattering on the resistivity of thin film is ρ_{MS}:

$$\rho_{MS} = (\rho_i/3)\ \left[\frac{1}{3} - \frac{1}{2}\alpha + \alpha^2 - \alpha^3 \ln\left(1 + \frac{1}{\alpha}\right)\right]^{-1} \tag{2.4a}$$

$$\alpha = \frac{l_0}{D}\frac{R}{1-R} \tag{2.4b}$$

where l_0 is the mean free path of a single crystal material, D is the grain size. Grain boundary scattering is known to be one of the most dominant scattering mechanisms of electron transport in thin metal films [15, 44]. Typically in metal films deposited via physical vapor deposition technique, grain boundary is known to scale proportional to the film thickness and so the decrease in the grain size increases grain boundary scattering [55, 56]. Our calculation shows that grain boundary model can approximate the resistivity scaling of Ag film at ultrathin thickness regime while surface scattering model severely underestimates as shown in Figure 2.12, which shows that grain boundary scattering plays a dominant role as film thickness reduces.

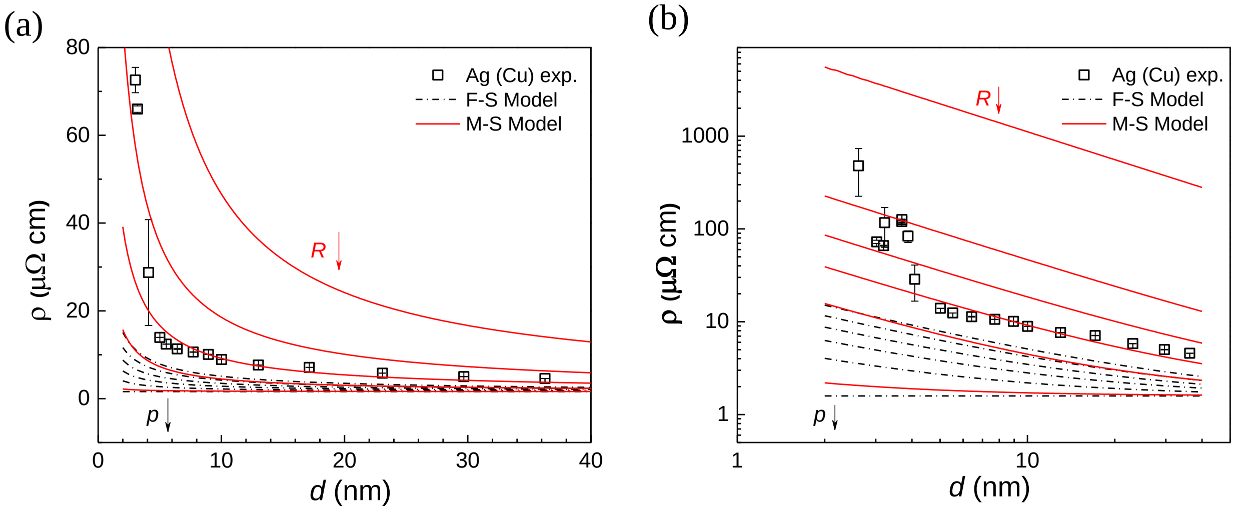

Figure 2.12 Theoretically calculated ρ - d plot in (a) linear-linear and (b) log-log scale of Ag (Cu) thin film using surface (F-S) or grain boundary (M-S) scattering models each model with varying specularity parameter p and reflection coefficient R, respectively. The open symbols are the measured data. F-S and M-S models are plotted in dotted-black and red-solid lines, respectively.

Theoretical values calculated for sweeping parameters where arrows indicate the direction of parameters (with ranges $0 \leq p \leq 1$ and $0 < R < 1$) in decreasing order.

Mayadas and Shatzkes further derived the resistivity model for the case where there is interplay between the grain boundary and surface scattering [57]. This model, so called Mayadas Shatzkes Surface (MSS) model, takes into account the grain boundary scattering as well as those electrons scattered at this boundary subsequently redirected to the film surface and gets scattered there. The expression of MSS model is:

$$\rho_{MSS} = \left[\frac{1}{\rho_{MS}} - \left(\frac{6}{\pi k \rho_i}\right)(1-p)\int_0^{\pi/2} d\phi \int_1^{\infty} dt \; \frac{cos^2\phi}{H^2(t,\phi)}\left(\frac{1}{t^3} - \frac{1}{t^5}\right)\frac{1-\exp\,[-kt\,H(t,\phi)]}{1-p\cdot\exp\,[-kt\,H(t,\phi)]}\right]^{-1} \quad (2.5a)$$

$$H(t,\phi) = 1 + \frac{\alpha}{\cos\phi\,\sqrt{1-1/t^2}} \quad (2.5b)$$

In principle, MSS model is a violation of the Matthiessen’s rule which states that each of the scattering sources are independent of each other. It is only at a low temperature regime where the thermal energy is low enough to depopulate the phonon density at the film surface that the mechanism in MSS model will likely to come into play. The summary and the essence of all the models discussed here are summarized in flow diagram as shown in Figure 2.13.

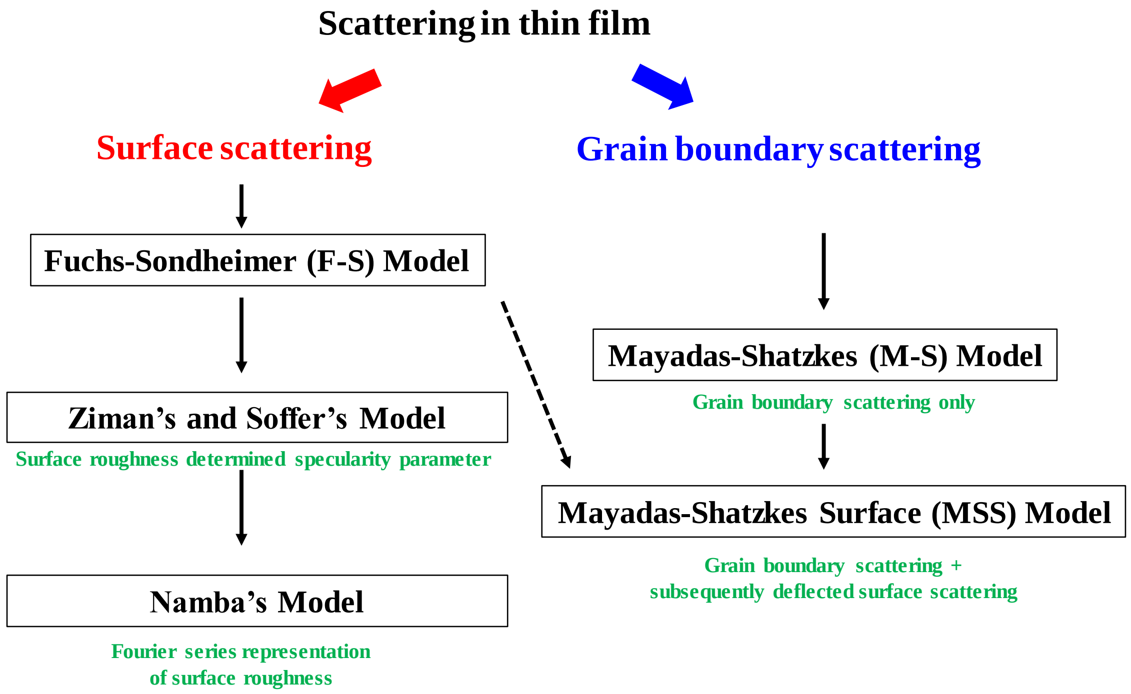

Figure 2.13 Schematic chart describing theoretical models of electron transport in thin metal film.

In practice, it is more likely that surface (or roughness) scattering and grain boundary scattering both take role in decreasing the conductivity, which is determined by the rate limiting step. To further quantify the contribution of each scattering event, Matthiessen's rule can be applied for various combinations of surface (roughness) scattering models and grain boundary model:

$$\rho_{size} = \rho_{Surf} + \rho_{GB} - \rho_i \tag{2.6}$$

The total resistivity is the summation of ρ_{Surf}, resistivity contribution determined by the surface scattering models and ρ_{GB}, that from the grain boundary scattering model, minus intrinsic resistivity of a bulk material ρ_i (as this portion was each included in ρ_{Surf} and ρ_{GB}). I applied MSS model to see if it would suffice to describe the empirical data. Also, each scattering model was used alone to see whether each of these models can fit the empirical data.

In the calculation of models, bulk resistivity of ρ_i = 1.59 μΩ·cm and electron mean free path of l_0 = 53 nm was used for silver film [58]. Surface roughness models by Soffer (*eq 2.2*) and Namba (*eq 2.3*) were adopted to calculate the resistivity. Ag film's RMS surface roughness values of R_a = 0.263 nm (Figure 2.11a) was used to extract physically meaningful r_1 and h values for these models. The extracted roughness amplitude was $r_1 = h = \sqrt{2} \times R_a = 0.37$ nm. r_2 of 0.71 nm was used to reflect the possible roughness caused by the seed layer. For M-S model, the grain size D is set equal to the film's thickness d, which is a reasonable approximation for physical vapor deposited metal films within relatively thin regime [55, 56, 59]. Grain size extracted from the film's XRD analysis scaled linearly with respect to the film's average thickness ($D \approx d$), which confirms the validity of this approximation (Figure 2.11b and c).

To determine which combination of models best describe the experimental resistivity data, the deviation δ of theoretical resistivity (ρ_{theory}) from experimental resistivity (ρ_{exp}) was quantified by the following equation:

$$\delta = \sum_d \left\{ \left(\rho_{theory}(d) - \rho_{exp}(d) \right) \times d \right\}^2 \tag{2.7}$$

where the deviation of resistivity at each thickness was weighed by d to depreciate the large resistivity deviation at lower thickness. For each or combinations of theoretical models, optimum fitting parameters that minimizes δ were selected to best represent experimental data. For the combination of models involving one or two fitting parameters, 1-dimensional plot or 2-dimensional plot of deviation was calculated for the entire range of parameters to find the optimum point. For example, applying Matthiessen's rule, the best combination of fitting parameters when using Namba and M-S models were p = 0.1 and R = 0.2, respectively (Figure 2.14a). In this manner, the optimum fitting parameters for each given theoretical model were found and the resulting resistivity-thickness curves for the selected combinations of models are plotted altogether in Figure

2.14b where d is the total average thickness of the Ag (Cu). Experimentally measured resistivity values are plotted in open symbol while theoretical models are plotted in lines.

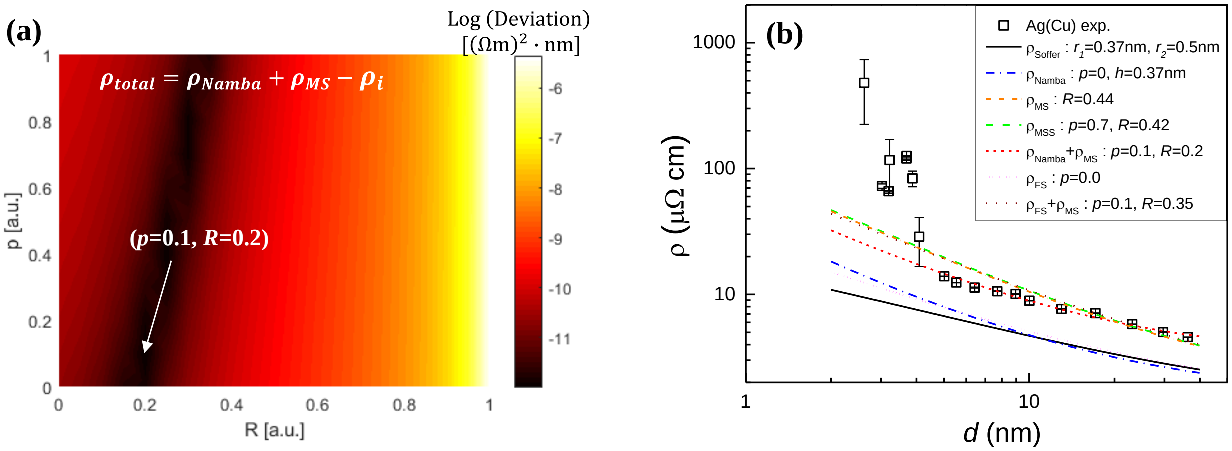

Figure 2.14 (a) Colormap of deviation (*eq 2.7*) in theoretical model (Namba [*eq 2.3*] + M-S [*eq 2.4*] models) from experimental data involving two parameters, p and R where optimum point is at p = 0.1 and R = 0.2. Colormap scale is plotted in log scale. (b) Comparison of resistivity data predicted by all the combinations of surface or grain boundary models. Data in symbol is measured data while that in lines are calculated from a single or sets of models.

First, among all discussed models, applying Matthiessen's Rule by summing Namba model (p = 0.1, h = 0.37 nm) for surface scattering model and M-S model (R = 0.2) for grain boundary scattering best describes the actual resistivity-thickness data of Ag (Cu) film at least above d = 5 nm regime. Other models either poorly underestimates the resistivity or fails to follow the exact slope of measured data points. Namba model shows stronger scaling compared to that described by the Soffer model as the film thickness reduces known to well reflect experimental data by considering film roughness [36, 53]. Portion of surface scattering induced by grain boundary scattering described in MSS model is quite insignificant (p = 0.7, R = 0.42). This is because the interaction between the two becomes substantial only at low temperature [15], which is why resistivity described by MSS model shows similar behavior as grain-boundary-only MS model (R

= 0.44). Overall, the decoupling of surface and grain boundary scattering by using Matthiessen's rule best explains our empirical data which is consistent with other works [15, 16]. Nevertheless, none of these models succeed to describe the resistivity for $d < 5$ nm. This leads to a hypothesis that a completely different mechanism governs the transport at extremely thin regime which cannot be explained by existing size effect theories of thin metal films.

2.5.4 Modeling by Mean-field Theories

At the lower thickness limit of metal film near percolation threshold, the resistivity scaling encounters a phase transition problem, often described as percolation effect. In such extreme limit of reduced thickness where the film is no longer continuous but instead behaves as a random network of conductors (so called metal-insulator composites), rapid change in resistivity occurs in the vicinity of percolation threshold following a power-law behavior. Electrical percolation model has been widely used to describe the resistivity scaling in metal-insulator composite materials [60, 61]. However, the key limitation of this model is that it applies only to near the conductor-insulator transition region [62]. EMA of electrical conductivity such as Landauer's theory [32] is also a commonly accepted model to describe the resistivity of metal-insulator composites. Despite EMA models can predict the resistivity for a relatively wide range of composite volume fraction, they fail to predict the resistivity of a composite material close to the conductor's percolation threshold [63]. In view of these problems within the framework of both percolation and effective medium theories, GEM equation was proposed by McLachlan et al. where effective conductivity σ_{GEM} is expressed as [35]:

$$(1-\phi)\cdot\frac{\sigma_m^{-t}-\sigma_{GEM}(\phi)^{-t}}{\sigma_m^{-t}+A\cdot\sigma_{GEM}(\phi)^{-t}}+\phi\cdot\frac{\sigma_0^{-t}-\sigma_{GEM}(\phi)^{-t}}{\sigma_0^{-t}+A\cdot\sigma_{GEM}(\phi)^{-t}}=0 \tag{2.8a}$$

$$A = \frac{1-\phi_c}{\phi_c} \tag{2.8b}$$

where ϕ is the metal fraction, σ_0 is the bulk conductivity of metal, t is the critical exponent of conductivity, ϕ_c is percolation threshold fraction, A is the constant, σ_m is the conductivity of the medium which can be approximated as ~ 0 (for insulator). This equation includes both effective medium approximation with the critical exponent of conductivity which can describe the resistivity (inverse of conductivity) for a wide range of composite volume fraction including that near the percolation threshold which is known to well describe resistivity for various composite materials [64-67]. Here, I attempt to use this model to describe the resistivity scaling of Ag (Cu) film.

There are few parameters that need to be extracted to see if GEM model can express the experimental resistivity scaling for extremely thin regime. First, percolation threshold fraction ϕ_c and critical exponent of conductivity t need to be determined. To determine p_c and t, the data have been fit to the power law:

$$\rho = \rho_0[(\phi - \phi_c)/(1-\phi_c)]^{-t} \tag{2.9}$$

where ρ_0 is the resistivity scaling factor. Metal fraction of each metal films was extracted from TEM images (Figure 2.11d - f).

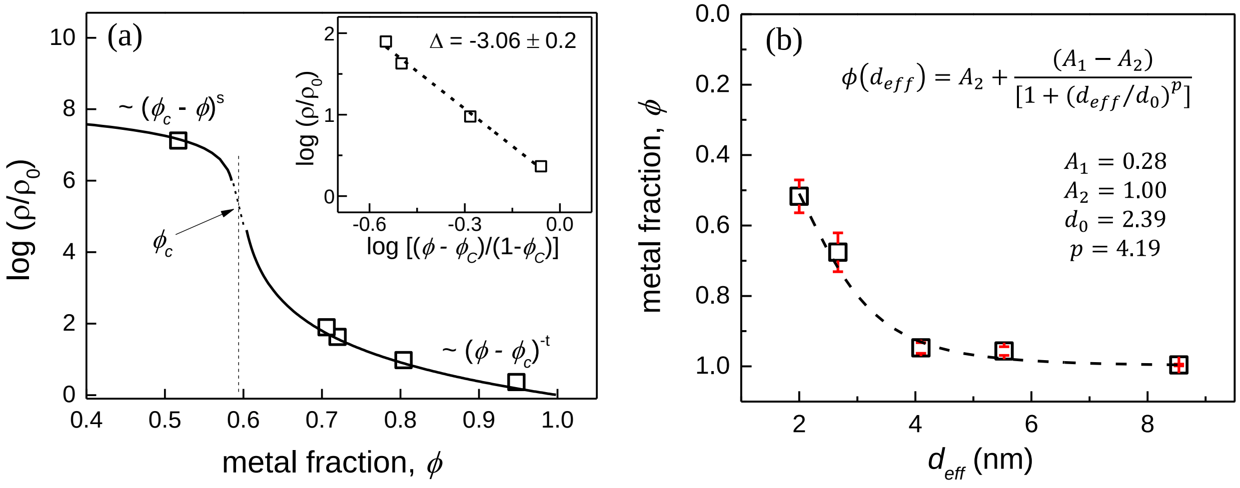

Figure 2.15 (a) Log plot of normalized resistivity ρ/ρ_0 as a function of metal fraction for measured and theory. Percolation theory of conductivity with $\rho/\rho_0 = (\phi - \phi_c)^{-t}$ for $\phi > \phi_c$ and $\rho/\rho_1 = (\phi_c - \phi)^s$ for $\phi < \phi_c$ was used as a model for theoretical calculation. Percolation threshold ϕ_c of 0.59 (indicated as dotted line), critical exponent values of t and s of 3.06 and 1.0, respectively, metal-insulator resistivity ratio of $\rho_0/\rho_1 = 10^8$ was used where resistivity scaling factors ρ_0 and ρ_1 are the resistivity of metal and insulator, respectively. Inset graph shows a plot of ρ/ρ_0 as a function of $(\phi - \phi_c)/(1 - \phi_c)$ in log-log scale where the negative of the slope Δ represent t found here as 3.06 ± 0.2. (b) The measured metal fraction ϕ of Ag (Cu) film as a function of film's effective thickness d_{eff} shown as a symbol. Its empirical relationship was extracted using logic function plotted in dotted line where its equation is in the inset.

The negative of the slope in the inset figure of Figure 2.15a is the critical exponent of conductivity t [68], which was extracted as $t = 3.06 \pm 0.2$, with a percolation threshold value ϕ_c of 0.59 and resistivity factor ρ_0 of 7.66 μΩ cm (value at which film becomes completely free of voids). The R-Square value for the fit is 0.9932, indicating a reasonable fit. It has been verified experimentally that the critical exponent of a metal-insulator composite follows a three-dimensional network with theoretical universal value of $t = 2$ [62, 69, 70] although non-universal behavior of values close to 3 have been commonly observed [68, 71], which is explained in terms of the mean-field behavior [72]. For our film's case, the critical exponent of conductivity follows more of the mean-field value that may be affected by the existence of the underlying seed-layer. In case of percolation threshold ϕ_c, a theoretically calculated value for bond percolation for a disk shape (which may resemble a typical metal cluster) is 0.6763 [73]. However, wide range of values from 0.47 [27] to 0.63 [70] were experimentally reported for a metal film's case. For our film's case, with $\phi_c = 0.59$ and $t = 3.06$, electrical percolation model [62] of $\rho/\rho_0 = (\phi - \phi_c)^{-t}$ for $\phi > \phi_c$ and $\rho/\rho_1 = (\phi_c - \phi)^s$ for $\phi < \phi_c$ well represents the experimental resistivity data as shown in Figure 2.15a. Here, critical exponent value s at lower metal fraction of $s = 1$ and metal-insulator resistivity ratio of ρ_0/ρ_1 = 10^8 was used [62]. Asa a further evidence, I observed the real part of the optical dielectric function changing its sign from negative to positive in the vicinity of ϕ_c= 0.59 (Figure 2.16) which is indicative of metal-to-insulator transition [69].

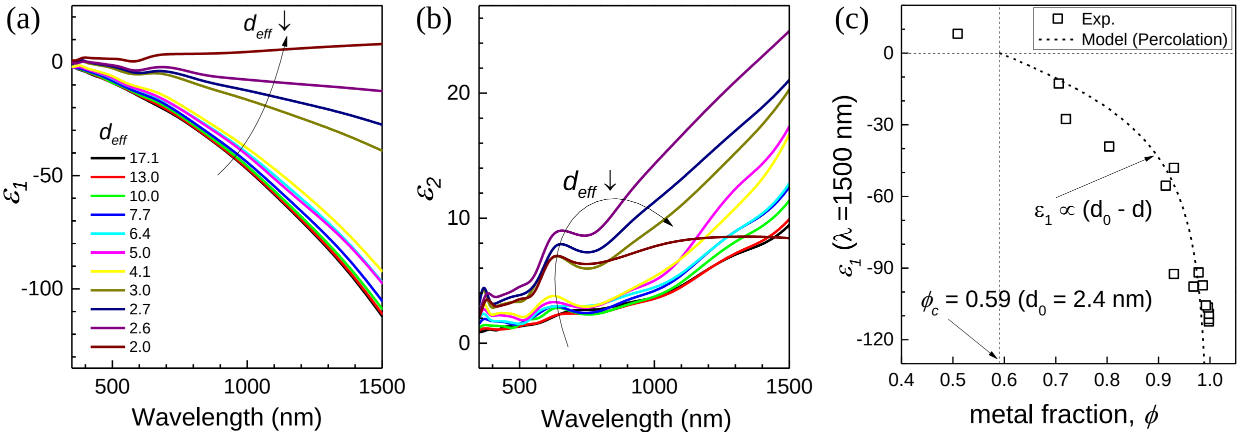

Figure 2.16 (a) Real part ε_1 and (b) imaginary part ε_2 of Ag (Cu) film's dielectric function for different film thickness d_{eff}. Black arrows indicate the curve change behavior as decreasing d_{eff}. (c) Measured ε_1 (in symbol) at wavelength of 1500 nm as a function of film's metal fraction ϕ, where ϕ for a given film thickness was obtained from empirical relationship in Figure 2.15b. Modeled ε_1 (dashed line) using percolation model [M. Hovel et al. Phys. Rev. B 81, 035402]. Percolation threshold ϕ_c of 0.59 is indicated in vertical black dotted line. ϕ_c coincide with the metal fraction at which ε_1 crosses 0 indicative of metal-insulator transition.

From these results, the extracted values of ϕ_c and t best represent the physical nature of our film and so are reasonable values to use for GEM model in representing percolation effect. Next, relationship between effect thickness d_{eff} versus metal fraction ϕ is needed to use GEM model to express resistivity as a function of thickness. Although effective thickness may be more appropriate to use for inhomogeneous type of film but both average and effective thickness hold identical meaning and so will be interchangeably used to represent the film's thickness of entire thickness range throughout the text. Figure 2.15b shows the empirical relationship obtained for effective thickness versus metal fraction using logistic function which is a reasonable approximation as the metal fraction will saturate to either 0 or 1 as film thickness goes to lower or upper extreme.

Using $\phi(d_{eff})$, ϕ_c, and t values, resistivity value from GEM model was calculated using *eq 2.8* ($\rho_{GEM} = 1/\sigma_{GEM}$) which is plotted as blue dotted line in Figure 2.17. Percolation threshold ϕ_c of 0.59 which corresponds to d_{eff} = 2.4 nm is marked as a grey dotted line in the figure. Despite the power law in GEM model allows rapid increase of resistivity in the proximity of percolation threshold ϕ_c (grey dashed line), the GEM model alone is insufficient to accurately describe the resistivity at d_{eff} near 5 nm regime. The discrepancy between the model and the measured value remains even if the resistivity factor ρ_0 is set to a higher value where $\phi \sim 1$ approximation holds. This discrepancy arises from the fact that the model assumes a constant resistivity throughout the entire range of $\phi(d_{eff})$ which may be an oversimplification of the problem. In practice, as the resistivity due to classical size effect ρ_{size} is a strong function of thickness, the resistivity factor in GEM model needs to be treated as a variable instead of ideal bulk property. The resistivity size effect can be incorporated into GEM model by substituting ρ_0 with ρ_{size} in *eq 2.8*, which is the extended version of GEM model noted as $\rho_{ext.\ GEM}$.

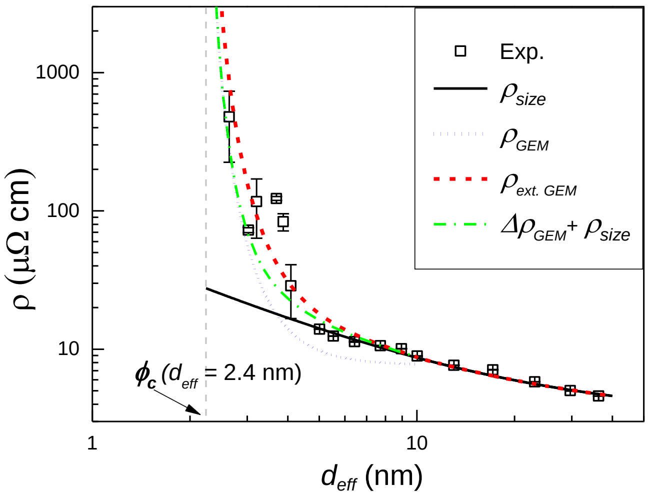

Figure 2.17 Resistivity ρ of Ag (Cu) film as a function of film's effective thickness d_{eff}. The open symbols are experimental resistivity values and lines are calculated values from the theoretical models based on size effect (ρ_{size} [*eq 2.6*], black solid line), GEM (ρ_{GEM} [*eq 2.8*], blue dotted line), extended GEM ($\rho_{ext.GEM}$ [*eq 2.8* with replacing σ_0 with σ_{size}= $1/\rho_{size}$], red dashed line), or applying Matthiessen's rule ($\Delta\rho_{GEM}$+ρ_{size} [*eq 2.6* and *eq 2.8*], green dashed-dot line). Thickness that corresponds to the percolation threshold ϕ_c is shown as vertical grey dashed line for reference.

The result is plotted in Figure 2.17 with red short-dashed line which excellently represent the empirical data for the entire thickness range including the d_{eff} < 5 nm regime. For the range of film thickness sufficiently large where the film is free of voids ($\phi = 1$), $\rho_{ext.\ GEM}$ converges to ρ_{size}. One can argue if Matthiessen's Rule can be applied instead, where the total resistivity can be represented as a summation of resistivity portion due to composite medium effect only noted as $\Delta\rho_{GEM}$ ($= \rho_{GEM} - \rho_0$) and size effect noted as ρ_{size}. This is plotted as green dash-dot line in Figure 2.17 which shows a slight under-estimation of the resistivity in the d_{eff} slightly below 5 nm. In principle, Matthiessen's rule applies only when scattering events are assumed to be independent of each other. As the film thickness decreases, the size effect of resistivity will increase the scattering rate (governed by surface and grain boundary scattering) of an electron that is traveling inside metal-insulator medium where its effective path scales by a power law described by GEM model. As the scattering due to size effect theory directly influence the conduction within metal-insulator medium, these two events cannot be decoupled. Therefore, Matthiessen's rule is not applicable in this case but extended GEM model, which couples size effect with GEM model is physically more relevant.

Also, only the GEM model can correctly follow the resistivity change with respect to d_{eff} while neither effective medium approximation (by Landuaer's model [32]) nor electrical percolation model [62] alone are sufficient in describing the experimental result. Let us investigate these models. Electrical percolation model ($\rho_{percolation}$) approaching from higher metal fraction ϕ [62]:

$$\rho_{percolation}/\rho_0 = (\phi - \phi_c)^{-t} \tag{2.10}$$

where ρ_0 is the resistivity scaling factor, ϕ_c is the percolation threshold fraction, t is the critical exponent of conductivity. This electrical percolation theory which uses power law to describe the transition of conductivity applies only to near the conductor-insulator transition region. Next, I look into the effective medium approximation (EMA) by Landauer model (ρ_{EMA}) which describes the electrical conduction in inhomogeneous medium [32, 33] given as:

$$\rho_{EMA}/\rho_0 = (1 - \phi_c)/(\phi - \phi_c) \tag{2.11}$$

Theoretically predicted resistivity values from each above-mentioned model was calculated with setting ϕ_c a 0.59, t as 3.06, ρ_0 as 7.66 Ω cm. Also, empirical relationship between d_{eff} and ϕ described in Figure 2.15b was used to transform these models into d_{eff} domain. The result from all four models are plotted in Figure 2.18.

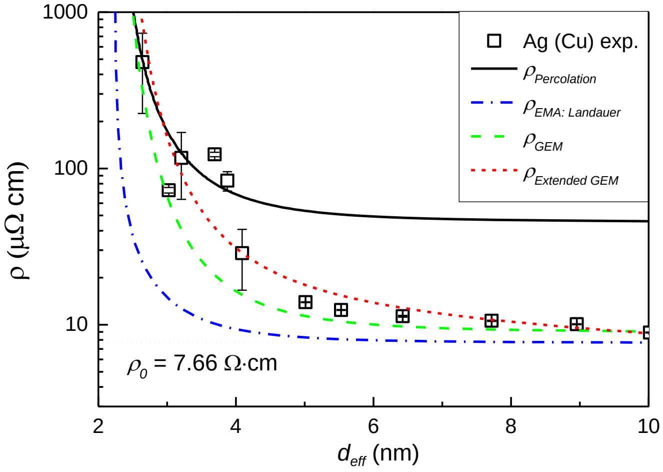

Figure 2.18 $\rho - d_{eff}$ plot from theory by percolation model [$\rho_{percolation}$, *eq 2.10*], Landauer model [ρ_{EMA}, *eq 2.11*], GEM model [ρ_{GEM}, *eq 2.8*] and extended GEM model [$\rho_{ext.GEM}$, *eq 2.8* with $\rho_0 = \rho_{size}$]. Grey horizontal line indicates resistivity scaling factor (or baseline resistivity) of ρ_0 = 7.66 Ωcm. Experimental resistivity values are plotted in symbol for reference.

From this result, extended GEM best describes the resistivity scaling near or below 5 nm. In case of percolation model, the power-law nature of the model gives good approximation near the percolation threshold of 2.4 nm. However, the resistivity scaling factor to the power of t prevents it from converging to ρ_0 at high metal fraction. For the case of EMA model, despite its convergence to ρ_0 at larger d_{eff}, it gives poor approximation near the percolation threshold thickness, which is the limitation of this model. GEM model which excludes the size effect theory, better represent the overall resistivity scaling compared to former two models but still showing a level of insufficiency (due to the absence of size effect theory). By considering size effect into GEM, extended GEM shows good prediction to the experimental data which is a more physically correct and relevant picture for our ultrathin Ag (Cu) film. In sum, to the best of my knowledge, this extended version of GEM model is the only theoretical model that can comprehensively express the resistivity scaling of thin metal film down to ultrathin or extremely thin regime including percolation region.

2.6 Verification and Implication of Model

2.6.1 Dielectric function of inhomogeneous medium

Dielectric function of Ag film at ultrathin regime was modeled using Bruggeman's effective medium theory (BEMT) to optically verify the inhomogeneous behavior of metal film near film thickness of 5 nm. According to BEMT, dielectric function of inhomogeneous metal film ε_{eff} can be solved by solving the following equation [74]:

$$f_m \cdot \frac{\varepsilon_m - \varepsilon_{eff}}{\varepsilon_{eff} + L(\varepsilon_m - \varepsilon_{eff})} + f_{air} \cdot \frac{\varepsilon_{air} - \varepsilon_{eff}}{\varepsilon_{eff} + L(\varepsilon_{air} - \varepsilon_{eff})} = 0 \qquad (2.12)$$

Here, f_m and f_{air} (= 1 - f_m) are the volume fractions of metal and air (or void) in inhomogeneous metal film, respectively and ε_m and ε_{air} (= 1) are dielectric functions of metal and air, respectively. L is the depolarization factor where in BEMT, it is identical to the critical filling factor at the percolation threshold [75]. L was approximated as 0.59 for our film. Dielectric function of void-free 13 nm thick Ag (Cu) film was chosen as ε_m in the calculation. Measured real part of dielectric function ε_1 of inhomogeneous metal films with air fraction ϕ_{air} (= 1 - ϕ) ranging from 0 to 48.3 ± 4.7 % is plotted as solid lines in Figure 2.19.

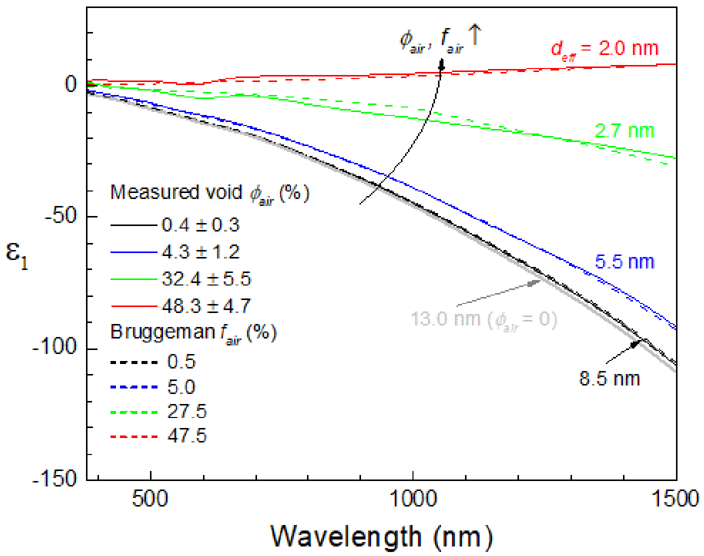

Figure 2.19 Ag (Cu) film's real part of dielectric function ε_1 as a function of wavelength for different air fraction. Solid lines are the measured ε_1 for varying projected air fraction ϕ_{air}. Dashed curves are ε_1 (real part of ε_{eff}) calculated from BEMT model (*eq 2.12*) for varying volumetric air fraction f_{air}. For each curve, corresponding film thickness d_{eff} are noted as well. The curves show a trend of increase in ε_1 for entire wavelength range as air fraction increases.

Note there is a minute change in ε_1 at the visible to near-infrared wavelength range when the thickness of the film is reduced from 13 nm to 8.5 nm as long as the metal fraction much larger than the air fraction. It is around the thickness of 5 nm or below at which ε_1 dramatically changes, which indicates that ε_1 is strongly influenced by ϕ_{air} as air fraction portion becomes substantial. Also, it is within the ϕ_{air} range of 32.4 ~ 48.3 % at which ε_1 changes its sign from negative to positive (Figure 2.16) which indicates metal-to-insulator transition [28, 69]. This transition point is consistent with the electrical percolation model discussed above. BEMT was used to model such change in the dielectric function and explain inhomogeneity of the metal film. Measured ε_1 were compared with ε_{eff} calculated from *eq 2.12* where the value of f_{air} was selected that best represent the measured result. Then, f_{air} was compared with ϕ_{air} to see if BEMT reflects the physical nature of the film. Only real part of the dielectric function was modeled as the imaginary part involves loss terms such as plasmonic extinction which is not considered in BEMT model. The calculated ε_{eff} for each ϕ_{air} case is plotted with dotted lines in Figure 2.19 with corresponding f_{air} (in %) indicated in the label. In general, f_{air} from the BEMT model matches well with the empirically obtained air fraction ϕ_{air} of the film. A slight difference in these values were observed for the film thickness of d_{eff} = 2.7 nm where empirical ϕ_{air} was 32.4 $\pm$ 5% while extracted f_{air} from BEMT was 27.5 %. This slight difference (within error bound) may be attributed to the absence of percolation effect in the BEMT. Nevertheless, consistency in ε_{eff} with the measured dielectric function clearly indicates the inhomogeneous behavior of the film at extremely thin regime. This further justifies the validity of treating film's inhomogeneity into our extended GEM model in describing the resistivity scaling at such thickness regime.

2.6.2 Implication of critical thickness in $\rho_{ext.\ GEM}$

As discussed in Figure 2.10a, Ag film's measured resistivity-thickness plot in log-log scale showed a clear double-sloped behavior where the intersection occurs at d_{eff} of 5 nm. This resistivity scaling was theoretically modelled by using extended GEM model which comprehensively described the transition in the conduction mechanism from size effect dominated regime to effective medium dominated regime. Although this transition should be a continuous process rather than discrete one as described by the extended GEM model, it is convenient to quantify the onset of this transition by defining critical thickness d_c (5 nm for our film's case) as the thickness at which two slopes intersect in Figure 2.10a. In the context of extended GEM model, this critical thickness can be understood by looking at the contribution of size effect in determining the total resistivity. From the model, d_c occurs at a thickness that satisfies ρ_{size}/ρ_{total} = 0.8

(where $\rho_{total} = \rho_{exp.\ GEM}$). Physically, this implies that the size effect dominates the total resistivity only down to thickness of d_c.

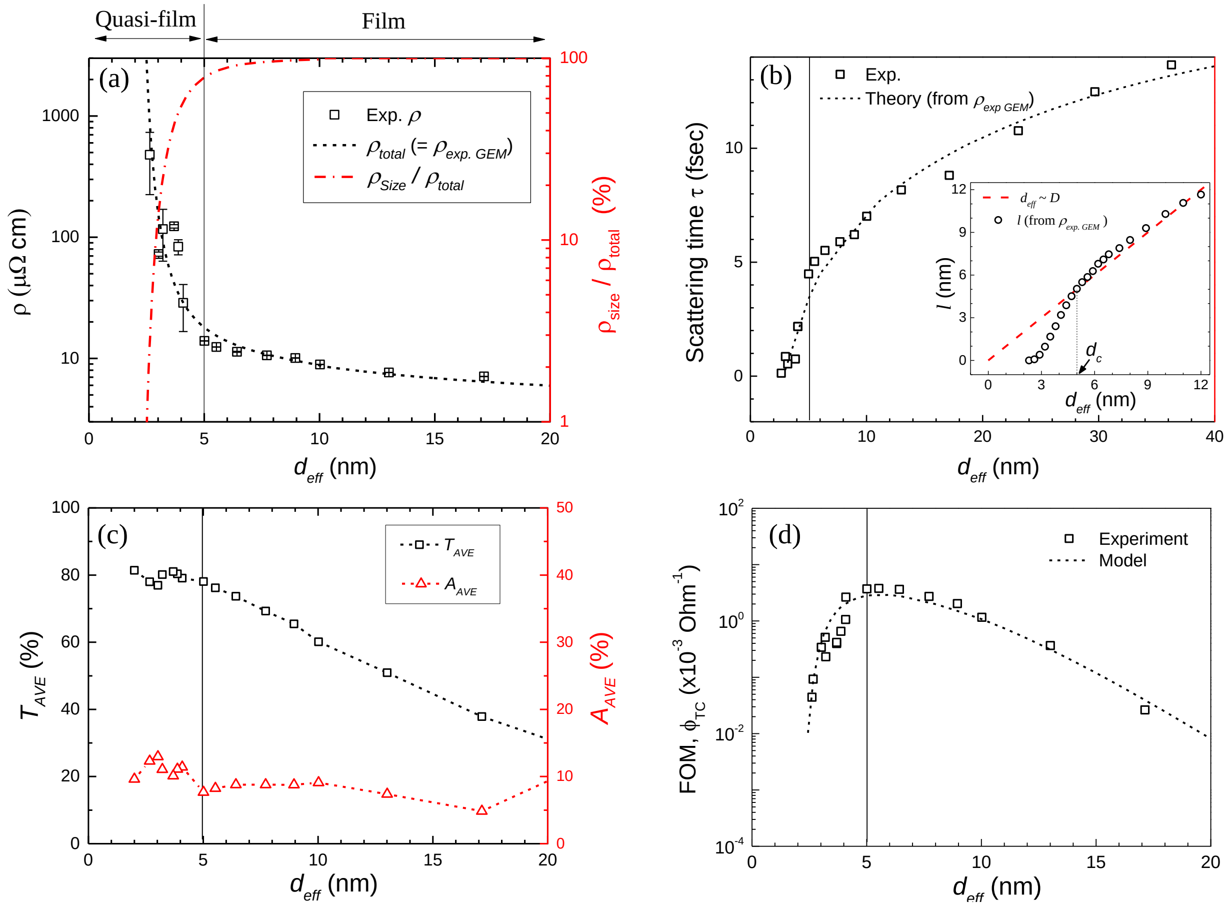

Figure 2.20 (a) Ag (Cu) film's total resistivity ρ_{total} (= $\rho_{ext.GEM}$, dashed black line) on the left axis and contribution of size effect model over total resistivity, ρ_{size}/ρ_{total} (dashed-dot red line) on the right axis both as a function of film thickness d_{eff}. Symbols on left axis are measured experimental resistivity values. (b) Experimental (symbol) and theoretical (from $\rho_{ext.GEM}$, dashed line) scattering time τ of Ag (Cu) film as a function of d_{eff}. Inset figure plots the film's predicted effective mean free path l (symbol) as a function of d_{eff} where proportionality relation of grain size D with d_{eff} is plotted (red dashed line). (c) Film's measured average transmission (T_{AVE}) and absorption (A_{AVE}) over visible wavelength (380 – 780 nm) plotted as a function of d_{eff}. (d) Haacke's figure-of-merit ϕ_{TC} (= T^{10}/R_s) of Ag (Cu) film as a function of d_{eff} where T is

transmission at 550 nm wavelength and R_s is sheet resistance. Symbols and dotted line are experimental and modelled ϕ_{TC}, respectively. For the modelling of ϕ_{TC}, R_s was calculated from extended GEM model and T is calculated from measured Ag (Cu) film's optical constants using transfer-matrix method. In all four figures, Ag (Cu) film's critical thickness d_c (= 5nm) is indicated as a vertical solid line.

This is shown in Figure 2.20a where left axis is the modelled resistivity and the right axis is the contribution of size effect over total resistivity shown as ρ_{size}/ρ_{total} as a function of d_{eff}. In the graph, d_c is represented as a solid vertical line. Note that, log scale plot of ρ_{size}/ρ_{total} (%) shows a rapid decrease below d_c, conversely indicating that the electron conduction is strongly dominated by percolation and effective media effect due to inhomogeneity of the film. From morphological view, the film can be considered a continuous "film" above d_c (possibly with the existence of voids) and "Quasi-film" below d_c. Interestingly, d_c coincides with the thickness that gives minimum value of $\rho \times d_{eff}$ (Figure 2.21b) which is consistent with observation by others [36]. I observe interesting change in electrical and optical properties of metal film with respect to this critical thickness.

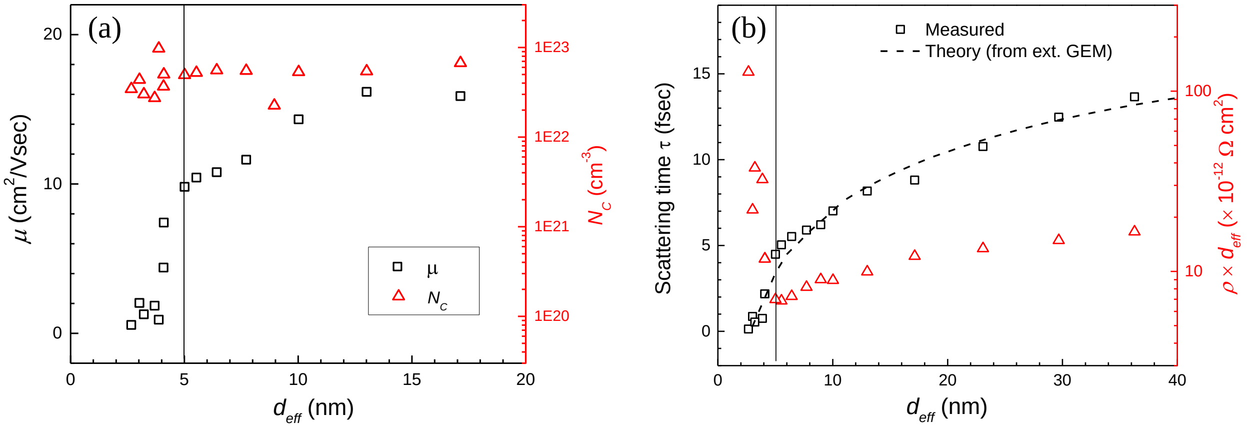

Figure 2.21 Ag (Cu) film's (a) mobility μ, carrier concentration N_c, (b) scattering time τ, and $\rho \times d_{eff}$ plotted as functions of film's effective thickness d_{eff}. Solid black lines in each figure

indicates the critical thickness d_c. Dashed line in (b) shows theoretical τ calculated from extended GEM model (*eq 2.8*).

First, below d_c, electrical and optical properties of the film undergo a drastic change where free carrier's mobility μ drops while its concentration N_c remains constant (Figure 2.21a). From this, electron scattering time τ $(= \mu \cdot m_e/q$, where m_e is free electron mass and q is charge) is extracted and plotted in Figure 2.20b. For the film thickness above d_c, gradual decrease in the scattering time is attributed to the increase in the scattering of electrons described by size effect models. The scattering times extracted here falls within the reasonable range of τ reported by other works [56, 76]. When the film's thickness reduces to below d_c, τ rapidly diminishes. This trend is well predicted by τ calculated from extended GEM model using $\tau^{-1} = \rho_{exp.\ GEM} \cdot N_c \cdot q^2/m_e$ relationship, where N_c of $5.85\times10^{22}\text{cm}^{-3}$ was used [77]. Predicted theoretical scattering time calculated from $\rho_{exp.\ GEM}$ at d_c is 3.4 fsec, which also rapidly decays below this critical thickness. Optically extracted scattering time also showed a similar behavior further consolidating this observation (Figure 2.22).

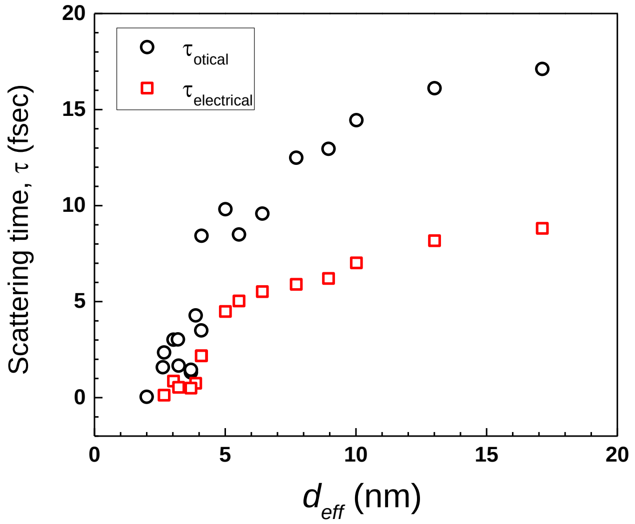

Figure 2.22 Comparison of Ag (Cu) film's optical (black circle) and electrical (red square) scattering time τ as a function of d_{eff}.

Taking a step further to understand the physical meaning of d_c in extended GM model, effective mean free path of electron l $(= \tau \cdot v_F,\ )$ was calculated from the model with fermi velocity v_F set as 14.5x10^5 m/sec [58]. If simplify the problem by approximating that grain boundary is the dominant scattering mechanism in size effect model (valid approximation to a certain extent, see Figure 2.12), the effective mean free path will be determined by the grain size D because electron will scatter at each grain boundary. Also, as assumed earlier in M-S model, the proportionality of film thickness with grain size $(d_{eff} \sim D)$ is what induces strong resistivity scaling as film thickness decreases in the grain boundary scattering model. Therefore, it is the point at which l becomes smaller than D (or d_{eff}) that the scattering event is no longer fully described by size effect model. As shown in the inset of Figure 2.20b, l coincides with d_{eff}~D relation (red dotted line) for d_{eff} above d_c which implies that the scattering event can be described by size effect model. However, l starts to deviate from $d_{eff} \sim D$ relation as the film thickness goes below d_c. This may be explained by the increase in the insulator (air) voids in the metal film where in specific, metal-insulator boundaries that are perpendicular to the direction of electric field can result in a complete reflection of electron wave. As the measured electrical resistivity is the measure of average scattering events of electrons traveling over a given path, increase of such metal-insulator boundaries can significantly impede the electron travel and decrease the scattering time, thereby lowering the effective mean free path (see schematic in Figure 2.23) to below the size of grain boundary. In such, physical picture of the transition in the conduction mechanism with respect to the critical thickness is explained using extended GEM model.

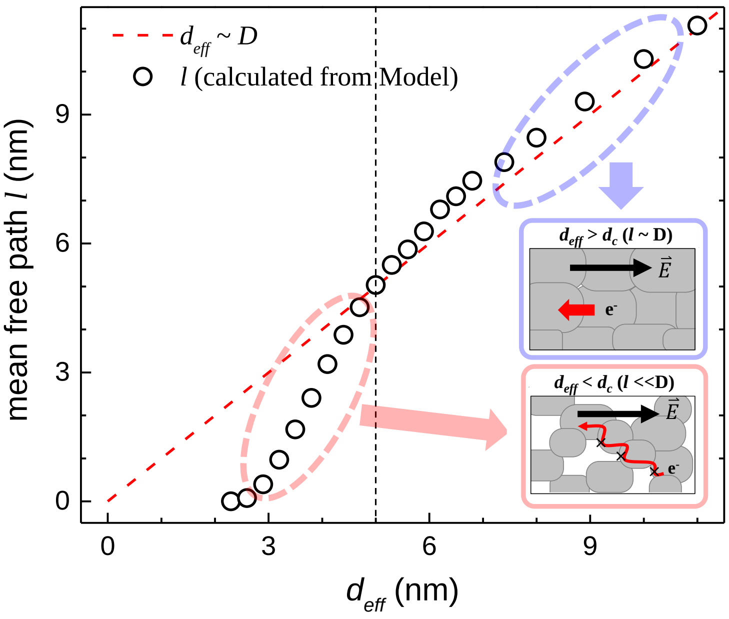

Figure 2.23 Film's predicted effective mean free path l (symbol) as a function of d_{eff} where proportionality relation of grain size D with d_{eff} (red dashed line) is plotted as well. The figure is identical to the inset figure of Figure 2.20b but with top-down schematic view to illustrate the film's morphology in relation with the l and D under the presence of electric field ($\vec{E}$).

Second, optical property of Ag film experiences a transition in behavior with respect to d_c. Figure 2.20c shows the average absolute transmission (T_{AVE}) and absorption (A_{AVE}) of the Ag (Cu) film with the substrate in the visible wavelength range (380 – 780 nm). Note the film's optical transmission gradually increases as the film's thickness is reduced to d_c. This is anticipated because metal film can transmit electromagnetic wave when its thickness comparable to the skin depth (~30nm for Ag [78]). As the film's thickness is further reduced to below d_c, T_{AVE} reaches a plateau followed by increase in the film's absorption. This may be due to the increased absorption of light by quasi-particle like metal cluster network via localized surface plasmon resonance. Depending on the type of application involving metal film, one can design the range of metal film's thickness to be above d_c to maximize optical transmission while suppressing the loss.

Aside from scientific implication of the film's critical thickness associated with the transitioning of film's electrical and optical properties, it also has practical engineering impact. One good example of application of metal film that involves both electrical and optical properties is a transparent conductor (TC), in which the objective is to minimize electrical resistance while maximizing optical transmission (minimize loss). This performance of TC is characterized by Haacke's figure-of-merit ϕ_{TC} ($= T^{10}/R_s$) [79] where T is the transmittance at wavelength of 550 nm and R_s is the sheet resistance. It will be shown that ϕ_{TC} shows maximum value at the critical thickness where extended GEM model is used as a theoretical framework in modelling ultrathin Ag (Cu) film's electrical sheet resistance ($R_s = \rho_{exp.GEM}/d_{eff}$). T is simulated from the measured refractive index of Ag (Cu) film by using transfer matrix method. Figure 2.20d shows the measured and modeled ϕ_{TC} of Ag (Cu) film on a substrate as a function of film thickness. ϕ_{TC} reaches maximum at d_{eff} near d_c (= 5 nm). This is anticipated because below this critical thickness, the resistivity rapidly increases while the film's optical transmittance reaches plateau. As one additional remark, I observed significant hysteresis in resistivity over a span of time for metal films with thickness below d_c (Figure 2.24), in which stability of the electrical property is critical for its practical application. In these aspects, the definition of d_c is not only scientifically interesting but also can serve as a metric for optimizing the film's property for applications including but not limited to transparent conductor.

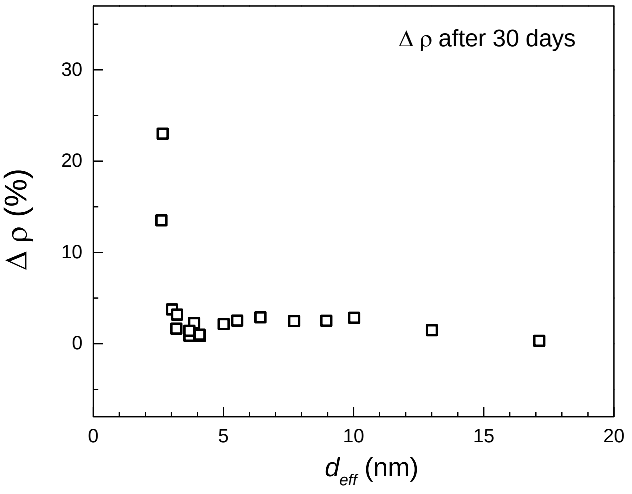

Figure 2.24 Change in resistivity $\Delta\rho$ of Ag (Cu) film for different d_{eff} after exposure in air for 30 days.

Lastly, it is worth emphasizing that the theoretical modeling of the film's resistivity via extended GEM model becomes handy in accurately modeling ϕ_{TC} as a function of film thickness. This is important because research on metal film-based TC so far deals only with measured ϕ_{TC} while lacking theoretical basis that reflects film's electrical property. For this reason, determining optimum thickness that gives highest FOM values based on measured data may be subjected to ill-defined values due to either discretized points [21, 80-83] or the fluctuation in the measurement especially at a ultrathin thickness regime [84] showing difficulty in accurate comparison among TCs. Although Ellmer showed theoretical FOM curve for metal-film based transparent conductor [85], it was stated that this FOM curve was calculated from experimental conductivity data and so the basis of theoretical model is unclear which may be absent of percolation effect. On the other hand, as our extended GEM model is strictly based on a theoretical model which comprehensively describes the film's electrical property for a thickness down to near the percolation, using this model enables accurate modeling of ϕ_{TC} which can serve as a basis for systematically engineering.

2.7 Conclusion

In conclusion, various seed layer materials were studied to obtain continuous and smooth film down to ultrathin regime where Cu of 5Å was shown to be most effective in obtaining low electrical and optical loss films. Next, resistivity scaling behavior in this ultrathin metal film was discussed. In specific, electron conduction in ultrathin Ag (Cu) film was fully described using a theoretical model that combines classical size effect theory with generalized effective medium theory, so called extended GEM. So far, this model is the only model that can comprehensively describe the resistivity scaling of the film with thickness all the way down to near the percolation threshold. As the model implies, transition in conduction mechanism occurs with respect to the critical thickness d_c which was found to be 5.0 nm for Ag (Cu) film's case. The critical thickness is defined in the extended GEM model as the thickness that satisfies ρ_{size}/ρ_{total} = 0.8. Above d_c, the film can be considered as homogeneous film and the model converges to ρ_{size} where the resistivity is described via size effect of grain boundary (M-S model, R = 0.2) and surface roughness (Namba model, p = 0.1) induced scattering. Below d_c, the conduction of electron is strongly influenced by the inhomogeneous nature of metal film. Bruggeman's effective medium theory was used to optically model the metal-insulator composite nature of the film which showed consistent result with the film's measured dielectric function and the composite ratio. The definition of critical thickness of the Ag (Cu) film was found to have both scientific and engineering values. First, the film's electrical mobility and optical scattering time significantly decrease below this critical thickness. This was explained via diminishing of electron's mean free path in extended GEM model. Second, the film’s optical transmittance plateaus while absorption increase below the critical thickness. Finally, it was shown via extended GEM model that the calculation of Ag(Cu) film’s figure-of-merit as a transparent conductor peaks at d_c which originates from above discussed electrical and optical properties with respect to d_c. This work of understanding and modeling of electrical/optical behavior of thin metal film down to extremely thin regime is not only scientifically meaningful but also can provide us a valuable framework in designing the film for various photonic and electronic application.

Chapter 3 Flexible Transparent Conductor for Organic Light Emitting Device

3.1 Introduction

In this chapter, I will discuss how extremely thin Ag as a transparent anode can fundamentally solve light trapping problem in organic light emitting devices (OLED). In specific, light management and extraction in organic light-emitting diodes (OLEDs) are the key issues to address in obtaining high external quantum efficiency (EQE).

There are three major factors that limit the EQE of OLEDs [86, 87]. First, a portion of the generated photons from the emission layer (EML) are lost at the interface between contact metal and the organic stacks due to the excitation of surface plasmon-polariton (SPP) mode. Here the organic stack includes the organic emitting layers and the electron and hole transporting layers. Second, light residing in the substrate cannot escape the device due to total internal reflection at air/substrate interface. Third, a significant amount of generated light in OLED exists in the form of guided mode, and hence trapped within the waveguide layers formed by organic stacks and thick transparent conducting electrode (TCE). There have been extensive research and reports to suppress plasmonic mode and extract trapped light from the substrate [4, 88, 89], but extracting or minimizing guided mode in the waveguide still remains the biggest challenge, because the organic stack requires certain thickness for optimal emission performance, and the transparent conductive oxides (TCO) based anode needs sufficient thickness to ensure low film resistivity.

Previously, several strategies were introduced to efficiently outcouple the waveguide mode by inserting additional layers into OLEDs such as low-index materials, gratings, or corrugated structures. For example, Sun [90] and Qu.[91] embedded low-index and sub-anode grids near organic stacks, respectively. Koo. [92] and Y. Li [93] showed decoupling methods using buckling patterns and reactive ion etching-induced nanostructures, respectively. However, all these previous approaches are either wavelength dependent due to the existence of coupling resonance or intrusive to the OLEDs device structure , e.g. embedding grid or introducing corrugation [89, 94]. Some require complex fabrication steps that not only increases cost but also incompatible with large-area manufacturing. Therefore, there is a strong need for a simpler, more scalable, and effective solution that is compatible with the conventional OLED structure and fabrication. Such a solution, if developed, can have immediate impact to commercial display products.

Here, we introduce a novel and simple approach of using an ultrathin Ag film as an anode to completely eliminate waveguide modes and enhance outcoupling efficiency of OLEDs. Previous research on various TCEs such as carbon-based materials [95-97], metal nanostructures[98-100], or thin metal-films[101, 102] to replace indium-tin-oxide (ITO) showed excellent optical and electrical properties with superior flexibility, but there have not been thorough studies of the effects of these TCEs on light outcoupling aspect in OLEDs [95, 96, 99, 100, 102]. We show that the negative permittivity, extremely thin thickness (~ 5 nm), and highly conductive properties achieved by a uniform Cu-seeded Ag film as a transparent electrode enhance EQE without compromising any other characteristics of OLEDs. This simple yet effective method of suppressing waveguide modes formation will pave the way for cost-effective high efficiency

OLEDs in future displays and lightings industry. The work was conducted with a close collaboration with Changyeong Jeong from Professor L. Jay Guo's group.

3.2. Figure of Merit and Anti-reflective Effect of Ag Film inside OLED

3.2.1 Ag Film's Electrical and Optical Properties versus d_{Film}

Based on the optimum thickness of the Cu seed layer, electrical and optical properties of a Cu-Ag film (Ag film on the Cu seed layer) in comparison with a bare Ag film (without any seed layer) were thoroughly investigated (as shown in Figure 3.1a and b). Figure 3.1c shows R_{Sh} as a function of total film thickness (d_{Film}) for Cu-Ag and bare Ag films. Both the films show significant increase with reducing d_{Film}, however the Cu-Ag film has lower limit of d_{Film} for low R_{Sh}. The insertion of the seed layer makes the film electrically conducting even at d_{Film} ~ 4 nm, which can never be achieved with bare Ag.

Thickness-dependent T_{AVE} of Cu-Ag and bare Ag films is plotted in Figure 3.1d, where the spectra were averaged over wavelength range from 380 to 780 nm. The Cu-Ag film experiences minimum light absorption and scattering due to the smooth and continuous film morphology compared to the bare Ag, resulting in higher T_{AVE} in a sub-10 nm range. In a film thickness range of 5 – 6 nm, the Cu-Ag film can achieve T_{AVE} close to 80% but still maintains R_{Sh} of 20 Ω/sq or below. Simulated T_{AVE} and R_{AVE} also showed similar trends with the measured data. However, slight discrepancy was observed at an extremely thin regime below 5 nm in the Cu-Ag film, where measured T_{AVE} slightly decreases due to the quasi-particle-like behavior of the films with the increased absorption near the percolation threshold [69, 103]. It is consistent the rapid increase of R_{Sh} below d_{Film} = 5 nm due to the film discontinuity as shown in Figure 3.1c. This points out that the optimum thickness of an Ag film should be selected above the percolation regime to guarantee maximum transmittance.

Thickness-dependent reflectance (R_{AVE}), and absorbance (A_{AVE}) of Cu-Ag and bare Ag films on the glass substrate were measured in Figures 3.1e and f, respectively, where the spectra were averaged over wavelength range from 380 to 780 nm. The Cu-Ag film experiences minimum light absorption and scattering due to the smooth and continuous film morphology compared to the bare Ag, resulting in higher T_{AVE} and significantly lower A_{AVE} in a sub-10 nm range. As will be discussed later, significant amount of reflected light can be salvaged via anti-reflective effect of hole transporting layer and so R_{AVE} can be reduced down close to 5 % when the film is embedded into the device.

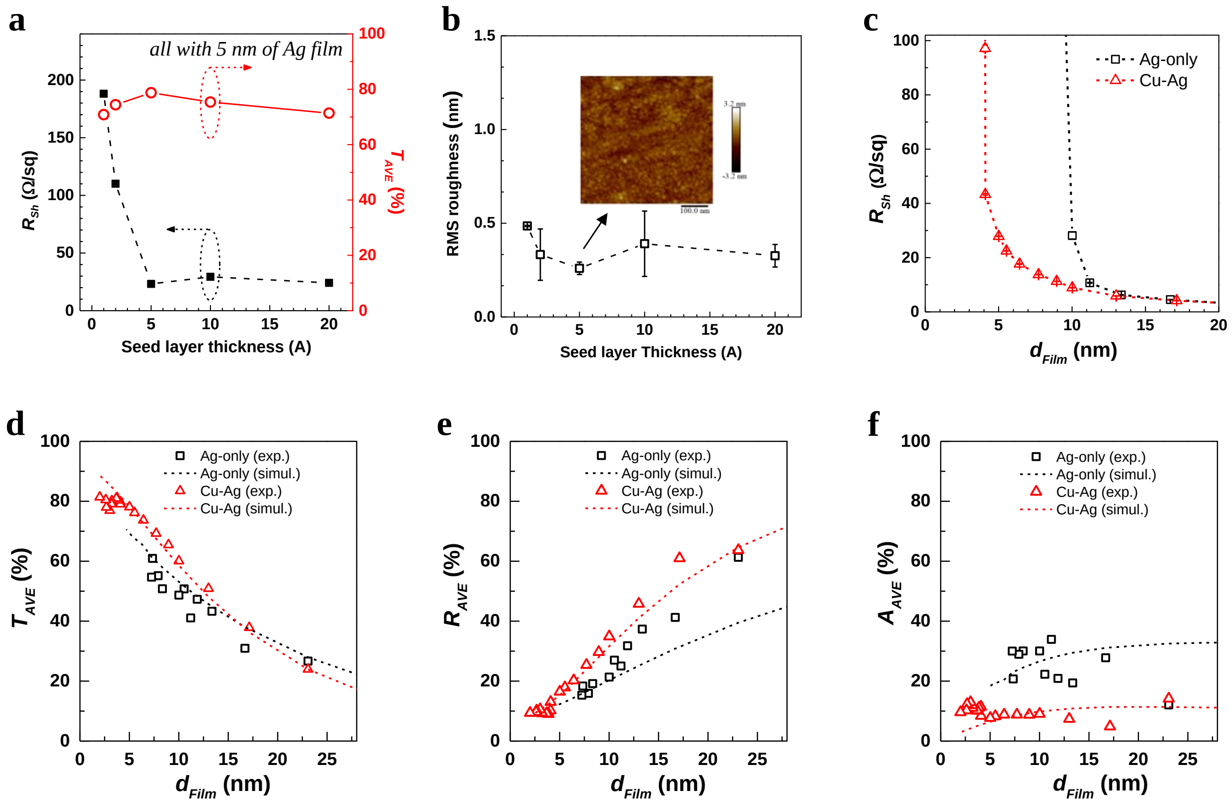

Figure 3.1 (a) Sheet resistance R_{Sh}, average optical (λ = 380 - 780 nm) transmission T_{AVE}, and (b) root-mean-square (RMS) surface roughness of 5 nm Ag film with varied Cu seed layer thickness. Inset in (b) is AFM image of Ag film with 5 Å Cu-seed. (c) R_{Sh} of Cu-Ag and Ag-only films as functions of film thickness d_{Film}. Average optical (d) transmittance T_{AVE}, (e) reflectance R_{AVE}, and (f) absorbance A_{AVE} as a function of film thickness d_{Film} for Cu-Ag and Ag-only films. Experimental data (in symbol) and simulated data (dotted line) of Ag-only film (black) and Cu-Ag film (red) are plotted together.

3.2.2 Theoretical Calculation of Sheet Resistance

For the calculation of sheet resistance of ideal Ag film, film was assumed to be epitaxial film. For such a film, grain boundary scattering does not exist and only the surface scattering contributes to the resistivity with reduced film size. Thickness-dependent resistivity due to surface scattering described by Fuchs-Sondheimer (F-S) model in *eq 3.1* was used for the calculation. Bulk resistivity of ρ_i = 1.59 μΩ·cm and electron mean free path of l_0 = 53 nm was used for silver film [58]. The degree of inelastic scattering that an electron faces at film surface is represented by specularity parameter p, where p = 0 means completely diffusive scattering, whereas p = 1 means specular scattering. In this calculation, p = 0.9 was used to reflect the ideal Ag film, and R_{Sh} was calculated by $R_{Sh} = \rho_{FS}/d$. Such an ideal Ag epitaxial film experiencing only surface scattering shows excellent conductivity and high ϕ_{TC}. The resulting sheet resistance is plotted in Figure 3.2a. For the experimental Cu-Ag and Ag-only films, simulated resistance values obtained from extended general effective medium discussed in Chapter 3 are used for the calculation.

The modeling of sheet resistance of ITO was calculated from the following grain boundary scattering model [104]:

$$R_{Sh} = 1/(M\delta)$$

$$M = \frac{nq^2t}{\sqrt{(2\pi m_n kT)}} \exp\left(\frac{-\phi_B}{kT}\right) \tag{3.1}$$

where δ is the grain size, n is the free electron concentration, q is the electron charge, t is the film thickness, m_n is the electron effective mass, ϕ_B is the grain boundary potential barrier, kT is the thermal energy. This model was used to fit the represented state-of-the-art ITO films including the commercial ITO (Lumtec), which showed good representation of the empirical data. Left axis of Figure 3.2b shows theoretical R_{Sh} of the ITO films as a function of its thickness, where δ = 50 nm and ϕ_B = 40 meV.

3.2.3 Optical Simulation

ITO refractive index from Konig was used in this work [105]. Refractive index from Johnson and Christy was used to represent the ideal Ag film [106], and extracted refractive index from Ellipsometry was used to simulate optical properties of the experimental Cu-Ag or bare Ag films. Figures 3.2a and b show calculated R_{Sh} and T_{550} (T at 550 nm) for the ideal Ag film and ITO films as functions of film thickness, respectively. The fluctuation in T_{500} with respect to the film thickness was observed in the ITO film, which results from the cavity resonance shift of the ITO film. Figure 3.2a shows that ideal Ag film has significantly lower R_{sh} than ITO and comparable T_{550} at d_{Film} ~ 5 nm, implying that high quality Ag films have great potential for TCs.

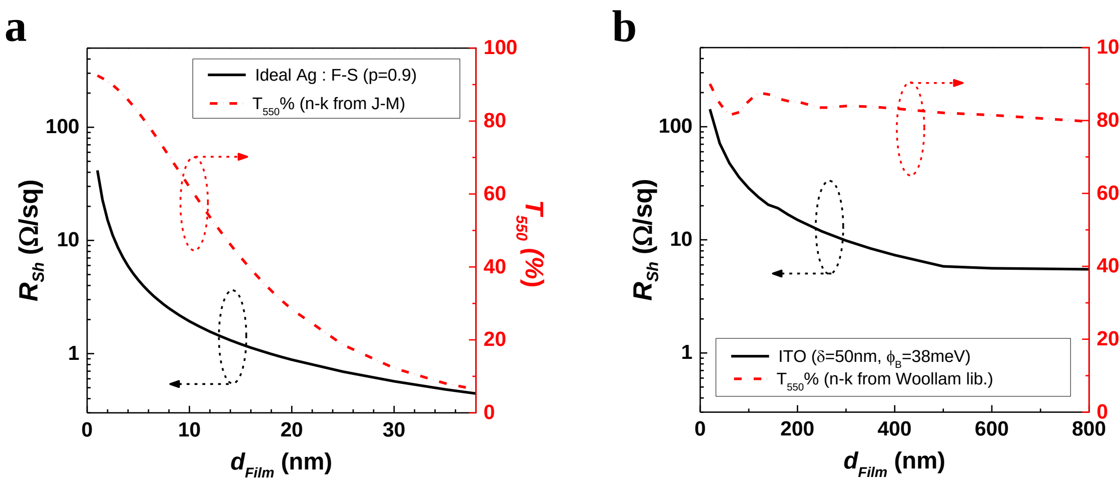

Figure 3.2 Theoretically calculated sheet resistance R_{Sh} as functions of film thickness d_{Film} for (a) ideal Ag film with F-S model (*eq 3.1*) and (b) ITO film (*eq 3.1*). Right axis of (a) and (b) shows simulated average optical transmittance T_{AVE} for ideal Ag film and ITO film, respectively.

3.2.4 Figure-of-Merit Comparison and Anti-reflective Effect

In choosing the optimum thickness condition of Ag film for TCE, Haacke's figure of merit ($\phi_{TC} = (T_{550})^{10}/R_{sh}$) [79] was calculated for a varying film thickness, where T_{550} is the transmission at wavelength of 550 nm. Figure 3.3a shows measured and calculated ϕ_{TC} of TCEs (Cu-Ag, bare Ag, and ITO films) as a function of d_{Film}. Note significant improvement in ϕ_{TC} is observed with the aid of only 5 Å of Cu, where the value reaches maximum at d_{Film} = 5.0 nm, with T_{550} = 80.7% and R_{Sh} = 21.3 Ω/sq which was chosen as optimum Ag thickness. ϕ_{TC} of various state-of-the-art ITOs including commercial ITO (Luminescence Technology Corporation)'s experimental and theoretical ϕ_{TC} are all plotted in Figure 3.3a. ϕ_{TC} of the commercial ITO (R_{Sh} = 15 Ω/sq and T_{550} = 85.0%) is higher than that of the fabricated Cu-Ag film but lower than that of the ideal Ag film which only considers surface scattering, indicating that theoretical limit of the Ag film with improved film quality can surpass performance of ITO as a TCE. However, as will be discussed later, TCEs located at top-left in Figure 3.3a is expected to bring higher device performances when they are embedded in OLEDs due to better outcoupling.

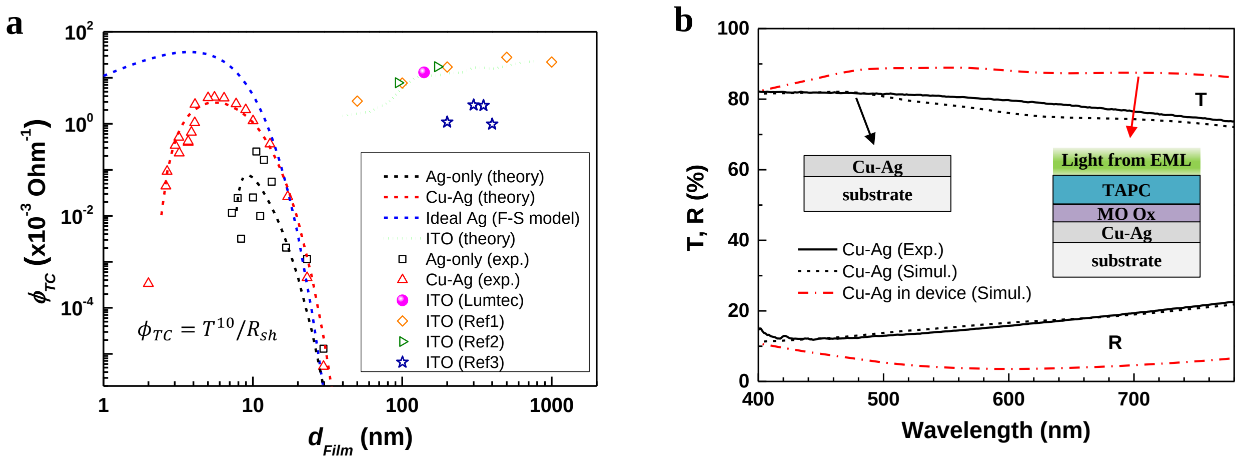

Figure 3.3 (a) Haacke's figure-of-merit ϕ_{TC} as a function of film thickness for Cu-Ag, Ag-only, and ITO based transparent conductors. Experimental data (in symbol) and simulated data (dotted line) of Ag-only film (black) and Cu-Ag film (red) are plotted together. Theoretical ϕ_{TC} of ideal Ag film is also plotted (blue dotted line) as a reference to show the potential of metal-film based TCE. Reference for ITO values used are Ref1 [107], Ref2 [108], and Ref3 [109]. (b) Measured (black solid line) and simulated (black dashed line) transmittance (T) and reflectance (R) of Cu-Ag films in air. Simulated T and R of Cu-Ag films inside an OLED structure is plotted (red dashed line) as well showing enhancement of transmittance owing to AR effect of HTL layer. Schematics of simulated optical stacks for each case are illustrated in inset for each curves.

The extremely thin Cu-Ag film is highly transparent, reaching measured T_{AVE} = 79.3 % and R_{AVE} = 16.1%. This optical property can be further enhanced by hole transporting layer (HTL) and hole injection layer (HIL) in OLEDs directly adjacent to the anode, which functions as an effective anti-reflective (AR) layer. Figure 3.3b shows calculated transmittance (T) and reflectance (R) of 5 nm Cu-Ag films on a glass substrate (black dashed) and embedded in an OLED structure as an anode (red dashed-dot). Light was incident from the top of the structures in Figure 3.3b. CBP, TAPC, and MoO_x were used for EML, HTL, and HIL, respectively. HTL and MoO_x were fixed to 70 and 5 nm, respectively, and acted as effective AR coatings for the Cu-Ag film. The calculation showed that R_{AVE} is suppressed from 16.0% to 5.7% (i.e. to a level like that of the substrate) and T_{AVE} is enhanced from 77.5% to 86.9%, indicating the effectiveness of the AR effect from the HTL. The transmittance can even reach 88.9% at the peak emission wavelength of 530 nm.

3.3. Ag Diffusion Inhibition by AZO

As silver can easily diffuse, stabilizing Ag film via passivation is important for its practical use especially as a transparent anode where Ag can get oxidized. As shown in Figure 3.4, Ag film as a transparent anode under device operation experiences high electric field. In such circumstance, Ag can get oxidized at the anode surface by losing an electron. The ionized Ag atom is then driven toward the cathode side by the electric field. Considering the organic thickness used is around 150 nm and the operating voltage of 10 V, the electric field can get as high as ~ 0.7 MV/cm. For this reason, a layer thin enough to not optically impact the film while effectively suppressing the Ag diffusion is needed.

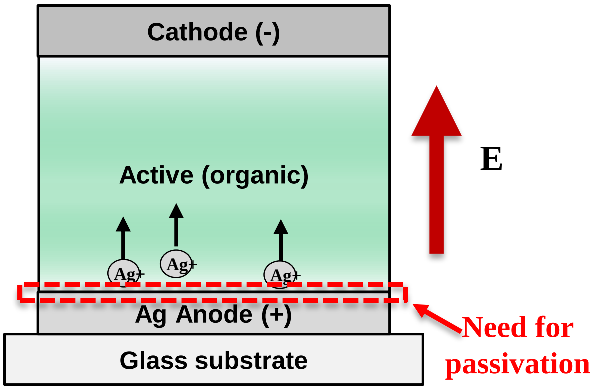

Figure 3.4 Schematic image illustrating the Ag migration process in organic light emitting device (OLED) under operation (presence of high electric field).

Any material that has high activation energy of Ag diffusion should be a good candidate for this purpose. Wang et. al. carried out first-principle calculation and showed that adding aluminum dopant inside zinc-oxide (AZO) complex can increase barrier energy of silver from 0.75 to 0.89 eV [110]. Based on this result, we tested the inhibition effect of ZnO and AZO. In specific, Ag (Cu) anode passivated with 3 nm of ZnO or AZO films deposited by atomic layer deposition (ALD) method were prepared along with the control sample having no passivation. Then, subsequent device layers were fabricated on top of each transparent anodes.

The devices were then put under a constant voltage stress by applying 10 V in between the cathode and the anode and the current was monitored over time. As shown in Figure 3.5a, Ag (Cu) anode device with AZO passivation showed a stable current even under the high voltage test. On the other hand, the device with ZnO passivation or without any passivation showed increase in the current which is indicative of the Ag diffusion process resulting in leakage path in the device. The Ag diffusion phenomenon was observed via SEM-EDS where the formation of Ag filament was shown to penetrate through the active organic layer. Also shown in Figure 3.5b, AZO passivated Ag (Cu) device shows a stable operation even after multiple scans of current-voltage curve with strong illumination while those devices with ZnO or without passivation showed increased leakage current at subthreshold regime. By using ALD coated AZO on Ag (Cu) film, stable operation of Ag (Cu) anode is maintained under OLED operation. The passivation of AZO using ALD was conducted by collaborator Tae Cho from Neil Dascupta’s group.

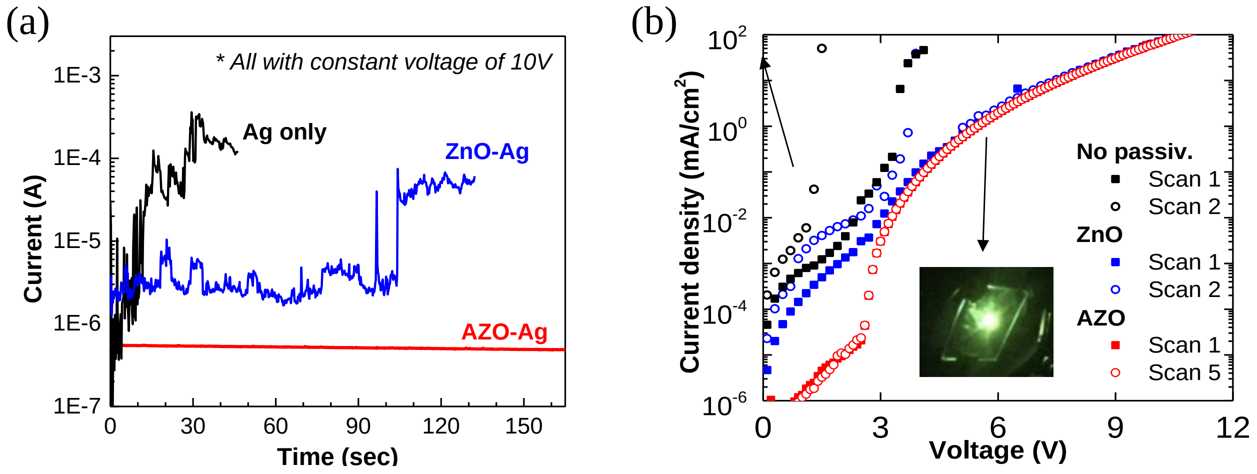

Figure 3.5 (a) Constant voltage stress test (10V) with measured current as a function of time for Ag anode OLED devices without passivation, with ZnO or AZO passivation. (b) Current density versus voltage characteristic curve of OLED without any passivation or with 2 nm of ZnO or AZO passivation layer. After several cycles of voltage scan, ZnO-passivated Ag anode results in Ag migration thereby increasing the subthreshold current. AZO-passivated Ag anode device shows stable operation even after multiple voltage scans. Inset picture shows stable device operation with strong illumination for AZO-Ag anode device.

3.4. Device Performance of OLED with Cu-Ag Anode

3.4.1 Modal Power Dissipation Analysis

Next, the optical effect of Ag (Cu) anode on OLED is studied. Here to acknowledge that the works involving optical simulation of the device as well as measurement were conducted by Changyeong Jeong. In specific, modal analysis was simulated to calculate the modal distribution power as a function of wavelength vs in-plane wave vector in 2-dimensional color map for ITO device and Cu-Ag device in which the structure is shown in Figure 3.6a. In Figure 3.6b for ITO device and Figure 3.6c for Cu-Ag device, region between each modes (air, glass, WG, SPP) are distinguished in red line, in which the in-plane vector changes as a function of wavelength because of the index dependent refractive index. As shown in Figure 3.6b, there is a strong intensity of modal power confined as a WG mode in the wavelength of green emission range (480 – 650 nm). This indicates that the green light emitted from the active region can get strongly confined within the medium between substrate and the metal cathode, which is within the ITO plus active layers (including HTL, EML, and ETL). Commercially available ITO on glass used in this experiment is 150 nm in thickness where typically ITO of such thickness is used to ensure R_S below 15 Ω/sq. If adding all the dielectric thickness within the WG mode region with ITO thickness as 150 nm, this adds up to 300 nm in total. Even if ITO thickness can be reduced down to 100 nm with a trade-off in the R_S value, the total thickness that could serve as a medium to confine light as WG mode is difficult to be reduced below 250 nm for the case of ITO.

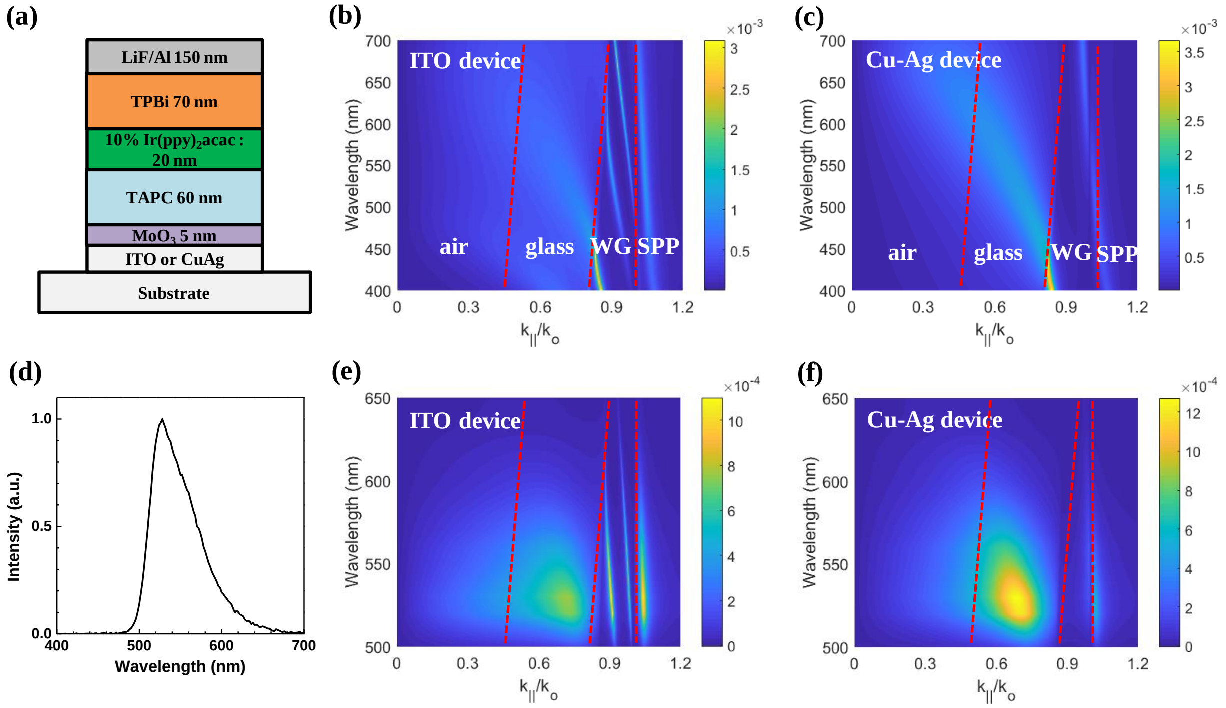

Figure 3.6 (a) Green OLED device structure. Dispersion relation from modal power distribution analysis of (b) ITO and (c) Cu-Ag device. (d) Spectrum of green emission material. Light intensity distribution from modal power distribution integrated over green emission material spectrum.

Now, taking a look at the case of Cu-Ag device in Figure 3.6c, there is clearly no modal power distribution in the WG mode region at a green emission wavelength. In fact, much of the power is dissipated into glass mode region which indicates that much of the generated light is confined in the substrate. Given the emission spectrum of 10% Ir(ppy)2 acac dopant material in CBP matrix as shown in Figure 3.6d, modal power distribution map can be integrated by this spectrum to give a relevant light intensity distribution in each mode specific to the green emission OLED device. The result is shown in Figure 3.6e and f for ITO and Cu-Ag based device, respectively. It is very evident that the green light that comes out from active region gets strongly confined as WG mode for the ITO device whereas the WG mode is completely eliminated in the case of Cu-Ag device. This is a remarkable advantage of using Cu-Ag thin film as an anode which cannot be achieved with traditional transparent conductive oxides such as ITO. Then the question arises: Is this as a result of having Cu-Ag or is it because of not having thick dielectric layer like ITO? In other words, can WG mode be simply suppressed by reducing the total organic layer's thickness or is having ultrathin metal film helps suppression of the confinement?

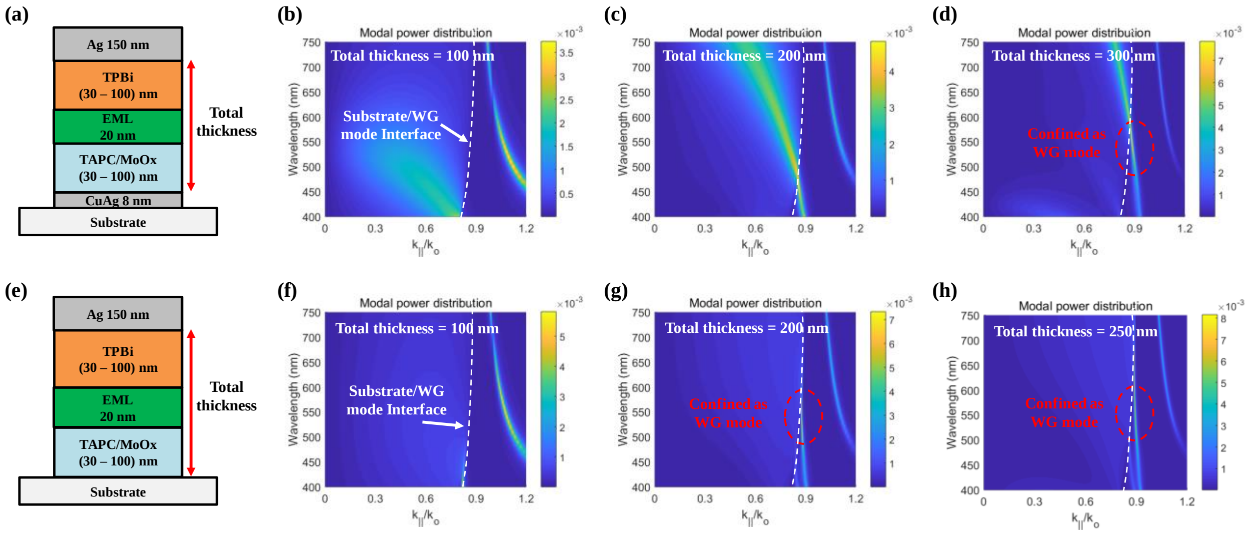

Figure 3.7 Simulated OLED device structure (a) with and (e) without Cu-Ag anode. Modal power distribution map with total thickness of (b) 100 nm, (c) 200 nm, and (d) 300 nm for OLED with Cu-Ag and (f) 100 nm, (g) 200 nm, and (h) 250 nm for OLED without Cu-Ag.

To verify this, modal power distribution was calculated for OLED structure with or without Cu-Ag anode by varying total active layer's thickness. In all modal power distribution maps, interface between substrate and WG mode is indicated in white dashed lines. As shown in Figure 3.7b - d, the modal power distribution gets strongly confined at the substrate even up to 200 nm of total thickness at a green emission wavelength. Only when the total thickness is further increased to 300 nm, light gets trapped as a WG mode which is marked as red dotted circle in Figure 3.7d. For the case without Cu-Ag anode, WG mode disappears when the total thickness is 100 nm. However, unlike Cu-Ag's case, WG mode starts to appear at a green wavelength even at 200 nm of total thickness and strongly confined at 250 nm. Comparing the case with total thickness of 200 nm for Cu-Ag, it shows that ultrathin layer of Cu-Ag film does prevent light from getting confined as a WG mode in the active region. Further detailed analysis is needed to carefully study this phenomenon but this is due to the nature of TE_0 mode being guided through the index n. Considering *n*-*k* property of Ag, it has *n* close to 0 and *k* value in the range of 2-3 at a visible wavelength which makes the ε value negative. As *n* is close to 0 and so slab waveguide mode cannot be supported and so light is more loosely confined within the active region.

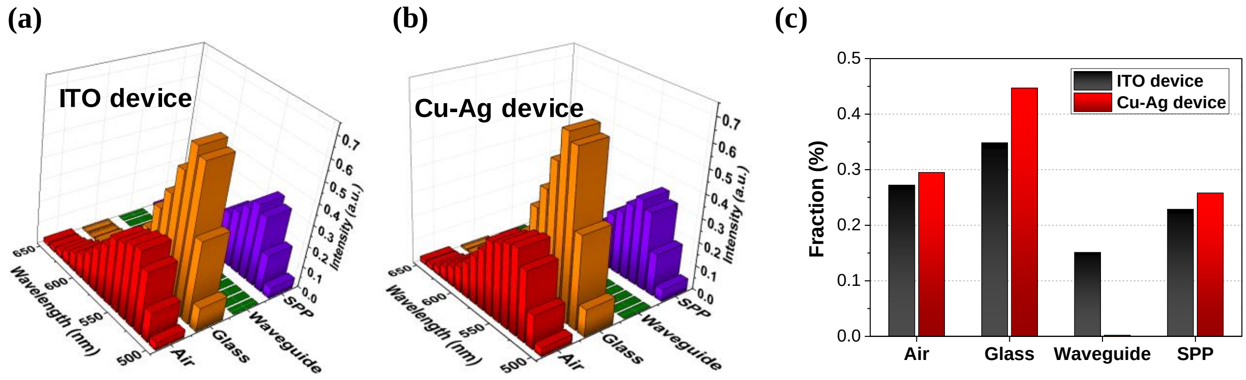

Figure 3.8 Dissipated modal power in each modes as a function of wavelength for (a) ITO and (b) Cu-Ag devices, respectively. (c) Fraction of each mode's modal power integrated over wavelength range for ITO and Cu-Ag devices.

Dissipated modal power for each modes were plotted as a function of wavelength for ITO and Cu-ag devices as shown in Figure 3.8a and b, respectively. Simply put, this result is obtained by integrating all dissipated power at in-plane wave vector regions that corresponds to each modes for a given wavelength (Figure 3.6e and f). From this result, fraction of light portion at each mode can be calculated by summing over entire emission wavelength range, which is shown in Figure 3.8c. This is a convenient way of depicting how much fraction of light is trapped in each mode. In this result, Cu-Ag device clearly shows fraction value close to zero for waveguide mode, although the value is nonzero which indicates the portion of light absorbed by ultrathin Cu-Ag film. In case of Cu-Ag device, as the waveguide mode is not confined within the device layer, it is further extended to the glass substrate and gets confined there. This is why the fraction of glass mode for Cu-Ag is much larger than ITO device. In comparison, ITO device shows insignificant portion of light fraction trapped as a waveguide mode with smaller fraction of glass mode compared with Cu-Ag device. As discussed earlier, researchers have developed novel methods like micro-lenses or diffusers to salvage the trapped light inside glass substrate. This indicates significantly larger amount of light can be extracted for Cu-Ag device compared to ITO device when excluding glass substrate mode.

3.4.2 Fabricated Device EQE Comparison

To verify this outcoupling simulation, OLEDs with Cu-Ag or ITO as transparent anode was fabricated. Figure 3.9a shows the EQE of ITO and Cu-Ag devices with and without applying

IMF. In figure 3.9a, Cu-Ag shows EQE of 14% which is lower than ITO's 18%. This may be due to intrinsically lower *T* of Cu-Ag film compared to ITO despite the effect of utilizing AR effect from adjacent HTL and HIL layers. However, when IMF is applied in between the device and the photodetector to allow all the light inside the substrate to be extracted, EQE of Cu-Ag device showed EQE close to 40% which outperformed that of ITO device that showed 34%. This significant boost in the EQE with applying IMF clearly testifies the optical simulation result presented in Figure 3.8c. To confirm that this is attributed to the optical outcoupling effect and not to the difference in electrical injection of carriers for ITO and Cu-Ag, current density – voltage (*J*-*V*) characteristics were plotted for these devices as shown in Figure 3.9b. As can be seen, good overlap of the J-V curve for ITO and Cu-Ag devices without any significant shift in the onset voltage indicates that the electrical property is not the major reason. Also, as the work function of ITO and Ag are known to range in between 4.5-4.8eV, it is anticipated that the electrical property difference is not significant.

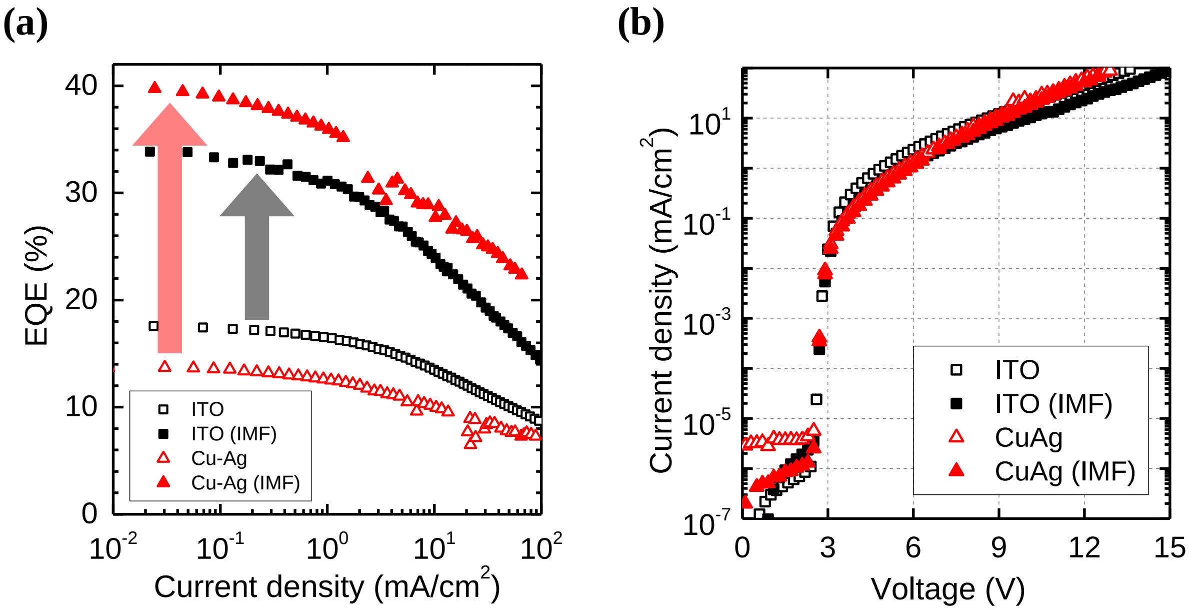

Figure 3.9 Device performances of ITO and Cu-Ag devices. (a) EQE and (b) current density - voltage characteristics (*J*-*V*) of ITO and Cu-Ag devices with and without IMF. IMF is used to extract light trapped in the substrate.

3.4.3 Experimental Observation of Waveguide Mode Elimination

We prepared organic waveguide samples grown on the ITO and Cu-Ag films to experimentally verify that the higher EQE enhancement in Cu-Ag device from Figure 3.9a originates from waveguide mode removal. Strip-line organic layers with commercial ITO on a glass substrate and sputtered Cu-Ag film (see next section) on fused silica substrate were prepared. The structure of the organic layers is identical to the OLEDs designed in the previous section except without the top Al cathode. This is because the waveguide mode experiences significant loss with Al cladding, the top Al was not deposited for more accurate measurement of waveguide mode intensity. Both index-matching fluid and prism for the glass and fused silica substrates were used to remove substrate modes out of the samples. Figures 3.10a shows schematics of top-down and cross-section views of the experiment setup. The strip-line waveguide sample was placed on holders of two silicon pieces having small gap underneath for IMF. A 405 nm Laser is used to excite the EML at center of the waveguide line and the mode intensity was measured at one end of the line. A bandpass filter with bandwidth of 510 – 560 nm was used to the measure intensity of the generated light at the EML that propagates through the waveguide strip while filtering out the excitation light source. The strip-line sample made on either ITO or Cu-Ag was measured with and without IMF to observe the power portion of the waveguide mode. The Measured light intensity without IMF results from sum of the waveguide and substrate modes. However, the use of IMF extracts the substrate mode and the index-matched prism completely removes this extracted substrate mode out of the sample, leaving only the waveguide mode in the sample to be detected.

Figure 3.10b shows measured intensities of the guided light in the waveguides on ITO and Cu-Ag films as a function of excitation intensity. Both waveguides showed similar trends without IMF (I_{wg+sub}) since similar amount of power was excited from the laser source and the generated light was trapped in the samples in the forms of waveguide and substrate modes. After applying IMF (I_{wg}/I_{wg+sub}), the measured light intensities dropped to 48.5% for the ITO based waveguide, and to a extremely low 1.9% of the original intensity for the Cu-Ag waveguides, in fact for the Cu-Ag the measured intensity becomes comparable to the noise level. This result shows that the significant amount of energy still stores in the ITO waveguide, whereas energy in the Cu-Ag waveguide is completely removed by the substrate mode extraction, showing almost flat and negligible light intensities regardless of the excitation. This result indicates that most of the excited energy was stored in the substrate and thus removed by the IMF and prism from the sample, with no energy stored in the waveguide. Figure 3.10c shows observed sample emission from the side-view of the ITO and Cu-Ag samples without and with IMF. Both samples showed distinct green emission without IMF (images *ii)* and *iii)*). When substrate mode was extracted after applying IMF, only Cu-Ag sample showed no emission (image *v)*), indicating that no energy propagated through the waveguide.

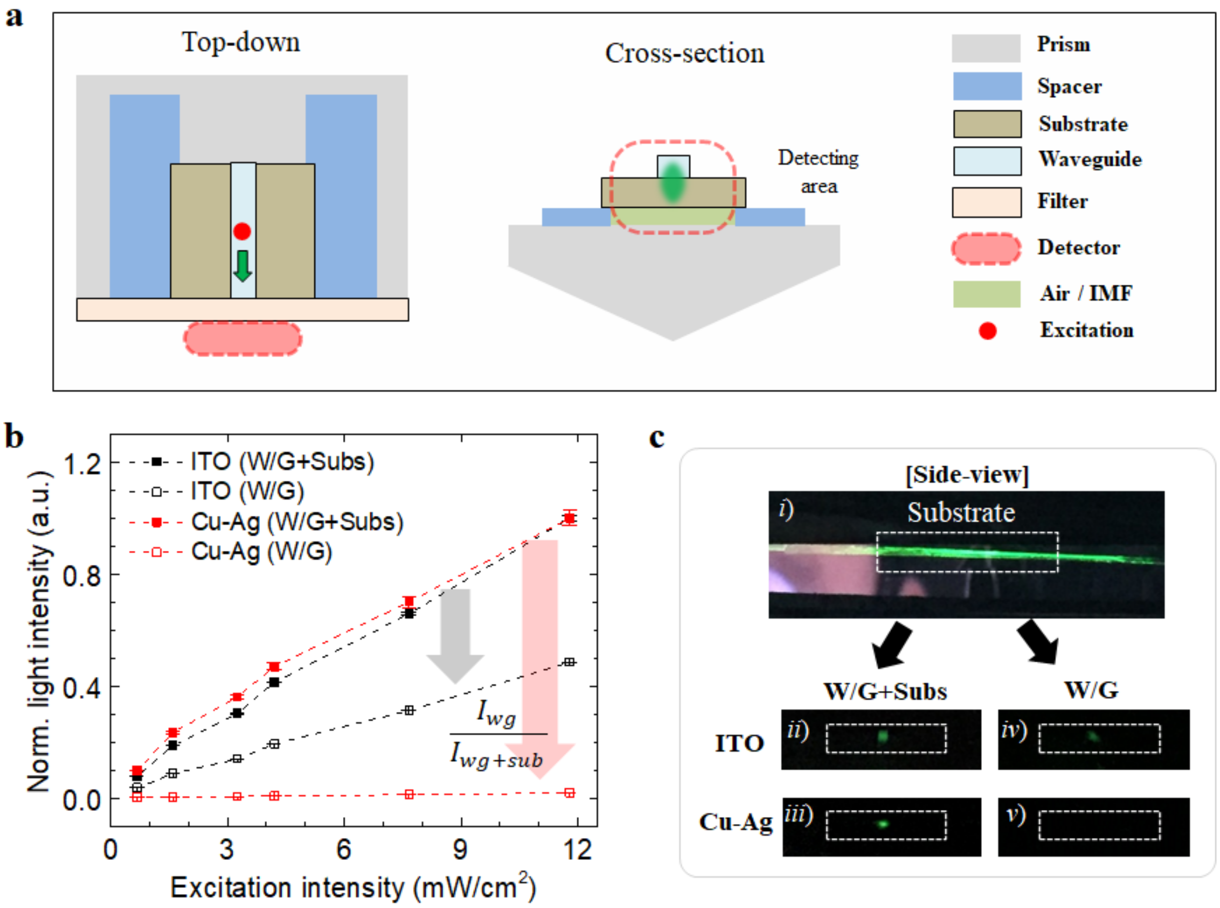

Figure 3.10 Experimental investigation of waveguide mode elimination. (a) Top-down and cross-sectional views of experiment setup in schematic. The sample was placed on top of holders with a small gap away from the prism. The gap was filled with IMF to remove substrate mode from the sample. The fabricated waveguide in this experiment consists of organic and anode layers used in OLEDs without the top cathode. (b) Measured intensities of waveguide and substrate modes as a function of excitation intensity. The Cu-Ag waveguide with IMF showed negligible measured light intensities that was similar to the noise level, indicating no optical energy in the form of waveguide mode. (c) Photographs of the Cu-Ag and ITO waveguide samples. *i*) Side-view image of the sample under ambient light. Photographs of *ii*) the ITO and *iii*) the Cu-Ag waveguide samples without IMF. Photographs of *iv*) the ITO and *v*) the Cu-Ag waveguide samples with IMF. The waveguide mode was observed in the ITO sample but completely disappeared in the Cu-Ag sample.

3.5. Conclusion

In summary, extremely thin Cu-Ag film as anode for OLED was demonstrated to completely eliminate light trapping inside the active device as a form waveguide mode. Simulation shows that the negative dielectric function of metal film induces this removal of waveguide mode which otherwise would appear in case of same device thickness without Cu-Ag film. The suppression of these waveguide modes was experimentally verified by measuring the guided light intensities using index-matched fluid and prism. With this approach, experimentally measured EQE of Cu-Ag device showed much higher performance compared to that of ITO device after extracting the substrate and air mode. The novelty of this work lies in the demonstration of complete waveguide mode removal, rather than extracting it by external means as previously reported approaches. The simple and novel approach taken in this work to eliminate waveguide mode will provide a new direction to increase device efficiency in the research area of OLEDs and other solid-state LEDs.

Chapter 4 Metal-based Transparent Conductor's Optical Property and Environmental Stability

4.1 Introduction

One of promising application of thin silver film is transparent conductor (TC). TC is a key element in current optoelectronic devices. It is widely used in devices for touch panels, solar cells, photodetectors, and light emitting diodes. Among these devices, the use of TC is by far dominated by the display industry with over 90% being used for displays and touch panels [IDTechEx]. Recently, with the emergence of flexible electronics, the market for TC films and materials has been rapidly changing. As current display technology is heading toward flexible and rollable electronics (Figure 4.1), transparent conductor with high transparency, conductivity, and mechanical flexibility is required. Currently ITO dominates most of the TC market, but its mechanical property will seriously limit its usage in flexible electronics and flexible displays. Though ITO can be deposited on flexible plastic substrate but the high temperature annealing required to render low-resistance is incompatible with the plastic substrate. Therefore, there exists a strong need for a new flexible transparent conductor (FTC) which could replace conventional transparent electrodes.

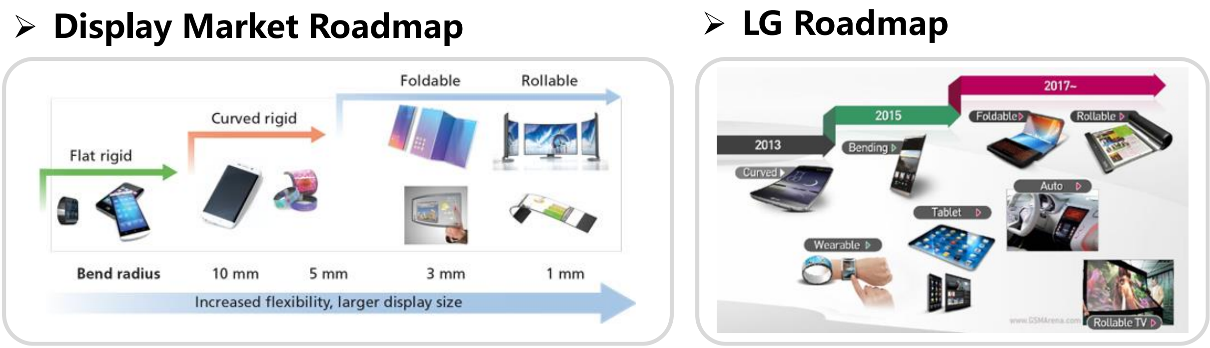

Figure 4.1 Technology roadmap of display industry including that from LG.

New materials for FTC have been extensively studied such as carbon-based materials (Graphene, CNT, conductive polymer, etc.) and metal meshes or metal nanowires. However, these are fundamentally limited by material/structural property. For example, carbon-based materials are not conductive enough compared to metal. Graphene, which is known to be highly conductive has an intrinsic sheet resistance of 30 Ω/sq [111]. Metal meshes or nanowires on the other hand are locally non-conductive, which are unsuitable for optoelectronic devices, such as PV and OLED.

As an alternative, researchers have widely investigated on the Ag-film based FTC. As with any metal films, reducing the reflection from thin metal film to enhance transmittance is crucial for FTC. This chapter will focus on using this Ag-based film to design FTC so that it shows good optical property and environmental stability. First part will focus on optical design of top and bottom anti-reflective coatings on a Ag-film (structure called dielectric-metal-dielectric, DMD) to maximize transmittance. Second part will focus on the optimization of dielectric layers to reduce this color contrast of Ag-film based FTC for touch panel application. Aside from the absolute transmittance, also equally important and yet often neglected parameter is a color contrast. This is especially important for touch panel application where FTCs are patterned and so reducing the color contrast those regions with and without patterns is critical. Third part will focus on strategies to design FTC having sheet resistance of 1Ω/sq. Such low resistance FTC can be used for ultrahigh density pixel displays or even transparent antenna with colored properties if desired. Fourth part will focus on tuning the DMD optical stack to tune its transmittance to specific red, blue, or green wavelength for light emitting device application. Final part will focus on discussing methods to enhance the environmental stability of Ag-based FTC which is extremely important criteria for practical application.

4.2 Criteria for Anti-reflective coating

Ultrathin Ag film has been widely studied for its use as a TC. Despite the strategies to make Ag film extremely thin so that light wave can penetrate, it is still prone to the significant amount of reflection. As an example, ultrathin Ag film of around 8nm in thickness reflects average of approximately over 20% visible wavelength. Therefore, researchers have studied certain dielectric coatings as an anti-reflective coatings sandwiching the Ag-film to reduce the reflection. Some of the commonly used top/bottom dielectric materials are ITO, TiO_2, WO_3, IZO and etc. However, so far there was no systematic study providing design rules for selecting top and bottom dielectrics that gives maximum transmittance. In this section, top and bottom dielectric layers of different index values were used to determine under what criteria the transmission can be maximized. The stack structure consists of top dielectric / metal (Cu-Ag) / bottom dielectric (DMD) on a flexible substrate PET (Poly-ethylene terephthalate). Transfer matrix method M, was used to calculate the reflection and transmission of light propagating through this DMD stack which is given as:

$$M = \prod_n c_n \tag{4.1}$$

where characteristic matrix, c_n is calculated for each layer as:

$$c_n = \begin{bmatrix} \exp(\beta_n) & r_{n,n+1}\exp(\beta_n) \\ r_{n,n+1}\exp(-\beta_n) & \exp(-\beta_n) \end{bmatrix} \tag{4.2}$$

Here, $r_{n,n+1}$ is Fresnel reflection coefficient between layer n and $n+1$ and β is a phase factor each given as:

$$r_{n,n+1} = \frac{k_n - k_{n+1}}{k_n + k_{n+1}} \tag{4.3a}$$

$$\begin{gathered} \beta_0 = 0 \\ \beta_n = ik_n d_n \end{gathered} \tag{4.3b}$$

where k_n and d_n are wavevector and thickness of layer n. From this M, the reflection R and transmission T of light from the can be calculated as:

$$R = \left|\frac{M_{01}}{M_{00}}\right|^2 \tag{4.4}$$

$$T = \frac{k_{n-1}}{k_0}\frac{1}{|M_{00}|^2} \tag{4.5}$$

The total medium is composed of 6 layers starting from air/D/M/D/substrate/air where air is as a medium. For the calculation, unpolarized light was considered for the light reflected and transmitted through each layers meaning that TE polarization and TM polarization were averaged out. Also, for the mediums that have much larger thickness than the wavelength of light such as air or substrate, the light in this medium was treated as an incoherent light. For dielectric materials, those with refractive index values ranging from 1.46 to 2.95 were selected for the calculation. Each material's optical index values (n and k) were referred from the Complete EASE library database provided by J.A. Woollam. First, bottom dielectric material and its thickness were changed while fixing the top dielectric to be HfO_x with its thickness as 54.7 nm. For the metal layer, Cu-Ag index was used with a fixed thickness of 8 nm. Substrate of PET was used with a thickness of 100μm. Average transmittance ($T_{ave}\%$) was calculated for a wavelength range of 400-700 nm. As the effect of anti-reflective coating will be reflected onto increase in the $T_{ave}\%$ value, $T_{ave}\%$ value was used as a measure to quantify the effectiveness of anti-reflective coating. Figure 4.2 shows the optical simulation result of varying the bottom dielectric's material and its thickness while keeping top dielectric and metal layer to be HfOx and Cu-Ag with 54.7 and 8 nm in thickness, respectively. Figure 4.2a shows the $T_{ave}\%$ value as varying dielectric thickness. Anti-reflection coatings work by producing two reflections which interfere destructively with each other. In other words, the thickness at which this destructive interference occurs is when two reflective waves at the top and bottom interface of the dielectric differs by π in phase, fulfilling dielectric thickness to be multiple of the wavelength plus a quarter wavelength:

$$d * n = (\mathrm{m} + \lambda/4) \tag{4.6}$$

where n is refractive index, m is integer, and λ is the wavelength of light wave. From this equation, as the n increases, the thickness d at which $T_{ave}\%$ is at maximum gets reduced (this is summarized in Figure 4.2d). Figure 4.2b plots the transmittance spectra of the DMD for dielectric with optimized bottom dielectric thickness. It is evident that the bottom dielectric as TiO_2 shows the best $T_{ave}\%$ showing 87.8%. One interesting aspect is that for varying bottom dielectric layer, the Fabry-Perot resonance either blue shifts or red shifts depending on the value of index.

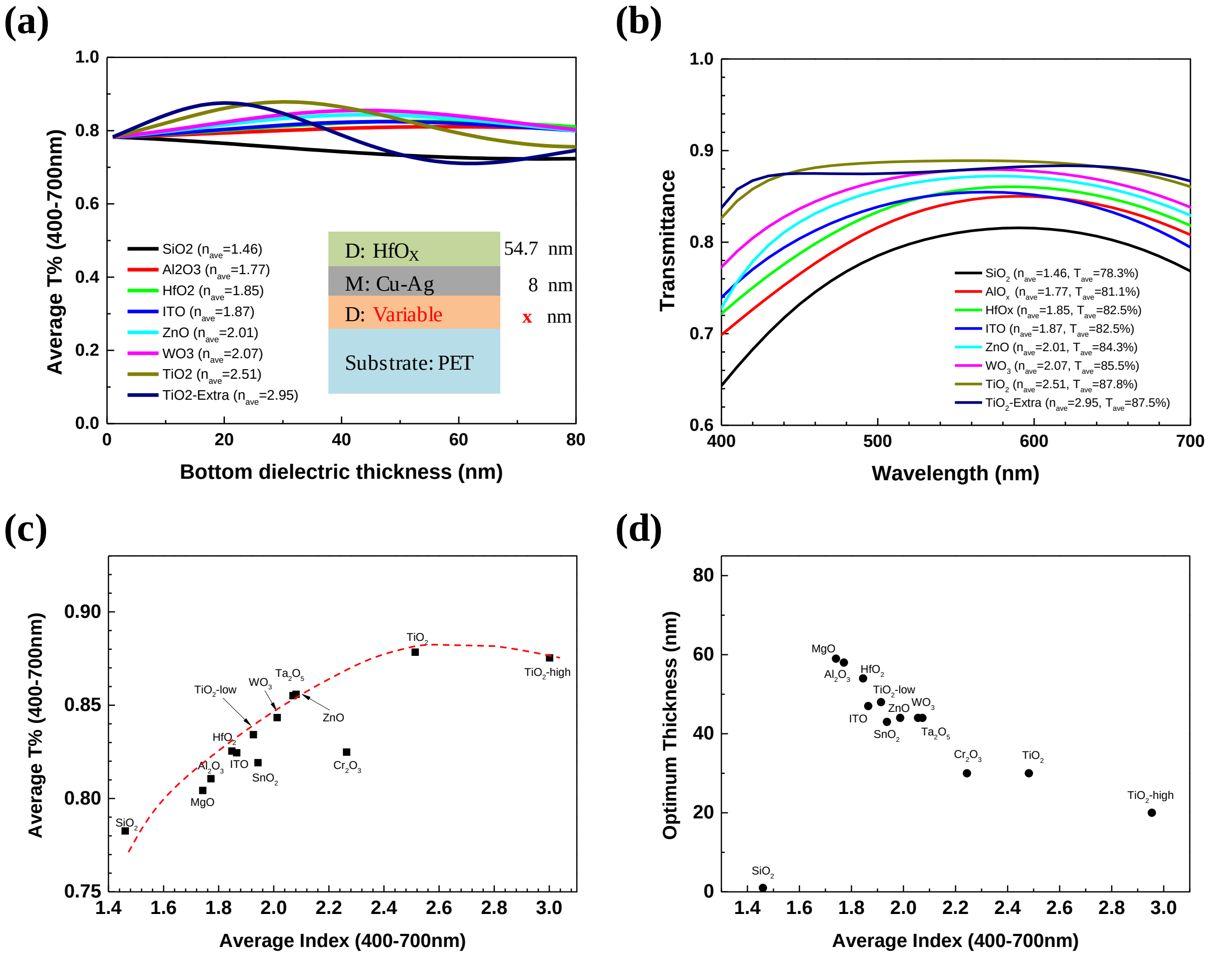

Figure 4.2 (a) $T_{ave}\%$ as a function of dielectric thickness for different bottom dielectric materials. Inset shows the DMD structure with bottom dielectric as a variable for simulation. (b) $T_{ave}\%$ - wavelength spectra for selected oxide materials each with optimum thickness. (c) $T_{ave}\%$ and (d) optimum bottom dielectric as a function of average index.

When plotting $T_{ave}\%$ as a function of average refractive index as shown in Figure 4.2c, it clearly shows a concave down trend with peak at a index of ~2.4. Intuitively speaking, from index matching point of view, index matching condition for bottom dielectric in between PET substrate and CuAg metal layer is:

$$n_d = \sqrt{n_{PET} \times n_m} \tag{4.7}$$

where n_{PET} is PET substrate index (~1.65) and n_m is index of CuAg layer. Since CuAg metal layer has $n_m \sim 3.34$ ($\hat{n} \sim k$) in the optical range as measured from ellipsometry, $n_d = 2.35$ should give index matching condition with reduced reflection. Although this may be an oversimplification of the problem, it still can give rough estimate of the index matching condition for bottom dielectric. Next, by fixing the bottom dielectric's thickness and index to be 30 nm and 2.4, respectively, the top dielectric layer's effect on the transmittance was simulated using TMM. Figure 4.3a shows the effect of changing the top dielectric thickness on the $T_{ave}\%$ value. Compared with varying the bottom dielectric case, changing the top dielectric thickness has more significant impact on the $T_{ave}\%$ value. For each dielectric's case, the minimum dielectric thickness that fulfills quarter wavelength condition in *eq 4.6* is also plotted in Figure 4.3d, in which d and n shows inverse relation for a given wavelength λ.

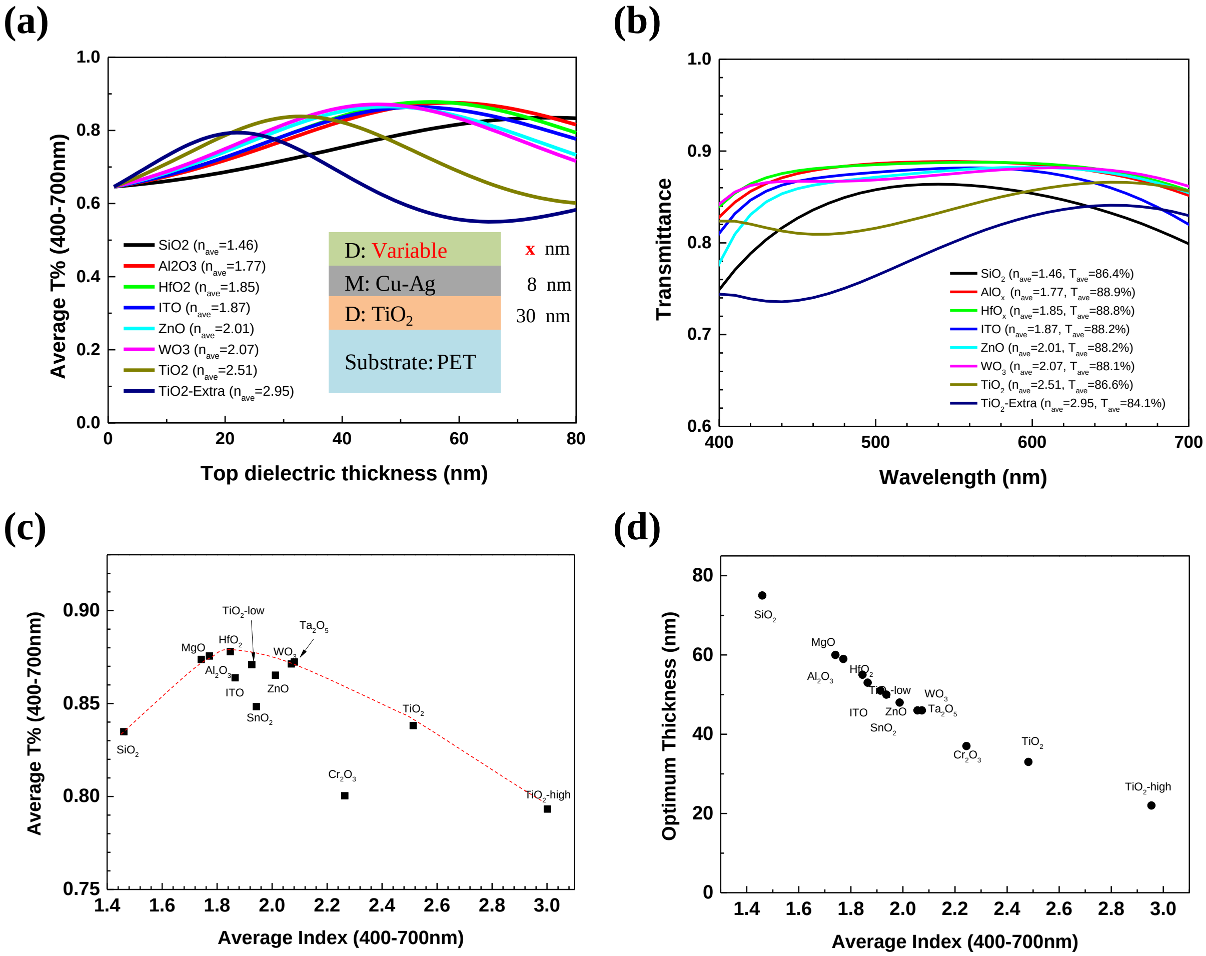

Figure 4.3 (a) $T_{ave}\%$ as a function of dielectric thickness for different top dielectric materials. Inset shows the DMD structure with top dielectric as a variable for simulation. (b) $T_{ave}\%$ - wavelength spectra for selected oxide materials each with optimum thickness. (c) $T_{ave}\%$ and (d) optimum top dielectric as a function of average index.

For each optimum dielectric thickness that gives maximum average transmittance, its corresponding transmittance is plotted in Figure 4.3b. One thing to pay attention is when n is small like 1.45, it shows a single resonance peak at around 520 nm. As n increases, the bandwidth starts to widen throughout the visible wavelength. This shows a maximum $T_{ave}\%$ at a case of HfO_x where n = 1.85. Beyond this n value, double shoulder peak starts to appear and becomes more prominent as n further increases to 2.45. Plotting $T_{ave}\%$ as a function of bottom dielectric's average refractive index shows a peak $T_{ave}\%$ value at n in range of 1.8-1.9. Few data points that diverge from this trend such as Cr_2O_3 or SnO_2 is due to the existence of loss inside the dielectric. Excluding for the dielectric with loss, similar approximation of index matching condition for top dielectric's index can be found as well using *eq 4.7* but this time replacing n_{PET} with n_{AIR} which is 1. From this approximation, n_d for top dielectric is ~ 1.83, which is consistent with the red dotted curve in Figure 4.3c.

By exploring the index and thickness of top and bottom dielectric materials, choosing bottom dielectric with index of $n_{d,b} \sim 2.4$ such as TiO_2 with a thickness of 30 nm and top dielectric with index of $n_{d,t} \sim 1.8$ such as HfOx or AlOx with a thickness of 55 nm sandwiching 8 nm of Cu-Ag on PET should guarantee a maximum transmittance at a visible wavelength range.

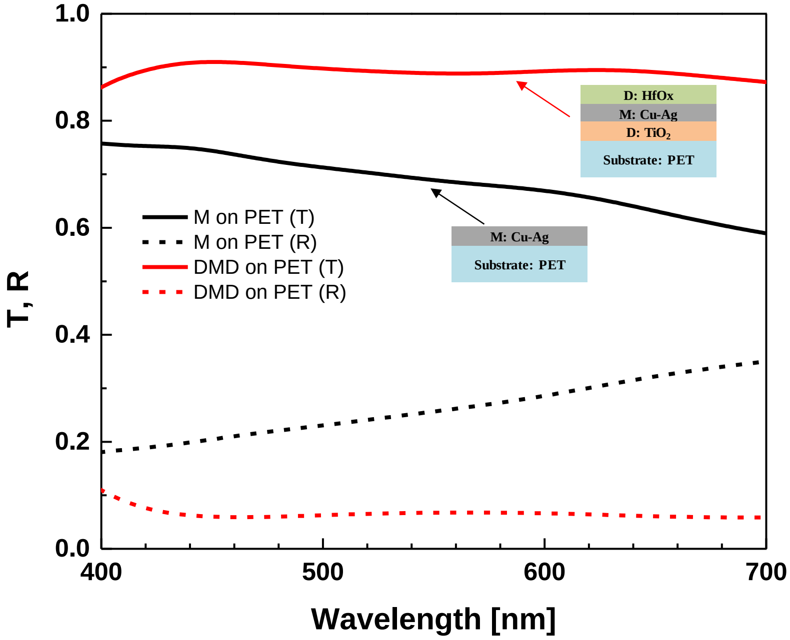

Figure 4.4 Effect of anti-reflection coating in a DMD structure on PET substrate.

This anti-reflection effect of top and bottom dielectrics in DMD structure is clearly shown in Figure 4.4. Black solid and dotted line represent transmittance and reflectance spectra of 8 nm of Cu-Ag film on a PET substrate. The average transmittance and reflectance are 69% and 26%, respectively, still showing high reflection from the metal layer despite thin Ag film. With DMD structure, average transmittance can be boosted up to 89% and reflectance suppressed to 6.5% showing the dramatic effect of anti-reflection coating. This dramatic improvement in the transmittance allows metal-based transparent conductors to compete against ITO.

4.3 Issue with reducing color contrast

Metal-based FTC using DMD structure on a flexible substrate has been extensively studied. Most of these studies focus on merely increasing the absolute transmittance of the DMD stack. Equally as important parameter in the FTC is the color contrast. For a typical application of these transparent conductors such as touch panels, patterning is required to make it into a matrix connected with peripheral circuitry. In such instances, it is likely that there exist a color contrast between those regions with and without DMD layers. Before introducing the term color contrast, it is important to define color in International Commission on Illumination (CIE) LAB color space. It expresses color as three values: $L*$ for the lightness from black (0) to white (100), $a*$ from green (−) to red (+), and $b*$ from blue (−) to yellow (+). These values are calculated from the XYZ color space in CIE 1931 with the following equation:

$$L^* = 116\, f\left(\frac{Y}{Y_n}\right) - 16 \tag{4.8a}$$

$$a^* = 500\,\left(f\left(\frac{X}{X_n}\right) - f\left(\frac{Y}{Y_n}\right)\right) \tag{4.8b}$$

$$b^* = 200\,\left(f\left(\frac{Y}{Y_n}\right) - f\left(\frac{Z}{Z_n}\right)\right) \tag{4.8c}$$

$$f(t) = \begin{cases} \sqrt[3]{t}, & \text{if } t > \delta^3 \\ \frac{t}{3\delta^2} + \frac{4}{29}, & \text{otherwise} \end{cases} \quad \text{with } \delta = \frac{6}{29} \tag{4.8d}$$

For a given spectra, X, Y, and Z are called tristimulus values for red, green, and blue color, respectively. X_n, Y_n, and Z_n are the normalized tristimulus values to the reference white light for each corresponding color. These values are calculated using the following equation:

$$X \; or \; Y \; or \; Z = \sum_{\lambda}(\bar{x} \; or \; \bar{y} \; or \; \bar{z}) \cdot \big(R(\lambda) \; or \; T(\lambda)\big) \cdot (white \; light) \qquad (4.9a)$$

$$X_n \; or \; Y_n \; or \; Z_n = \sum_{\lambda}(\bar{x} \; or \; \bar{y} \; or \; \bar{z}) \cdot (white \; light) \qquad (4.9b)$$

where $\bar{x}$, $\bar{y}$, and $\bar{z}$ are CIE XYZ standard observer color matching functions as plotted in Figure 4.5a. For the white light spectrum, c-white light as shown in Figure 4.5b was used for the calculation. For a given transmittance or reflectance spectra, L*, a*, b* can be calculated for the case with or without DMD on PET substrate. The color difference ΔE, formula in the CIELAB coordinates is defined as:

$$\Delta E = \sqrt{\Delta L^{*2} + \Delta C_{ab}^{*\,2}} \qquad (4.10a)$$

$$\Delta L^{*} = \sqrt{(L_2^{*} - L_1^{*})^2} \quad \text{and} \quad \Delta C_{ab}^{*} = \sqrt{(a_2^{*} - a_1^{*})^2 + (b_2^{*} - b_1^{*})^2} \qquad (4.10b)$$

Here, ΔC^{*}_{ab} corresponds to the difference in color value and ΔL^{*} corresponds to the degree of difference in light for two colors. Table 4.1 shows

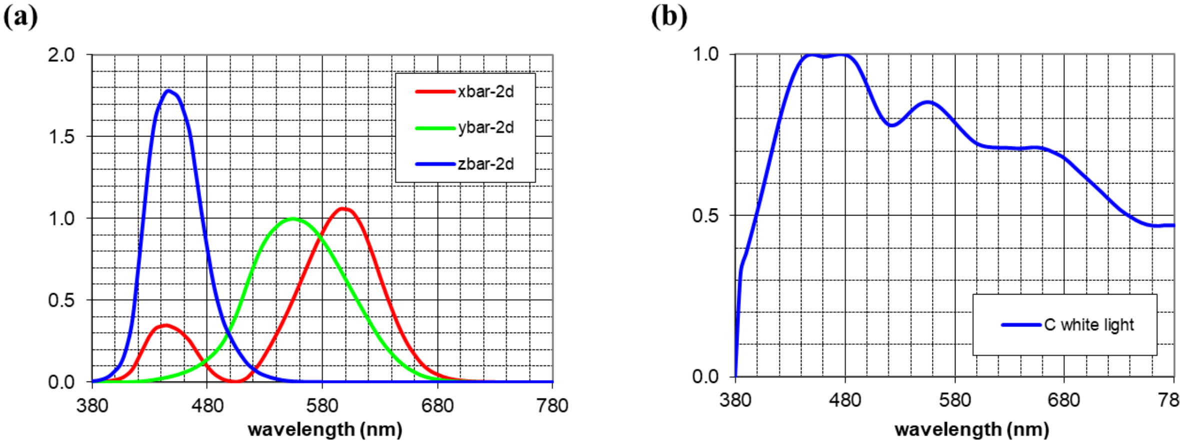

Figure 4.5 (a) CIE XYZ standard observer color matching functions and (b) c-white light spectra.

ΔE is a metric for understanding how the human eye perceives color difference. Table 4.1 gives a general guide on how human eye perceives two difference in colors given the range of ΔE values. Generally, if ΔE is less than 2, it would be difficult for a human eye to perceive the difference of two colors. Hence, it would be ideal to design a patterned transparent conductor with this value of less than 2.

Table 4.1 General guide on ΔE table with respect to human eye perception.

ΔE	**Perception**
<= 1.0	Not perceptible by human eyes
1-2	Perceptible through close observation
2-10	Perceptible at a glance
11-49	Colors are more similar than opposite
100	Colors are exact opposite

As mentioned earlier, there exist a ΔE value for both transmittance and reflectance spectra. It is important to suppress this color contrast for both spectra although in practice there could be a trade-off. The result from Figure 4.2b and 4.3b merely focused on maximizing transmittance values at a visible wavelength. Now calculating the ΔE values from the spectra for varying bottom and top dielectric materials is plotted in Figure 4.6a and b, respectively. In the figure, region with cyan shade is where ΔE value is below 1. For the case of transmittance, having bottom dielectric as TiO_2 and top dielectric as HfO_x or any other dielectric with *n* reside in between 1.8-2.2 shows low ΔE value. The contribution of ΔC^*_{ab} and ΔL^* are not plotted in the figure due to the limited space, but majority of ΔE comes from the ΔC^*_{ab} value for the optimum stack's case, which is due to the slight difference in the spectra shape between the region with and without DMD. This result shows that by selecting the optimum top and bottom dielectrics to suppress the reflection (or increasing transmission), color contrast was also effectively minimized for the case of transmittance spectra. This is somewhat obvious because boosting the transmission should make the stack appear “less visible” so the contrast should not be small.

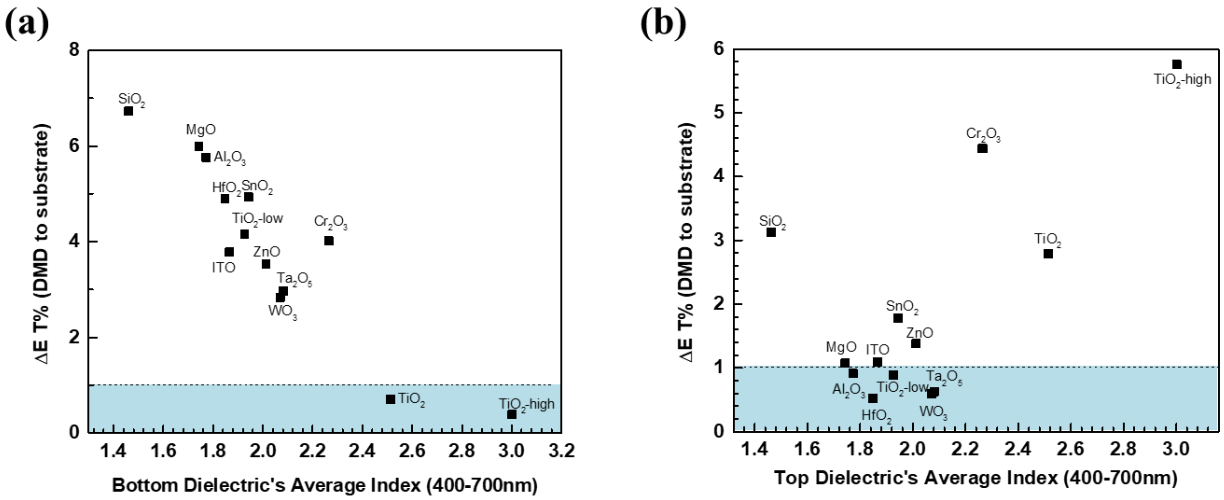

Figure 4.6 Calculated ΔE values from transmittance spectra of varying (a) bottom and (b) top dielectrics.

Now, taking a look at the color contrast from the reflectance spectra for various bottom and top dielectrics are shown in Figure 4.7a and b, respectively. Unlike for the case with the transmission, having bottom dielectric to be TiO_2 shows very high ΔE value over 12. Same for the case with setting top dielectric to be HfOx for example, still shows around 12. Taking a closer look at the contribution of ΔC^*_{ab} or ΔL^* on ΔE shows that majority of the color contrast is due to ΔL^*.

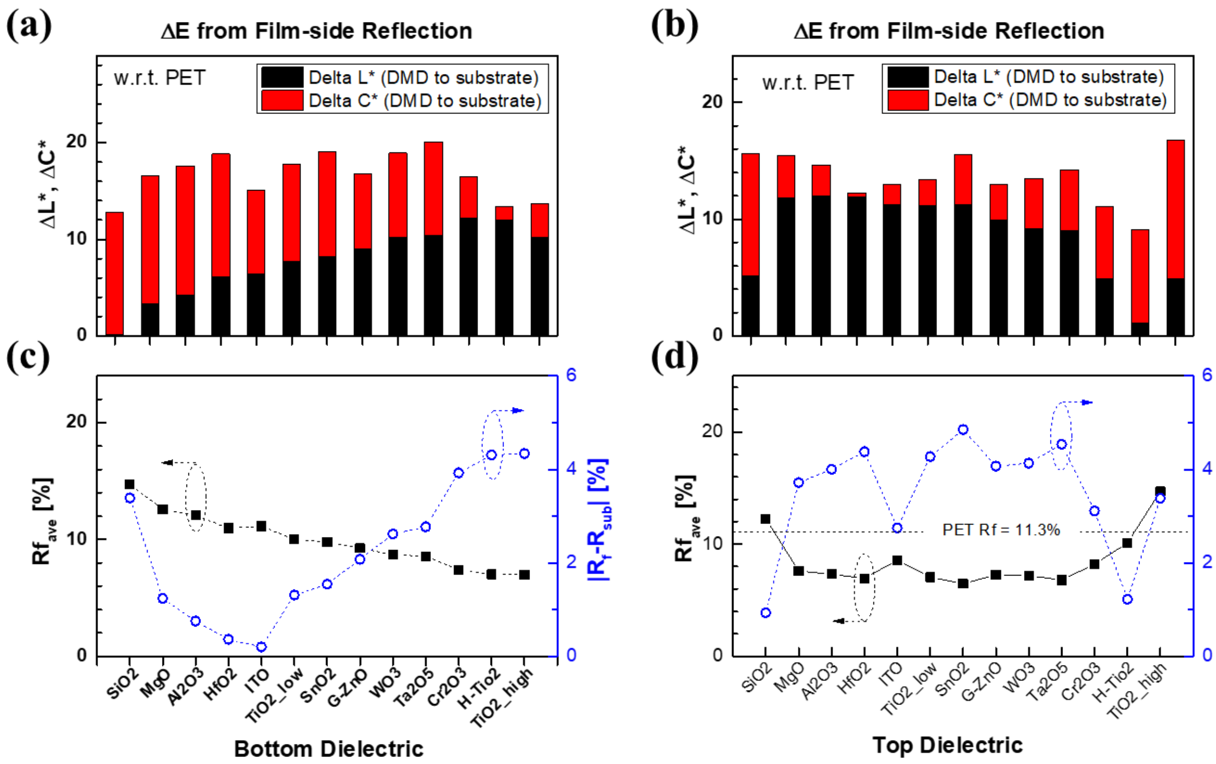

Figure 4.7 ΔE from film side reflection for varying (a) bottom and (b) top dielectric layers where black bar represents ΔL^* and red bar represent ΔCab^*. $R_{ave}\%$ and $|Rf\text{-}R_{sub}|\%$ over 400-700nm wavelength for various candidates of (c) bottom and (d) top dielectric materials.

To see what causes this large contrast, average film side reflectance ($Rf_{ave}\,\%$) as well as its difference with the reflection from the PET substrate ($R_{sub}\,\%$) are plotted in Figure 4.7c and d. Considering the average reflection from the PET substrate is $R_{sub}\,\% = 11.3\%$, in attempt of minimizing the reflection to boost the transmission aggravated the reflection contrast. This is evidently shown in blue curve in Figure 4.7c and d where optimum dielectric that gave maximum transmission has very high $|R_f - R_{sub}|\,\%$. It is very clear that there exists a trade-off in the color contrast problem.

4.4 Non-linear Optimization to Minimize Color Contrast

4.4.1 Optimization Method

DMD stack's thickness can be optimized to meet the target specification of a transparent conductor. Especially with the trade-off problem and without knowing whether this could result in a non-linear optimization problem makes the task difficult to achieve just by sweeping parameters. Here, Michael Waters's code developed in python for optimizing optical stack was used to optimize the DMD stack for transparent conductor application. In brief, this code imports open source code packages like *tmm* and *sciPy* to perform transfer matrix calculation and nonlinear optimization method, respectively. The optimization process flow is shown in Figure 4.8. In this code, thickness of each layers are given as an input variable into the *sciPy.optimize.minimize* function with certain constraints imposed, while other parameters such as optical properties (n, k) and total number of layers are fixed. Then, so called penalty of merit (POM) values are assigned for each target specifications like *Y %*, which is the transmittance normalized to human eye response, R_f *%*, an average reflectance, and *ΔE* for R_f *%* and *T%*. POM is a quantification of how much current stack performance is deviating from the target specification.

For each target specifications, appropriate weighting function is imposed onto each POM values so that when it deviates from the target value, it puts significant weight onto the POM value penalizing it. Example of these weighting functions are shown in Figure 4.8. For example, I set (*Y%*, R_f*%*, *ΔE* R_f, *ΔE T*) = (87%, 7%, 2, 2) so that for a given thickness set of values if the stack performance deviates from any of these values, then I penalize that criteria. The total POM would be merely a summation of each of these POM criteria. After defining the target specification of the stack, the code uses minimize function available in *sciPy* package to minimize the POM value by varying the thickness. It will go through iterations of TMM by utilizing so called *sequential* *least squares programming (SLSQP)* method in a way to minimize the POM value. This is a gradient based method in which the optimization will stop when the *ΔPOM*, which is the difference in the POM value of current iteration to the previous one becomes within the tolerance value. As a final output, the code will give the optimum set of *(t_1, t_2, t_3)* values that guarantees the minimum POM value indicating possible fulfilling of target criteria. For this optimization, the number of layers in the stack is not limited to 3 but can have any finite integer values.

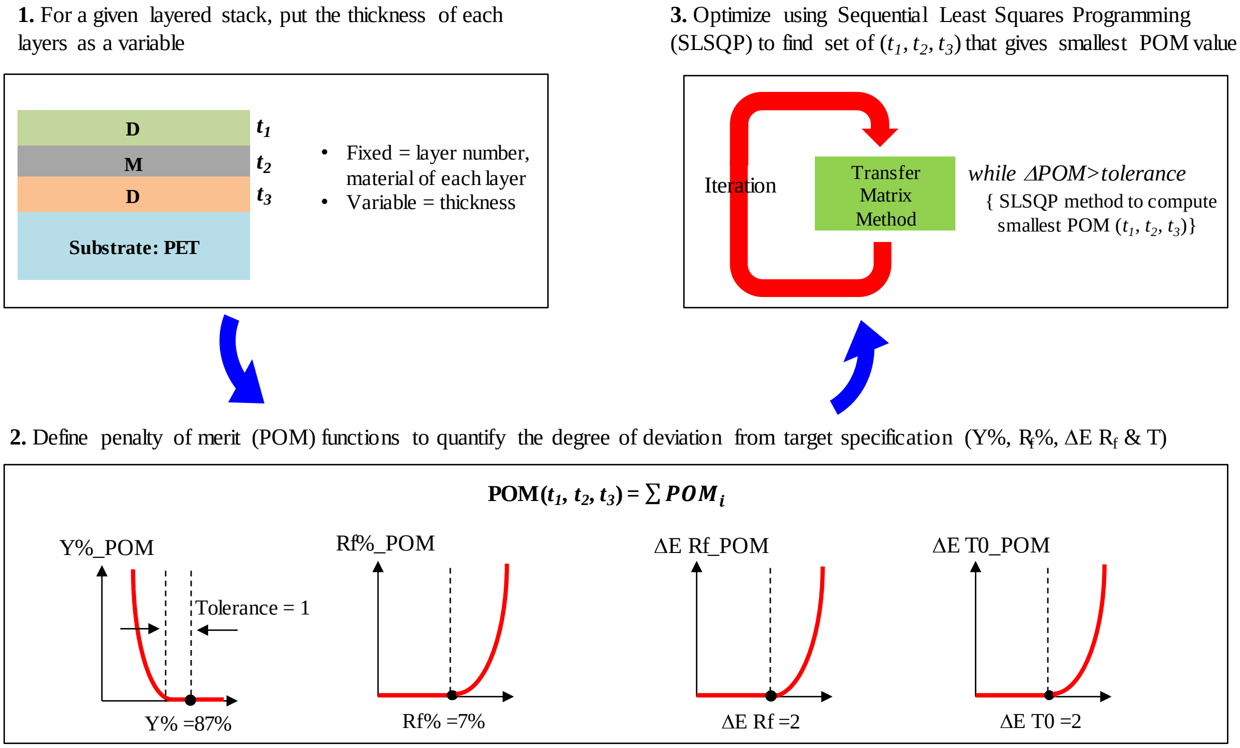

**Courtesy: Michael Waters for POM optimization code*

Figure 4.8 Optimization process flow of transparent conductor to meet various target specifications.

4.4.2 Optimization of 3-layered stack

For a 3-layered DMD stack transparent conductor, the stack was optimized to satisfy both the transmittance (T_{ave} %) and color contrast. Black solid and dotted curves in Figure 4.9 shows the transmittance (T) and reflectance (R) spectra obtained from the optimization that focused only to maximize the T_{ave} %, respectively. As shown on the left bottom of inset figure, this stack with optimum thickness as indicated shows T_{ave} % of 89.1% but with a significantly large $\Delta E\ R$ of 10.1. When I optimize the stack with respect to both T_{ave}% and color contrast parameters as how it is described in step 2 of Figure 4.8, the T and R spectra are plotted with solid and dotted red lines, respectively. This stack with corresponding thickness and stack properties are shown at the right bottom section of inset figure. The T_{ave} % is compromised down to 86.4% with a slight reduction of $\Delta E\ R$ down to 4.8. This is induced by a change in the thickness of top and bottom dielectric layers. At the expense of attempting to reduce the $\Delta E\ R$ down to 4.8, almost 3% of T_{ave} % was compromised, which is undesirable for a transparent conductor.

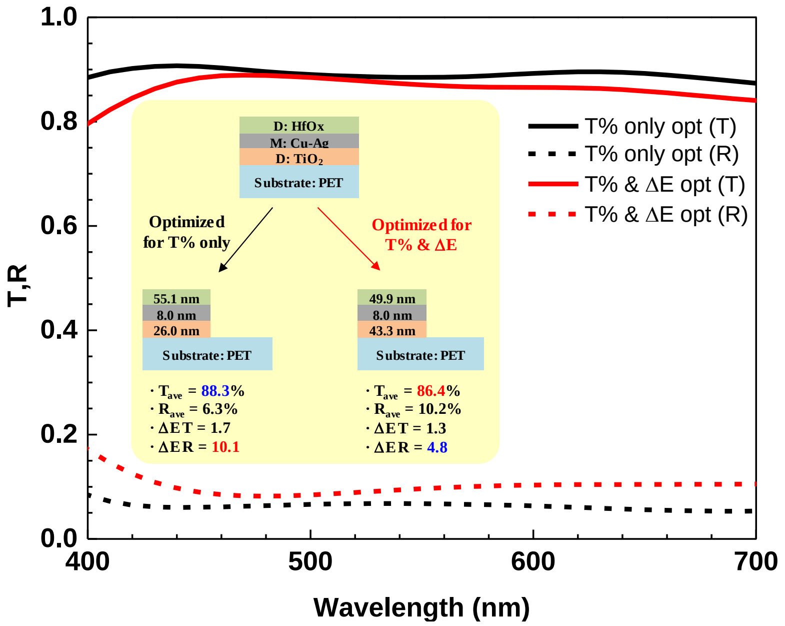

Figure 4.9 T and R spectra for the DMD stack optimized only for T_{ave} % or for T_{ave} % and ΔE.

4.4.3 Optimization of 4-layered stack

As seen in the 3-layered DMD stack, there is a fundamental trade-off between trying to balance the color and increase the *T*. Owing to the fact that the reduction of $\Delta E\ R$ is done in a way to balance the reflection from DMD to be close to that from bare PET which is R_{ave} = 11.3%, compromise in the *T* seems indispensable. However, if I can introduce another optical layer that has a good etching selectivity under DMD patterning thereby remains on top of PET to act as an anti-reflective layer, then the decoupling of $T_{ave}\ \%$ and $\Delta E\ R$ would be possible. As PET substrate has an index of ~1.65, index matching layer of SiO_2 was chosen as an underlying layer in between DMD and PET substrate as shown in the inset of Figure 4.10a. SiO_2 has a good etching selectivity thereby will remain while patterning DMD layer. Figure 4.10a shows the simulated spectrum of *T* and *R* for the case of optimizing *T%* only (black) and *T%* and ΔE (red). The inset schematic shows the optimized stack condition for each optimization case when the specifications shown at the bottom. As shown on the bottom left of inset schematic where the stack is optimized for maximizing $T_{ave}\ \%$, having low index material like SiO_2 is not beneficial and so the optimizer forced the SiO_2 layer thickness to be zero. In such case, the stack reduces to 3-layered stack as shown in Figure 4.9. On the other hand, as shown in the bottom right of inset schematic, inserting SiO_2 layer and optimizing for both $T_{ave}\ \%$ and color contrast results in ΔE T and R to be less than 2 while not significantly jeopardizing $T_{ave}\%$ = 87.7% which is drastically different from the 3-layered stack's case. Significant reduction of ΔE is not only due to the balancing of *R%* between the etched (only SiO_2/PET) and unetched (HfOx / CuAg / TiO_2 / SiO_2 / PET) regions but also due to the balancing of a^* and b^* to be close to zero (The set of [a^*, b^*] values are [0.3, -1.2] for *T* and [0.3, 0.5] for *R*). This is due to the fine tuning of the T and R spectra so that it shows a neutral color. From *eq 4.8b* and *eq 4.8c*, a^* and b^* value each quantifies how much of red and blue spectrum take part in the total spectrum compared to the green spectrum. Figure 4.10b shows optimized 4-layer stack's T and R along with $\bar{x}$, $\bar{y}$, and $\bar{z}$ spectra. It is interesting to note that T has two peaks near 450nm and 660nm.

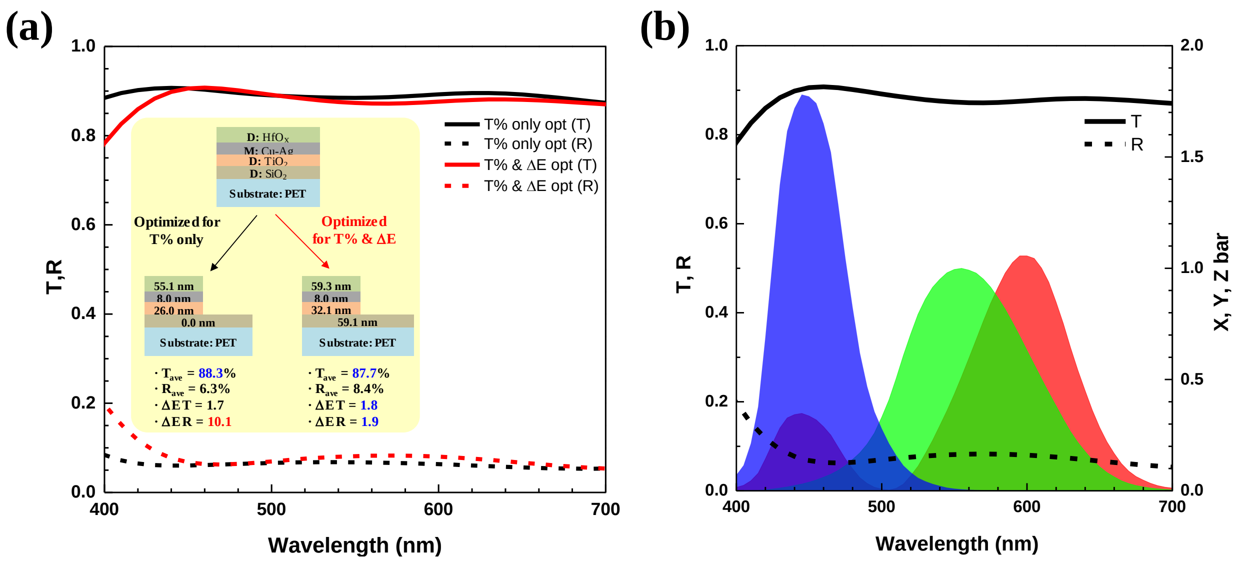

Figure 4.10 (a) T and R spectra for the 4-layered stack optimized for high $T_{ave}\%$ and low ΔE. (b) T and R spectra of optimized 4-layered stack with $\bar{x}$, $\bar{y}$, and $\bar{z}$ spectra.

To neutralize the color, dielectric thicknesses were adjusted so that more portion of blue and red light can be transmitted to balance the broad range of green spectra. Similar mechanism can be thought for R spectra as well. In principle, when dielectric materials are fixed, adjusting the thickness can blue or red shift the Fabry-Perot resonance thereby allowing for the tuning of spectrum so that neutral color can be obtained. This design rule should provide a good strategy when designing a transparent conductor especially almost all of the work focuses on merely increasing the $T_{ave}\%$.

4.5 Metal-Dielectric Photonic Crystal for Low Resistance FTC

4.5.1 1-dimensional photonic crystal structure

When the sheet resistance of a transparent conductor is as low as 1Ω/sq, it has enormous potential for ultrafast responsive touch panel for large area device. Unfortunately, conventional ITO based transparent conductive oxide materials require too thick of a layer to achieve such sheet resistance, which is impractical in terms of the cost as well as for the throughput. On the other hand, metal films can achieve much lower sheet resistance due to its intrinsically low resistivity. Despite its low resistivity, sufficiently thick film is still needed to guarantee sheet resistance as low as 1Ω/sq. High reflectance arising from such a thick metal film cannot be completely salvaged by using anti-reflective coating only. In this section, 1-dimensional metallo-dielectric photonic crystal (1-D MDPC) structure is introduced to achieve 1Ω/sq with reasonable visible transmittance. First, the impact of Ag film's thickness on the transmittance of DMD transparent conductor was studied as shown in Figure 4.11a. For this case, top and bottom dielectric layers that were used in Figure 4.4 were used in this case as well with adjusting thickness for each Ag film's thickness to maximize the transmittance. As the Ag film's thickness increased from 8 nm to 40 nm, the transmittance in the visible wavelength significantly decreased. The average T (T_{AVE}) and R (R_{AVE}) along with *Y%* (transmittance normalized to human eye response) as a function of Ag film thickness are plotted in Figure 4.11b. For Ag film thickness up to 11 nm, R_{AVE} is maintained well within 5 - 6%. However, beyond 11 nm, it increases almost linearly with the Ag film thickness which causes the T_{AVE} to reduce. This indicates that there is only so much that the top and bottom dielectric layers can salvage the reflection from the Ag film.

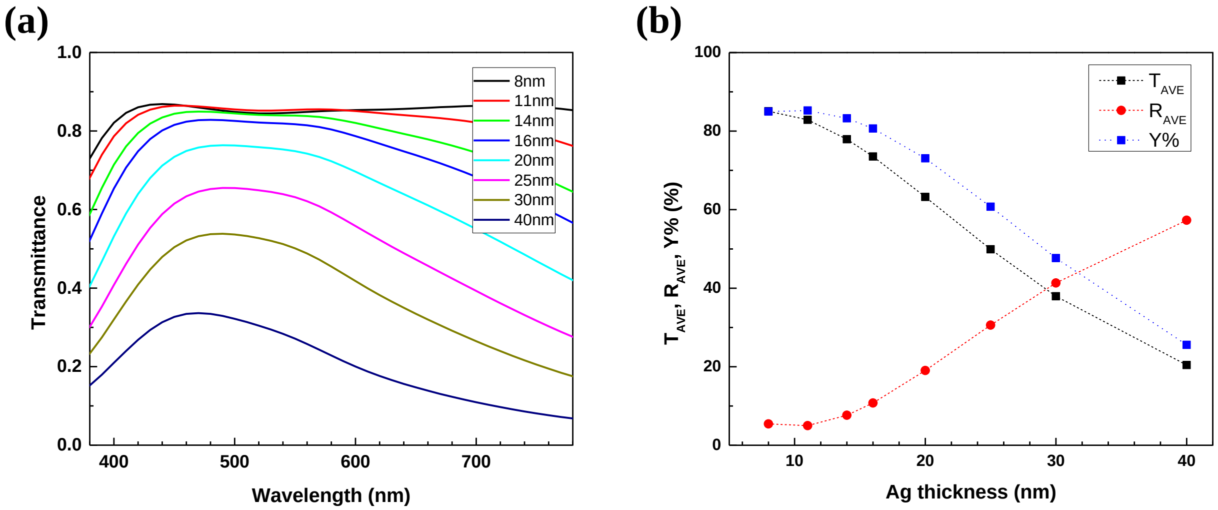

Figure 4.11 (a) Transmittance spectra of DMD structure with increasing Ag film layer thickness. (b) $T_{ave,}$ R_{ave}, and Y% as a function of Ag film layer thickness.

From the resistivity-thickness curve, 40 nm of Ag film should be sufficient to achieve sheet resistance of 1 Ω/sq. However, with conventional DMD structure with Ag film thickness of 40nm would have over 60% of average reflectance and slightly over 20% of transmittance, which would be too opaque for it to serve as a transparent conductor. 1-D MDPC structure can be used to significantly increase the transmittance of this optical stack. 1-D MDPC consists of alternating layers of metal and dielectric layers where the periodicity of these alternating layers creates a photonic bandgap for a light propagating through it. In this case, I will use thin Ag film for the metal layer and transparent conductive oxide like aluminum-doped zinc oxide (AZO – 3:97 = AlOx:ZnOx ratio) as a dielectric layer to ensure both high transmittance and conductivity. In visible wavelength range, Ag has a index value close to 0 and AZO has index value near 2. The alternating layers of this low and high index contrast can produce a photonic bandgap with a stop band in the visible region. These 1-D MDPCs have photonic properties in the transmission mode where the change of the displacement field of the first and second band by the inserted Ag layers results in the extension of bandwidth, while interference can enhance the transmission in visible spectra [112]. In specific, the structure of 1-D MDPC is shown in Figure 4.12a. Transmittance spectra for 1-D MDPC with varying number of Ag layers inside the structure was calculated while maintaining the total Ag thickness to be 40 nm for each structure. The number of Ag layer was varied from having just one layer sandwiched by AZO layers up to 4 layers of Ag layer each sandwiched by AZO layers. The resulting average transmittance ($T_{ave}\%$) value in the visible range and $Y\%$ are plotted in Figure 4.12b. As the number of Ag layers inside increases, the $T_{ave}\%$ and $Y\%$ increases up to 53% and 67.7%, respectively. Compared with having just one Ag layer of 40nm in thickness, when having 4 layers of 10 nm of Ag film shows significant improvement in the transmission in visible wavelength range. Not only the transmittance, but also the bandwidth throughout the visible range is broadened as the number of the layer increases. This 1-D MDPC strategy should provide a guideline for improving transmittance of a transparent conductor that requires extremely low sheet resistance.

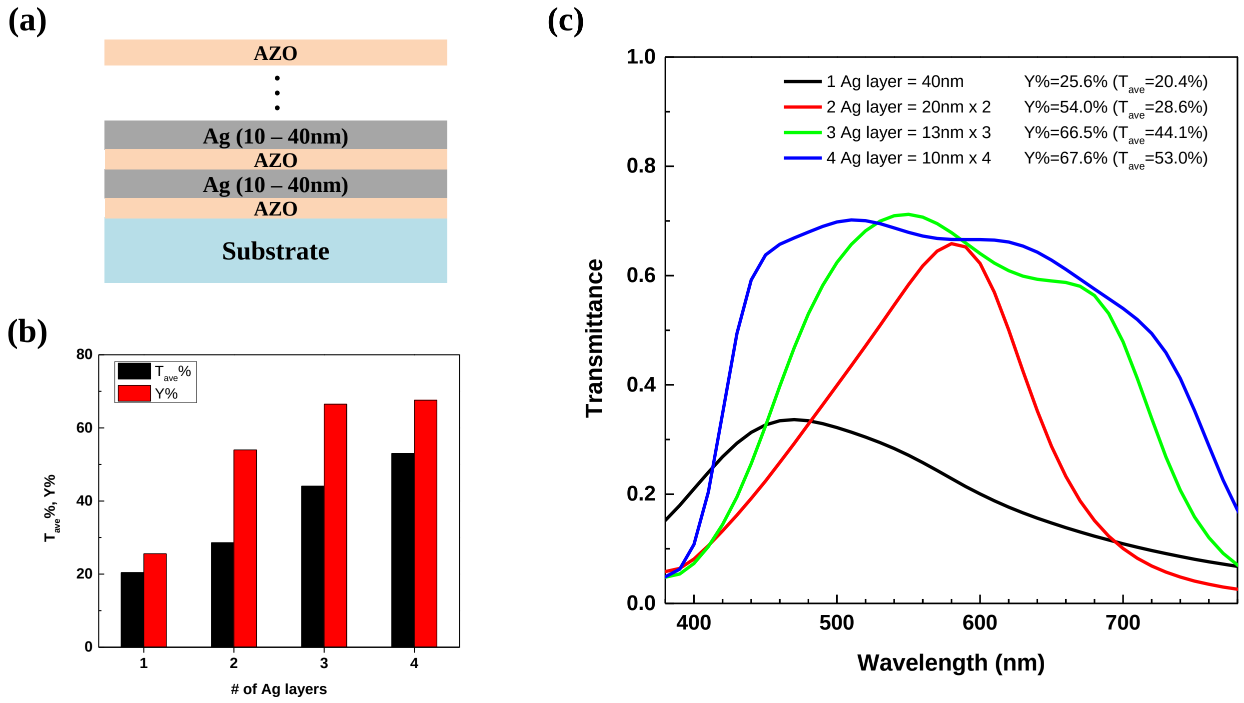

Figure 4.12 (a) Schematic of Ag-AZO based 1-D MDPC structure. (b) Average T% and Y% with respect to the number of Ag layers used in the 1-D MDPC where total thickness of Ag used in each case is fixed to 40nm. (c) Transmittance spectra of 1-D MDPC with varying number of Ag layer thickness.

4.5.2 Colored-Transparent Antenna

This 1-D MDPC is not limited to transparent interconnect for high density transparent display application but can be used to design semi-transparent antennas. Metal films can be patterned to configure resistance and capacitance to form antennas. Moreover, having a colored antenna to tailor transmission and reflection light spectrum through the film can be useful for aesthetic purposes. Such low-resistance FTC can be tuned to transmit only a desired wavelength at optical frequency. As shown in Figure 4.13, 1-D MDPC consisting of alternating layers of TiO_2 and Ag can be tuned simply by adjusting the thickness of each layers to transmit blue, green, or red spectrum. The color at which this stack appears becomes very sensitive to the environment (depending on how much of intensity difference between T and R). Depending on the purpose, such a trait can be found quite interesting.

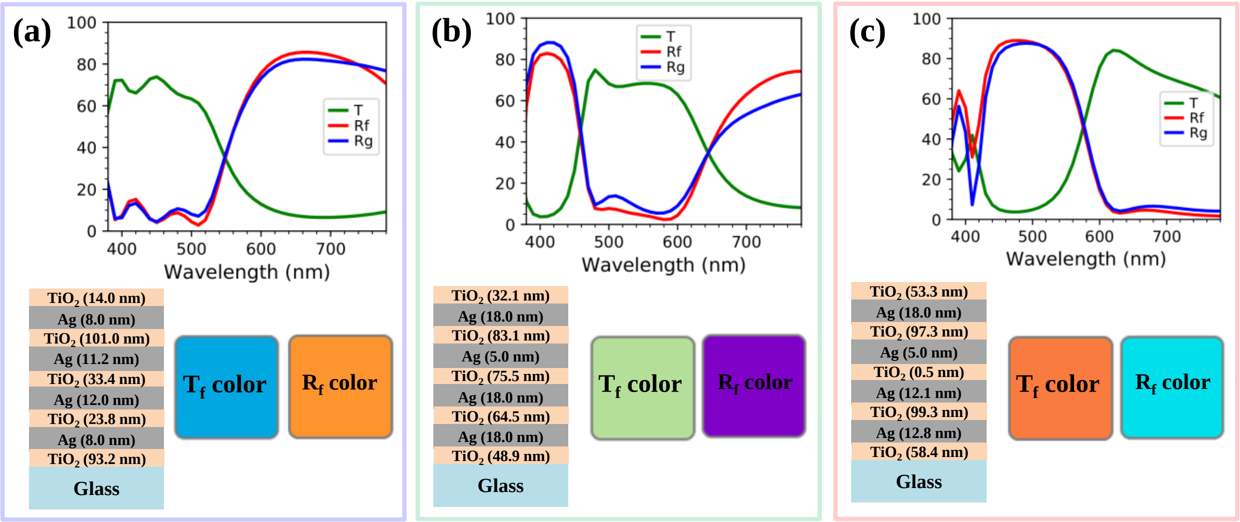

Figure 4.13 Low resistance 1-D MDPC transparent conductor with tunable property. By adjusting the metal and dielectric thickness, the stack can be designed to show bandpass filter properties at (a) blue, (b) green, and (c) red wavelength. Corresponding film-side transmission (Tf) and reflection (Rf) color calculated from the spectral curves are shown to illustrate the color of stack.

4.6 DMD for Highly Efficient OLED

One important aspect of designing DMD as a TC for OLED is to design layers so that it is optimized in terms of maximizing transmittance (*T%*) under the presence of OLED stack structure. However, research on TC so far focused on maximizing *T* of itself freestanding on a substrate. It is very likely that the optically optimum point of freestanding TC can be different from that of TC placed under OLED stack structure. To verify this, transfer-matrix method (TMM) calculation was performed for DMD-substrate structure when placed in air-air medium, organic-air medium, and organic-substrate medium as shown in 2D map of Figure 4.14a, b, and c, respectively. OLED structure of Figure 4.6a was considered for the calculation. For DMD, top and bottom ITO dielectric's thickness indicated as *T1* and *T2* were varied from 0 to 90 nm while fixing Cu-Ag thickness as 8 nm. For the case with TC inserted inside the OLED device configuration as in Figure 4.14b and c TAPC thickness was fixed to 40nm. Considering freestanding DMD-substrate in air medium, the 2D map shows that the optimum top and bottom ITO dielectric thickness that gives highest *T%* at green wavelength (430-630nm) is *T1* = 41.8 nm and *T2* = 51.8 nm. However, when this TC is interfaced with the emission layer and HTL layer, the optimum thickness that gives maximum *T%* shifts to *T1* = 38.6 nm and *T2* = 37.7 nm. In practice, scatterer or microlense [113] are used at the interface of the substrate to extract the light that is trapped at the substrate thereby maximizing the overall light extraction. Considering this aspect, TMM simulation for the case of excluding light trapping at the substrate was conducted by setting bottom medium as an index matching medium with the substrate as shown in Figure 4.14c. For this case of having top medium as organic layer and bottom medium as medium with same index as the substrate, the optimum point resides at *T1* = 39.0 nm and *T2* = 38.1 nm. These results indicate that the DMD based TC for OLED application needs to be optimized not for itself but needs to consider entire device stack as a whole in achieving maximum *T%*.

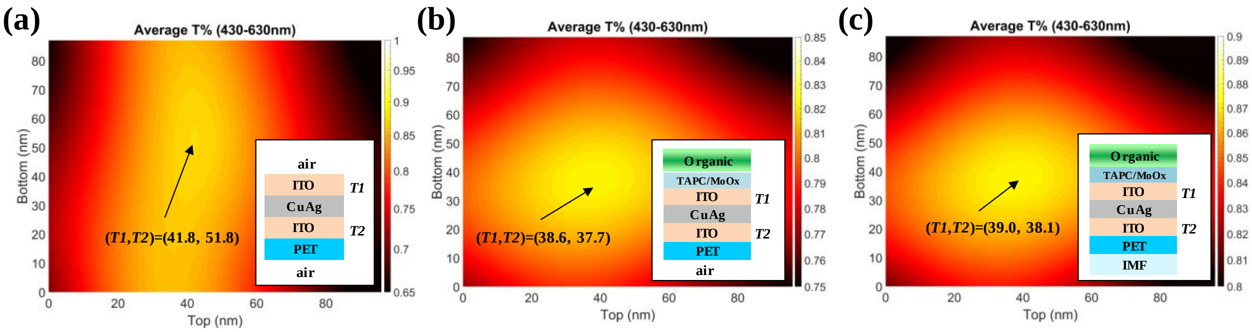

Figure 4.14 Average *T%* of DMD under (a) air-air medium (b) organic-air medium, and (c) organic-substrate medium.

Figure 4.15a shows *T* and reflectance (*R*) of fabricated DMD on a PET substrate based on optimum structure in Figure 4.14c and commercial ITO sample. Simulation spectra of these TCs are also plotted in dotted lines. The measured electrical sheet resistance of DMD and ITO are 12.8 and 10.0 Ω/sq, respectively. One argument which may weaken the metal-based TC over counterparts is that metal films are usually very reflective and so reflection gets aggravated especially at a large angle of incidence. To verify this point, TMM calculation for angle of incidence range from 0 to 80° was calculated for ITO and DMD as shown in Figure 4.3b. Surprisingly, simulation results show that metal-based DMD TC shows lower R intensity compared to ITO even up to 80° angle of incidence. This can be understood in context of top and bottom dielectric layers serving as anti-reflective coating layers which induce destructive interference for reflectance intensity.

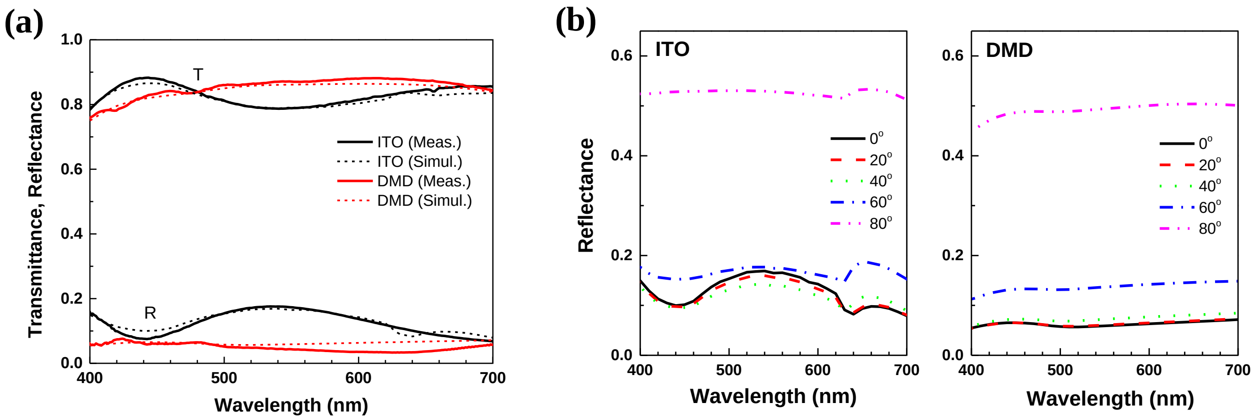

Figure 4.15 (a) Simulated/measured *T* and *R* of ITO and DMD. (b) *R* as a function of angle of incidence.

To demonstrate the DMD as FTC for OLED, device was fabricated with using ITO or DMD as an anode. Figure 4.16a shows current density (*J*) versus *EQE* plot for ITO and DMD device with and without using IMF in between the substrate and the detector. Without using the index matching fluid which is only considering light intensity in the air mode, ITO and DMD device shows EQE of 15.5% and 13.8%, respectively.

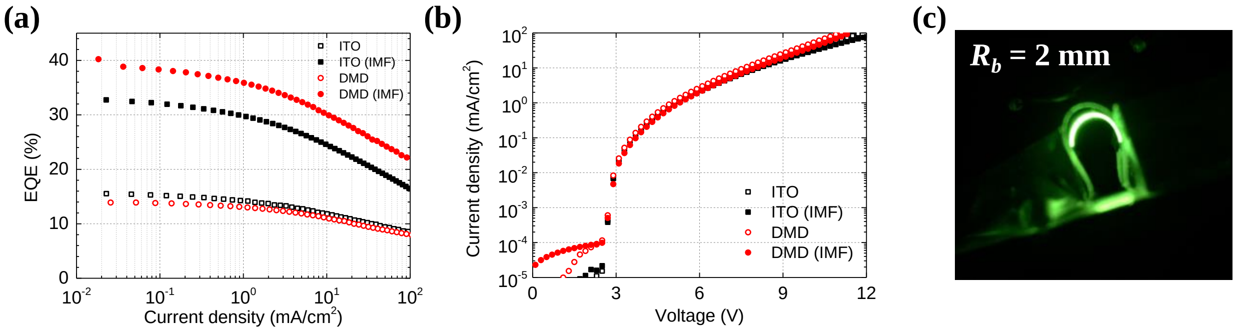

Figure 4.16 (a) External quantum efficiency (EQE) and (b) current density-voltage (J-V) characteristics of ITO and DMD devices with and without index-matching fluid (IMF). (c) DMD device on flexible substrate after bending with 2mm bending radius.

However, when accounting for both air mode and glass mode by using IMF, DMD device shows 40.2% whereas ITO device shows 32.7% of EQE. This is attributed to the better light outcoupling by using DMD. This is owing to the intrinsic property of the Ag film as discussed in Chapter 4. *J-V* curve is plotted in Figure 4.16b where it shows an overlap with ITO device. This indicates that using DMD as anode does not negatively affect the hole injection property. Figure 4.16c shows the DMD device fabricated on a PET substrate in operation under bending radius of 2mm showing excellent flexibility of DMD as FTC.

According to the simulation in Figure 4.15b, metal-based DMD does not necessarily show higher reflection at a higher angle of incidence owing to the top and bottom anti-reflective coating. To experimentally verify this point, angle dependent electroluminescence (EL) spectral data was collected for ITO and DMD device as shown in Figure 4.17a. First, as the angle was varied from 0 to 50°, the intensity of the spectrum decreased with increasing angle of incidence but there was no observable change in the spectral shape of EL. As it is desirable for light emitting device for display application to maintain same color with respect to viewing angle, the result signifies that DMD TC is a promising candidate for OLED for display application. Figure 4.17b shows the angular emission profile of ITO device and DMD device where black line shows the Lambertian profile. Although both the devices show very similar profile, the one with DMD is slightly closer to the Lambertian shape which makes DMD a strong candidate to replace ITO for FTC application.

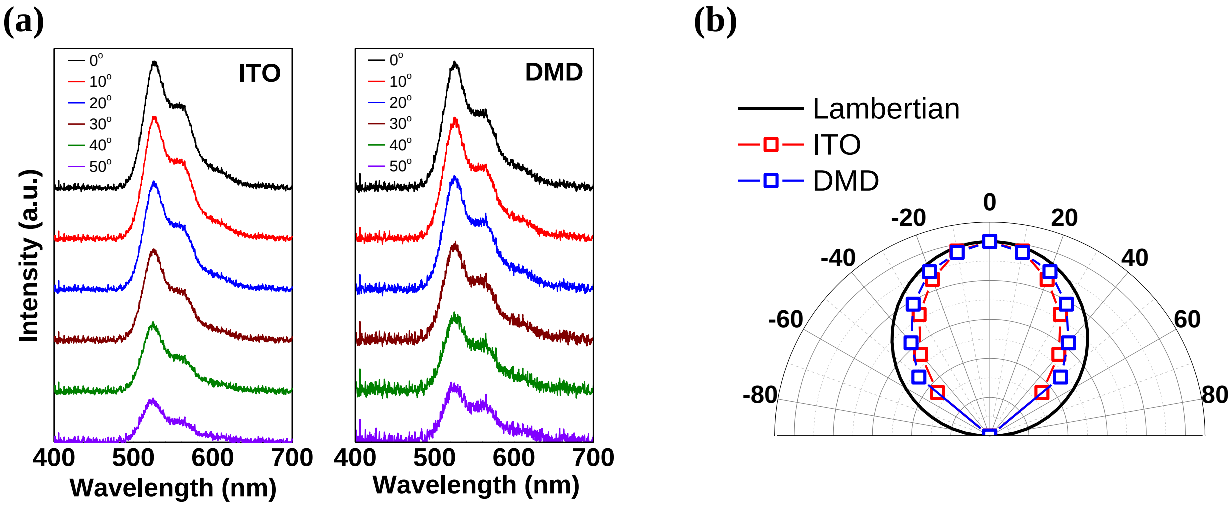

Figure 4.17 (a) Angle-dependent EL analysis and (b) polar radiation pattern of ITO and DMD device.

Finally, for display application, each pixel should have blue and red light emitting device (LED) as well. Depending on the emission wavelength, DMD can be optimized so that it shows the best transmittance at a target wavelength. For example, DMD for blue and red LED can be optimized as shown in Figure 4.18a and b, respectively. These simulations were conducted for the case of DMD-substrate placed in the air medium instead of in the OLED for a potential exclusion of difference coming from difference in emission / HTL layers. Figure 4.18c shows the comparison of DMD spectrum optimized for green, blue, and red emission range, where by changing the top and bottom dielectric thickness, resonance of destructive interference for reflection spectrum can be tuned at a visible wavelength range. This clearly shows the versatility of DMD as a FTC for maximizing transmittance at a target emission wavelength.

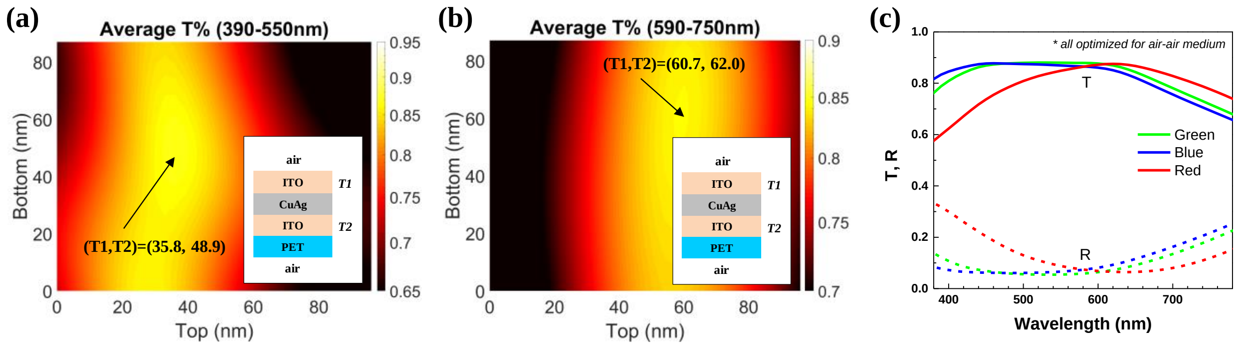

Figure 4.18 2D map of DMD optimization for (a) blue and (b) red emission. (c) *T* and *R* spectrum for DMD optimized for green, blue, and red emission.

4.7 Stability of transparent conductor

4.7.1 Stability Issue of Ag-based Transparent Conductor

Stability of metal-based transparent conductor is a fundamental issue that needs to be overcome for its commercialization. Silver (Ag) is known to have poor stability under ambient condition. Stability issue in this case includes oxidation of Ag atoms, tarnishing of the surface due to sulfide [114], or migration of the atoms or dopants over time or at elevated temperature condition. These issues are aggravated when the film size is reduced to a thin film regime where the surface boundary plays a crucial role and the recrystallization temperature is reduced. Also, introduction of humidity may accelerate oxidation reaction of Ag atoms which can lead to potential failure of the device as a transparent conductor application. Methods to enhance Ag film's stability under harsh environment condition (i.e. high humidity or high temperature) will be introduced. Also, electrochemical impedance spectroscopy will be used to evaluate the dielectric's passivation property under wet condition.

4.7.2 NiCr for Ag Atom Diffusion Barrier and Self-Assembled-Monolayer (SAM) for Humidity Resistance

In practice, transparent conductors should withstand harsh environmental conditions like highly humid and high temperature conditions. Under such condition, what is not easily observed in Ag-film at ambient condition can be pronounced at this accelerated condition. For example, grain boundaries in Ag film contain sufficient stored energy in the form of stress, large areas of grain boundaries with high concentration of vacancies, lattice defects and chemical free energy. Diffusion of Ag atoms through grain boundaries can happen at a room temperature due to the large energy stored in these boundaries. This can be significantly accelerated at a high temperature condition. Ag atoms migration could result in agglomeration of Ag into particles making film discontinuous and make the film electrically insulating. Barrier materials can be used to prevent metal atoms from migration. Careful choice of this material is needed so that optical transparency of the layer is not significantly compromised. In this section, NiCr (80:20 wt%) metal film is used as a barrier layer to prevent Ag from agglomeration. Widely used barrier materials like NiCr is known to act as a good adhesion layer to any substrate meaning that it can form a continuous film even at extremely thin film. Figure 4.19 shows the effectiveness of having 1.5 nm of NiCr on top of Cu-Ag in preventing Ag agglomeration at high temperature. After annealing of Cu-Ag film at 450 °C, the film no longer becomes continuous and agglomerates to form clusters of Ag particles as shown in Figure 4.19c. While the initial film shows 12.55 Ω/sq, the R_S is unmeasurable after annealing due to discontinuous film behavior. As shown in Figure 4.19d, non-uniformity in the film can be clearly indicated by visual inspection. On the other hand, having 1.5 nm of NiCr layer on top of Cu-Ag film keeps the film continuous inhibiting the Ag from agglomeration. The value of R_S changes from 14.24 to 17.60 Ω/sq after annealing, maintaining its integrity as a conductor.

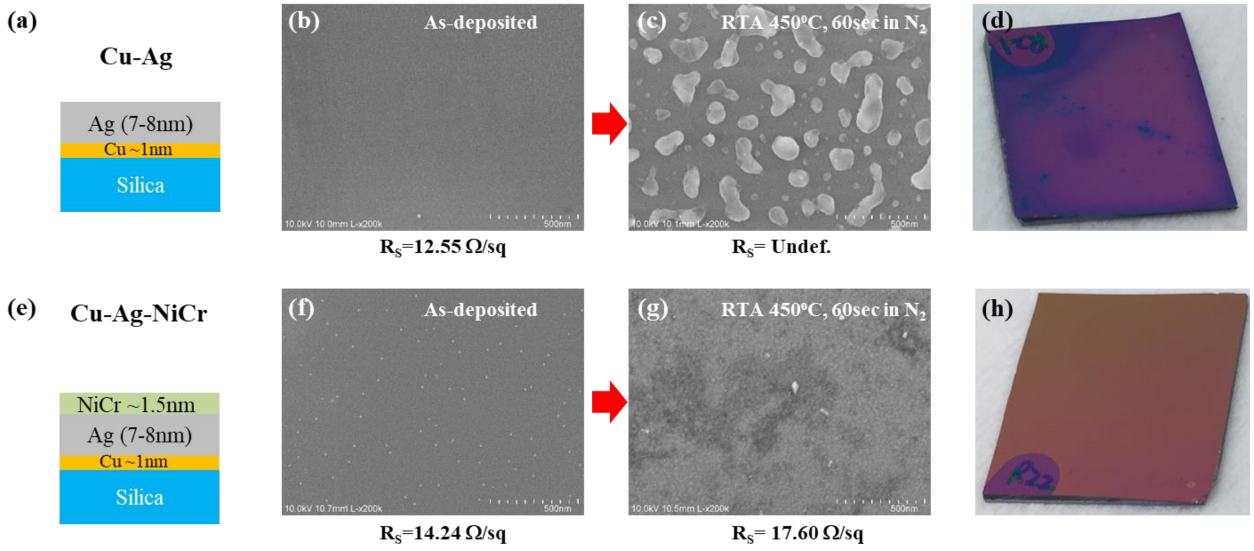

Figure 4.19 (a) and (e) are film stack schematic of Cu-Ag and Cu-Ag-NiCr film, respectively. Top-down SEM image of film surface before ((b) and (f)) and after ((c) and (g)) annealing of Cu-Ag film and Cu-Ag-NiCr film, respectively. (d) and (h) are photograph of sample surface after annealing of Cu-Ag and Cu-Ag-NiCr film, respectively.

Next, these films were put into the humidity chamber to test the stability. Under the present of humidity which could act as an electrolyte, silver can get ionized in which the mobility of silver is facilitated. Such reaction can result in dissolution of silver atoms or turns into an agglomeration of silver particles. The chamber condition was put at 80 °C with relative humidity of 85% where sample's change in resistance (ΔR_S) was monitored over span of time as shown in Figure 4.20a. As a result, Cu-Ag showed over 20% in ΔR_S after 60 hrs in the chamber. On the other hand, Cu-Ag film with 1.5 nm of NiCr layer shows less than 20% of ΔR_S after 170 hr in the humidity chamber. This may be explained in terms of two aspects. First, NiCr is acting as a thin layer preventing the moisture from entering the underlying Ag film, leading to a failure in the film. Even if there exist a non-uniformity in the NiCr film and so humidity can interface with underlying Ag film, NiCr layer still acts as a blocking layer to prevent majority of Ag atom from agglomeration due to humidity. Second, NiCr has higher oxidation potential than Ag meaning that when two materials are present under humidity condition, oxidation process is likely to happen at NiCr and reduction process at Ag. If ionization of Ag into Ag^+ is suppressed, then the migration of Ag atom can be suppressed despite the existence of humidity.

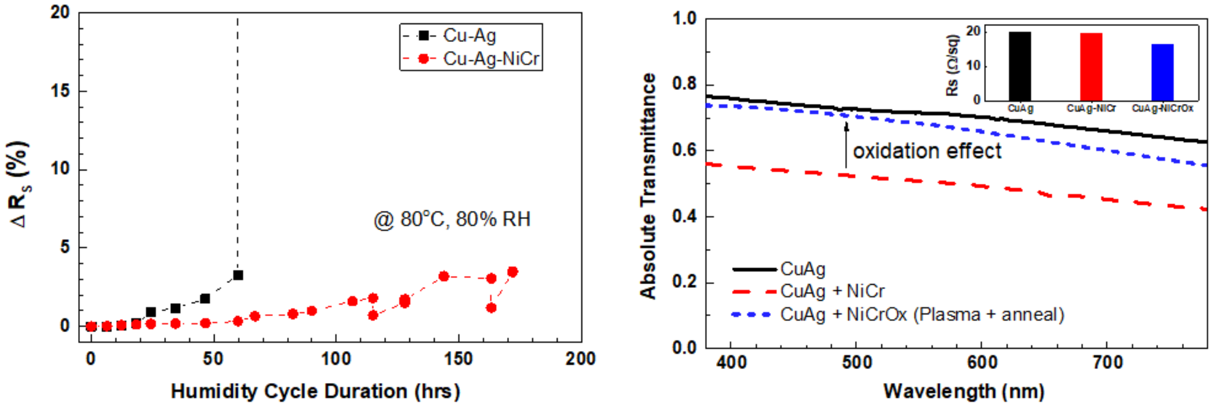

Figure 4.20 (a) Humidity cycle test result and (b) oxidation effect of NiCr layer on transmittance.

Despite NiCr film's effectiveness in increasing Ag film's stability, it has a significant optical loss as it absorbs light. As shown in Figure 4.20b, even 1.5 nm of NiCr layer can significantly decrease the transmittance at a visible wavelength range. For this reason, partial oxidation method was used to partially oxidize the surface of NiCr film into NiCrOx to minimize the loss while maintaining the electrical property as too thick of an oxidation layer could increase the electrical resistance. For oxidation process, Cu-Ag-NiCr film was put into plasma chamber with oxygen flow of 100 sccm and RF power of 800W, with a substrate temperature of 60°C for 120 seconds. Then the sample was put on 200°C hot plate for 10min to oxidize the surface. As a result of this, the transmittance is recovered to a level very close to the original Cu-Ag film. R_S value slightly decreased as shown in the inset of Figure 4.20b after this partial oxidation step which is likely attributed to the reduced resistivity of Ag film by annealing at high temperature. This approach of increasing the stability can be readily applied to the PVD system along with the transparent conductor fabrication process with just additional NiCr sputtered target source.

A more innovative approach would be to use thiol-based self-assembled monolayer (SAM) to passivate the Ag film surface. It is known that thiol compound adhere onto the Ag surface where anions provided from this compound can stabilize Ag ions despite the presence of electrolyte condition [115]. Such a monolayer of coating on Ag film is known to be effective in anti-corrosion of Ag film [116] while it has negligible impact on the optical property of Ag film unlike NiCr layer. Here, thiol-based 1-Hexadecanethiol (HT) and 1-Dedecanethiol (DT) were chosen as a SAM layer to passivate the surface of Cu-Ag film. For HT treatment, Cu-Ag film was immersed in 0.15M of HT in IPA solution for 1 hour. For DT treatment, Cu-Ag film was immersed in 0.01M of DT in ethanol-based solution for 30 minutes. Then, these samples were immersed in DI water to observe the resistance change (ΔR) over time as shown in Figure 4.21. For the film without any SAM, ΔR rapidly increased after 20 hrs of immersion and eventually became discontinuous at 23 hrs. The resulting microscope image of this film is shown in the inset figure. On the other hand, HT or DT coated Cu-Ag sample showed no change in resistance even after 240 hours. Visual inspection of the sample surface showed no sign of degradation even at any localized spot. Further verification of SAM formation on Ag film will be verified in the next section but this simple experiment demonstrates the how effectively thiol-based SAM can stabilize Cu-Ag film.

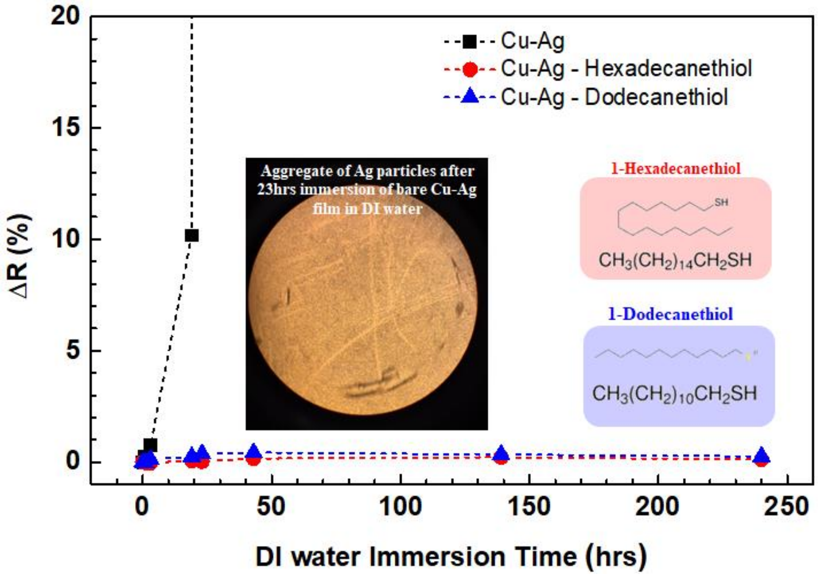

Figure 4.21 Change in *ΔR* of SAM coated Cu-Ag film under DI water immersion test.

4.7.3 Electrochemical Evaluation of Passivation Dielectric Layer

Electrochemical analysis can be used as a tool to analyze the microscopic interface between the film and the electrolyte. Impedance spectroscopy can give frequency dependent response of the charge transfer process that is happening at this interface. As the degradation of Ag film is accompanied by the charge transfer process, impedance measure can be used to quantify this process. Also, polarization curve measurement can give information on the corrosion behavior of the film. In this sub-section, potentiostat and frequency response analyzer is used to quantify the efficacy of dielectric or SAM as a passivation layer in preventing Ag corrosion under salt-water condition. Schematic of the experiment is shown in Figure 4.22a where Ag coated with passivation layer is used as a working electrode (WE) where epoxy is used to define the active area exposed to the 0.51M NaCl solution. Ag/AgCl or Saturated Caromel Electrode (SCE) was used as a reference electrode (REF) and sufficiently large size (1 cm x 2 cm) of platinum mesh was used as a counter electrode (CE). Equivalent circuit model of having metal film coated with dielectric coating is shown in Figure 4.22b where description of each elements are described in the figure as well.

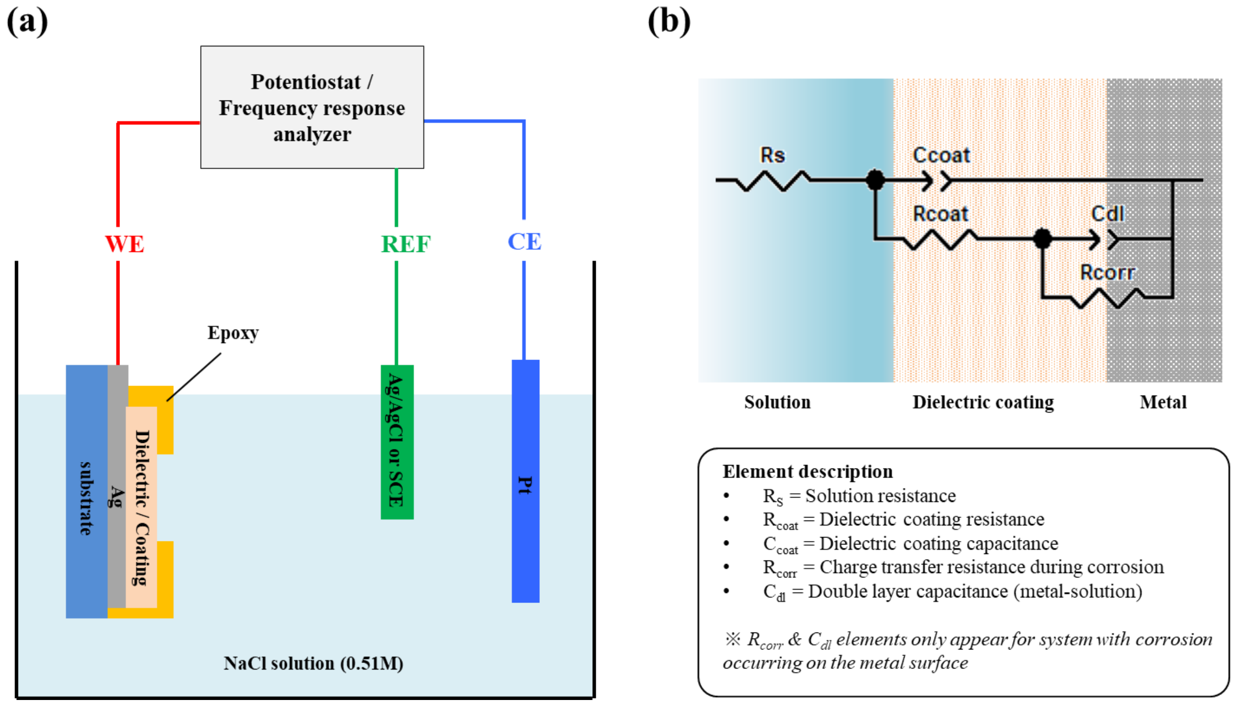

Element description

- R_S = Solution resistance
- R_{coat} = Dielectric coating resistance
- C_{coat} = Dielectric coating capacitance
- R_{corr} = Charge transfer resistance during corrosion
- C_{dl} = Double layer capacitance (metal-solution)

※ *R_{corr} & C_{dl} elements only appear for system with corrosion occurring on the metal surface*

Figure 4.22 (a) Schematic of experiment for analyzing passivation of Ag film. (b) Equivalent circuit of Ag-film with passivation dielectric immersed in electrolyte solution.

Impedance analysis measures the change in the output impedance (*Z*) response when small perturbation of alternating current (AC) signal is given as an input. In this measurement, input AC voltage amplitude of 10 mV was used and the frequency *f* was swept from 10 Hz up to 100 kHz. Before each measurement, the working electrode cell was immersed in the solution until the open circuit potential (OCP) is stabilized so that ΔOCP is within 10 mV for a span of 5 min. From this impedance measurement, both Nyquist plot and bode plot can be obtained. Nyquist plot is composed of real and imaginary part of *Z* value where the 4-th quadrant region represents the capacitive behavior of the reaction in cell. Although frequency dependence is not so obvious in this plot, the capacitive and resistive nature of charge transport reaction is obvious at a glance. For a typical electrochemical cell consisting of parallel R-C element is shown as a semi-circle in Nyquist plot. Figure 4.23a shows the change in the Nyquist plot of 30 nm ITO coated-CuAg sample inside the NaCl solution during 0 to 2 hrs of immersion time. Initially, the arc has a large radius of curvature indicating that the coating resistance (R_{coat}) is large for a given coating capacitance (C_{coat}) meaning the semi-circle has large radius. As the sample is more exposed inside the NaCl solution, the electrolyte infiltrates deeper through the ITO then interfaces with the underlying Cu-Ag film causing charge transfer reactions to happen in which corrosion resistance (R_{corr}) and double layer capacitance (C_{dl}) starts to take place. This results in the overall reduced impedance of the electrochemical reaction between the metal film and the electrolyte. During this process, dissolution or agglomeration of Cu-Ag film can induce the ITO film peeling off, which is shown in the inset figure. Bode plot, which is also a popular method plots the magnitude and phase of Z as a function of frequency. This plot gives frequency information of the equivalent circuit and is suitable to analyze the electrochemical elements that have frequency dependent components. For the same example, Bode plot of magnitude and phase curve is plotted in Figure 4.23b and c, respectively.

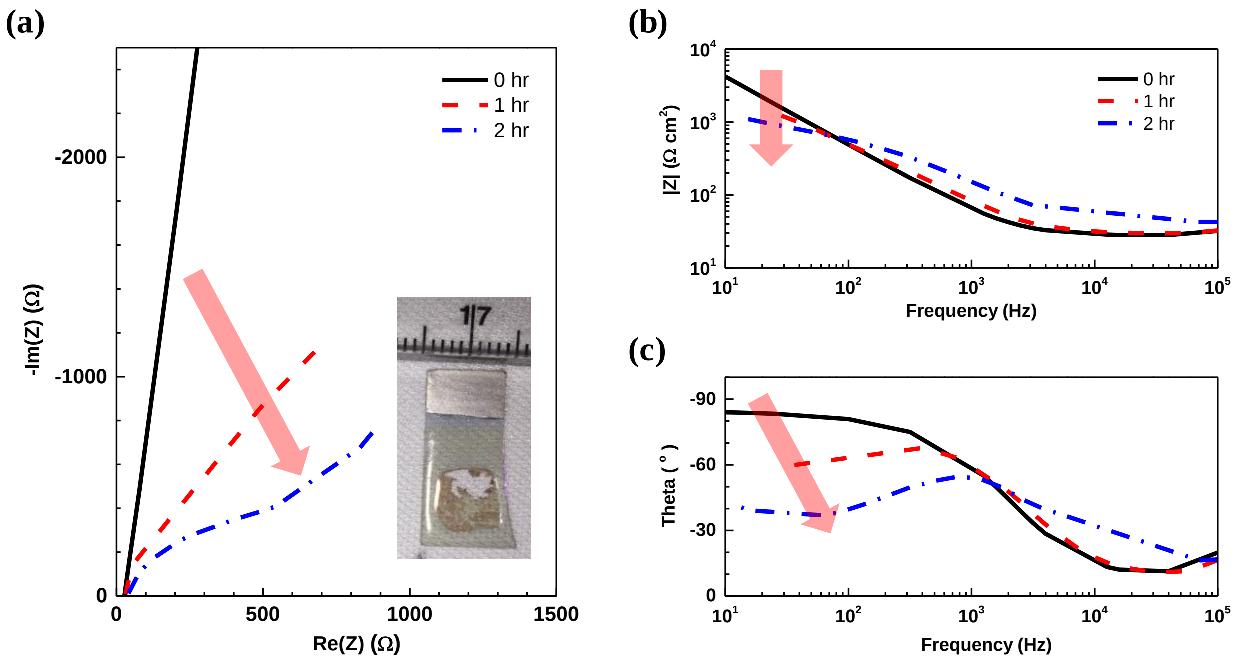

Figure 4.23 (a) Nyquist plot and (b) amplitude and (c) phase of Bode plot as a function of frequency for 30nm ITO-coated Cu-Ag film sample immersed under 0.51M NaCl for different time period.

Table 4.2 Types of passivation dielectrics used for experiment.

Passivation Dielectric	Deposition Method	Thickness [nm]
Al_2O_3	PVD: E-beam evaporation	26.8
ITO	PVD: Sputter	31.0
Si_3N_4	PECVD	29.5
Polymer IIR 4%	Spin coating	1500

Various types of dielectric layers were then evaluated to compare passivation effect where each of dielectric's thickness and deposition methods are described in Table 4.2. Impedance measurement and the parameters for each element are extracted for each sample as shown in Figure 4.24. Figure 4.24a and b shows bode plot of dielectric layers described in Table 4.2 immersed in NaCl solution after stabilization. The magnitude $|Z|$ (Figure 4.24a) at low frequency can indicate how well the passivation coating "impedes" the electrolyte penetration through the dielectric layer.

From this result, it shows efficacy in the order of IIR 4% > SiN > AlOx > ITO. As IIR 4% has a thickness 50 times thicker than other inorganic dielectrics, IIR 4% is anticipated to show the best passivation efficacy. Also, as PECVD is anticipated to show denser film than PVD, SiN shows better result than ITO or AlOx deposited by PVD. The phase diagram in Figure 4.24b is as a result of rather a complicated mixture of *R* and *C* components so direct analysis is not easy but it can be understood that if passivation coating is acting as an ideal layer, it would have theta difference of 90^{o} throughout the frequency range. Figure 4.24c shows the R_s (solution resistance) and R_{coat} for each dielectrics. R_s value is the x-intercept in the Nyquist plot indicating resistance at high frequency in which electrical series resistance or electrolyte solution resistance may take part in this. As same Cu-Ag film and electrolyte was used, it should show very similar values. R_{coat} indicates the ion's resistance in penetrating through the dielectric layer. For ideal dielectric coating, this value should have value close to infinity. The trend of R_{coat} for each coating are in line with the Bode plot's magnitude in the order of IIR 4% > SiN > AlOx > ITO.

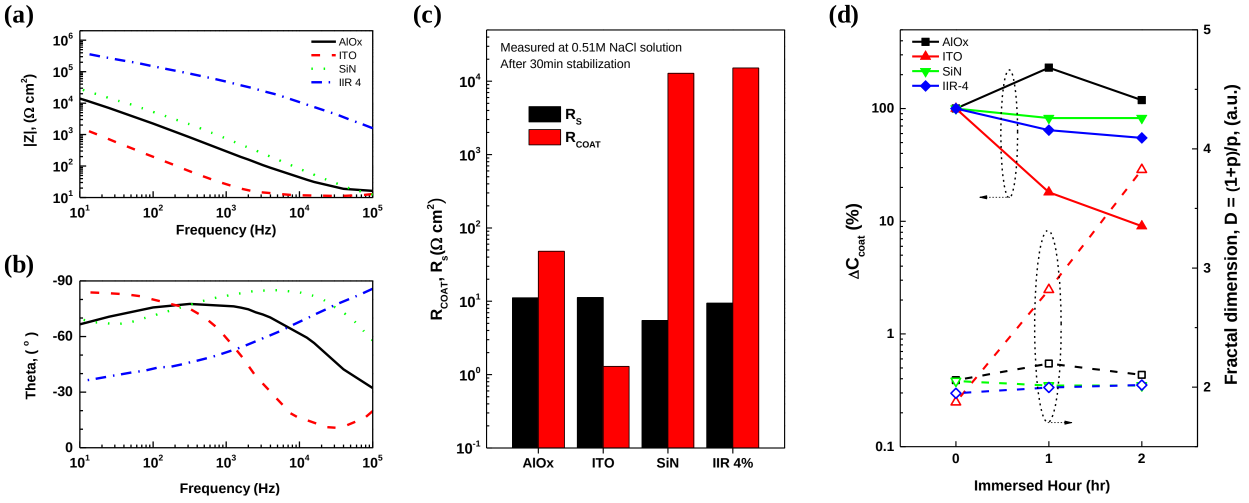

Figure 4.24 (a) Bode plot's *Z* magnitude, (b) phase, and (c) extracted *Rs* and R_{coat} for various dielectric layers after 0 hrs of immersion in NaCl. (d) change in Ccoat as a function of immersion time in NaCl.

For a non-ideal (i.e. surface roughness) electrochemical capacitance, constant phase element (CPE) is used where its impedance is defined as:

$$\mathrm{Z} = \frac{1}{Q \cdot (j \cdot w)^{p}} \tag{4.11}$$

where Q is frequency independent impedance value, w is angular frequency, and p is ideality factor. With extracted R_{coat}, physically relevant C_{coat} can be extracted based on the following equation:

$$\mathrm{C} = \frac{(Q \cdot R_{coat})^{1/P}}{R_{coat}} \tag{4.12}$$

Generally, when passivation coating degrades, it is accompanied by an increase in the surface area due to increase in the electrolyte infiltrating through the pores which gets reflected as a capacitance. However, at the same time if underlying Cu-Ag gets dissolved, then coating dielectric can get delaminated which reduces the active area therefore decrease in the capacitance. In such instance, the fractal dimension D given as $D = (1+p)/p$, which is a measure of the degree of how contorted the surface can indicate whether surface roughening is occurring. For ideal smooth surface, $p = 1$ and so $D = 2$. Based on above principle, C_{coat} values were extracted over a period immersion hours. Then the change in capacitance ΔC_{coat} and corresponding D is plotted over immersion time as shown in Figure 4.24d. As shown, ITO shows a significant reduction of ΔC_{coat} and increase in D value meaning both the delamination of the coating as well as the roughening of the surface is happening at the same time. PVD deposited AlOx shows increase in the ΔC_{coat} after 1 hr of immersion but then starts to decrease. This indicates that up to 1 hr, the coated layer increased surface area due to roughening of the surface. However, when past 2 hrs of immersion, the delamination of the coated dielectric also started happening. SiN and IIR 4% coatings, on the other hand, shows very robust behavior even after 2 hrs of immersion in NaCl solution, which is a harsh condition for ordinary electronic components to withstand. To further verify that the capacitance value extracted from the impedance measurement is in the order of physically reasonable range, capacitance value was calculated from considering the dimension and the permittivity assuming ideal parallel capacitor model. The calculated values are shown in Table 4.3. Except for ITO, extracted *Ccoat* values agree well with the calculated values. For the case with ITO, this large discrepancy could be because of the film already undergoing degradation during the process of 30 min of stabilization.

Table 4.3 Comparison table of calculated and extracted C_{coat}.

Dielectric	**Area [cm^2]**	**Thickness [nm]**	**ε_0**	**C_{coat} [F]**	
				Calculated	**Extracted**
Al2O3	0.38	26.8	8.5	1.1e-7	1.2e-7
ITO	0.40	31.0	3.3	3.8e-8	6.1e-7
Si3N4	0.17	29.5	6.2	3.2e-8	4.0e-8
IIR 4%	0.47	1500	3.5	9.7e-10	7.0e-10

$$C = \frac{\varepsilon_r \, \varepsilon_0 \, A}{t}$$

$$C = \frac{(Q_0 * R)^{(\frac{1}{p})}}{R}$$

As discussed in the previous section, coating of SAM on Cu-Ag surface is a powerful method to increase the stability of the film. In this section, polarization curve and impedance measurement is performed for Cu-Ag film coated with 1-dodecanethiol as a SAM layer. Polarization curve is widely used in corrosion industry to extract the corrosion rate of a material under certain electrolyte environment. Detailed discussion of this subject will not be discussed in here and only a brief explanation of the technique is sufficient in this scope of thesis. In brief, it scans through a very narrow voltage range (±20mV) near the corrosion potential (E_{corr}) and study the anodic and cathodic current with a slow scan rate. By plotting this in a *E* vs *log (I)* Tafel plot, anodic (β_a) and cathodic (β_c) exponent can be extracted from the Tafel slope by using the Butler-Volmer equation given as:

$$I = I_{corr} * \left(\exp\left(\frac{E-E_{corr}}{\beta_a}\right) + \exp\left(-\frac{E-E_{corr}}{\beta_c}\right)\right) \quad (4.13)$$

where I_{corr} is the corrosion current. Corrosion rate *MPY* (mils per year) can be calculated from this using:

$$MPY = \frac{I_{corr}\ (A/cm2) \cdot Equivalent\ Weight\ (g/equivalent) \cdot 393.7(mils/cm)}{Density(g/cm3) \cdot 96500(coulomb/equivalent)} \quad (4.14)$$

Figure 4.25a shows the polarization curve of bare Cu-Ag and Cu-Ag with SAM coated sample inside 0.51M of NaCl electrolyte solution. The voltage was scanned at a rate of 0.5 mV/sec. With respect to E_{corr} where anodic and cathodic current are at balance, right side of the potential indicates anodic reaction and left side a cathodic reaction. Cu-Ag film with SAM shows significantly suppressed anodic and cathodic current compared to that with bare Cu-Ag film. Slight shift in the E_{corr} to more positive potential is shown for SAM treated Cu-Ag film, which is usually an indication of the passivation of electrode surface[117]. Using CView from Scribner Associates, Inc. corrosion parameters were calculated using *FIT AutoTafel* option by selecting only the data points in the potential range of ±20mV with respect to E_{corr}, in which these parameters are summarized in Table 4.4. It is evident that parameters like I_0, β_a, and β_c have been suppressed by at least two-fold after SAM treatment indicating effective suppression of corrosion reaction. Calculating the corrosion rate as given in *eq 4.14* gives 2.29×10^{-10} for Cu-Ag and 1.14×10^{-10} mils/year for Cu-Ag with SAM indicating two-fold decrease in the corrosion rate.

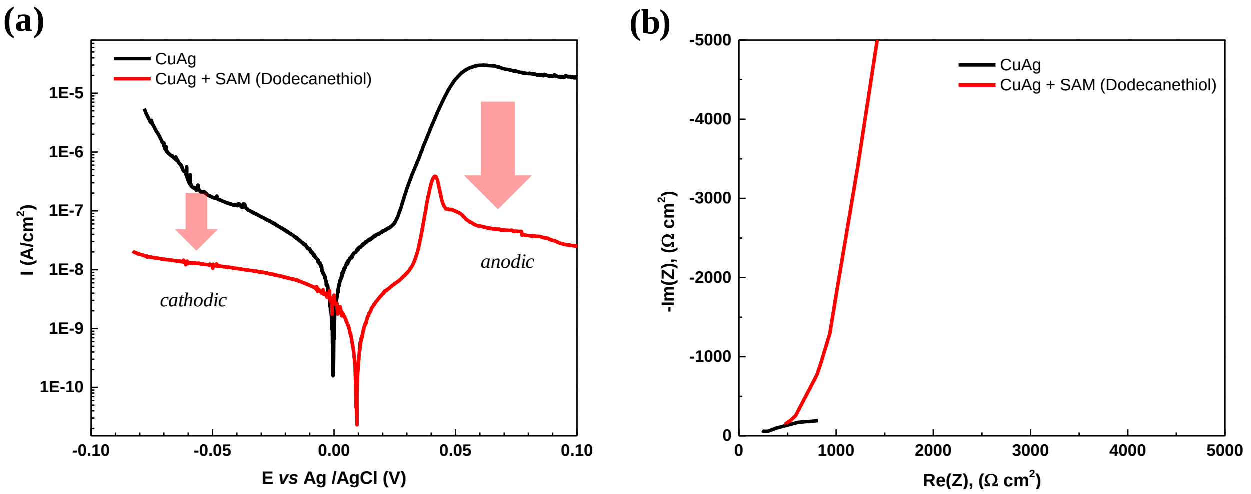

Figure 4.25 (a) Polarization curve and (b) Nyquist plot of Cu-Ag film without and with SAM treatment.

Figure 4.25b shows the Nyquist plot for Cu-Ag film with and without SAM treatment where large semi-circle radius is observed for the film with SAM. This is a direct evidence that the magnitude of the impedance value impeding the corrosion behavior is greatly increased with a SAM coating. This also shows a direct evidence of successful formation of SAM layer on a Cu-Ag film.

Table 4.4 Corrosion parameters extracted from polarization curve of Cu-Ag and Cu-Ag-SAM.

	Cu-Ag	**Cu-Ag - SAM**
E_0 (V) w.r.t. NHE	0.196	0.206
I_0 (A/cm^2)	1.24e-8	6.20 e-9
B_a (mV/dec)	29.0	63.9
B_c (mV/dec)	33.2	154.9
Corrosion Rate (MPY)	**2.29e-10**	**1.14e-10**

Stability of dielectric coatings deposited by various deposition methods were evaluated by using electrochemical impedance spectroscopy analysis. Each coating's resistance to the corrosion of underlying Cu-Ag film and the coating capacitance values were quantified by extracting parameters from the Nyquist plot. Evolution of change in capacitance value indicates the coating's degradation under immersion in NaCl solution. Also, using polarization curve and Nyquist plot, effect of SAM treatment on suppressing the corrosion of Cu-Ag film is evaluated. This metrology can be used as a method to better quantify and evaluate the stability of a metal-based transparent conductor and gives a guideline on choosing suitable top dielectric layer that could passivate Cu-Ag film from any environmental degradation.

4.8 Conclusion

Optical property of metal-film based transparent can be significantly enhanced by engineering anti-reflective coatings via DMD structure. Also, careful selection of such optical stack can greatly minimize color contrast issue while not compromising transmission, which is a crucial factor in DMD based FTC for touch panel application. Further expanding metal-dielectric structures into a photonic crystal structure allows us to achieve low resistance FTC in which the stack can be tuned not only to maximize visible transmittance but also to selectively filter desired wavelength range. Also, the design guideline of DMD as a transparent anode for OLED was suggested and DMD-based OLED was fabricated, which exhibited high light extraction efficiency with excellent mechanical flexibility. Finally, methods to enhance the durability of metal-film based FTC was suggested and electrochemical metrologies were used to quantify the degradation process of metal-based FTCs.

Chapter 5 Thin Film-Based Photodetector for Optical Fingerprint Sensor

5.1 Introduction

Embedding fingerprint sensor into the display pixel is a technology roadmap that display industry is pursuing (Figure 5.1). This enables the displays in mobile phones to dominate the form factor allowing end-users to fully immerse in the display. The practicality of in-cell fingerprint sensor depends on the cost, compatibility, and its readiness in terms of integration into the conventional display manufacturing process. Three major sensing schemes being considered in the industry are using capacitive, ultrasonic, or optical methods. Among these, optical sensing via photodetector is considered as the most practical solution due to its low cost, good compatibility with display process, and easy material integration. As the display technology is heading toward flexible display, this urge photodetector components including its transparent electrode to be mechanically flexible and its process to be compatible with the flexible substrate.

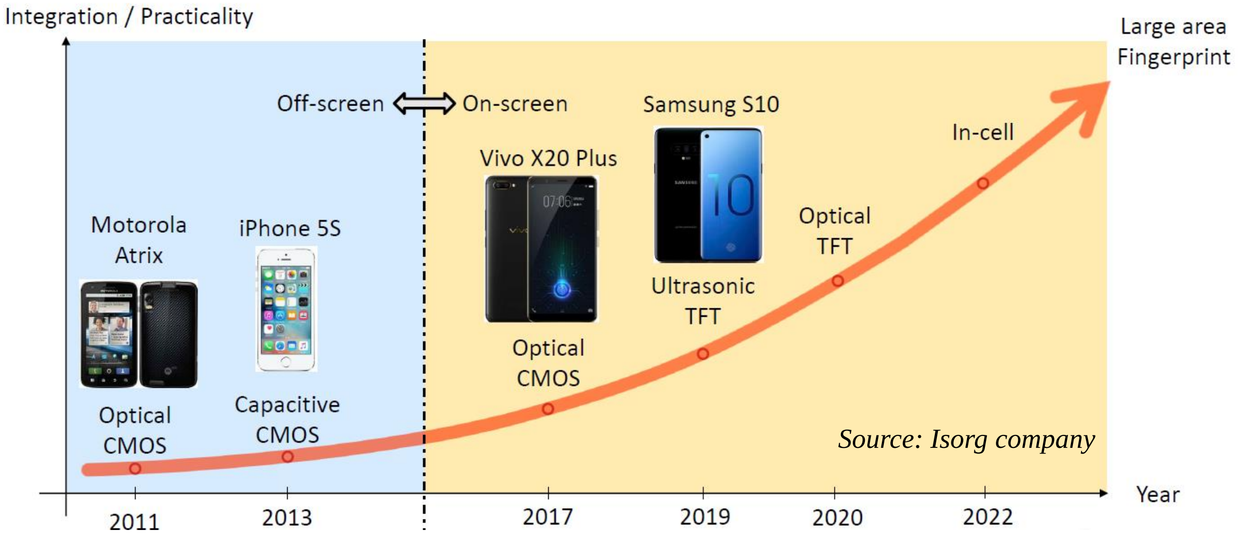

Source: Isorg company

Figure 5.1 Technology roadmap of fingerprint sensor in display technology.

The application of ultrathin Ag film as a flexible transparent conductor is not limited to organic light emitting diodes (OLED) as discussed in the last chapter but can be widely used in photodiodes for flexible display technology. In this chapter, I focus on a heterojunction type of photodiode sensor that enables in-display (in-cell) optical sensor for fingerprint detection. The heterojunction photodiode is composed of active layer sandwiched by carrier transporting layers each with contacts in which one side needs to be transparent. Here, amorphous silicon (a-Si) was used as a photo-absorbing active layer with using metal-oxides as electron and hole transporting layers. Such a-Si based heterojunction photodiode is advantageous over conventional silicon-based p-n or p-i-n homo-junction photodiodes because it can accommodate wide range of photo-active materials including inorganic or organics. With a careful choice of the active layer, all the process can be done at a room temperature showing excellent process compatibility with flexible substrates. Moreover, as the basic device structure is similar to the OLED structure, replacing active region to organic material allows for monolithic integration of light emitting component and photo sensing component at a single display pixel area. As both components require transparent conductor to either transmit or receive light, ultrathin Ag film-based transparent conductor can be used for these devices. Excellent process compatibility of ultrathin Ag film-based technology makes it a great choice for display device application.

In this chapter, I will focus on developing thin film-based heterojunction photodiode including the transparent electrode component to enable optical sensing using low temperature process. In specific, first part of the chapter will discuss on the issue of leakage current at reverse bias and suggest a way to solve the problem. The uniqueness of my contribution to this work is in using the device simulation software to verify the dominant leakage path in the device and engineer the device to suppress leakage current. The optoelectronic characteristic of the heterojunction photodiode is simulated using SILVACO to identify the issue and alter the film deposition condition to improve the device condition. Then, the problem arising from patterning photodiode into an array for fingerprint detection will be discussed and finding the origin of suppressing the leakage path in the array of patterned devices will be dealt. Then, more than 20,000 photodiodes are integrated on a thin-film-transistor (TFT) circuitry to test the actual fingerprint detection, in which the TFT circuitry and fingerprint detection methods were provided from the funding sponsor. Finally, Cu-Ag film is used as a transparent anode for the photodiode array to demonstrate its feasibility for photodiode application.

5.2 Leakage in a-Si Heterojunction Photodiode Device

Thin film-based heterojunction photodiode is composed of a 10/60 nm of Mo/Al as cathode, 50 nm of TiO_2 as electron transporting layer (ETL), varying thickness of a-Si as photo-absorbing active layer, 40 nm of MoOx as hole transporting layer (HTL), and ITO as transparent anode (Figure 5.2a) on a substrate. The device is illuminated from the top (top illumination device) and so the light enters the device through the transparent electrode. The device layers excluding the photo-absorbing layer were all optimized to show maximum external quantum efficiency (EQE) although not much emphasis will be put onto this topic. Instead, logic of determining the thickness of the active layer will be discussed in detail.

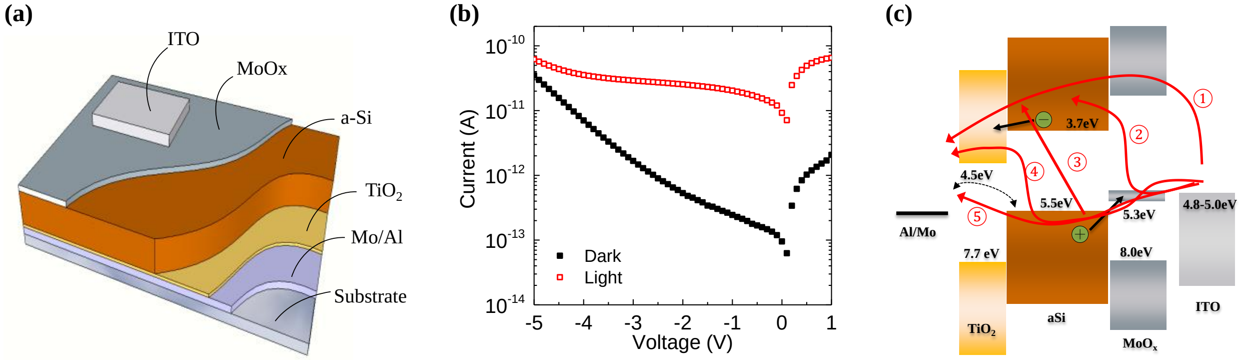

Figure 5.2 (a) Device structure of top illumination-type a-Si thin film heterojunction photodiode structure. (b) Current-voltage characteristic of conventional a-Si photodiode device under dark or light illumination. (c) Energy level of a-Si heterojunction photodiode with possible leakage paths marked in red arrows.

Especially for its use in fingerprint sensing where single light source with fixed wavelength is used, the key specification narrows down to low dark current at reverse bias and high EQE at low light intensity (due to the configuration of the in-pixel optical sensing). Especially when embedding the device with the pixel read-out circuitry, suppressed leakage especially at large negative voltage can be beneficial.

One major problem with heterojunction-type photodiode is that there are multiple current leakage paths owing to the existence of multiple interfaces at each junction. For this reason, initial performance of the device (a-Si layer thickness of 300 nm) showed high reverse current at dark state as shown in Figure 5.2b. Especially for a voltage of -4V or below, the dark current increases to a level comparable to the photocurrent (excitation source of 460 nm blue led was used). For a proper sensing operation of the photodiode device, the difference between the dark and light response should be at least few orders of magnitude higher. Despite, this ratio depends on the light intensity, ideal photodiode would need extremely low dark current level at reverse bias voltage. Few possible paths of leakage are possible. Indicated as red arrows in Figure 5.2c, multiple leakage path of electrons directly from ITO anode to the Al/Mo cathode can take place. Although specifically identifying each current path may be challenging in practice, device simulation software can be used to simulate the factors that can lead to the verification of the dominant paths.

First, speculation of leakage current behavior with respect to the voltage in Figure 5.2b suggests that the leakage increases exponentially at a significant band bending state. At a severe band bending, band-to-band tunneling (BTBT) can become quite significant especially when there exists a significant density of traps within the bandgap of a semiconductor. Despite the existence of Schottky junction at a multiple interface in our structure, most of the voltage drop will occur at the a-Si layer as other junctions like ETL or HTL are usually heavily doped materials. Considering this aspect, tunneling via a-Si layer (corresponding to path 2, 3, 4 in Figure 5.2c) either as a form of direct BTBT or trap-assisted tunneling at the a-Si/ETL (or HTL) interface can be a dominant factor. Also, experimental/simulation result of varying ETL and HTL thickness did not impact the leakage current much, further supporting above argument.

To test the impact of a-Si's quality (defects & traps) on the leakage current, simulation was performed by putting defect into the a-Si layer. Material parameters of a-Si like bandgap, carrier lifetime, and mobility were taken from various literatures for the simulation [118, 119]. The refractive index of a-Si was extracted from the measured Ellipsometer for simulating optical response. Material parameters of ETL and HTL layers were chosen from literatures which the film deposition condition was closest to ours [120, 121] which is a good approximation. For the case of inserting defect into the bandgap of a-Si, defect density was varied from 0 to 2e17 cm^{-3} for a single-energy donor and acceptor level traps. The energy level of donor trap was set to 0.8 eV above the valence band while that of acceptor trap was set to 0.8 eV below the conduction band. The commonly used acceptor and donor state profile of a-Si layer was also used to show the impact of trap level on the leakage current. Figure 5.3a shows that the leakage current increases as the defect density increases from 0 to 2e17 cm^{-3}. Also, adding trap-assisted tunneling into the model further increased the leakage current. This trend signifies the importance of reverse current especially at a larger bias voltage. As putting each donor and acceptor energy level at a single energy level can be an over-simplification of the problem (despite significant advantage in terms of computation power and convergence of mesh), defect state profile resembling the actual a-Si was adopted for a comparison. Density of state (DOS) of defect profile consists of tail and bump states for both acceptor and donor states which is plotted in Figure 5.3b. With such DOS, the resulting reverse current at dark is also plotted in Figure 5.3a. It is evident that the defect in a-Si significantly impacts the leakage current. This points out that the suppression of the leakage current in our device is expected upon improving the quality of a-Si by passivating dangling bonds.

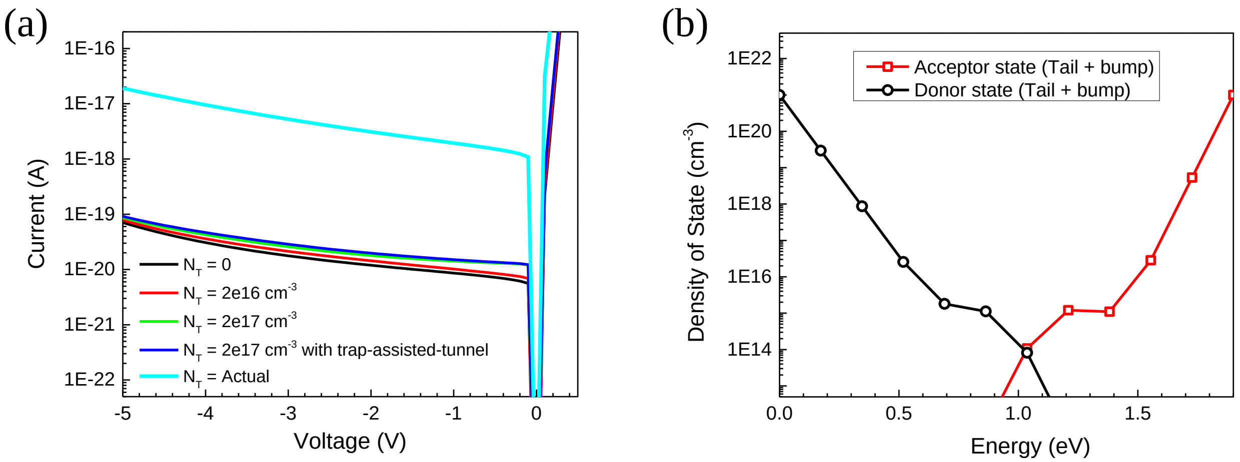

Figure 5.3 (a) Reverse dark current of a-Si heterojunction photodiode with varying trap density for both acceptor and donor traps. The result named “Actual” represents the donor and acceptor defect profiles resembling actual a-Si material used in the literature. (b) Density of state (DOS) profile as a function of energy level respect to the valence band edge of a-Si. Red curve represents acceptor state which includes tail and bump states and black cure represent donor state which also includes tail and bump states. This DOS was used for simulating “Actual” curve in (a).

The defect in can be impacted by various deposition conditions like deposition rate, deposition temperatures, or radiofrequency (RF) power in the case of chemical vapor deposition (CVD) [122]. Also, passivating the dangling bonds of a-Si can significantly reduce the defect level within the bandgap of a-Si. Among such wide scanning range of parameter spaces, our process is limited in terms of the process temperature (< 230ºC) which needs to be considered for the integration into underlying fingerprint sensing circuitry. Moreover, the defect density is kept minimal at a deposition temperature of 250ºC which rapidly increase below and above this point [122]. Considering all these aspects, deposition condition was varied to find the optimum condition that gives lowest level of leakage current as shown in Table 5.1. Compared to the conventional deposition condition, both pressure and temperature were adjusted with adding extra hydrogen gas during the deposition to further passivate dangling bonds. Modified deposition condition resulted in faster deposition rate (1.2 ~ 1.4 nm/sec) compared to the conventional one (0.1 nm/sec).

Table 5.1 Deposition condition of conventional and optimized a-Si material

Sample	**Temperature (ºC)**	**Pressure (Torr)**	**RF Power (W)**	**SiH_4:He:H_2 (sccm)**
Convent.	260	1	25	45:4:0
250ºC (with H_2)	250	3	30	60:478:22
220ºC (with H_2)	220	3	30	60:478:22

Device was then fabricated for different a-Si layer deposition conditions while fixing a-Si thickness as 300 nm. Cathode, ETL, and a-Si layers were blank deposited without patterning while HTL and ITO was deposited by shadow mask to define the active region. The result of current-voltage characteristic of dark and light response (100mW/cm^2, 1 sun) of the device is shown in Figure 5.4. Compared to the conventional deposition condition, the modified condition with flowing H_2 at 250°C showed significant reduction in the reverse bias current. As mentioned earlier, this can be understood in terms of the optimum deposition temperature to give lowest defect density in a-Si. Unfortunately, the process temperature is limited to below 230°C and so the deposition temperature of 220°C was also tested. Although not as remarkable as the 250°C, close to two-fold decrease in the reverse current at negative bias was observed for the device with a-Si deposited at 220°C. As a result, a-Si deposition condition at 220°C was selected for the optimum a-Si material deposition condition.

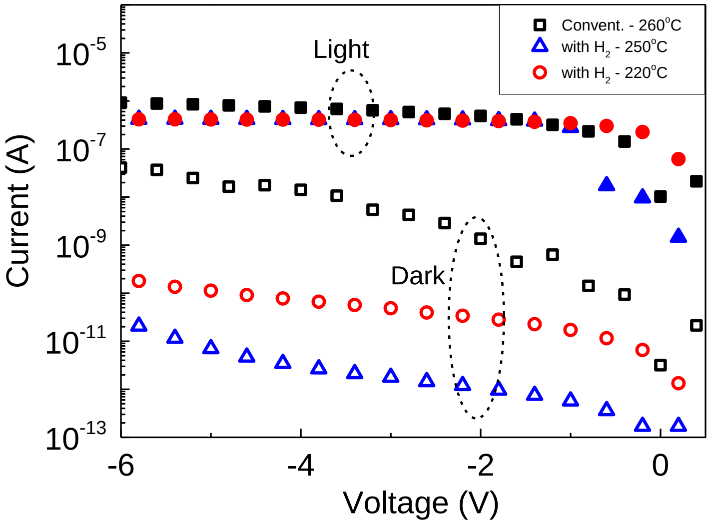

Figure 5.4 Current-voltage characteristic of a-Si photodiodes with varying deposition conditions of a-Si layer (specified in Table 5.1) with and without light response.

5.3 Thickness Choice of a-Si Layer

Next, optimum thickness of a-Si layer was selected based the simulation and verified by device fabrication and measurement. In specific, the photon-absorption rate and photogeneration rate of photodiode with a-Si thickness of 300 nm is plotted in Figure 5.5a. As the light in incident from the top anode, the photogeneration rate will peak at the HTL/a-Si interface. This is a great advantage because hole mobility in a-Si is significantly lower than that of electron. Therefore, populated concentration of holes near HTL interface can be extracted without significantly losing these photogenerated carriers. Also, plotted photon absorption rate also rapidly diminishes toward a-Si region closer to the ETL interface. By varying the a-Si layer thickness from 150 nm to 700 nm, the photon absorption rate inside a-Si layer (with respect to the HTL interface) is plotted in Figure 5.5b. Considering photon absorption rate, 150 nm of a-Si may be insufficient in thickness to fully absorb the incoming photons. With a-Si's thickness of 300 nm or thicker, the a-Si layer seems to be sufficient in absorbing the light. While having a thicker light absorbing layer seems beneficial in terms of light absorption, it can be limited by the electrical quality of the material in practice, in which all the details may not be expressed by simulator. For this reason, actual device with a-Si thickness of 150, 300, 500, and 700 nm were fabricated and tested.

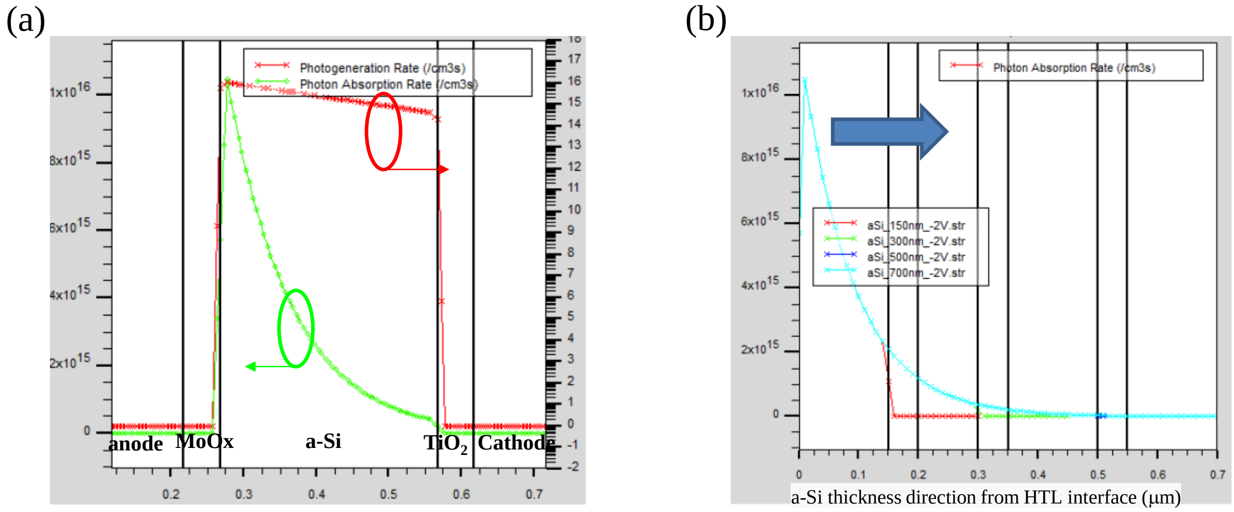

Figure 5.5 (a) Plot of photogeneration rate and photon absorption rate inside a-Si photodiode. (b) Plot of photon absorption rate as a function of a-Si thickness with respect to the HTL interface. The plot has an overlap of curves for varying a-Si thickness from 150 to 700 nm.

Figure 5.6a and b shows the simulated and measured current-voltage curve of a-Si photodiode with varying a-Si thickness, respectively. The light intensity of 50 lux was used for the measurement. In case of the simulation result, there is a clear thickness dependence on the leakage current. For 150 nm thick a-Si, the reverse bias current at dark rapidly increases for bias below -1V. At a bias of -3V or below, reverse bias current converges to the photocurrent meaning that the current is no longer dominated by the photocurrent. Similar trend is observed in the measured data. In Figure 5.6b, the device with 150 nm thick a-Si shows clear trend of increase in leakage current as more negative bias voltage is applied. Such behavior is anticipated because of the larger electric field applied over the a-Si with reduced thickness. However, thicker a-Si is not necessarily beneficial in practice because as the measured 500 nm thick a-Si shows, the device starts to become too resistive. Although not plotted here, the 700 nm's case was too resistive for the device to show any noticeable light response. Despite the benefit of suppressing reverse current at dark, increasing the film thickness too much will significantly deteriorate the electrical property of photodiode.

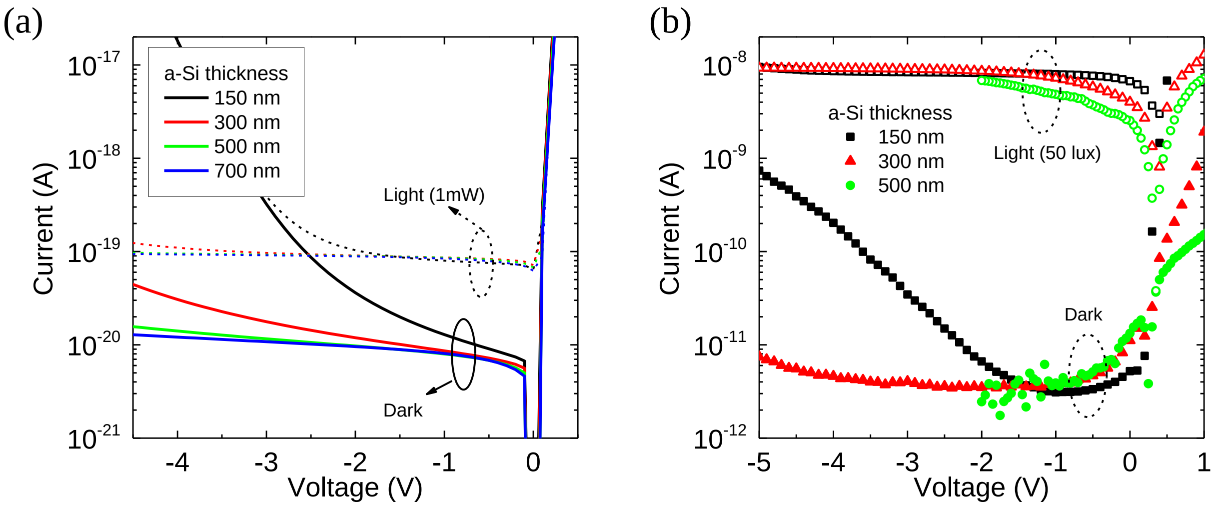

Figure 5.6 (a) Simulated and (b) measured dark and light response of a-Si photodiode with different a-Si thickness.

Another important factor to consider in determining the thickness is the response speed of the photodiode. This is important for the fingerprint sensor because the light pulse is applied to the detector and its photocurrent is integrated over the duration of the pulse. For this reason, switching speed is determined by the capacitance of the device where having a small capacitance is advantageous considering the RC delay. As our photodiode is operating at a reverse bias, diffusion capacitance does not exist and only the depletion capacitance plays a role in determining the total capacitance of the device. As our a-Si is undoped, this layer can be assumed to be fully depleted with having most of the voltage drop across the a-Si layer. Therefore, the thickness of the a-Si will most likely determine the capacitance of the device where having a thicker layer is beneficial. As shown in Figure 5.7, capacitance of the simulated and measured devices both decreases as a-Si thickness increases. Also, at a-Si thickness of 150 nm, both simulated and measured capacitance values are comparable in terms of the magnitude. And yet, the measured capacitance is slightly lower than simulated one. As a-Si thickness further increases, the difference between the simulated and measured capacitance becomes even larger. This discrepancy may be due to the existence of parasitic capacitance as well as the non-ideal capacitive behaviors of the deposited films. Considering all aspects mentioned above, a-Si thickness of 300 nm was chosen as an optimum thickness for photodiode device.

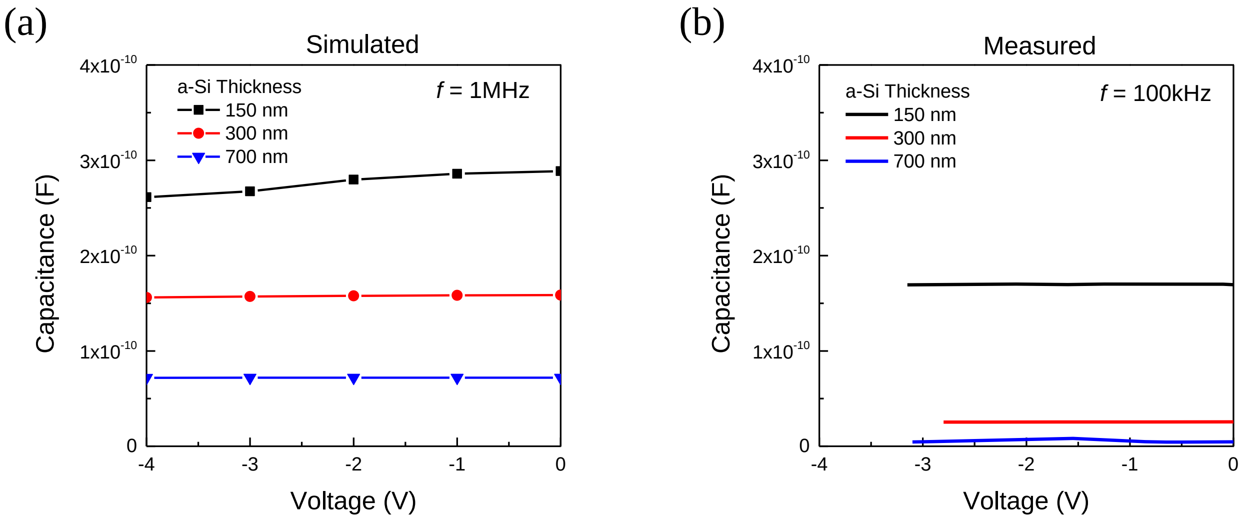

Figure 5.7 (a) Simulated and (b) measured capacitance of a-Si photodiode with different a-Si thickness as a function of reverse bias voltage. Applied frequencies are indicated in the figures.

5.4 Process Optimization to Suppress Leakage

For the integration of our a-Si heterojunction photodiode onto TFT panel, the device was patterned into 10 by 10 array of cells for the test. Unlike the un-patterned device where the active area was defined by using a shadow mask to selectively deposit HTL and ITO, patterned device consists of patterning of each layers. The current-voltage characteristics of un-patterned and patterned devices are shown in Figure 5.8a where the light excitation of 460 nm LED with 50 lux (~40 $\mu W/cm^2$). Despite all the material depositions were done simultaneously, stark difference in the current level was observed especially at dark. Unlike the un-patterned device, the patterned device showed significantly increased leakage current which is not suitable for the optical sensor application. For better understanding of the possible difference between the two cases, cross-sectional schematic was drawn for un-patterned and patterned devices as shown in Figure 5.8b and c, respectively. For un-patterned device, MoOx was deposited via thermal evaporation with shadow mask to define the active area. Immediately after this, ITO was deposited via DC sputtering. As sputtered films have better step coverage than evaporated films, direct contact of ITO with a-Si layer at the periphery of the pattern can occur. This will cause the leakage of electron flowing to the anode from the a-Si layer. In fact, we have observed a significant increase in reverse bias current at dark when the device is fabricated without MoOx HTL layer. As HTL layer also serves a purpose to not only transport holes but block electrons from the a-Si, the absence of electron blocker will result in increased current. This possible leakage path named as “Path 2” is indicated as red arrow in Figure 5.8b. For the patterned device, as MoOx and ITO are deposited in a same manner except for the patterning (pattern via photoresist with lift-off process), “Path 2” will still exist as well. Despite both devices share the same “Path 2”, the contribution of this edge effect may diminish as the active device area becomes larger compared to the edge. Therefore, I cannot neglect this “Path 2” in patterned device. Another possible additional leakage path is via silicon nitride (SiN) layer which is marked as “Path 1” in Figure 5.8c. Despite SiN (150 nm) is used to electrically passivate the array devices, limited process temperature of SiN deposition may result in leakage current from ITO to Al/Mo via SiN layer. In addition, as drawn in Figure 5.8c, the patterning of TiO_2 and a-Si were all done at one step. The reason being not only to reduce the number of mask layer but also to account for the possible misalignment error after each sample in which the spacing between adjacent active device areas were too small to tolerate multiple levels of misalignment at each lithography steps. As the etching of TiO_2/a-Si was done via dry etching, there are regions at the sidewall of active device where TiO_2 is in direct contact with the SiN layer.

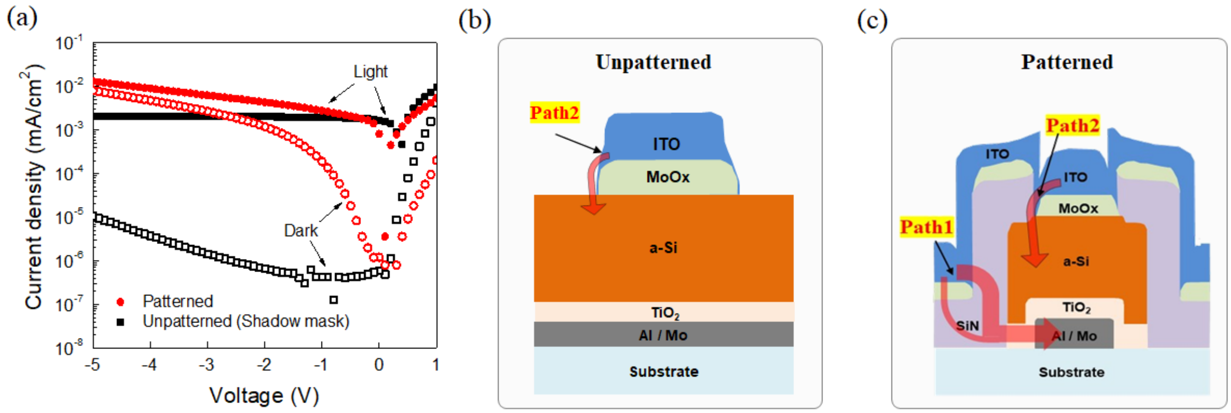

Figure 5.8 (a) Current-voltage characteristic of unpatterned and patterned device. Cross-sectional schematic of (b) unpatterned and (c) patterned device with possible leakage paths for each case.

Considering two possible reverse current leakage paths at dark (“Path 1” and “Path 2”), control devices were fabricated to eliminate each one of the paths or both. To eliminate “Path 1”, TiO_2 pattern was defined smaller than a-Si by using Al/Mo mask layer during photolithography step. To avoid misalignment of TiO_2 and Al/Mo, Al/Mo pattern was slightly over-etched using wet etching to make sure the TiO_2 covers the entire cathode contact in the active region despite the case of misalignment. Then, a-Si was patterned (larger than TiO_2 pattern) to cover the entire area of TiO_2 as shown in the schematic of device cross-section in Figure 5.9a. This way, “Path 1” is effectively eliminated. To eliminate “Path 2”, MoOx was deposited via sputtering to ensure no direct contact of a-Si with ITO for the subsequent ITO deposition as shown in Figure 5.9b.

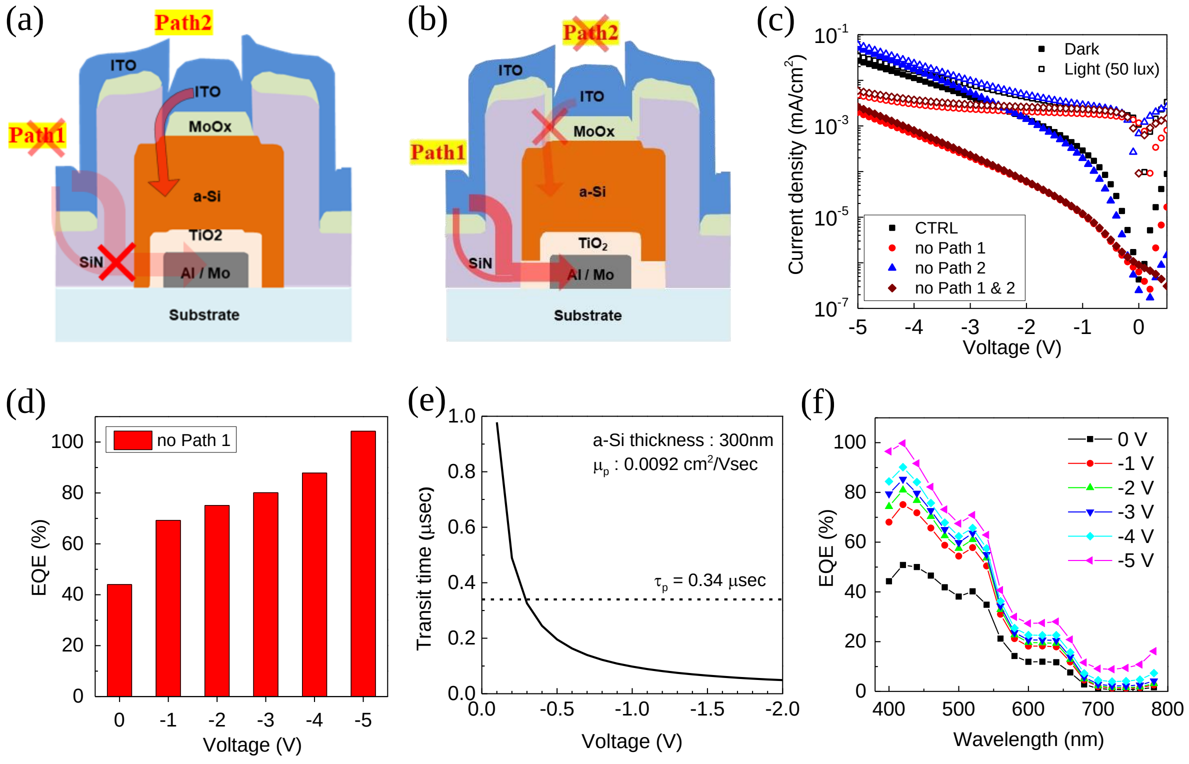

Figure 5.9 Schematic showing elimination of (a) "Path 1" via separating TiO_2 and a-Si patterning process and (b) "Path 2" via sputtered MoOx. (c) Current density – voltage characteristic of patterned devices with elimination of "Path 1", "Path 2", or both. (d) Measured EQE of the optimized device as a function of bias voltage. (e) Calculated transit time of the photo-generated hole inside 300 nm of a-Si. (f) Measured EQE – wavelength plot of the device for each applied reverse bias voltage.

The current density – voltage curve of the device with eliminating "Path 1", "Path 2", or both are plotted in Figure 5.9c. Control sample represents the unmodified reference device where both "Path 1" and "Path 2" exist. From this result, it is very clear that the dominant leakage path in the patterned device is via "Path 1" while the device with intending to eliminating "Path 2" only aggravates the reverse bias leakage current at dark. This could be because of the uncontrolled stoichiometry of sputtered MoOx compared to the evaporated MoOx resulting in a poor electron blocking capability. Although the quality of the sputtered MoOx can also be tuned to show better electrical performance, the difficulty in doing lift-off process of sputtered film prompts us to use the evaporated film as long as “Path 2” is not a dominant factor. The device that eliminated “Path 1” shows a good light on-off ratio even at large negative bias considering only 50 lux of light is used as an input. EQE of this device is calculated from the photocurrent minus the dark current, which is plotted as a function of bias voltage in Figure 5.9d. As more negative bias voltage is applied, large increase in the EQE is observed. Larger increase in the EQE value is observed especially at smaller absolute reverse bias voltage. This can be explained in terms of the transit time of holes as shown in Figure 5.9e. As hole mobility is known to be much smaller than that of electron in a-Si, the transit time of holes through a-Si will become a bottleneck. Assuming the hole mobility in i-region of 9.2×10^{-3} $cm^2/V\cdot sec$ and lifetime of 0.34 μsec [123], the field at 0 bias is too weak for holes to transit a-Si before getting annihilated. At a voltage below -0.3V, the field is sufficiently large enough for holes to transit within its lifetime. This can roughly explain a big jump in the EQE as the bias is changed from 0 to -1 V. Below -1V, the EQE gradually increases as the voltage is further reduced. Figure 5.9f shows the EQE as a function of wavelength for different bias voltages. Our a-Si material shows a higher EQE at shorter wavelength meaning that the device can be used with blue or green light source inside the display pixel for efficient photodetector.

One thing to pay attention to is that the EQE exceeds 100% at a bias of -5 V. EQE of above 100% is commonly observed in photodiodes although various mechanism can be used to explain this phenomenon [124-127]. One possible scenario is by the carrier multiplication via impact ionization under the presence of high electric field. Another possible explanation discussed among community is the photoinjected carriers from the metal contact side [125]. All these explanations may be responsible for EQE higher than 100%. In addition, owing to the heterojunction nature of our a-Si photodiode, it is possible for photo-generated carriers to populate the trap/interface states in a-Si layer thereby lowering the barrier energy for electrons to travel from anode to cathode as shown in Figure 5.10. Due to the barrier lowering of heterojunction interfaces by photo-generated carriers, the current previously described as “leakage” current is increased compared to the dark case. The photo-excitation of carriers from the contact may not be a suitable explanation because such transport would also require energy from the photon. As energy is conserved, energy gets consumed even for a photo-excitation process which still makes it difficult to explain EQE above 100%. The mechanism of diode current increase by photo-assisted barrier lowering may be more conspicuous in our heterojunction structure, which may be beneficial if engineered carefully.

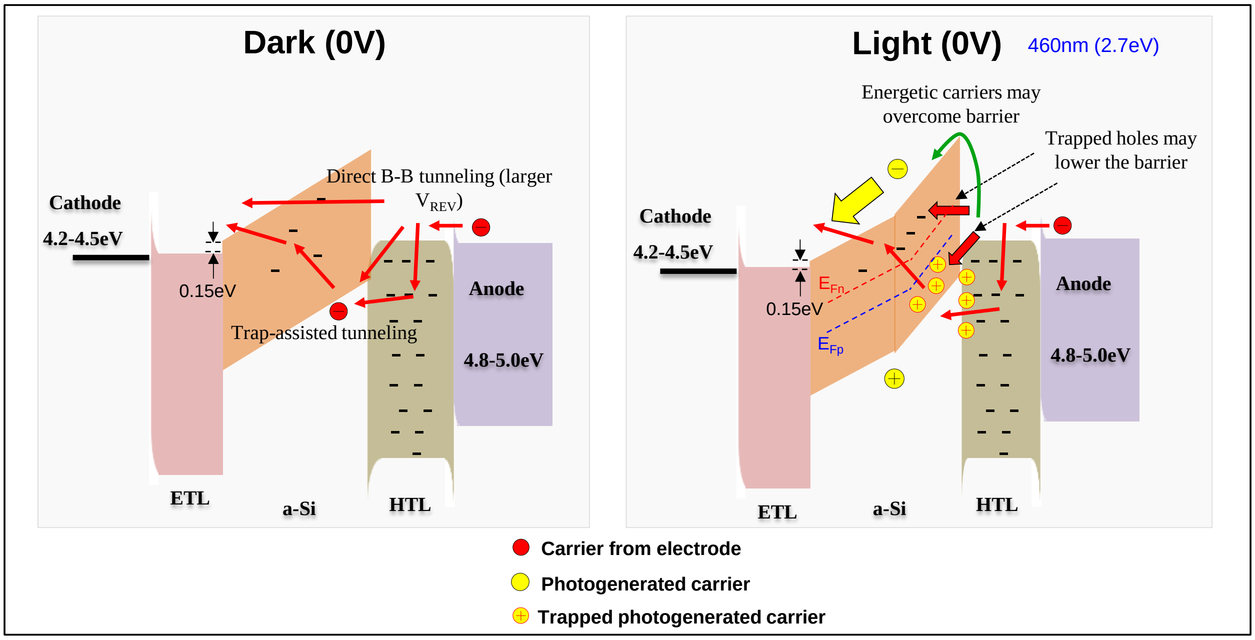

Figure 5.10 Possible mechanism of carrier transport in a-Si heterojunction photodiode under dark and light condition.

5.5 Array Level for Fingerprint Detection and Potential of Cu-Ag Anode

With optimized device structure and process discussed above for patterned a-Si photodiode, the arrays were integrated onto a TFT pixel circuitry (chip) provided by the sponsor. This consists of over 20,000 photodiodes each in a pixel where single device area was 50 μm x 30 μm. The photodiode array fabricated on a TFT chip with glass substrate is shown in Figure 5.11a.

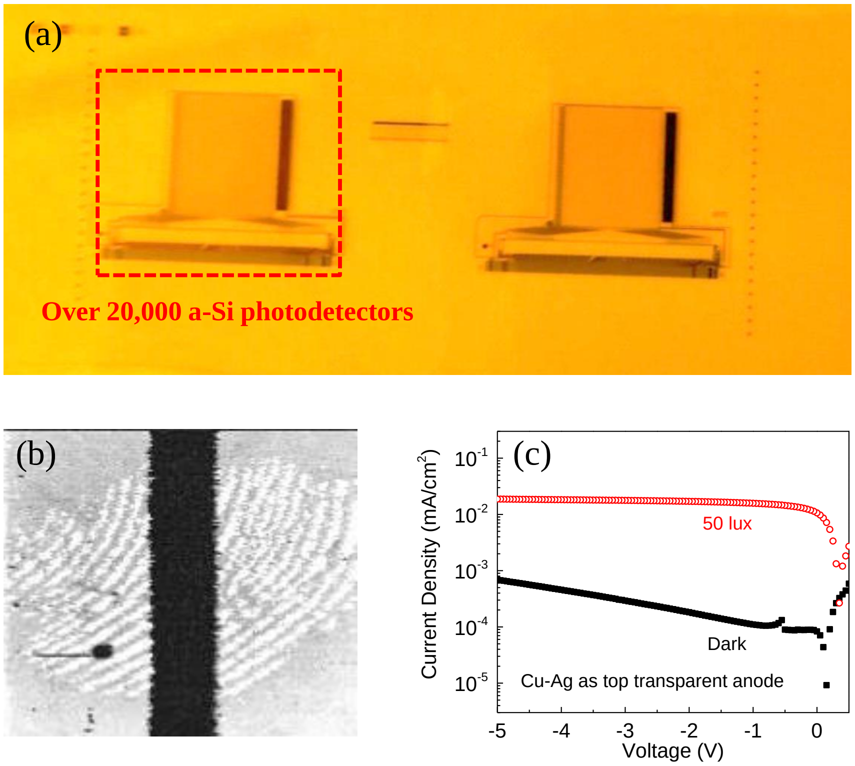

Figure 5.11 (a) Photograph of arrays of a-Si photodiode integrated on a TFT pixel circuitry chip for fingerprint detection. (b) Image processed result of the fingerprint mark detected by our a-Si photodiode. (c) Current density – voltage characteristic of dark and light (50 lux) response of a-Si photodiode with Cu-Ag as top transparent anode.

Figure 5.11b shows the image processed result of the fingerprint ridges and valleys detected using our a-Si photodiode. The measurement algorithm and sensing scheme circuitry are not disclosed. Owing to the suppressed reverse bias current at dark and high EQE of our device, the fingerprint detection was successfully accomplished. Moreover, it is important to note that our thin film a-Si photodiode is highly compatible with the display manufacturing process and can be done in a large-area with high throughput. The maximum process temperature for the current device structure is limited to 220ºC and so compatible only with certain polymer substrates like polyimide. However, as discussed earlier, our structure can easily accommodate other types of photo-sensitive active layer like perovskite or organic molecules as all these share similar device structures. By doing so, the device fabrication can be done at a room temperature, showing excellent flexibility in terms of substrate requirements. Moreover, our device is compatible with emerging transparent conductors like thin metal-based films. As an initial attempt, ultrathin Cu-Ag film as a transparent anode was used to replace ITO (Figure 5.11c). All the device structures were kept the same except replacing 150 nm of brittle ITO with 7 nm of Cu-Ag. The a-Si photodiode with Cu-Ag anode shows excellent dark current as well as high light response even at 50 lux of light illumination. This also suggests Cu-Ag film as a promising candidate as a transparent anode for photodiode application.

5.6 Conclusion

In conclusion, thin film-based a-Si (via CVD) heterojunction photodiode for in-display fingerprint detection was demonstrated. The device was optimized in terms of suppressing the reverse bias current at dark to achieve high dark/light response contrast at negative bias voltage. In the process of integrating arrays of a-Si photodiode into the TFT pixel circuitry chip, possible leakage current paths were eliminated, thereby leading to a successful demonstration of in-display (in-cell) fingerprint detection with our device. As our heterojunction photodiode structure can easily accommodate other types of photo-sensitive layer like perovskite or organic molecules, this gives us flexibility in terms of material choice and integration into manufacturing process. Moreover, as the basic device structure is common to OLED, monolithic integration of both light emitting device and light sensing device within a single pixel in display can easily be achieved. Finally, our device showed good compatibility with using Cu-Ag film as a transparent anode, which signifies that our photodiode is compatible with emerging flexible transparent conductors showing potential for mechanically flexible photodiode array. This suggests a potential of using a-Si photodiode with metal-transparent conductor for in-display optical fingerprint detection in flexible display technology.

Chapter 6 Silver Nanoparticle to Tailor Sunlight for Low-e Application

6.1 Introduction

Silver (Ag) thin films are widely used in the low-emissivity (low-e) coating. This is owing to Ag thin film's excellent property of transmitting visible wavelength while rejecting infrared (IR) wavelength range. The reflection of infrared radiation linked to the conductivity of the material which is given by the Hagen-Rubens relation [128]:

$$R \cong 1 - 2\sqrt{\frac{2\varepsilon_0 w}{\sigma}} \tag{6.1}$$

where σ is the conductivity of metal, ε_0 is the permittivity, and w is the frequency of the electromagnetic radiation at IR. For the case of thin film, this form can be further developed as

$$R \cong 1 - \frac{4\varepsilon_0 c}{\sigma d} \tag{6.2}$$

where c is the speed of light and d is the thickness of the film. Typically for a 12 nm of Ag film, reflectance of λ at 30 μm is R = 0.986 showing extremely effective IR rejection capability [56]. For this reason, Ag film-based low-e coatings are widely used to improve the energy balance of buildings, houses and automobiles by reflecting infrared radiation. As shown in Figure 6.1, low-e coatings can prevent the radiant heat from escaping out during the cold weather while it can also block the solar heat from entering during the warm weather thereby cool environment can be maintained inside the building.

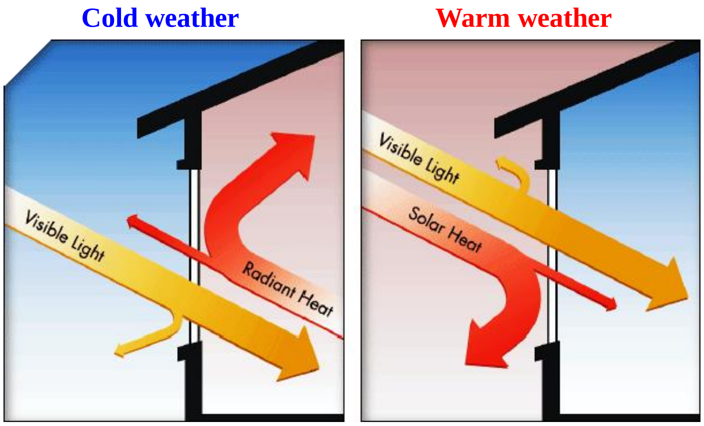

Figure 6.1 Schematic illustrating the concept of low-e coating window for cold and warm weather.

The basic concept of low-e coating window is to transmit visible light while rejecting IR portion of light which is the major source of heat. The working principle of low-e coating can be thought under the context of 1-dimensional metallo-dielectric photonic crystal (1-D MDPC). Having multiple number of alternating layers of metallo-dielectric can enhance the sharp increase in the reflection at IR wavelength range while not significantly jeopardizing transmittance at a visible wavelength range as shown in Figure 6.2. Transmittance (*T*), film-side reflectance (*Rf*), and glass-side reflectance (*Rg*) are also plotted for the number of alternating layers to show the change in the spectral shape as layer numbers increase. The thickness of Ag films inserted in these layers range from 10-20 nm. The specific dielectric's type and thickness are not specified for proprietary reason.

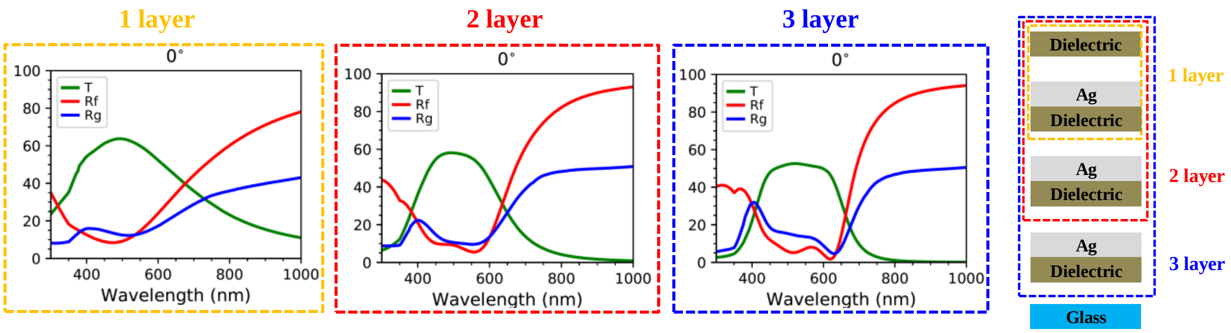

Figure 6.2 Commercial Ag-based low-e coating with 1, 2, and 3 alternating 1-D MDPC layers case and their *T*, *Rf*, and *Rg* spectra.

Among multiple factors that determine the specification of the low-e coating, one important aspect which will be dealt here in this chapter is the angle insensitivity of the low-e coating. There is a large demand especially for building windows application in making the color of low-e coating windows to be insensitive to the viewing angle. For example, Figure 6.3 shows an example of typical low-e coating window's *Rg* a* and b* values as a function of viewing angle. As Rg a* and b* indicate the color of the reflection from the glass substrate side, the measure of the a* and b* as a function of angle should indicate the change in the color with change in viewing angle. Taking a look at a* value, it oscillates with relatively small amplitude from -4 to 2 as from angle of incidence changes from 0 to 85°. On the other hand, b* starts with -16.5 at normal incidence but rapidly increases above angle of 50°. Among a* and b*, the dominant pole that determines the color is b* as the magnitude of b* is much larger than a*. At normal incidence, this will show bluish color. However, beyond incident angle of 50 ° it will turn into greenish color due to rapid decrease in the magnitude of b*. Such a change in color with respect to viewing angle is undesirable especially for building construction application.

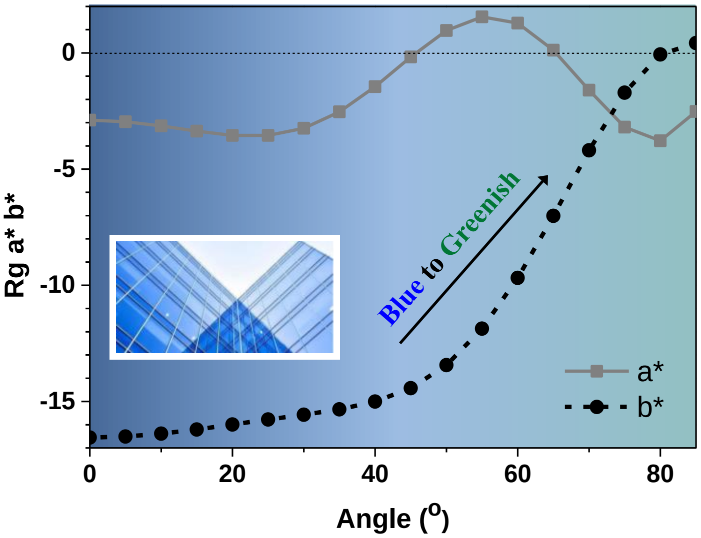

Figure 6.3 Example of a color-shift with respect to viewing angle in a blue-colored low-emissive window. Plot shows calculated a* b* from a simulated glass-side reflection (Rg) spectrum as a function of viewing angle.

In this chapter, meta-material layer composed of metal-nanostructure embedded inside the host dielectric will be studied to tackle this angle-sensitivity issue. To screen which material will be suitable for this application, parameter space of 11 different metals (Ag, Al, Au, Be, Cr, Cu, Ni, Pd, Pt, Ti, W) in 3 dielectric matrices (SiO_2, Si_3N_4, TiO_2) were explored and stack simulation was performed for each set of metal-matrix to screen the best performing meta-materials. By this way, two final candidates of metal-matrix were chosen. In specific, chromium (Cr) metal nanodisk (ND) inside the TiO_2 dielectric layer is demonstrated to fabricate high refractive index material that is intended to enhance light refraction even at high angle of incidence. Second, silver nanoparticle (NP) embedded in Si_3N_4 is demonstrated to induce absorption at a specific target wavelength so that it becomes less sensitive to the angle as LSPR-induced scattering of light is insensitive to angle. The resulting refractive index values of these materials are shown in Figure 6.4 which was simulated by finite-difference time-domain (FDTD) method. For these two leaderboard meta-materials, metal NP size of 2nm in diameter and volume inclusion percentage of 2-5% showed the best stack performance in terms of minimizing the angle-sensitivity of colored window.

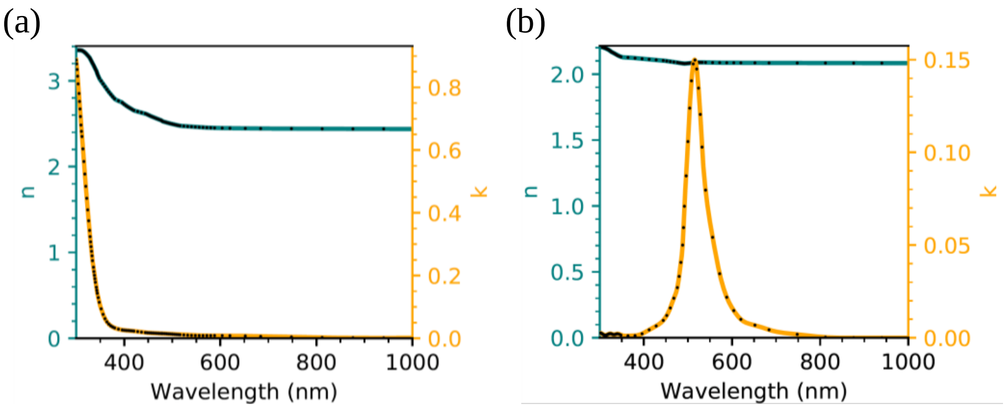

Figure 6.4 Simulated refractive index of (a) Cr-TiO_2 and (b) Ag-Si_3N_4 meta-material matrix.

6.2 Fabrication of Meta-Material

6.2.1 Cr-TiO_2 Meta-Material

Cr ND embedded in TiO_2 dielectric matrix is fabricated by using anodized-aluminum oxide (AAO) as a shadow mask to create Cr ND first and then followed by TiO_2 deposition as shown in Figure 6.5a. The resulting feature size is obtained from scanning electron microscope (SEM) and atomic force microscope (AFM) images as shown in Figure 6.5b and c, respectively, where the Cr ND has a diameter of 30 - 35 nm, thickness of 14 nm, and volume density of 22% inside the 34 nm thick TiO_2 matrix. One fundamental problem with using AAO as a shadow mask to pattern Cr ND is that the feature size is limited by AAO and that it is not scalable to a large size. To overcome this problem, so called laser ablation method will be briefly introduced at the later part of this chapter as a facile way to pattern nanostructures with high controllability and throughput.

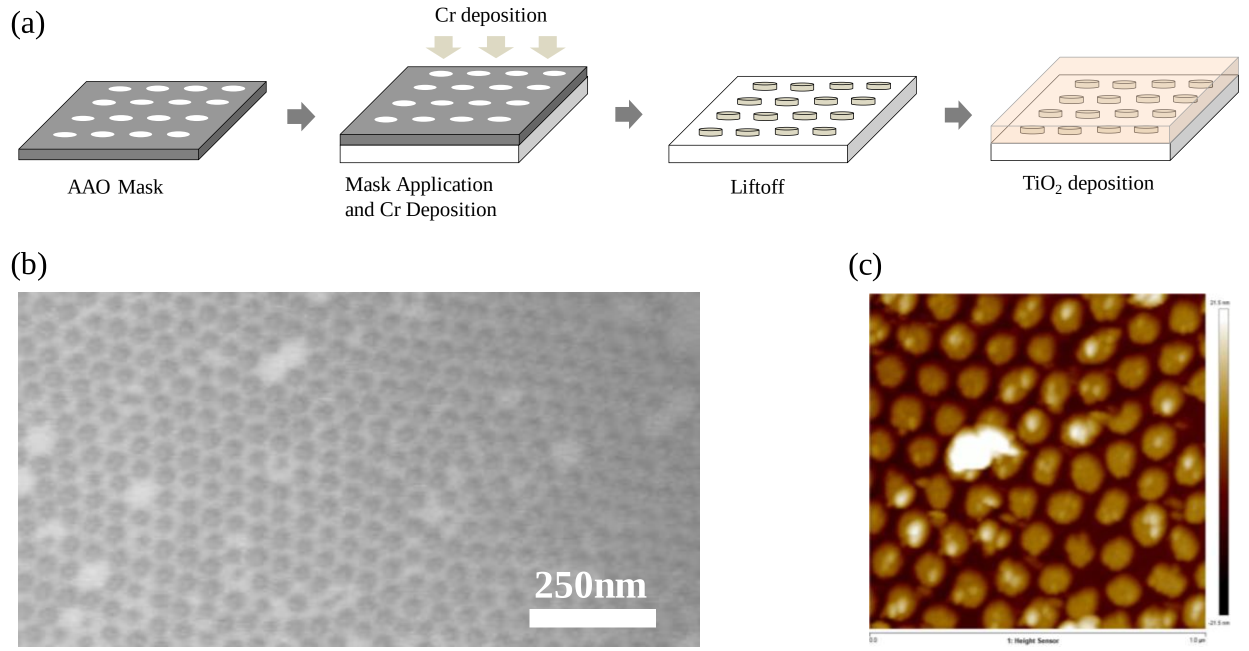

Figure 6.5 (a) Fabrication process of Cr-TiO$_2$ meta-material using lift-off process. Top-down (b) scanning electron microscope (SEM) and (c) atomic force microscope (AFM) images of Cr ND.

6.2.2 Ag-Si$_3$N$_4$ Meta-Material

Next, fabrication of Ag NP inside the Si$_3$N$_4$ matrix is demonstrated by controlling the underlying nucleation layer. Among various seed-layer materials (which will be discussed in Chapter 4) to create a smooth Ag film, the choice of aluminum (Al) as a seed layer was least effective in forming continuous and smooth Ag film. Originating from this idea, Al can be used as a nucleation layer to create well-controlled Ag NPs by depositing significantly thin Ag film. In specific, Al thickness was varied from 2Å to 10 Å and subsequent Ag of thickness ranging from 6 Å to 15 Å was deposited. The resulting transmittance (T), reflectance (R), and absorbance (A) spectra of these AlAg NPs are shown in Figure 6.6c - e, respectively. AFM and SEM image of one specific sample with Al of 5Å and Ag of 12Å are shown in Figure 6.6a and b as a representative morphology of fine-size Ag NPs where the average NP diameter was in the range of 10-15 nm.

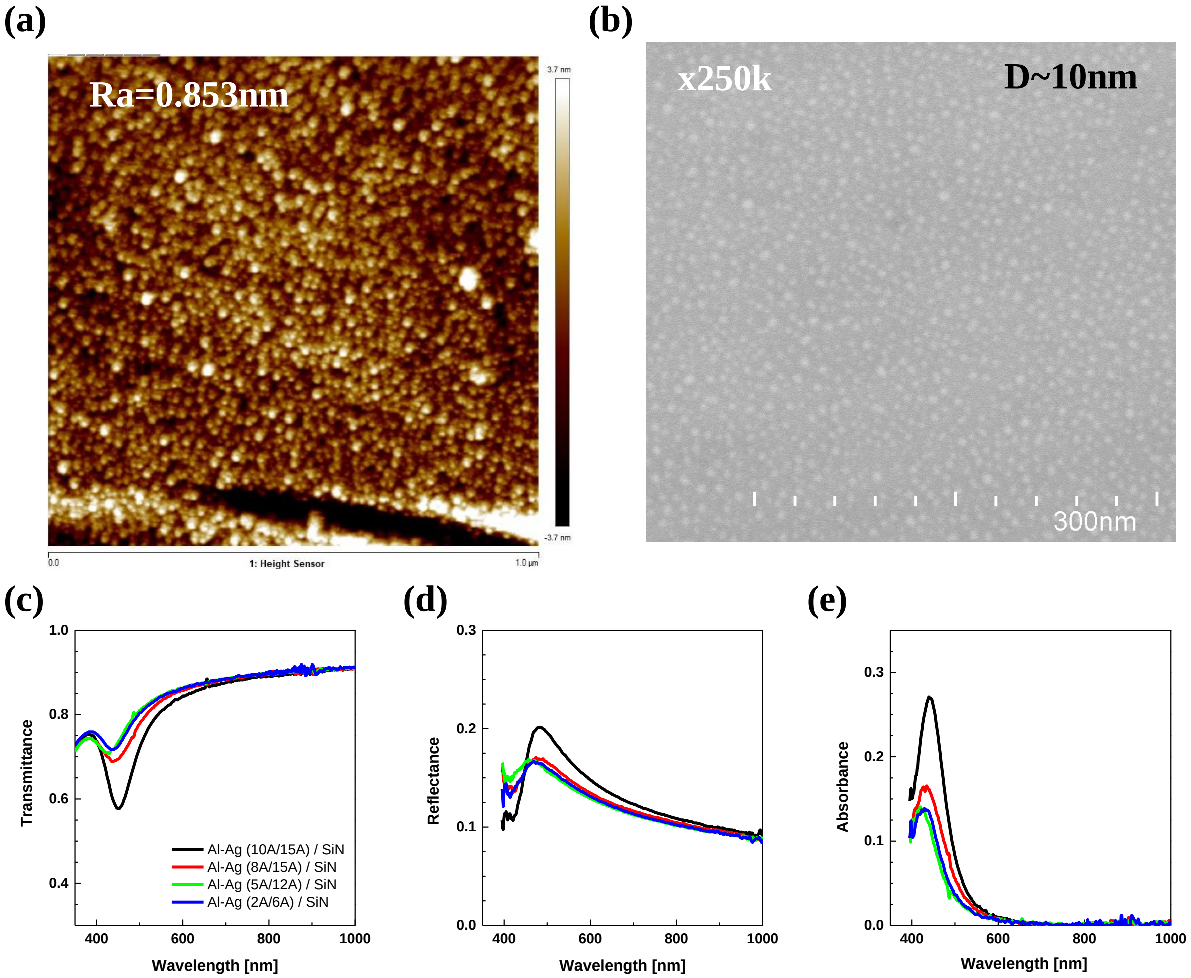

Figure 6.6 Fabricated nucleation layer assisted Ag NP's (a) AFM and (b) SEM image. (c) *T*, (d) *R*, and (e) *A* spectra of AlAg-Si_3N_4 meta-material matrix various AlAg thickness condition.

As shown in Figure 6.6c – e, there is an obvious dip in the *T* spectra at 450-500nm wavelength range which corresponds to the absorption of light by LSPR resonance due to metal NPs. This absorption clearly gets reduced as the thickness of the Al-Ag layer gets reduced. However, below Al-Ag thickness of 5 Å / 12 Å, the absorbance value does not change much. As this meta-material layer will be inserted in the low-e coating stack where absolute transmittance is crucial, it is important for these layers to be not too absorptive. The simulated leaderboard samples shown in Figure 6.4 all showed less than 10% volume inclusion of metal inside the dielectric with particle size being 2nm in diameter. Experimental demonstration of Al-Ag shows that the nanoparticle size can be reduced down to 10nm diameter in size, but still as this is being deposited using blank deposition of Al and Ag, the density is difficult to be reduced and the absorbance cannot be maintained low enough. For this reason, a new method of further reducing the density and diameter of Ag NP embedded into dielectric is proposed as shown in Figure 6.7.

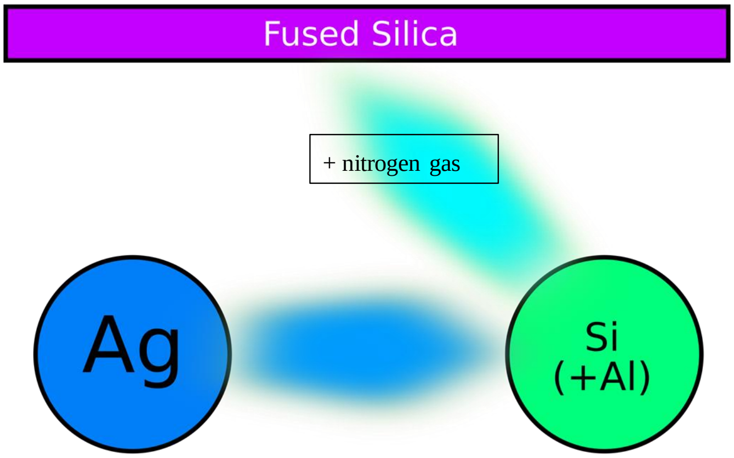

Figure 6.7 Rotation sputtering method for the fabrication of Ag-Si_3N_4 matrix.

This so-called rotation sputtering method is developed with *Guardian Industries* where the coating was done at a sputtering production line at *Guardian Industries*. Ag is sputtered onto the Si target in which Ag atoms will be adhered to the Si target. As Ag target is being sputtered onto Si target, Si is sputtered onto the fused silica substrate with nitrogen as a reactive gas to form Si_3N_4. As Ag wetting on Si is not facile, Ag will form small islands on Si which is then sputtered to the substrate thereby forming Ag NPs embedded inside the Si_3N_4 matrix. For this experiment, the ratio between Si and Ag's sputtering power was varied from 90/10, 80/20, to 70/30. Higher sputtering power of Ag target is expected to show higher density of Ag inside Si_3N_4 matrix. The rest of the parameters were kept identical.

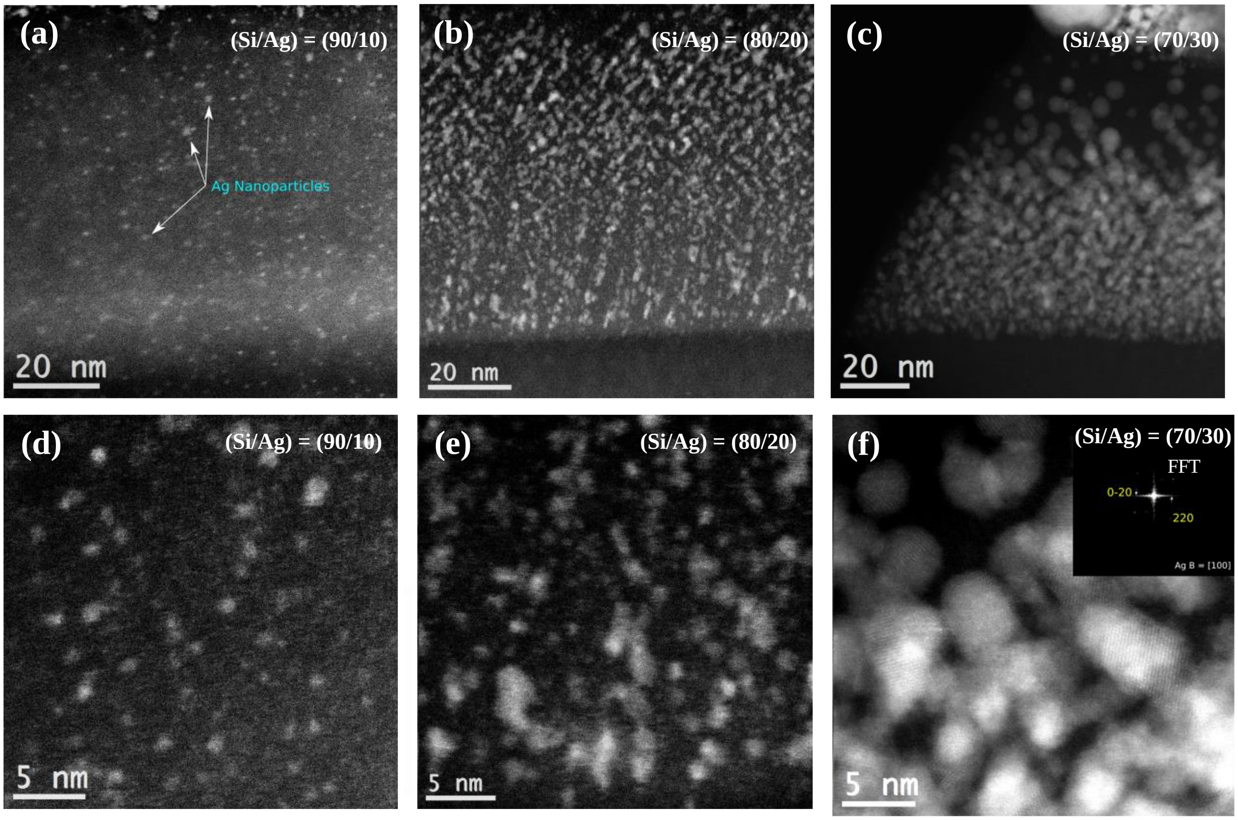

Figure 6.8 HAADF-TEM images of Si/Ag power ratio of (a), (d) 90/10, (b), (e) 80/20, and (c), (f) 70/30.

Total thickness of each sample was aimed to be approximately 90 - 100 nm. Figure 6.8 shows the result of High Angle Annular Dark Field (HAADF) - Transmission electron microscopy (TEM) for different Si/Ag power ratios. As the Si/Ag power ratio decreased from 90/10 to 70/30, the Ag NP size gradually increased as well as the density of Ag NP. As shown in Figure 6.8d, Ag NP diameter ranges from 1-3 nm which is close to the simulated result shown in Figure 6.4b. Next, the volume fraction needs to be determined. As shown on the simulation result, it is ideal to have volume fraction of 2 - 5% of Ag inside the Si_3N_4 matrix. Volume fraction can be calculated by analyzing the electron energy loss spectroscopy (EELS). Figure 6.9 shows the EELS result from the HAADF TEM image for varying Si/Ag power ratio. Average thickness for each sample is given in the inset EELS spectra. For a given volume, the number of particles were counted, and the resulting density of Ag NP was calculated to be 5.65e-3 #/nm^3 and 7.16e-3#/nm^3 for Si/Ag power ratio of 90/10 and 80/20, respectively. For the case with Si/Ag ratio of 70/30, the density could not be extracted as the density was too high and the data was difficult to extract. From this density, assuming the average Ag NP diameter is 2nm, the volume inclusion is calculated to be 2.4% and 8.8% for Si/Ag power ratio of 90/10 and 80/20, respectively. For the case of Si/Ag power ratio of 90/10, Ag NP's physical dimension is very close to that in the Ag-Si_3N_4 metal-material from simulated leaderboard in Figure 6.4b. TEM and EELS analysis were performed by our collaborator *Benjamin Derby* from *Professor Amit Misra*'s group.

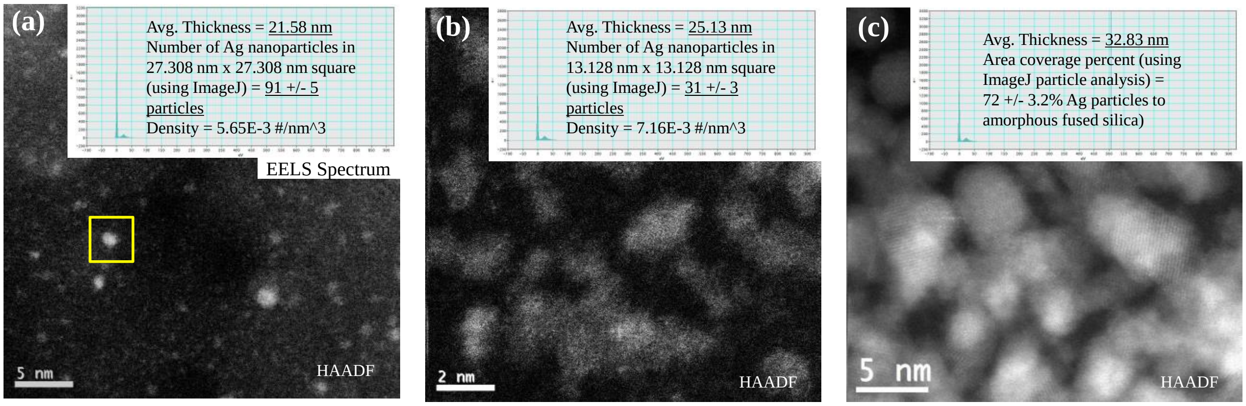

Figure 6.9 EELS spectra from HAADF-TEM for Si/Ag power ratio of (a) 90/10, (b) 80/20, and (c) 70/30.

Next, *T*, *R*, and *A* spectra for above three samples are plotted in Figure 6.10. With increase in Ag power from Si/Ag=90/10 to 70/30, transmittance spectra significantly decrease. As the reflectance spectra remains unchanged, this decrease in transmittance is attributed to the absorbance of light by dense Ag NP inside the Si_3N_4 matrix. For the sample with Si/Ag power ratio of 90/10, there is an absorption at 400 nm wavelength which gradually decreases as wavelength is increased to 500 nm. As this meta-material layer will be inserted in the low-e coating window where having high visible transmittance is a crucial parameter, it is unrealistic to use a layer that is too absorptive. In this aspect, Si/Ag power ratio of 90/10 would be a suitable choice for Ag-Si_3N_4 based meta-material.

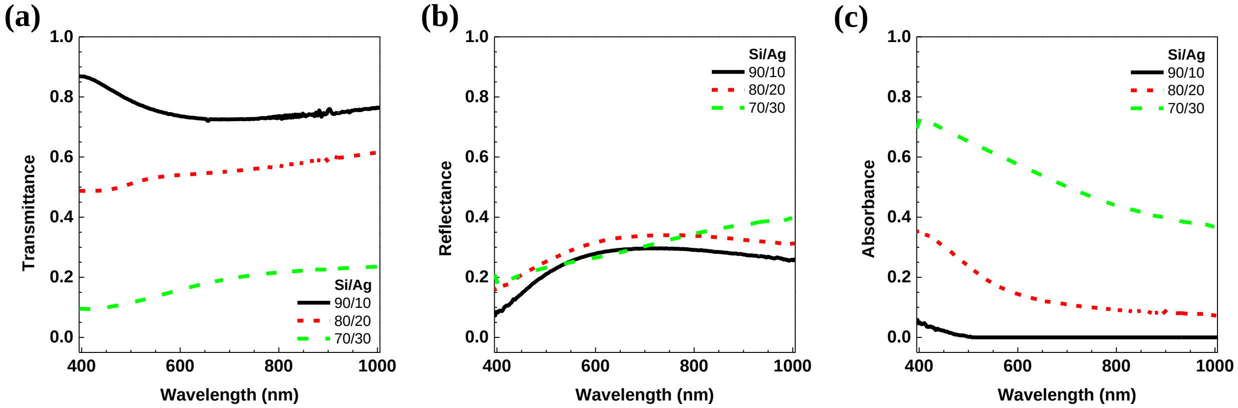

Figure 6.10 (a) *T*, (b) *R*, and (c) *A* spectra of Ag-Si_3N_4 meta-material samples with Si/Ag power ratio of (a) 90/10, (b) 80/20, and (c) 70/30 deposited on fused silica substrate.

6.3 Optical Properties of Meta-Material

Complex refractive index of meta-material can be fitted to film stack spectra using open source software package named TRANK [129] provided by *Michael J. Water*. TRANK is implemented purely in Python 3 using SciPy/NumPy, and the tmm simulation package of Steve Byrnes [130]. Using TRANK package, complex refractive index of Cr-TiO_2 and Ag-Si_3N_4 meta-material was fitted from *T*, *R*, and *A* spectra as shown in Figure 6.11. Important thing to note is that for both meta-materials, there is an enhancement of real part of refractive index values throughout the broad or partial wavelength range as intended, in which the *n*-*k* values of bare dielectrics are also plotted as a comparison. Despite the overall tendency follows the simulation result shown in Figure 6.4, there is a slight discrepancy between the *n*-*k* values of fabricated and simulated meta-material. For Cr-TiO_2 sample, fitted *n*-*k* spectra in Figure 6.11a differs from the simulated target spectra in Figure 6.4a which is likely due to significantly large Cr ND compared to the dimension of simulated Cr NP which has diameter of 2 nm. This is reflected in higher *k* value across the visible and near-IR wavelength range. This results in higher *n* values throughout the broad spectral range in which *n* and *k* are linked by Kramers–Kronig relations. Also, for the case of experimental Ag-Si_3N_4, fluctuation of *n* happens throughout broader wavelength due to broad absorption compared to the simulated result shown in Figure 6.4b. This may be due to the broad distribution of Ag NP size in the fabricated meta-material (Figure 6.8a and d) as opposed to the simulated case where the diameter of simulated Ag NP was fixed to a single size of 2 nm in diameter. As will be discussed in the later section, this broad absorption at a shorter visible wavelength turns out to remarkably improve angle-sensitivity issue in low-e coating.

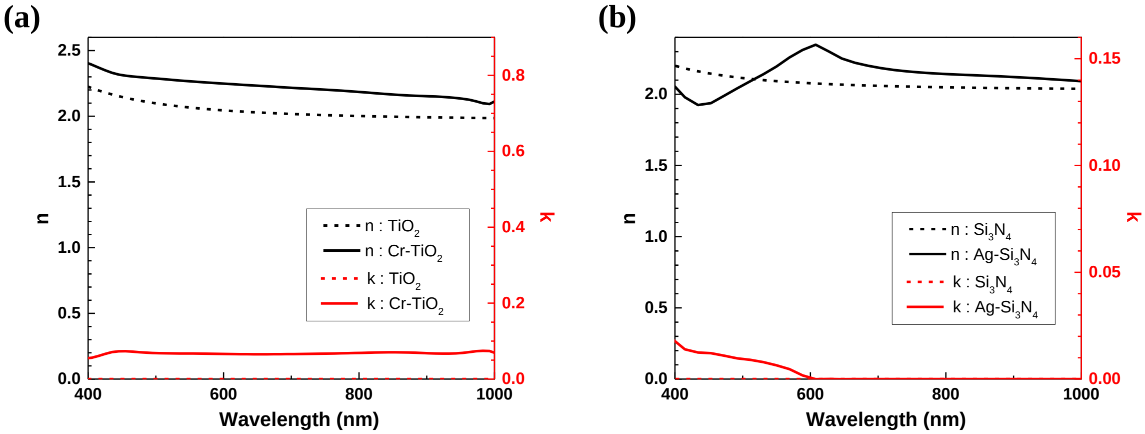

Figure 6.11 Refractive index of (a) Cr-TiO_2 and (b) Ag-Si_3N_4 meta-materials.

6.4. Application of Meta-Material on Commercial Low-e Stack

Low-e coating for window application needs to fulfill several criteria that determine the performance of the stack. The feasibility check of meta-material on improving the angle-insensitivity of low-e coating window holds meaning only when other criteria as low-e coatings are met as well. Figure 6.12 shows six different categories used to optimize for low-e coating window with prioritizing each category. These six categories are composed of parameters related to glass-side reflection *Rg0*, color-sensitivity of glass-side reflection *RgΔ*, thickness sensitivity factor *Sa**, transmission T_0, film-side reflection Rf_0, and ratio between transmission and g-factor *T/g*. Each category is composed of *Y*, *a**, *b**, RMS *Δ*a*, RMS *Δ*b*, or combinations of these parameters. The target specifications for the compositions of each categories are indicated as x. As already discussed in chapter 5.4, this involves non-linear optimization where sweeping multiple dimensions of parameter sweep is necessary to find the solution that meets all these criteria. Please refer to Chapter 6.4 for details on how each criterion are considered into defining penalty of merit (POM). For every parameter in each criterion, priority values are defined in the rating from 0 to 4 where priority of 0 shows parameters that deserves highest priority henceforth puts highest weight on the POM value of that category. The weights are imposed by dividing the total POM with 2^n where *n* is the priority number and having larger n means putting lesser weight on that category.

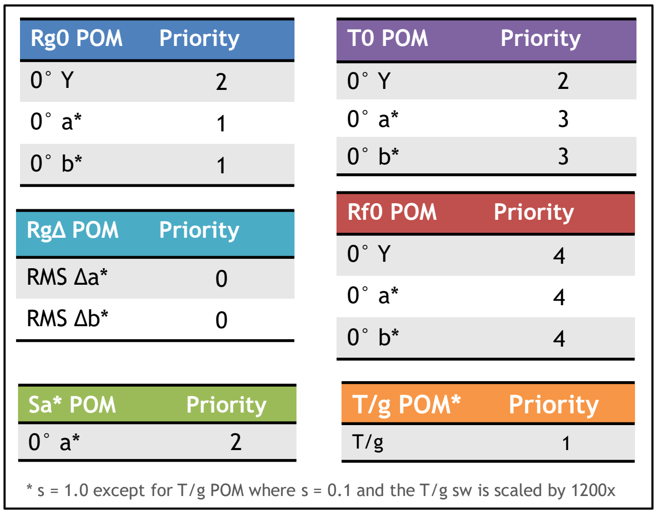

Rg0 POM	Priority
0° Y	2
0° a*	1
0° b*	1

RgΔ POM	Priority
RMS Δa*	0
RMS Δb*	0

Sa* POM	Priority
0° a*	2

T0 POM	Priority
0° Y	2
0° a*	3
0° b*	3

Rf0 POM	Priority
0° Y	4
0° a*	4
0° b*	4

T/g POM*	Priority
T/g	1

* s = 1.0 except for T/g POM where s = 0.1 and the T/g sw is scaled by 1200x

Figure 6.12 Six major criteria for low-e coating windows and its priority during optimization is shown. The target specifications are not shown for proprietary reasons.

For example, hypothetically *Rg0* of 0°Y with $x = 10$ and tolerance of 1.5 with priority of 2 indicates that the stack has a target specification of Rg0 Y=10% at a normal incidence which can tolerate deviation of at most Y=11.5%. This POM value will be divided by 4 (= 2^2) as it has a priority of 2. The most important criteria is *RgΔ* where RMS Δa* or Δb* given as *eq 6.3* representing the angle-sensitivity of the reflection color:

$$RMS\ \Delta a^* = \sqrt{\frac{\sum_\theta [a^*(\theta) - a^*(0°)]^2}{N_\theta}} \tag{6.3}$$

The highest priority of 0 is assigned to this criterion as the scope of this project is to design less angle- sensitive low-e window. Aside from this, another important parameter is *T/g* where *T* is the transmission in the visible wavelength normalized to human eye and *g* is the solar energy transmittance which is total solar heat gain over incident solar radiation. The key of low-e coating lies in maximizing *T/g* value. Setting these target specifications, stack optimization was conducted for meta-materials in which this layer was inserted in between the Ag film and dielectric film composing 1D-MDPC structures.

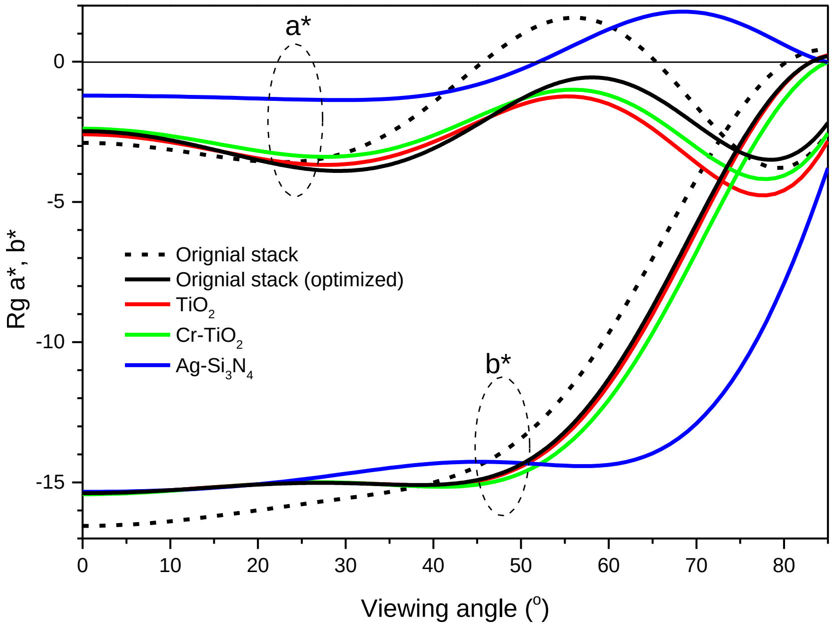

Figure 6.13 Plot of a* b* of Rg as a function of viewing angle for low-e coating with various meta-materials.

With inserting meta-materials into the original stack, optimization of the thickness was conducted based on the POM to meet the target specification and most of all to obtain stack having large angle-insensitivity while meeting other target criteria. Then, Figure 6.13 shows the plot of Rg's *a** and *b** as a function of viewing angle when different types of meta-materials are used for low-e coating. First, taking a look at the *b** of Cr-TiO_2 sample which is intended to enhance the angle-insensitivity by using increased refractive index value, its absolute value remains constant for wider range of viewing angle and starts to decrease rapidly beyond 50°. Compared with original stack, this can be considered non-negligible improvement. But when compared with the case of putting TiO_2 into the "Meta" layers as TiO_2 material is known to have large index value, the angle-insensitivity of b* value for Cr-TiO_2 is slightly better than that of TiO_2. This weakens the argument of necessity of using Cr NP into the TiO_2 matrix as the angle-insensitivity of b* is improved by only a slight amount. This indicates that enhancing the index value over the entire visible wavelength by using meta-material shows only a limited improvement in the angle-insensitivity of low-e stack. Next, looking at the low-e coating with having Ag-Si_3N_4 layer, there is a remarkable improvement in the angle-insensitivity of b* value where the value somewhat remains unchanged until 65°. This could be attributed to having absorption at a specific range of visible wavelength in which this LSPR extinction (absorption + scattering) due to Ag NPs does not depend of incident angle. It is noteworthy to take a closer look into the behavior of Rg spectra for these samples as a function of viewing angle as shown in Figure 6.14 to better understand this phenomenon. For the case of original low-e coating stack and meta-material with enhanced index value using Cr-TiO_2, the peak at wavelength around 550 nm becomes more conspicuous beyond incident angle of 55°

and 60°, respectively. Beyond this incident angle, the intensity of spectral peak at 550 nm increase further where the total spectral shape at a visible wavelength significantly deviates from that at incident angle of 0°. This appearance of peak at 550 nm is attributed to the appearance of greenish color of low-e window when viewing from large angle of incidence. However, looking at the case with Ag-Si_3N_4 meta-material layer in Figure 6.14c, it is evident that this peak at 550 nm is not conspicuous at a larger viewing angle. In fact, the overall spectrum at a visible wavelength range maintains its spectral shape even at a large angle of incidence (or same as viewing angle).

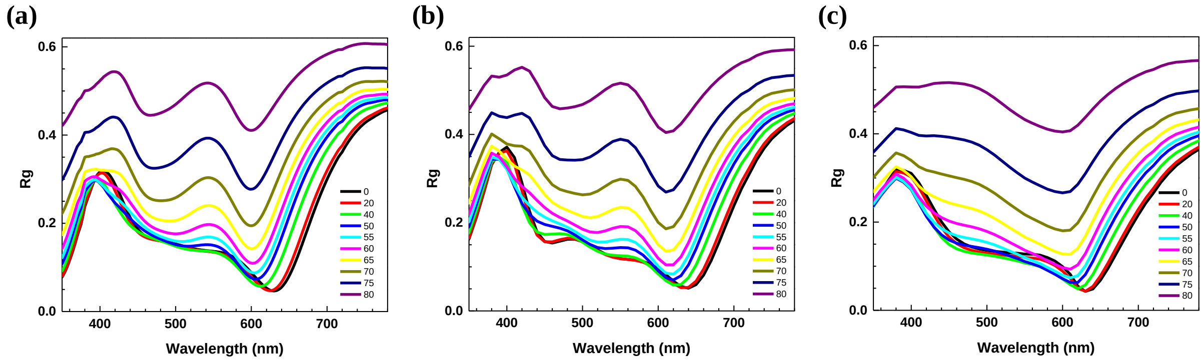

Figure 6.14 *Rg* as a function of angle of incidence (or viewing angle) with respect to normal incidence of low-e stack window of (a) original stack and with (b) Cr-TiO_2 and (c) Ag-Si_3N_4 inserted as a meta-material layer.

The angle insensitive spectral shape is attributed to the *n-k* spectral shape of Ag-Si_3N_4 meta-material layer as shown in Figure 6.11b where at the wavelength range between 450-600 nm, the refractive index *n* value increases due to the existence of extinction coefficient *k* value. A typical dielectric layer shows a dispersion relation where refractive index changes as a function of wavelength. When using typical dielectric layers for this specific low-e coating window, there is a higher reflection at 550 nm as angle of incidence increases. This may be thought of as typical trait for this low-e coating product. Now, if the meta-material layer can be designed with the refractive index enhancement only in the green wavelength such that the light gets refracted even at a large angle of incidence instead of being reflected, the window appearing as a greenish color can be circumvented. Ag-Si_3N_4 shows high index value at green wavelength which indicates that more portion of this wavelength light can be guided into the stack even at large angle of incidence.

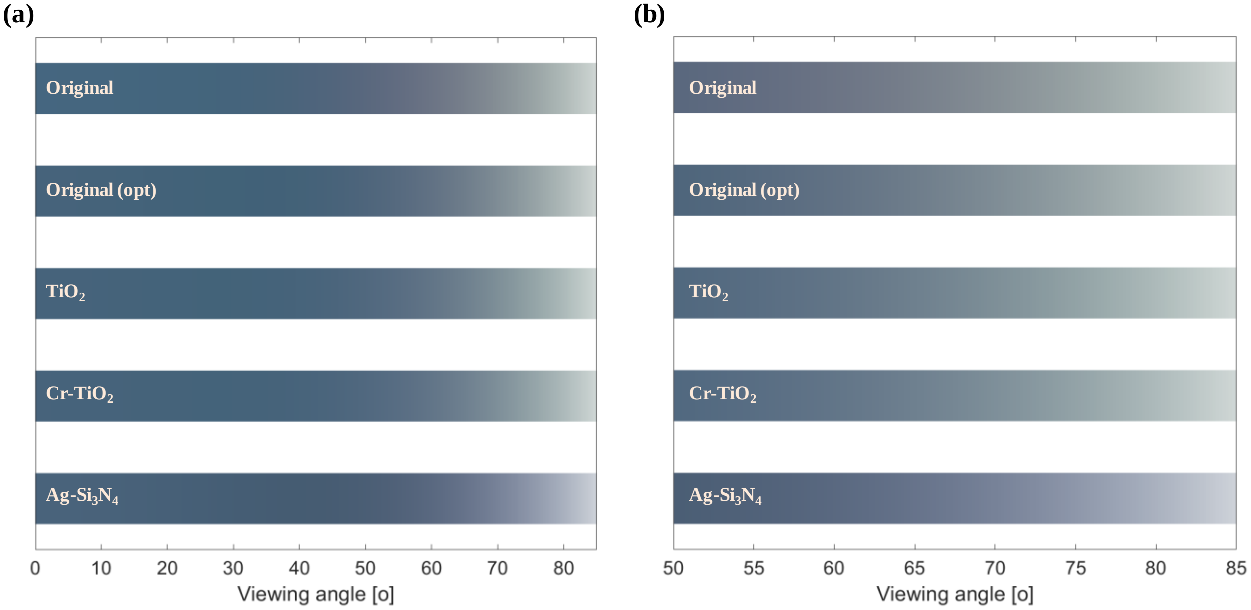

Figure 6.15 Low-e coating's *Rg* color as a function of viewing angle (a) 0° – 85° and (b) 50° – 85° for each type.

Figure 6.15 shows how the low-e coating's *Rg* appear in color as a function of viewing angle for original stack as well as that with various meta-materials. *L*, *a**, and *b** are converted to *r*, *g*, and *b* values which are plotted as function of viewing angle. For all the stacks except Ag-Si_3N_4, glass that appears to be blue at a 0° viewing angle starts to turn into turquoise color beyond 60° in which the color transforms more into greenish color. Interestingly, the low-e coating stack with Ag-Si_3N_4 sample does not show any turquoise color even up to 75° or beyond which is a remarkable difference compared to original stack or those using high refractive index. Figure 6.15b shows the color change for a narrow range of angle from 50 - 85°, which shows more noticeable difference.

6.5 Conclusion

Two candidate sets of meta-materials (metal nanoparticle inside dielectric) of Ag-Si_3N_4 and Cr-TiO_2 were simulated and fabricated to solve angle-sensitivity problem in colored windows for low-e coating application. The approach of enhancing the refractive index at a entire visible wavelength via Cr-TiO_2 shows minute improvement in the angle-insensitivity. On the other hand, Ag-Si_3N_4 meta-material layer was shown to significantly improve the angle-robustness of colored low-e windows. By taking advantage of the de-wetting property of Ag atom on a dielectric layer, close to 2 nm of Ag nanoparticle was formed inside the Si_3N_4 matrix via rotation sputtering method. Inducing a specific light absorption peak at green wavelength even at high angle of incidence, the angle-robust low-e stack was achieved.

Chapter 7 Growth and Characterization of Single Crystalline III-V Nanostructure for Solar Energy Harvesting Application

7.1 Introduction

Growth of highly crystalline In-rich $In_xGa_{1-x}N$ is one of the most important technologies for III-nitride semiconductor devices. The tunability of its direct bandgap energies from ~0.65 to 3.4 eV makes it a very promising material for a broad range of optoelectronic devices including light emitting diodes (LEDs) [131, 132] lasers, solar cells [133, 134] and photoelectrochemical cells [135-137] as well as electronic devices such as high mobility transistors [138-140]. However, creating highly crystalline In-rich $In_xGa_{1-x}N$ heterostructures is difficult due to defects, threading dislocations, and stacking faults caused by the lattice mismatch between InN and GaN (-11%) [141-143]. To solve this problem, nanowire [144], nanoridge, and nanowall [145, 146] structures have been created that incorporate indium into GaN crystal. These nanostructures have low densities of extended defects and efficient surface stress relaxation in lattice-mismatched heterojunctions [147] so they can incorporate high In-content in their structures, thereby tuning the wavelength in the entire visible and near-infrared spectrum [144].

While nanowire structures have been extensively studied, there have been very few reports on the growth of InGaN nanoridge or nanowall structures. Compared to conventional nanowires, the unique structure of nanoridges or nanowalls make them well suited for edge-emitting lasers and fin field effect transistors [148]. As wall thickness approaches a few nanometers, In(Ga)N can exhibit unusually large exciton binding energy (up to 1.4 eV) [149], which rivals that of the extensively studied single-layer transitional metal dichalcogenides and therefore offers a new quantum material platform.

To date, however, the fabrication, synthesis, and characterization of InGaN nanoridge or nanowall structures is still in its nascent stage. Recently, Chouksey *et al.* reported well-ordered InGaN nanowall structure, but their approach to fabrication relies solely on top-down etching of InGaN film, which is fundamentally limited by the aforementioned difficulties in planar structures showing peak emission below 500 nm wavelength [150]. Random InGaN nanowall networks can be formed during epitaxy of InGaN epilayers on a Si substrate, but these networks exhibit uncontrollable size, morphology and properties [151]. To date, there has been no demonstration of the controlled synthesis of InGaN nanoridge or nanowall arrays using a bottom-up approach.

We have combined top-down etching and bottom-up molecular beam epitaxy to create a new method of fabricating well-ordered InGaN nanoridge arrays. We also investigated the effects of the growth conditions on the structural and optical properties of these nanoridge arrays. InGaN nanoridges are formed on a Ga-polarity c-plane. Initial growth of InGaN on a patterned GaN/sapphire substrate is limited by the dominant formation of the $(10\bar{1}1)$ plane. Increasing the growth duration leads to the formation of a very narrow (~50 nm) fin-shaped InGaN nanoridge structure above the InGaN nanoprism array. The resulting fin-shaped InGaN nanoridge structure shows strong photoluminescence (PL) intensity with wavelength centered at 524-560 nm and a narrow linewidth, as compared to previously reported InGaN nanowire structure. High-resolution high-angle angular-dark-field (HAADF) suggests that the InGaN nanoridge exhibits single crystalline structure largely free of phase separation or dislocations with homogeneous In-distribution throughout the growth direction. These improvements over previously reported nanowire [144] or nanoridge/nanowall structures [145, 146] are attributed to the combination of the top-down and bottom-up method, which will be useful for device fabrication.

In the last section, as one promising application of InGaN-based optoelectronic devices, we will study the impact of InGaN nanoridge's material quality on the performance of its use as photoanode for photoelectrochemical cell. We will compare this property with widely used InGaN nanowire structure to show the superior property of InGaN nanoridge for solar energy application. This study provides not only a better understanding of InGaN epitaxial growth, but also benefits the development of nanostructured InGaN-based electronic devices.

7.2 Fabrication/Growth of InGaN Nanoridge

GaN nanowall structures were formed by projection lithography and etching on an n-type GaN template on a sapphire substrate. First, a stripe pattern of silicon dioxide (SiO_2) was patterned on the GaN template parallel to the $[11\bar{2}0]$ a-direction. With the SiO_2 as a masking layer, 1 μm of n-type GaN was etched by reactive ion etching (RIE) with Cl_2 gas as shown in Figure 7.1a.

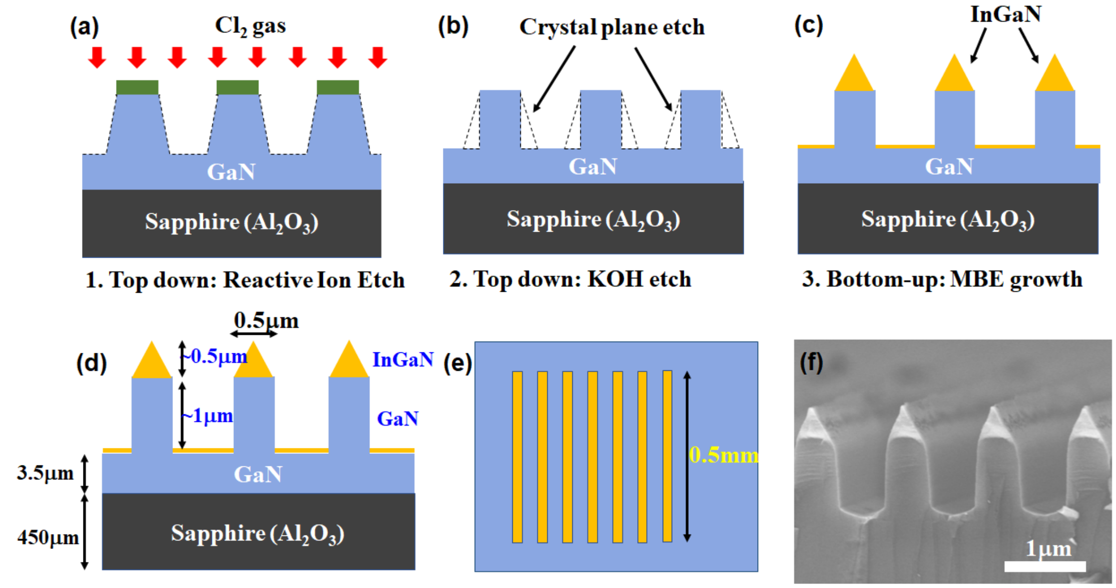

Cross section

Top section

Figure 7.1 Schematic illustration of fabrication process of InGaN nanoridge/nanoprism with integration of top-down and bottom-up approach. Top-down: (a) RIE etching and (b) KOH crystallographic wet etching of GaN nanowall array. Bottom-up: (c) MBE growth of InGaN on GaN nanowall array. (d) Cross-sectional view and (e) Top view illustration of the nanoridge/nanoprism dimension. (f) SEM of cross-section of InGaN nanoridge/nanoprism array.

Second, the sample was immersed in 30 wt% KOH solution at elevated temperature of 120 ℃ for 5 min to reveal the crystal plane and to achieve smooth and vertical sidewall as shown in Figure 7.1b [152, 153]. Finally, the SiO_2 masking layer was removed using HF solution. SEM images of the GaN nanowalls after each step are shown in Figure 7.2.

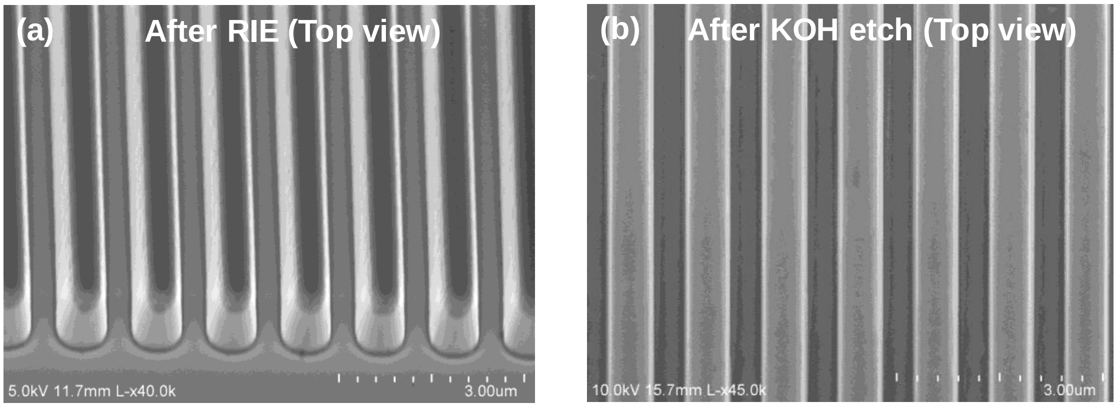

Figure 7.2 SEM images of top view of GaN nanowall after (a) Reactive Ion Etching (RIE) with 500 nm of SiO_2 masking layer and (b) subsequent crystallographic etching using 30 wt% of KOH.

In this study, the GaN nanowall template had a wall width, spacing, and height of 500 nm, 400-500 nm, and 1μm, respectively (Figure 7.1d). Smaller sizes can be readily achieved using e-beam lithography. The length of each segment of GaN nanowall was 0.5mm as indicated in Figure 7.1e. The sample was subsequently loaded in a Veeco Gen II MBE system equipped with a radio frequency plasma-assisted nitrogen source for InGaN growth. To study the growth conditions of the InGaN, the III-N ratio was varied by altering nitrogen flow rate from 1.5 sccm down to 0.45 sccm. In beam equivalent pressure (BEP) was maintained at 9.8×10^{-8} Torr, Ga BEP at 2.7×10^{-8} Torr, and growth temperature at 755 ℃. Samples A, B, and C had nitrogen flow rates of 1.5, 0.8, and 0.45 sccm, respectively, as listed in Table 7.1. Due to the In desorption above 540 ℃ [154], an accurate III-V ratio is difficult determine, so the boundary between the metal-rich condition and the nitrogen-rich condition was determined by the presence the metal-droplets on the sample.

Table 7.1 MBE growth condition for InGaN nanoridge.

Sample	Ga flux / Torr	In flux / Torr	N_2 flow / sccm	III-V ratio
A	2.7e-8	9.8e-8	1.5	N_2 – rich
B	2.7e-8	9.8e-8	0.8	N_2 – rich

C	2.7e-8	9.8e-8	0.45	Metal – rich

We investigated the effect of N flow rate on the epitaxy of InGaN nanostructures. For Sample A, the abundance of nitrogen plasma induces 3-dimensional growth of the InGaN grown on GaN nanowall template, shown in Figure 7.3a and b. As the plasma flow was reduced to 0.8 sccm, we observed less roughness on the InGaN but nanoscale roughness is still present on the surface, as illustrated in Figure 7.3c and d. Once the nitrogen flow reached 0.45 sccm in sample C, the InGaN surface became smooth, as seen in Figure 7.3e and f, resembling what is typically observed for high quality InGaN epilayers grown by plasma-assisted MBE under a nearly metal rich condition [155]. The most interesting feature of this growth regime is the emergence of a very narrow, fin-shaped InGaN nanoridge on top of the triangular InGaN nanoprism, which is the focus of our results.

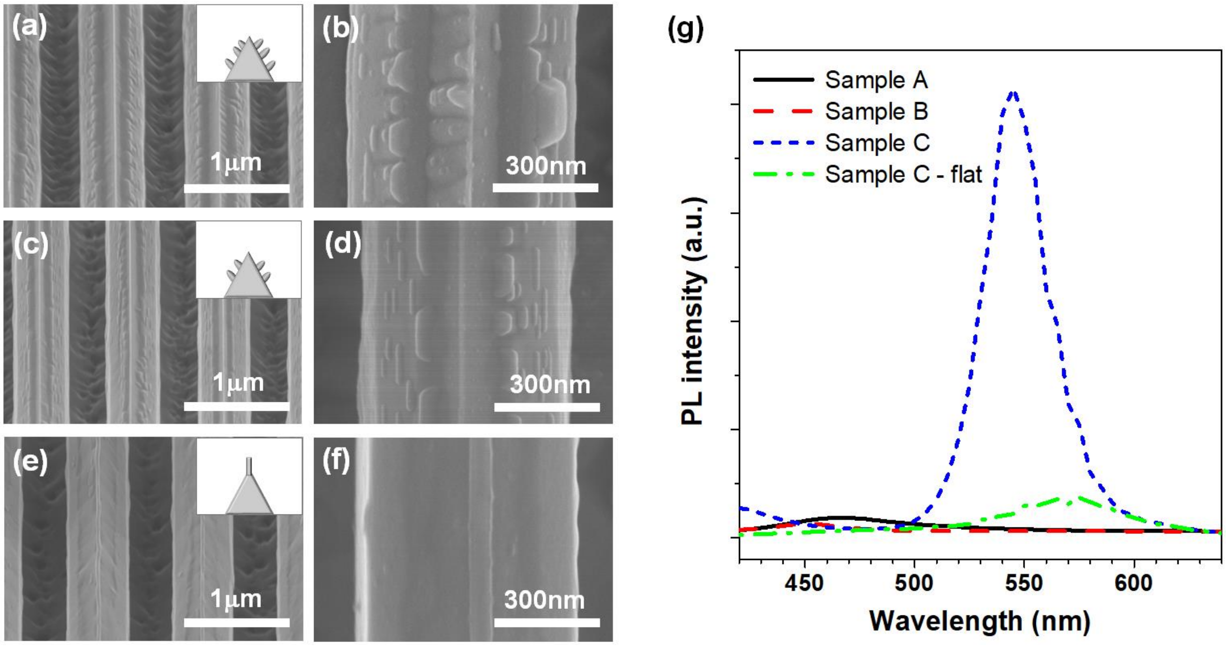

Figure 7.3 Bird's-eye view SEM image of InGaN/GaN structure grown in MBE under (a) Sample A, (c) Sample B, and (e) Sample C condition. The inset shows the cross-sectional schematic illustration of surface roughness after growth. High resolution top-down view of SEM image of

InGaN/GaN nanowall grown in MBE under (b) Sample A, (d) Sample B, and (f) Sample C condition. Refer to Table 7.1 for the growth condition of each sample. (g) Room temperature micro-PL emission comparison of InGaN nanowall with Sample A (black solid line), Sample B (red dashed line), Sample C (blue short dash line) conditions, and InGaN planar grown with Sample C condition (green dash dotted line). The peak wavelength is at 468, 452, 545, and 575 nm for InGaN nanowall with Sample A, B, C, and InGaN planar with Sample C condition, respectively.

7.3 Growth Morphology and Photoluminescence

PL emission spectra of Samples A, B and C were measured at room-temperature, and are given in Figure 7.3g. A 405 nm laser source was used as the excitation source with a 100× objective and a beam approximately 1μm in diameter. For Samples A and B, the peak wavelengths of InGaN nanostructures were 468 and 452 nm, respectively. For Sample C, the PL emission of InGaN nanoridge/nanoprism showed a peak at 545 nm with intensity nearly two orders of magnitude stronger than that of Samples A and B. In addition, a weak emission of ~450 nm was measured from Sample C. For comparison, optical emission from the planar region for Sample C is also shown. This shows that the emission from the InGaN nanoridge/nanoprism under optimum growth conditions is significantly stronger than that from InGaN epilayers. These studies suggest that under optimum growth conditions (nearly metal-rich epitaxy conditions), the optical quality can be significantly enhanced for InGaN nanoridge/nanoprism structures. Furthermore, the presence of two emission peaks suggest nonuniform indium distribution.

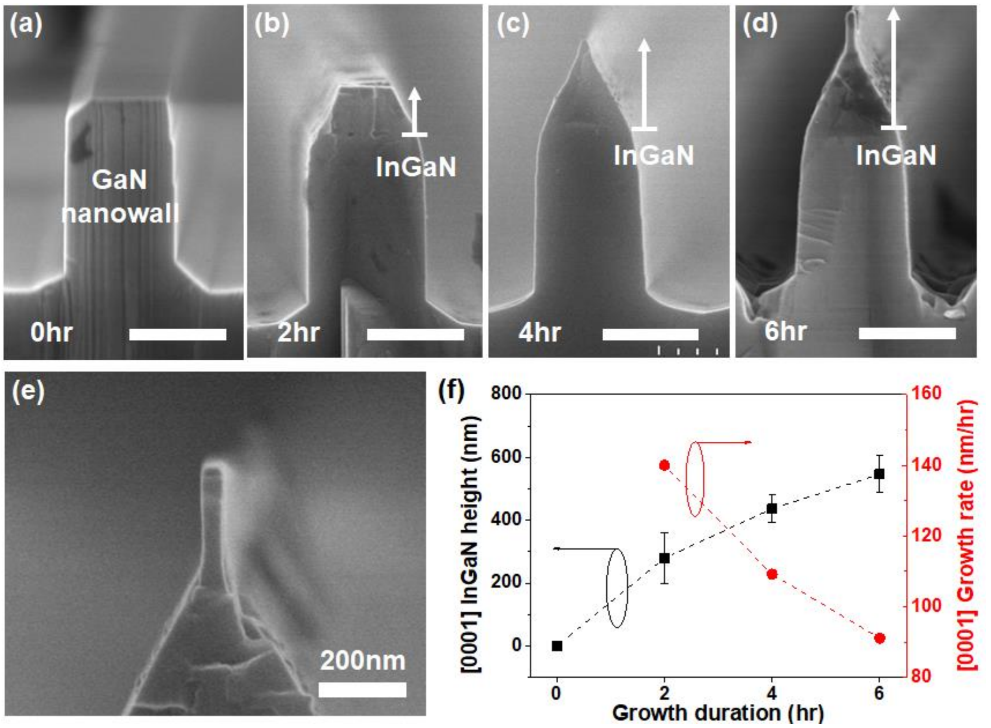

Figure 7.4 Cross-sectional SEM image of single GaN nanowall segment with InGaN growth duration of (a) 0, (b) 2, (c) 4, and (d) 6 hrs. In (b)-(d), InGaN region is shown with arrow to indicate the growth length along c-axis. All scale bars represent 500 nm unless specified. (e) High magnification cross-sectional SEM image of very narrow fin-shaped InGaN nanoridge elongated on top of InGaN nanoprism after 6 hours of growth. (f) Measured InGaN height (black square) and calculated [0001] direction growth rate (red circle) with respect to growth time.

To further study the formation of InGaN nanoridge structures, we observed the evolution of InGaN structure grown on top of the single GaN nanowall segment using the growth conditions from Sample C. Illustrated in Figures 7.4a, b, c, and d are cross-sectional SEM images of the GaN nanowall template and InGaN nanostructure after 2, 4, and 6 hrs of growth, respectively. InGaN grows on top of the c-plane GaN nanowall in the form of a prismatic shape for up to 4 hrs, as seen in Figures 7.4a, b and c. This InGaN forms a nanoprism structure that is bound by r-planes. In crystal growth, the slowest growing facet will eventually determine the crystal plane [156]. From observation, growth in the [0001] direction is faster than that in the $[10\bar{1}2]$ or $[10\bar{1}1]$ directions.

Therefore, the (0001) facet will diminish and the r-plane will dominate resulting in pyramidal shape as growth proceeds [157]. The angle between inclined side planes and the (0001) plane was 63° (Figure 7.5), which indicates that the r-plane of InGaN nanoprism has a $(10\bar{1}1)$ facet [156, 157].

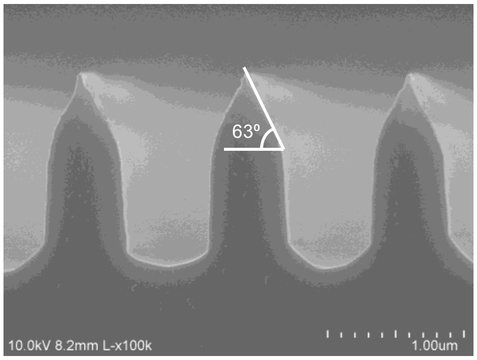

Figure 7.5 Cross sectional SEM image of 4 hrs of InGaN nanoridge/nanoprism growth with measured angle between (0001) c-plane and inclined side plane of 63°

The formation of a semipolar $(10\bar{1}1)$ r-plane facet in the nanoprism is consistent with the hexagonal pyramid formation in self-assembled growth (SAG) of wurtzite GaN nanowires [157, 158]. The only difference is that SAG nanowires have 6 r-plane facets of equal size on top of perfect hexagonal pyramid, whereas our structure shows elongated prismatic shape along the $[11\bar{2}0]$ a-direction. Growth interface of SAG nanowire and nanoprism are represented in Figure 7.6.

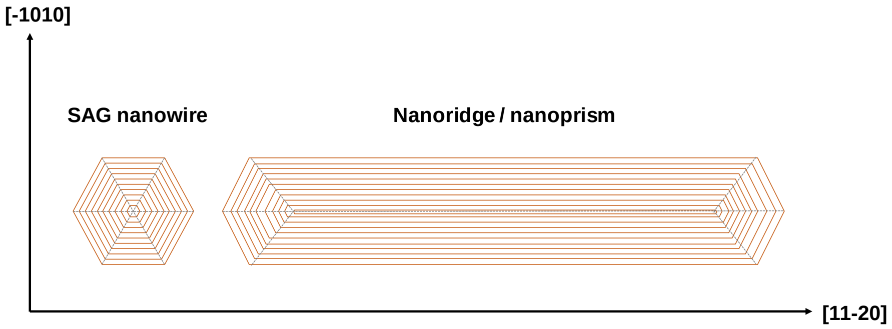

Figure 7.6 Schematic illustration of growth interface in self-assembled growth (SAG) nanowire and nanoridge/nanoprism representing hexagonal pyramid and prismic shape, respectively, after long time integration showing facetted morphology. The x-axis and y-axis represent the [112¯0] and [1¯010] direction, respectively. SAG nanowires have 6 equal-sized r-plane facets, whereas nanoridge/nanoprism sample has 6 r-plane facets with elongated (101¯0) and (1¯010) planes along [112¯0] direction. The schematic is illustrated only to depict the growth contour over time scale and has been referred to work by V. Jindal et al.

After 4 hrs of growth, the structure evolves into a fin-shaped nanoridge on top of the nanoprism which starts to elongate proportional to the growth duration. This fin-shaped nanoridge structure has the growth along [0001] direction with their sidewalls being m-planes $(10\bar{1}0)$ and $(\bar{1}010)$ planes. This narrow fin-shaped InGaN nanoridge has not been observed in any other work. Figure 2.4e shows the magnified cross-sectional SEM image of a nanoridge segment on top of the InGaN nanoprism. As shown in Figure 7.4f, the growth rate along the c-axis decreases from an average growth rate of 140 nm/hr in the first 2 hrs of growth to 109 nm/hr from the 2nd to 4th hr of growth. We attribute this to the reduced probability of Ga and In adatoms reaching the top of the nanoprism [159, 160]. When the narrow fin-shaped InGaN nanoridge starts to form, the chance of Ga and In adatoms migrating to the tip lowers even farther, reducing the growth rate to 91 nm/hr from the 4th to 6th hr of growth. This growth rate reduction is consistent with the previous studies of reduced axial growth rate of self-assembled GaN nanowires over time [159]. In SAG nanowires, Ga adatoms supplied by diffusion on a Mo mask need to diffuse to the top of GaN nanocolumns to contribute to the axial growth [158]. Similarly, in InGaN nanoridge, both Ga and In adatoms will need to diffuse to the tip of the nanoridge, which will be more challenging as the growth along the axial direction proceeds.

In this study, we did not observe any significant growth (>20 nm/hr) along the lateral direction on the sidewall of the GaN nanowall. The epitaxy proceeds in a way to reveal the plane that has the lowest surface energy. The surface energy of the m-plane is lower than that of other nonpolar crystal planes [158, 161, 162]. Therefore, the m-plane, which is the slowest growing plane, will be what forms the nanowall sidewall, which is supported by our observations. This is analogous to the previously reported SAG nanowire going through morphological evolution toward a thermodynamically stable hexagonal shape with m-planes [158].

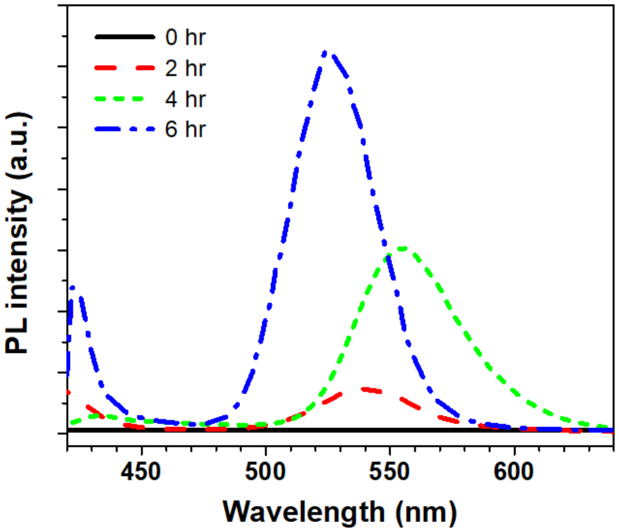

Figure 7.7 Room temperature micro-PL of InGaN nanoridge/nanoprism with duration of 0 (black solid line), 2 (red dashed line), 4 (green short dash line), and 6 hrs (blue dash dotted line). The peak wavelength position for duration of 2, 4, and 6 hrs are 540, 560, and 524 nm, respectively.

Room-temperature micro-PL spectra of the InGaN nanostructure grown on GaN nanowall with various growth durations are shown in Figure 7.7. As the growth duration increased from 2 to 6 hrs, we observed an increase in the intensity of the peak emission above 500 nm. After 4 hrs, the narrow fin-shaped InGaN nanoridge structure emerged and we measured extremely strong PL emission. The indium incorporation is further derived using the following equation,

$$E_{In_xGa_{1-x}N} = xE_{InN} + (1-x)E_{GaN} - bx(1-x) \qquad (7.1)$$

InGaN nanostructure sample is shown to have x~0.3, where we used b=1.10 eV as the average bowing parameter [163]. To further verify that the emission is coming from the narrow fin-shaped InGaN nanoridge structure, we compared the signal from InGaN grown on a planar region near nanoridge/nanoprism. The PL from the planar region showed negligible intensity compared to that from the nanoridge/nanoprism region suggesting that the signal is coming from the InGaN grown on the GaN nanowall array template. This leaves two possible cases: the signal is from the nanoridges or the signal is from the InGaN between the nanowalls. If the emission originates from the InGaN between the GaN nanowall segments, these samples would show a strong PL emission at around 524-560 nm regardless of the GaN nanowall width. On the other hand, if the emission is coming from the InGaN nanoridge/nanoprism, the emission will depend on the presence of the nanoridge/nanoprism because InGaN growth atop wider GaN nanowalls does not have the InGaN nanoridge. To confirm that the signal is not from the InGaN grown between GaN nanowall segments, we prepared GaN nanowall templated samples with widths of 500, 800, and 1200 nm but the same spacing between walls. InGaN was grown on the GaN nanowall templates for 4 hours. For this growth time, we only expect to see an InGaN nanoridge on the 500nm-width sample. From Figure 7.8 a and b, emission from samples with wall widths of 800 and 1200nm shows a negligible peak around 524-560 nm, indicating that the strong emission at 524-560 nm is coming from the InGaN nanoridge. These studies also indicate that the weak emission measured below 500 nm is likely from InGaN nanoprism and/or InGaN layer grown on the bottom in between the GaN nanowall spacing.

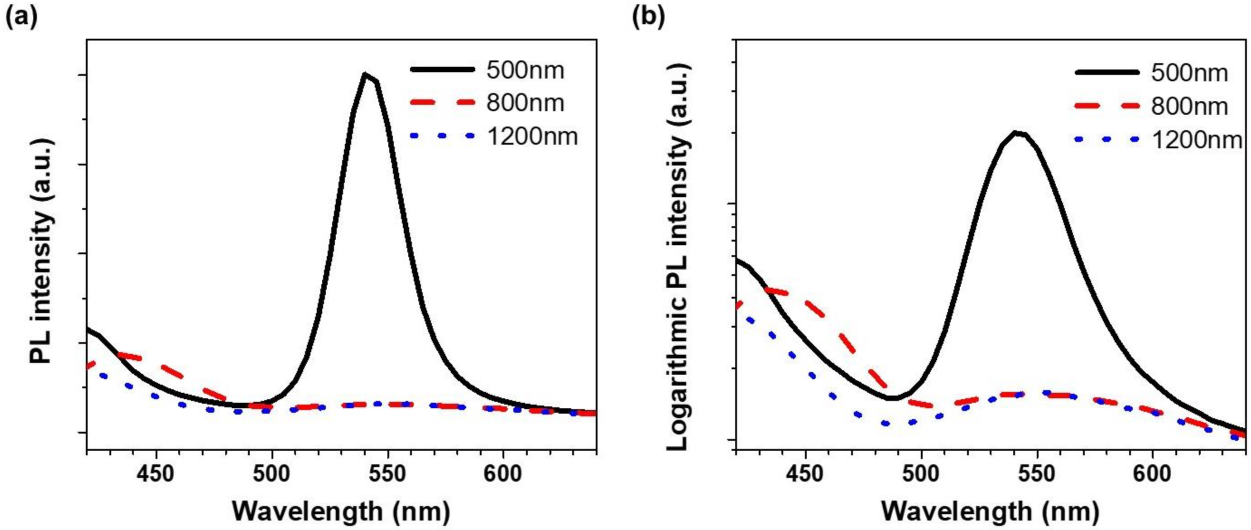

Figure 7.8 (a) Micro-PL of 4 hours of InGaN grown on GaN nanowall with nanowall spacing of 500 (black solid line), 800 (red dashed line), and 1200 nm (blue dotted line). Out of three samples, only the sample with 500 nm spacing showed peak at 540 nm indicating that the emission at this wavelength is coming from the narrow InGaN nanoridge emerging on top as shown in Figure 7.4e. All three samples showed peak in the range of 420-480 nm indicating the emission at this wavelength is coming from the bulk InGaN grown either on top of GaN nanowall or on the bottom in between the nanowall segments. (b) Logarithmic PL intensities of three samples for better intensity comparison. All samples were excited with 405 nm laser source with using 100X objective under room temperature.

PL emission was also measured for InGaN nanowire arrays with peak emission at 546 nm, as shown in Figure 7.9d. We found that the InGaN nanoridge structures exhibit intensity nearly 4 times higher than that of spontaneously formed InGaN nanowires, despite the relatively small surface area of nanoridge structures. Moreover, the emission of the nanoridge sample is sharper with a full-width-at-half-maximum (FWHM) value of 40 nm when compared to FWHM value of 101 nm for the nanowire sample.

7.4 Transmission Electron Microscopy of InGaN Nanoridge

InGaN crystals were grown with hierarchical order that spans the nano- to atomic- scale through lithographic templating (Figure 7.9a-c). Cross-sectional electron microscopy shows the periodic GaN nanowalls (width ~500 nm, height ~1 um, spacing ~400-500 nm) that template confined InGaN growth (Figure 7.9a). The single crystallinity of the InGaN nanoridge (~50 nm width) that forms along the top of each InGaN nanoprism is reflected in the sharply faceted termination of <100> sidewalls and <001> top (Figure. 7.9c) of the 6 hour-grown sample. In confined geometry heteroepitaxy, increased In incorporation can occur due to the onset of strain relaxed growth [164]. In the 4 hour sample, the InGaN nanoridge was formed with smaller width and height than that of the 6 hour sample. In addition, this nanoridge was highly crystalline but lacked the sharp facets and contained a partially amorphous surface termination—suggesting that with further growth the nanoridge may crystallize and facet. An energy dispersive x-ray (EDS) map shows a well-defined InGaN nanoridge after 6 hours of growth, homogeneously composed of Ga, In, and N without phase segregation (Figure 7.9b). This homogeneous distribution of Ga and In elements in our InGaN nanoridge is superior to that of InGaN growth on a randomly oriented c-axis GaN nanowall, where Rodriguez *et al.* observed strong fluctuation of the In composition in their structure.[146] Energy dispersive X-ray (EDX) spectra collected from four InGaN nanoridge regions estimates In occupies 27 ± 5% of Ga sites (i.e. $x=0.27\pm0.05$). Pure GaN regions confirmed EDX quantification of Ga concentration to within ~10%. This In occupancy result is consistent with the PL result estimated to having x~0.3 for InGaN. Atomic resolution dark field scanning transmission electron microscopy (STEM) show lattice spacing of 2.85 Å and 2.95 Å (Figure 7.9e) and confirms an In-rich InGaN crystal (GaN and InN spacing are 2.75 and 3.06 Å, respectively). This corresponds to the (100) lattice plane of InGaN with an orientation that indicates preferred growth along the [0001] c-axis direction. Lastly, the highly ordered 1D InGaN provides strong PL emission (Figure 7.9d).

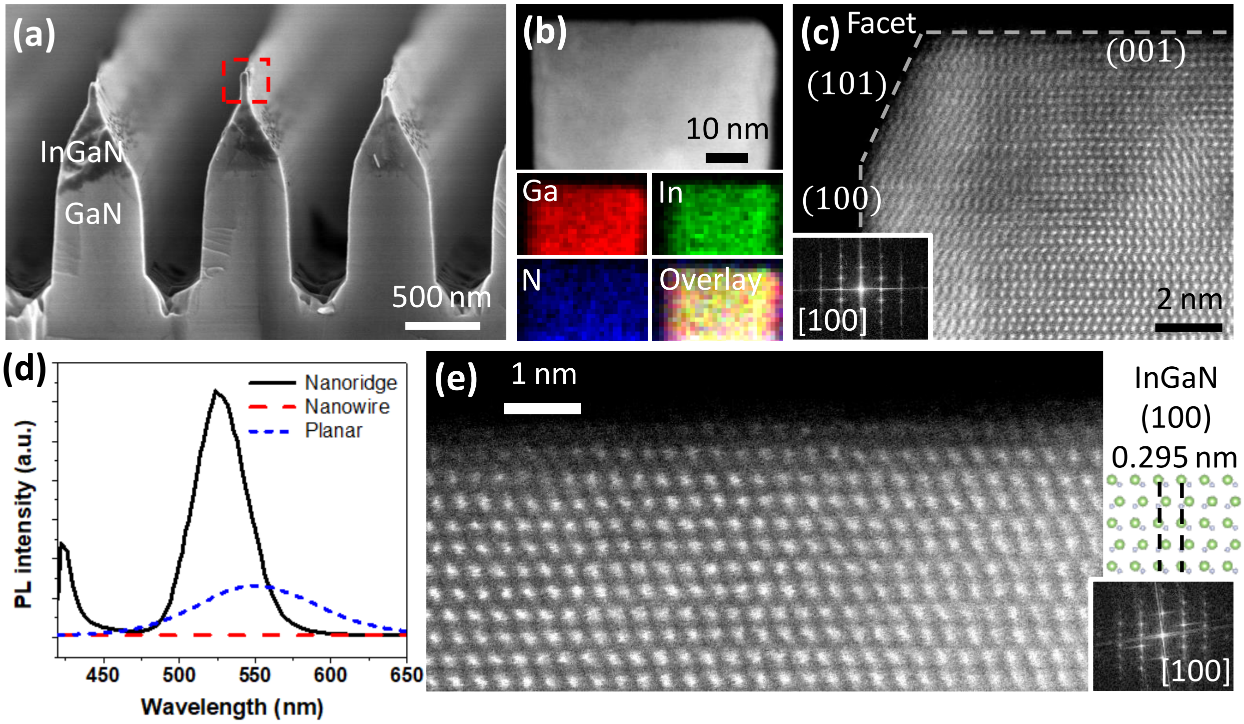

Figure 7.9 Single crystal 1D InGaN nanoridge grown on GaN nanowall array (a) Side-view SEM (b) HAADF STEM image on cross-sectional fin-shaped InGaN nanoridge from one of the InGaN nanoridge/GaN nanowall array in a and simultaneous STEM EDS spectroscopic mapping showing the grown InGaN tip primarily comprised of Ga (red), In (blue), and N (green). (c) High resolution HAADF STEM on the sharply-faceted InGaN nanoridge in c indicating highly single crystalline. (d) Room temperature micro-PL of InGaN nanoridge (black solid line), planar (red dashed line), and nanowire (blue dotted line) measured with 405 nm laser source. Peak wavelength position and full-width at half maximum (FWHM) values for 6 hrs InGaN nanoridge and InGaN nanowire sample are 40 and 101 nm, respectively. € Atomic resolution HAADF STEM on the termination of the InGaN tip in c indicating the lattice constant that is consistent with InGaN.

7.5 InGaN Nanoridge for Solar Energy Conversion Application

7.5.1. III-nitride for Solar Energy Conversion

The production of hydrogen via water-splitting using photoelectrochemical (PEC) device has attracted tremendous research work in recent years, with the hope of fulfilling demands for environmentally-friendly energy. III-nitride is a promising candidate for solar water splitting because of its direct band gap, which can be tuned to cover the entire solar spectrum through band gap engineering [137]. In specific, InGaN and GaN are good candidates to serve as a photoanode as their adequate band-edges can straddling the water redox potentials. The performance of these devices is impacted by unavoidable surface-states present at the semiconductor-liquid junction as well as the crystal quality of the material itself [165].

In this section, InGaN nanoridge is used as a photoanode for converting solar energy into chemical energy through the oxidation of water molecules. Electrochemical impedance spectroscopy is used to study the semiconductor-liquid junction and the charge transfer kinetics occuring at this interface. Steady-state photocurrent of InGaN nanoridge is compared with InGaN nanowire structures or GaN planar or nanowall structrues. Owing to highly crystalline nature of InGan nanoridge, high photocurrent and fill factor of InGaN nanoridge is explained in junction with reduced charge recombination.

7.5.2. Photoelectrochemical Cell Measurement

A schematic of the PEC experimental setup is presented in Figure 7.10a. Only the active area of InGaN photo-anode is exposed to the electrolyte while the rest of the sample area is covered by epoxy. The sample is immersed in electrolyte solution of either 1M of hydrogen bromide (HBr) or 0.2M of potassium chloride (KCl) with 0.1 phosphate buffer (pH7) solution. The InGaN photo-anode is used as a working electrode. For counter electrode and reference electrode, Pt mesh and

Ag/AgCl were used, respectively. These electrodes are connected to the Bio-logics SP-200 potentiostat in a three-electrode configuration. For the illumination source, Newport LCS-100 Solar Simulator with Xenon arc lamp was used.

The charge transfer process at the photo-anode happens by the transfer of photo-generated holes to the water oxidation potential at the electrolyte as described in Figure 7.10b. This process can happen via two routes: a direct transfer of holes from the valence band of semiconductor or surface state-assisted transfer of holes. It is discussed Klahr et. al. that the surface states of photo-anode plays a significant role in the water oxidation process [166]. To study this charge transfer process, widely used equivalent circuit shown in Figure 7.10c is used. Here, C_{bulk} is composed of series connection of Helmholtz double layer capacitance and depletion capacitance at the semiconductor junction. As depletion capacitance is much smaller than the Helmholtz capacitance, this C_{bulk} is dominated by the depletion capacitance of the semiconductor material. Next, C_{ss} is the capacitive charging of the holes at the surface states during the oxidation process. It will be shown later that the carrier annihilation time in the surface state may vary depending on the material quality. Regarding resistance components, R_s, R_{trap}, and $R_{ct,SS}$ are the electrolyte solution resistance, hole resistance trapped at surface state, and hole transfer resistance from surface state to the electrolyte, respectively.

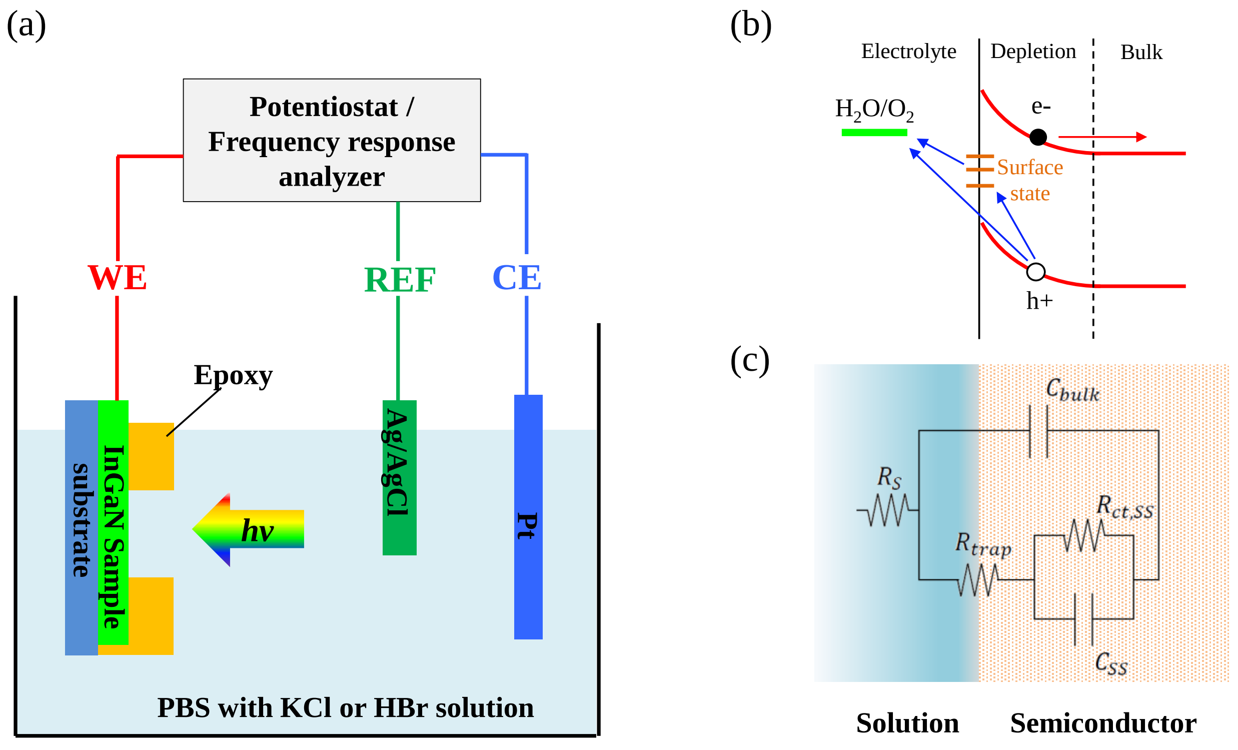

Figure 7.10 (a) Schematic of experimental setup for photoelectrochemical cell under light illumination. (b) Band-diagram of semiconductor-liquid junction illustrating the charge transfer process of photo-generated hole from semiconductor anode to the redox potential of electrolyte. (c) Equivalent circuit representing charge transfer process in semiconductor-liquid junction.

Above discussed elements in the equivalent circuit can be extracted by electrochemical impedance spectroscopy analysis (refer to previous chapter for details). By varying the frequency of ac small signal, one can see the impact of reaction rate dependence on the frequency which will be reflected in the complex impedance value. The frequency ranged was varied from 10k Hz down to 0.5 Hz. From the Nyquist plot, we can extract circuit elements defined in equivalent circuit of Figure 7.10c. One can carry out frequency sweep measurement with varying dc bias which will give information on the kinetics of reaction under different band bending condition in semiconductor.

7.5.3. Photoelectrochemical Performance Comparison

A linear sweep voltammetry was performed for PEC cells by sweeping the working electrode's voltage from 0 or below to the 1.2 V, with respect to the reference electrode. The amount of current corresponds to the oxidation process. The current-voltage plot of InGaN nanowire and nanoridge samples under HBr and KCl solution are shown in Figure 7.11a and b, respectively. Oxidation process of HBr solution is a one-hole transfer process and is much faster compared to the true water splitting (i.e. PBS solution with KCl) which involves 4-hole process [167]. PEC performance in the HBr solution is a fast process which mostly involves process via valence band transfer of holes and so may be a good indicator to show the potential capability of the material.

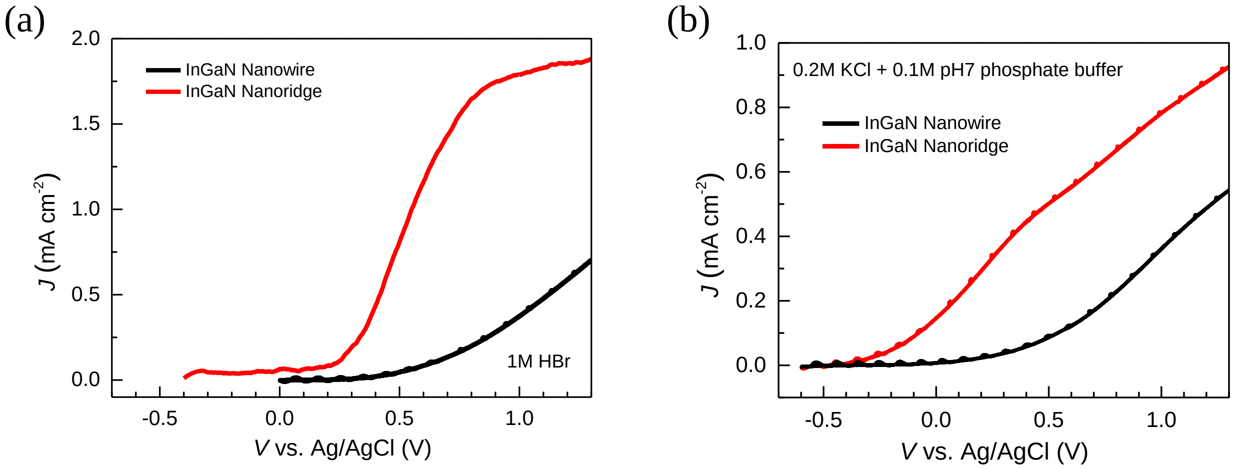

Figure 7.11 Current density (*J*) versus voltage (*V*) plot of InGaN photo-anode with nanowire or nanoridge structure under 1-sun illumination with electrolyte being (a) 1M HBr or (b) 0.2M KCl with 0.1M of phosphate buffer (pH7) solution.

As shown in Figure 7.11a, InGaN nanoridge sample shows a much larger current density and higher fill factor (sharper rise in slope) compared to conventional nanowire structure. Considering the higher surface coverage with high density of nanowires compared to the nanoridge, this signifies that photo-generated holes in InGaN nanoridge efficiently participate in the reaction process while those in InGaN nanowires may get lost due to the poor material quality. We attribute higher performance in InGaN nanoridge structure do to highly crystalline nature compared to InGaN nanowire which has lower recomb. rate. By testing these samples at a slightly more complex charge transfer process in the PBS solution with KCl (as shown in Figure 7.11b), reaction kinetics of actual water oxidation process in these materials are better studied. In case of PBS solution with KCl, InGaN nanoridge sample show a decreased level of current density as well as less steep slope showing reduced performance compared to HBr oxidation's case. For the PBS solution with KCl, charge transfer process involves 4-holes which is a slow reaction process in nature and so carriers that are in the queue of participating in the reaction are stored as a form of capacitive charging in the surface states. In specific, photo-holes are not transferred directly to the electrolyte but likely to be trapped in the surface states before participating in the reaction. Depending on the quality of the material, carrier lifetime in the surface state can be too short for holes to get annihilated at the defect sites before participating in the reaction.

From the impedance measurement of InGaN nanowire and nanoridge samples, R_{trap}, $R_{ct,SS}$, C_{SS}, and τ_{IS} which is the lifetime of carrier in surface state are plotted in Figure 7.12a-d, respectively. First, lower R_{trap} value for nanowire sample compared to the nanoridge sample indicates easier trapping of carriers into the traps, including to the surface state. This trap resistance value for nanoridge is approximately 2-fold higher than that of nanowire which supports the above statement that the major charge transport of nanoridge sample is via valence band (Nevertheless, low current density is due to the complex 4-hole process of oxidation in which the bottle-neck may be coming not from material property but elsewhere). Second, $R_{ct,SS}$ indicating the charge transfer resistance of holes from semiconductor to the electrolyte shows much lower value for nanoridge compared to nanowire. This shows that the charge transfer of carriers via surface states for nanoridge is facile. While the exact reason behind lower $R_{ct,SS}$ of nanoridge sample needs further attention, it can be inferred that the lesser level of defects or dangling bonds at the incomplete surface atoms can promote this charge transfer process. Third, surface state capacitance C_{SS} for InGaN nanowire and nanoridge samples are plotted as a function of potential. As the applied voltage corresponds to the difference in the fermi potential in the semiconductor-liquid Schottky junction, C_{SS} at a given potential indicates the density of surface states in the energy band diagram (dividing C_{SS} by charge gives density of surface states). At an extreme case of applying high voltage to the working electrode, semiconductor junction in the Figure 7.10b will severely bend upward supplying more than enough of over potential for the photo-generated holes to participate in the reaction with high energy. Having this physical picture in mind, sample with higher C_{SS} at lower potential (or having higher surface states closer to the conduction band) will result in lower onset potential of oxidation reaction. Having a low onset potential in PEC is always advantageous because the oxidation reaction of photoanode can be induced even at a small bias voltage. The key message we would like to deliver here is the carrier lifetime at this surface states. From the RC time constant, the lifetime of carriers residing at this surface state is given as $\tau_{IS} = (R_S + R_{trap}) \cdot C_{SS}$. Simply speaking, it can be viewed as the time it takes for carriers to get annihilated while residing at the surface state. This τ_{IS} extracted from the impedance measurement is plotted in Figure 7.12d. Interestingly, τ_{IS} of nanowire is much smaller than that of nanoridge. Having a longer carrier lifetime is beneficial as it gives more time for the carriers to participate in the reaction, especially at a water oxidation reaction which involves 4-holes where the bottleneck of kinetic reaction may come elsewhere other than material quality itself. In case of nanowire, low R_{trap} and high $R_{ct,SS}$ indicates that carriers easily fallen into surface states quickly gets annihilated.

The reason for annihilation may be understood in terms of having poor material quality. On the other hand, the carrier lifetime of InGaN nanoridge is shown to be few times larger than that of nanowire especially at a lower bias voltage which may be originating from a better material quality.

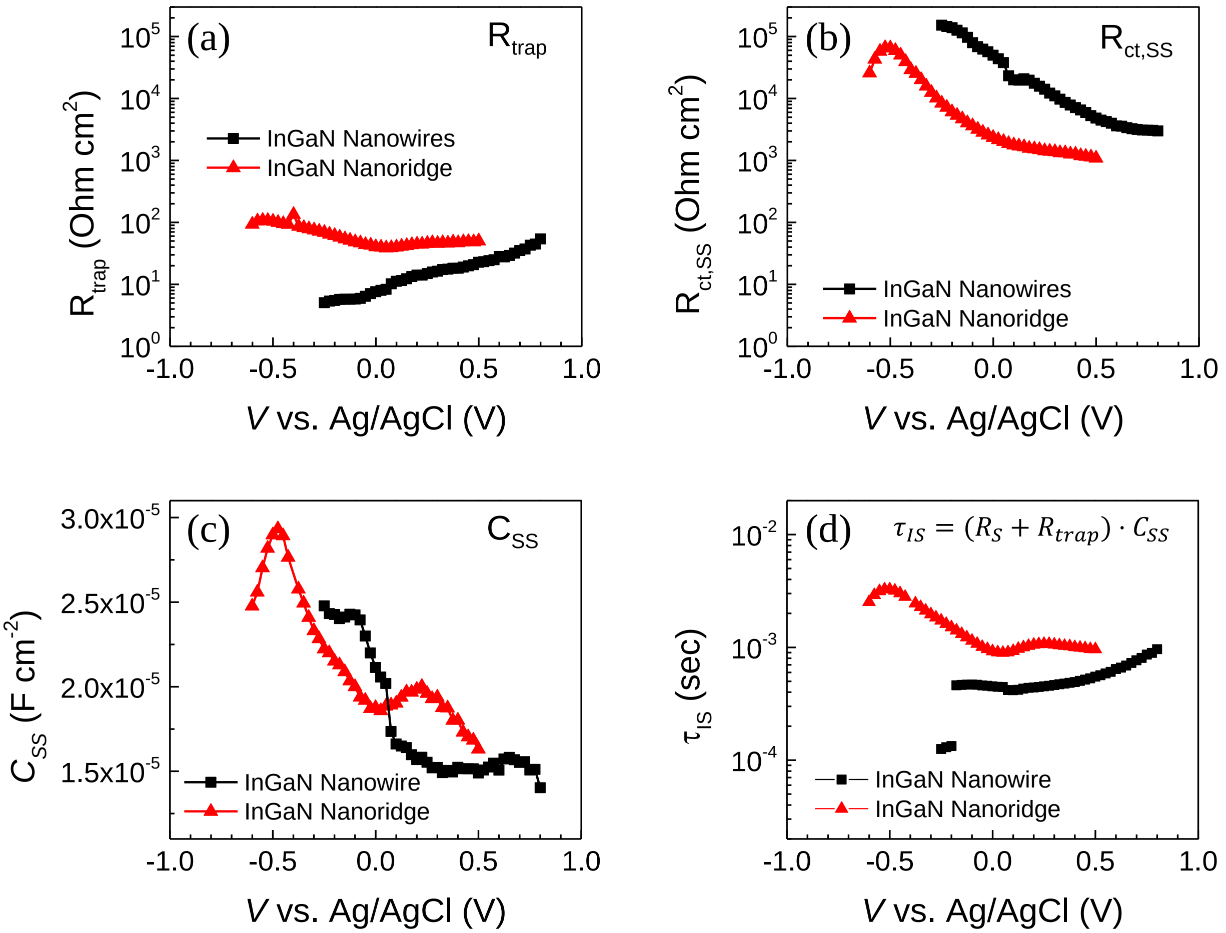

Figure 7.12 Extracted elements of (a) R_{trap}, (b) $R_{ct,SS}$, (c) C_{SS}, and (d) τ_{IS} of InGaN nanowire (black) and nanowire (red) photo-anode cells under 1-sun illumination with varying voltage. The measurements were done with samples immersed under 0.2M of potassium chloride (KCl) with 0.1 phosphate buffer (pH7) solution.

7.6 Conclusion

In summary, we have investigated the epitaxy and structural and optical characterization of InGaN nanoridge structures grown on a Ga-polarity GaN nanowall template. It is observed that a nearly defect-free fin-shaped InGaN nanoridge emerges from the c-axis InGaN bulk nanoprism structure, which can exhibit superior structural and optical properties. Under optimized growth conditions, PL emission from this InGaN nanoridge structure exhibits much higher intensity than InGaN grown on a planar structure or spontaneously formed InGaN nanowire arrays. Detailed structural study of this growth regime over the growth time clearly shows the structural evolution of the bulk triangular InGaN nanoprism into a very narrow, fin-shaped InGaN nanoridge. Atomic resolution HAADF STEM and simultaneous STEM EDS spectroscopic mapping also suggests that this InGaN nanoridge structure is single crystalline with homogeneous In distribution. We envision that our integration of top-down and bottom-up approaches to obtain single crystalline InGaN nanoridges with high In content will emerge as a viable architecture for designing a broad range of III-nitride devices. Moreover, further reducing the dimensions to the nanometer range may provide an extremely scaled quantum material platform for next-generation ultrahigh efficiency electronic, photonic, and solar energy devices and systems.

We have also demonstrated the use of InGaN nanoridge as a photo-anode to oxidize water for solar energy conversion application. Compared to the widely studied spontaneously grown InGaN nanowire structures, this highly ordered single crystalline InGaN nanoridge structure is less susceptible to the charge recombination owing to its high material quality. Electrochemical impedance spectroscopy analysis was conducted to study the charge transfer behavior in water oxidation process and show the superior material property of nanoridge structure over spontaneous nanowire structure.

Chapter 8 Conclusion and Outlook

In this thesis, we have explored methods to control the growth of metal / semiconductor thin films and nanostructures that can provide solutions to various engineering problems. All three growth modes were discussed throughout the thesis by either using PVD, CVD, or MBE technique. In chapter 2, meta-material layer comprised of silver (Ag) nanoparticle in silicon nitride dielectric was fabricated in a one-step process by taking the advantage of low surface tension of silver. This resulted in a growth regime of “island-like” growth under PVD system. By targeting to having absorption at a green wavelength, this meta-material was embedded inside the commercial low-emissive coating to make the colored stack angle-robust, which resulted in enhancing the angle sensitivity to about 20 degrees higher than that of commercial stack. In chapter 3, Ag film growth mode was controlled to take as a form of “island plus layered” growth by using seed-layer method, which enabled the Ag film to become continuous down to extremely thin regime. The selection criteria of the seed-layer was discussed in detail, which plays a crucial role in impacting the pre- and post-film growth condition. As a result of using copper (Cu) as a seed-layer, the percolation threshold was significantly reduced down to 2.4 nm. The electron conduction mechanism at such extremely thin regime was comprehensively discussed by using general effective medium theory in combination with the classical size effect theory. The scientific and engineering implication of metal film’s critical thickness was discussed, in specific for its transparent conductor application. In chapter 4, extremely thin Ag film was used as a transparent anode to completely eliminate waveguide mode in organic light emitting diodes. Owing to the intrinsic optical property of Ag film having negative permittivity (refractive index close to 0) at visible wavelength was found to be responsible for the elimination of waveguide mode in the device. In chapter 5, optical and stability properties of Ag film-based transparent conductor was examined. In specific, top and bottom dielectric layers were explored to minimize the reflection of Ag film and maximize the overall transmission of the film. Also, Ag film-based transparent conductor's color contrast issue was address by carefully selecting the anti-reflective coatings, which is an important criteria for applications like touch panel. Then, methods like using NiCr barrier layer or thiol-based self-assembled monolayer were introduced as a solution to enhance the stability of Ag film. Moreover, electrochemical impedance spectroscopy was used to quantify the passivation effect of top dielectric coatings under salt water to mimic environmental test conditions. In chapter 6, extremely thin Ag film was used as a transparent conductor for amorphous silicon thin film photodiode device. As a starting point, amorphous silicon photodiode device was optimized to suppress the reverse bias current under dark condition. This was achieved by choosing the optimum deposition condition of the active layer under CVD by flowing hydrogen to passivate the dangling bonds. As a result, significant reduction in leakage current was observed. Using this method for fabricating array of amorphous silicon based photodiode array onto TFT pixel chip, successful demonstration of optical fingerprint detection was achieved. Furthermore, utilizing ultrathin Ag film was demonstrated as a transparent anode for this amorphous silicon-based photodiode, which shows this approach as a promising solution for flexible in-display fingerprint sensor application. In chapter 7, using ultrahigh vacuum system via MBE, single-crystalline indium-gallium-nitride (InGaN) nanoridge semiconductor was grown. This so-called "layer-by-layer" epitaxial growth of material was possible due to the pre-patterned substrate which effectively enabled relaxation of the lattice strain despite large lattice mismatch with incorporation of indium in gallium nitride. This InGaN nanoridge was demonstrated as a photoelectrochemical cell for solar energy conversion application. Compared to conventional InGaN nanowire, InGaN nanoridge showed superior performance as a photoanode which is attributed to better quality of the material.

For a future plan, we will further study methods to enhance the quality of silver film by varying growth conditions or changing the underlying substrate. Despite the film can be made continuous down to less than 5 nm, the electrical property of the film is very much susceptible to scattering events due to the small grain size of the film. Our preliminary results show that a high quality Ag film can be grown on a zinc-oxide substrate where the film’s electrical resistivity is superior to that of the film with using germanium or copper as a seed layer. This was originating from the increased grain size of the Ag film when grown on a zinc-oxide underlayer. If there are ways to grow Ag film with high quality and yet significantly reduce the percolation threshold to 2.4 nm or even below, this would have a significant impact for its application in optoelectronic or plasmonic application. In regard to the photodiode application, our current process temperature is limited by the deposition of amorphous silicon layer. By changing this active layer with other photo-sensitive materials that can be done at a room temperature such as organic or perovskite, it may be possible to fabricate our device all at a room temperature. Moreover, as the current device’s response time is limited by the material quality, if this can be replaced by highly crystalline material like perovskite, the significant improvement in response time may be expected too. Finally, as introduced in Chapter 6, metal-film based transparent conductor can be designed to show low sheet resistance of 1 Ω/sq by adopting metal-dielectric 1 dimensional photonic crystal structure. This alternating layers of metal and dielectrics can hold enormous benefit in tailoring the light transmission and reflection at a visible wavelength for functional properties. Moreover, such low electrical resistance films can even be used as interconnect lines for ultra-high resolution large area fully-transparent displays where these lines need to be transparent and yet require to have low resistance to minimize RC delay in the matrix circuit.

Bibliography

1. Oura, K., et al., *Surface Science: An Introduction*. 2013: Springer Berlin Heidelberg.
2. Bass, M., et al., *Handbook of Optics, Third Edition Volume II: Design, Fabrication and Testing, Sources and Detectors, Radiometry and Photometry*. 2009: McGraw-Hill, Inc.
3. Neelakanta, P.S., *Handbook of Electromagnetic Materials: Monolithic and Composite Versions and Their Applications*. 1995: Taylor & Francis.
4. Anders, A., et al., *Smoothing of ultrathin silver films by transition metal seeding.* Solid State Communications, 2006. **140**(5): p. 225-229.
5. Zhao, D., et al., *High-Performance Ta2O5/Al-Doped Ag Electrode for Resonant Light Harvesting in Efficient Organic Solar Cells.* Advanced Energy Materials, 2015. **5**(17): p. 1500768.
6. Chen, W., et al., *Ultra-thin ultra-smooth and low-loss silver films on a germanium wetting layer.* Optics Express, 2010. **18**(5): p. 5124-5134.
7. Formica, N., et al., *Ultrastable and Atomically Smooth Ultrathin Silver Films Grown on a Copper Seed Layer.* ACS Applied Materials & Interfaces, 2013. **5**(8): p. 3048-3053.
8. Jeong, S., et al., *Role of Polymeric Metal Nucleation Inducers in Fabricating Large-Area, Flexible, and Transparent Electrodes for Printable Electronics.* Advanced Functional Materials, 2017. **27**(22): p. 1606842.
9. Gu, D., et al., *Ultrasmooth and Thermally Stable Silver-Based Thin Films with Subnanometer Roughness by Aluminum Doping.* ACS Nano, 2014. **8**(10): p. 10343-10351.
10. Seebauer, E.G. and C.E. Allen, *Estimating surface diffusion coefficients.* Progress in Surface Science, 1995. **49**(3): p. 265-330.
11. Kim, H.C., T.L. Alford, and D.R. Allee, *Thickness dependence on the thermal stability of silver thin films.* Applied Physics Letters, 2002. **81**(22): p. 4287-4289.
12. Ciesielski, A.S., L.; Górecka, E.; Kierdaszuk, J.; Szoplik, T, *Growth model and structure evolution of Ag layers deposited on Ge films.* Beilstein J. Nanotechnol., 2018. **9**: p. 66–76.
13. Rossnagel, S.M. and T.S. Kuan, *Alteration of Cu conductivity in the size effect regime.* Journal of Vacuum Science & Technology B: Microelectronics and Nanometer Structures Processing, Measurement, and Phenomena, 2004. **22**(1): p. 240-247.
14. Zhang, W., et al., *Influence of the electron mean free path on the resistivity of thin metal films.* Microelectronic Engineering, 2004. **76**(1): p. 146-152.
15. Sun, T., et al., *Surface and grain-boundary scattering in nanometric Cu films.* Physical Review B, 2010. **81**(15): p. 155454.
16. Chawla, J.S., et al., *Electron scattering at surfaces and grain boundaries in Cu thin films and wires.* Physical Review B, 2011. **84**(23): p. 235423.
17. Guilmain, M., et al., *A damascene platform for controlled ultra-thin nanowire fabrication.* Nanotechnology, 2013. **24**(24): p. 245305.
18. Logeeswaran, V.J., et al., *Ultrasmooth Silver Thin Films Deposited with a Germanium Nucleation Layer.* Nano Letters, 2009. **9**(1): p. 178-182.

19. Bi, Y.-G., et al., *Ultrathin and ultrasmooth Au films as transparent electrodes in ITO-free organic light-emitting devices.* Nanoscale, 2016. **8**(19): p. 10010-10015.
20. Yang, X., et al., *Optimizing ultrathin Ag films for high performance oxide-metal-oxide flexible transparent electrodes through surface energy modulation and template-stripping procedures.* Scientific Reports, 2017. **7**(1): p. 44576.
21. Zhao, G., et al., *Ultrathin Silver Film Electrodes with Ultralow Optical and Electrical Losses for Flexible Organic Photovoltaics.* ACS Applied Materials & Interfaces, 2018. **10**(32): p. 27510-27520.
22. Wang, H., et al., *Highly Transparent and Broadband Electromagnetic Interference Shielding Based on Ultrathin Doped Ag and Conducting Oxides Hybrid Film Structures.* ACS Applied Materials & Interfaces, 2019. **11**(12): p. 11782-11791.
23. Erdogan, N., et al., *ITO/Au/ITO multilayer thin films on transparent polycarbonate with enhanced EMI shielding properties.* Current Applied Physics, 2020. **20**(4): p. 489-497.
24. Moresco, F., et al., *Plasmon Confinement in Ultrathin Continuous Ag Films.* Physical Review Letters, 1999. **83**(11): p. 2238-2241.
25. Sun, M., et al., *High-Performance GaN Vertical Fin Power Transistors on Bulk GaN Substrates.* IEEE Electron Device Letters, 2017. **38**(4): p. 509-512.
26. Fahsold, G., et al., *Adsorbate-induced changes in the broadband infrared transmission of ultrathin metal films.* Physical Review B, 2002. **65**(23): p. 235408.
27. Abeles, B., H.L. Pinch, and J.I. Gittleman, *Percolation Conductivity in W-${\mathrm{Al}}_{2}$${\mathrm{O}}_{3}$ Granular Metal Films.* Physical Review Letters, 1975. **35**(4): p. 247-250.
28. Efros, A.L. and B.I. Shklovskii, *Critical Behaviour of Conductivity and Dielectric Constant near the Metal-Non-Metal Transition Threshold.* physica status solidi (b), 1976. **76**(2): p. 475-485.
29. Sahimi, M., et al., *Critical exponent of percolation conductivity by finite-size scaling.* Journal of Physics C: Solid State Physics, 1983. **16**(16): p. L521-L527.
30. Sieradzki, K., K. Bailey, and T.L. Alford, *Agglomeration and percolation conductivity.* Applied Physics Letters, 2001. **79**(21): p. 3401-3403.
31. Shao, W.Z., et al., *Conductivity critical exponents lower than the universal value in continuum percolation systems.* Journal of Physics: Condensed Matter, 2008. **20**(39): p. 395235.
32. Landauer, R., *The Electrical Resistance of Binary Metallic Mixtures.* Journal of Applied Physics, 1952. **23**(7): p. 779-784.
33. Abeles, B., et al., *Structural and electrical properties of granular metal films.* Advances in Physics, 1975. **24**(3): p. 407-461.
34. Landauer, R., J.C. Garland, and D.B. Tanner, *Electrical conductivity in inhomogeneous media.* AIP Conference Proceedings, 1978. **40**(1): p. 2-45.
35. McLachlan, D.S., M. Blaszkiewicz, and R.E. Newnham, *Electrical Resistivity of Composites.* Journal of the American Ceramic Society, 1990. **73**(8): p. 2187-2203.
36. Vancea, J., H. Hoffmann, and K. Kastner, *Mean free path and effective density of conduction electrons in polycrystalline metal films.* Thin Solid Films, 1984. **121**(3): p. 201-216.
37. Maaroof, A.I. and B.L. Evans, *Onset of electrical conduction in Pt and Ni films.* Journal of Applied Physics, 1994. **76**(2): p. 1047-1054.

38. Zhang, D., et al., *Effect of silver evolution on conductivity and transmittance of ZnO/Ag thin films.* Journal of Applied Physics, 2011. **109**(10): p. 104318.
39. Neugebauer, C.A. and M.B. Webb, *Electrical Conduction Mechanism in Ultrathin, Evaporated Metal Films.* Journal of Applied Physics, 1962. **33**(1): p. 74-82.
40. Swanson, J.G., D.S. Campbell, and J.C. Anderson, *A study of electrical conduction in island structure nickel and 80:20 nickel-chromium films.* Thin Solid Films, 1968. **1**(5): p. 325-342.
41. Angadi, M.A., *Some transport properties of transition metal films.* Journal of Materials Science, 1985. **20**(3): p. 761-796.
42. Dobierzewska-Mozrzymas, E., et al., *Conduction Mechanisms in Discontinuous Pt Films.* Crystal Research and Technology, 2001. **36**(8-10): p. 1137-1144.
43. Lin, H., et al., *Thermal and Electrical Conduction in Ultrathin Metallic Films: 7 nm down to Sub-Nanometer Thickness.* Small, 2013. **9**(15): p. 2585-2594.
44. Camacho, J.M. and A.I. Oliva, *Surface and grain boundary contributions in the electrical resistivity of metallic nanofilms.* Thin Solid Films, 2006. **515**(4): p. 1881-1885.
45. Sungjun, K. and L. Jong-Lam, *Design of dielectric/metal/dielectric transparent electrodes for flexible electronics.* Journal of Photonics for Energy, 2012. **2**(1): p. 1-22.
46. Sugimoto, Y., et al., *Thermal durability of AZO/Ag(Al)/AZO transparent conductive films.* Japanese Journal of Applied Physics, 2016. **55**(4S): p. 04EJ15.
47. Barnat, E.V., et al., *Real time resistivity measurements during sputter deposition of ultrathin copper films.* Journal of Applied Physics, 2002. **91**(3): p. 1667-1672.
48. Chuang, N., et al., *The Film Thickness Effect on Electrical Conduction Mechanisms and Characteristics of the Ni–Cr Thin Film Resistor.* IEEE Journal of the Electron Devices Society, 2016. **4**(6): p. 441-444.
49. Sondheimer, E.H., *The mean free path of electrons in metals.* Advances in Physics, 1952. **1**(1): p. 1-42.
50. Ziman, J.M., *Electrons and Phonons: The Theory of Transport Phenomena in Solids*. 2001: OUP Oxford.
51. Soffer, S.B., *Statistical Model for the Size Effect in Electrical Conduction.* Journal of Applied Physics, 1967. **38**(4): p. 1710-1715.
52. Namba, Y., *Resistivity and Temperature Coefficient of Thin Metal Films with Rough Surface.* Japanese Journal of Applied Physics, 1970. **9**(11): p. 1326-1329.
53. Liu, H.D., et al., *Thickness dependent electrical resistivity of ultrathin (<40 nm) Cu films.* Thin Solid Films, 2001. **384**(1): p. 151-156.
54. Mayadas, A.F., M. Shatzkes, and J.F. Janak, *ELECTRICAL RESISTIVITY MODEL FOR POLYCRYSTALLINE FILMS: THE CASE OF SPECULAR REFLECTION AT EXTERNAL SURFACES.* Applied Physics Letters, 1969. **14**(11): p. 345-347.
55. Tu, K.N., A.M. Gusak, and I. Sobchenko, *Linear rate of grain growth in thin films during deposition.* Physical Review B, 2003. **67**(24): p. 245408.
56. Philipp, M., *Electrical Transport and Scattering Mechanisms in Thin Silver Films for Thermally Insulating Glazing*, in *Fakultät Mathematik und Naturwissenschaften*. 2011, Technische Universität Dresden.
57. Mayadas, A.F. and M. Shatzkes, *Electrical-Resistivity Model for Polycrystalline Films: the Case of Arbitrary Reflection at External Surfaces.* Physical Review B, 1970. **1**(4): p. 1382-1389.

58. Gall, D., *Electron mean free path in elemental metals.* Journal of Applied Physics, 2016. **119**(8): p. 085101.
59. Mayadas, A.F., R. Feder, and R. Rosenberg, *Resistivity and Structure of Evaporated Aluminum Films.* Journal of Vacuum Science and Technology, 1969. **6**(4): p. 690-693.
60. Cohen, M.H., J. Jortner, and I. Webman, *Percolation conductivity in granular metal films.* Physical Review B, 1978. **17**(12): p. 4555-4557.
61. Kogut, P.M., et al., *An approximate calculation of the dimensionality dependence of the resistor lattice conductivity exponents.* AIP Conference Proceedings, 1978. **40**(1): p. 382-387.
62. Taya, M., *Electronic Composites: Modeling, Characterization, Processing, and MEMS Applications*. 2005: Cambridge University Press.
63. Clerc, J.P., et al., *The electrical conductivity of binary disordered systems, percolation clusters, fractals and related models.* Advances in Physics, 1990. **39**(3): p. 191-309.
64. Kim, W.J., et al., *Percolation study on electrical resistivity of SiC/Si3N4 composites with segregated distribution.* Journal of Applied Physics, 1998. **83**(5): p. 2593-2598.
65. Brosseau, C., *Generalized effective medium theory and dielectric relaxation in particle-filled polymeric resins.* Journal of Applied Physics, 2002. **91**(5): p. 3197-3204.
66. McLachlan, D.S., et al., *AC and DC percolative conductivity of single wall carbon nanotube polymer composites.* Journal of Polymer Science Part B: Polymer Physics, 2005. **43**(22): p. 3273-3287.
67. Abbasi, H., M. Antunes, and J.I. Velasco, *Recent advances in carbon-based polymer nanocomposites for electromagnetic interference shielding.* Progress in Materials Science, 2019. **103**: p. 319-373.
68. Heaney, M.B., *Measurement and interpretation of nonuniversal critical exponents in disordered conductor--insulator composites.* Physical Review B, 1995. **52**(17): p. 12477-12480.
69. Hövel, M., B. Gompf, and M. Dressel, *Dielectric properties of ultrathin metal films around the percolation threshold.* Physical Review B, 2010. **81**(3): p. 035402.
70. Dobierzewska-Mozrzymas, E., et al., *The fractal structure of discontinuous metal films: copper films on glass substrates.* Vacuum, 1997. **48**(3): p. 293-297.
71. Lee, S.-I., et al., *Experimental observation of nonuniversal behavior of the conductivity exponent for three-dimensional continuum percolation systems.* Physical Review B, 1986. **34**(10): p. 6719-6724.
72. Carmona, F. and A. El Amarti, *Anisotropic electrical conductivity in heterogeneous solids with cylindrical conducting inclusions.* Physical Review B, 1987. **35**(7): p. 3284-3290.
73. Mertens, S. and C. Moore, *Continuum percolation thresholds in two dimensions.* Physical Review E, 2012. **86**(6): p. 061109.
74. Aspnes, D.E., *Optical properties of thin films.* Thin Solid Films, 1982. **89**(3): p. 249-262.
75. Choy, T.C., *Effective Medium Theory: Principles and Applications*. 1999: Clarendon Press.
76. Ding, G., et al., *Thickness and microstructure effects in the optical and electrical properties of silver thin films.* AIP Advances, 2015. **5**(11): p. 117234.
77. Kittel, C., *Introduction to Solid State Physics*. 2004: Wiley.
78. Li, Y., *Plasmonic Optics: Theory and Applications*. 2017: SPIE Press.
79. Haacke, G., *New figure of merit for transparent conductors.* Journal of Applied Physics, 1976. **47**(9): p. 4086-4089.

80. Jeong, J.-A., Y.-S. Park, and H.-K. Kim, *Comparison of electrical, optical, structural, and interface properties of IZO-Ag-IZO and IZO-Au-IZO multilayer electrodes for organic photovoltaics.* Journal of Applied Physics, 2010. **107**(2): p. 023111.
81. Loka, C., et al., *High Transparent and Conductive TiO2/Ag/TiO2 Multilayer Electrode Films Deposited on Sapphire Substrate.* Electronic Materials Letters, 2018. **14**(2): p. 125-132.
82. Cho, K.-S., et al., *Highly flexible and semi-transparent Ag–Cu alloy electrodes for high performance flexible thin film heaters.* RSC Advances, 2017. **7**(72): p. 45484-45494.
83. Kermani, H., et al., *Very low resistance ZnS/Ag/ZnS/Ag/ZnS nano-multilayer anode for organic light emitting diodes applications.* Applied Optics, 2013. **52**(4): p. 780-785.
84. Ghosh, D.S., et al., *High figure-of-merit Ag/Al:ZnO nano-thick transparent electrodes for indium-free flexible photovoltaics.* Solar Energy Materials and Solar Cells, 2012. **107**: p. 338-343.
85. Ellmer, K., *Past achievements and future challenges in the development of optically transparent electrodes.* Nature Photonics, 2012. **6**(12): p. 809-817.
86. Brütting, W., et al., *Device efficiency of organic light-emitting diodes: Progress by improved light outcoupling.* physica status solidi (a), 2013. **210**(1): p. 44-65.
87. Salehi, A., et al., *Recent Advances in OLED Optical Design.* Advanced Functional Materials, 2019. **29**(15): p. 1808803.
88. Gifford, D.K. and D.G. Hall, *Emission through one of two metal electrodes of an organic light-emitting diode via surface-plasmon cross coupling.* Applied Physics Letters, 2002. **81**(23): p. 4315-4317.
89. Lee, K.M., et al., *Enhanced outcoupling in flexible organic light-emitting diodes on scattering polyimide substrates.* Organic Electronics, 2017. **51**: p. 471-476.
90. Sun, Y. and S.R. Forrest, *Enhanced light out-coupling of organic light-emitting devices using embedded low-index grids.* Nature Photonics, 2008. **2**(8): p. 483-487.
91. Qu, Y., M. Slootsky, and S.R. Forrest, *Enhanced light extraction from organic light-emitting devices using a sub-anode grid.* Nature Photonics, 2015. **9**(11): p. 758-763.
92. Koo, W.H., et al., *Light extraction from organic light-emitting diodes enhanced by spontaneously formed buckles.* Nature Photonics, 2010. **4**(4): p. 222-226.
93. Li, Y., et al., *Tailor-made nanostructures bridging chaos and order for highly efficient white organic light-emitting diodes.* Nature Communications, 2019. **10**(1): p. 2972.
94. Xu, L.-H., et al., *Microcavity-Free Broadband Light Outcoupling Enhancement in Flexible Organic Light-Emitting Diodes with Nanostructured Transparent Metal–Dielectric Composite Electrodes.* ACS Nano, 2016. **10**(1): p. 1625-1632.
95. Han, T.-H., et al., *Extremely efficient flexible organic light-emitting diodes with modified graphene anode.* Nature Photonics, 2012. **6**(2): p. 105-110.
96. Liu, Z., J. Li, and F. Yan, *Package-free flexible organic solar cells with graphene top electrodes.* Adv Mater, 2013. **25**(31): p. 4296-301.
97. Zhou, Y. and R. Azumi, *Carbon nanotube based transparent conductive films: progress, challenges, and perspectives.* Science and Technology of Advanced Materials, 2016. **17**(1): p. 493-516.
98. Wu, H., et al., *A transparent electrode based on a metal nanotrough network.* Nature Nanotechnology, 2013. **8**(6): p. 421-425.

99. Kang, M.-G., et al., *Transparent Cu nanowire mesh electrode on flexible substrates fabricated by transfer printing and its application in organic solar cells.* Solar Energy Materials and Solar Cells, 2010. **94**(6): p. 1179-1184.
100. Kang, S., et al., *Capillary Printing of Highly Aligned Silver Nanowire Transparent Electrodes for High-Performance Optoelectronic Devices.* Nano Letters, 2015. **15**(12): p. 7933-7942.
101. Yun, J., *Ultrathin Metal films for Transparent Electrodes of Flexible Optoelectronic Devices.* Advanced Functional Materials, 2017. **27**(18): p. 1606641.
102. Maniyara, R.A., et al., *An antireflection transparent conductor with ultralow optical loss (<2 %) and electrical resistance (<6 Ω sq(-1)).* Nature communications, 2016. **7**: p. 13771-13771.
103. Gnanavel, M., D. Bharathi Mohan, and C.S. Sunandana, *Optics of quasi-particle phase transitions in nanostructured Ag thin films.* Thin Solid Films, 2008. **517**(3): p. 1058-1062.
104. Kulkarni, A.K., et al., *Dependence of the sheet resistance of indium-tin-oxide thin films on grain size and grain orientation determined from X-ray diffraction techniques.* Thin Solid Films, 1999. **345**(2): p. 273-277.
105. König, T.A.F., et al., *Electrically Tunable Plasmonic Behavior of Nanocube–Polymer Nanomaterials Induced by a Redox-Active Electrochromic Polymer.* ACS Nano, 2014. **8**(6): p. 6182-6192.
106. Johnson, P.B. and R.W. Christy, *Optical Constants of the Noble Metals.* Physical Review B, 1972. **6**(12): p. 4370-4379.
107. Kim, J.-H., et al., *The effects of film thickness on the electrical, optical, and structural properties of cylindrical, rotating, magnetron-sputtered ITO films.* Applied Surface Science, 2018. **440**: p. 1211-1218.
108. Mohmmadieyh, H.A.a.H.F.a.M.A.a.M.C., *Electrical and optical properties of ITO thin films prepared by DC magnetron sputtering for low-emitting coatings.* arXiv, 2014. **1409.5293**(cond-mat.mtrl-sci).
109. Eshaghi, A. and A. Graeli, *Optical and electrical properties of indium tin oxide (ITO) nanostructured thin films deposited on polycarbonate substrates "thickness effect".* Optik, 2014. **125**(3): p. 1478-1481.
110. Wang, T. and P.D. Bristowe, *Controlling Ag diffusion in ZnO by donor doping: A first principles study.* Acta Materialia, 2017. **137**: p. 115-122.
111. Eda, G., G. Fanchini, and M. Chhowalla, *Large-area ultrathin films of reduced graphene oxide as a transparent and flexible electronic material.* Nature Nanotechnology, 2008. **3**(5): p. 270-274.
112. Ye, Y.-H., G. Bader, and V.-V. Truong, *Low-loss one-dimensional metallodielectric photonic crystals fabricated by metallic insertions in a multilayer dielectric structure.* Applied Physics Letters, 2000. **77**(2): p. 235-237.
113. Sun, Y. and S.R. Forrest, *Organic light emitting devices with enhanced outcoupling via microlenses fabricated by imprint lithography.* Journal of Applied Physics, 2006. **100**(7): p. 073106.
114. Lee, J.I., et al., *Electrochemical interaction between silver and sulfur in sodium sulfide solutions.* Metallurgical and Materials Transactions B, 2001. **32**(5): p. 895-901.
115. Tani, T., *Silver Nanoparticles: From Silver Halide Photography to Plasmonics*. 2015: Oxford University Press.

116. Schoenfisch, M.H. and J.E. Pemberton, *Air Stability of Alkanethiol Self-Assembled Monolayers on Silver and Gold Surfaces.* Journal of the American Chemical Society, 1998. **120**(18): p. 4502-4513.
117. Zhang, X.G., *Corrosion Potential and Corrosion Current*, in *Corrosion and Electrochemistry of Zinc*, X.G. Zhang, Editor. 1996, Springer US: Boston, MA. p. 125-156.
118. Arch, J.K. and S.J. Fonash, *Origins of reverse bias leakage currents in hydrogenated amorphous silicon p-i-n detector structures.* Applied Physics Letters, 1992. **60**(6): p. 757-759.
119. Häcker, R. and A. Hangleiter, *Intrinsic upper limits of the carrier lifetime in silicon.* Journal of Applied Physics, 1994. **75**(11): p. 7570-7572.
120. Ziegler, J., et al., *Plasma-enhanced atomic-layer-deposited MoOxemitters for silicon heterojunction solar cells.* Applied Physics A, 2015. **120**(3): p. 811-816.
121. Mali, S.S., et al., *Efficient planar n-i-p type heterojunction flexible perovskite solar cells with sputtered TiO2 electron transporting layers.* Nanoscale, 2017. **9**(9): p. 3095-3104.
122. Street, R.A., *Hydrogenated Amorphous Silicon*. 2005: Cambridge University Press.
123. Swartz, G.A., *Computer model of amorphous silicon solar cell.* Journal of Applied Physics, 1982. **53**(1): p. 712-719.
124. Said, A.J., et al., *Extended infrared photoresponse and gain in chalcogen-supersaturated silicon photodiodes.* Applied Physics Letters, 2011. **99**(7): p. 073503.
125. Qiu, X., et al., *Trap Assisted Bulk Silicon Photodetector with High Photoconductive Gain, Low Noise, and Fast Response by Ag Hyperdoping.* Advanced Optical Materials, 2018. **6**(3): p. 1700638.
126. Zhang, M., et al., *High-Performance Photodiode-Type Photodetectors Based on Polycrystalline Formamidinium Lead Iodide Perovskite Thin Films.* Scientific Reports, 2018. **8**(1): p. 11157.
127. Jin, X., et al., *High-Performance Free-Standing Flexible Photodetectors Based on Sulfur-Hyperdoped Ultrathin Silicon.* ACS Applied Materials & Interfaces, 2019. **11**(45): p. 42385-42391.
128. Hagen, E. and H. Rubens, *Über Beziehungen des Reflexions- und Emissionsvermögens der Metalle zu ihrem elektrischen Leitvermögen.* Annalen der Physik, 1903. **316**(8): p. 873-901.
129. Waters, M.J., *TRANK*. 2018, GitHub: GitHub.
130. Byrnes, S.J., *Multilayer optical calculations*. 2016, arXiv: arXiv.
131. *<[n26]Itoh_jjap_Straight and smooth etching of GaN m plane_2006.pdf>*.
132. Kuniyoshi, O., et al., *Dislocation-Free m -Plane InGaN/GaN Light-Emitting Diodes on m -Plane GaN Single Crystals.* Japanese Journal of Applied Physics, 2006. **45**(11L): p. L1197.
133. Jani, O., et al., *Design and characterization of GaN/InGaN solar cells.* Applied Physics Letters, 2007. **91**(13): p. 132117.
134. Dahal, R., et al., *InGaN/GaN multiple quantum well solar cells with long operating wavelengths.* Applied Physics Letters, 2009. **94**(6): p. 063505.
135. Fan, S., I. Shih, and Z. Mi, *A Monolithically Integrated InGaN Nanowire/Si Tandem Photoanode Approaching the Ideal Bandgap Configuration of 1.75/1.13 eV.* Advanced Energy Materials, 2017. **7**(2): p. 1600952.

136. Fan, S., et al., *An In0.5Ga0.5N nanowire photoanode for harvesting deep visible light photons.* APL Materials, 2016. **4**(7): p. 076106.
137. Kibria, M.G. and Z. Mi, *Artificial photosynthesis using metal/nonmetal-nitride semiconductors: current status, prospects, and challenges.* Journal of Materials Chemistry A, 2016. **4**(8): p. 2801-2820.
138. Okamoto, N., et al., *MOCVD-grown InGaN-channel HEMT structures with electron mobility of over.* Journal of Crystal Growth, 2004. **272**(1-4): p. 278-284.
139. Laboutin, O., et al., *InGaN channel high electron mobility transistor structures grown by metal organic chemical vapor deposition.* Applied Physics Letters, 2012. **100**(12): p. 121909.
140. Wang, R., et al., *InGaN Channel High-Electron-Mobility Transistors with InAlGaN Barrier andfT/fmaxof 260/220 GHz.* Applied Physics Express, 2013. **6**(1): p. 016503.
141. Van de Walle, C.G. and J. Neugebauer, *Small valence-band offsets at GaN/InGaN heterojunctions.* Applied Physics Letters, 1997. **70**(19): p. 2577-2579.
142. Singh, R., et al., *Phase separation in InGaN thick films and formation of InGaN/GaN double heterostructures in the entire alloy composition.* Applied Physics Letters, 1997. **70**(9): p. 1089-1091.
143. Hori, M., et al., *Optical Properties of InxGa1—xN with Entire Alloy Composition on InN Buffer Layer Grown by RF-MBE.* physica status solidi (b), 2002. **234**(3): p. 750-754.
144. Guo, W., et al., *Catalyst-free InGaN/GaN nanowire light emitting diodes grown on (001) silicon by molecular beam epitaxy.* Nano Lett, 2010. **10**(9): p. 3355-9.
145. Tamura, Y. and K. Hane, *Optical characteristics of multiple layered InGaN quantum wells on GaN nanowalls grown on Si (111) substrate.* Materials Research Bulletin, 2016. **83**: p. 563-567.
146. Soto Rodriguez, P.E.D., et al., *Spontaneous formation of InGaN nanowall network directly on Si.* Applied Physics Letters, 2013. **102**(17): p. 173105.
147. Armitage, R. and K. Tsubaki, *Multicolour luminescence from InGaN quantum wells grown over GaN nanowire arrays by molecular-beam epitaxy.* Nanotechnology, 2010. **21**(19): p. 195202.
148. Liu, X., et al., *Molecular beam epitaxial growth and characterization of AlN nanowall deep UV light emitting diodes.* Applied Physics Letters, 2017. **111**(10): p. 101103.
149. Bayerl, D. and E. Kioupakis, *Visible-wavelength polarized-light emission with small-diameter InN nanowires.* Nano Lett, 2014. **14**(7): p. 3709-14.
150. Chouksey, S., et al., *Strong Size Dependency on the Carrier and Photon Dynamics in InGaN/GaN Single Nanowalls Determined Using Photoluminescence and Ultrafast Transient Absorption Spectroscopy.* Nano Lett, 2017. **17**(8): p. 4596-4603.
151. Zhong, A. and K. Hane, *Characterization of GaN Nanowall Network and Optical Property of InGaN/GaN Quantum Wells by Molecular Beam Epitaxy.* Japanese Journal of Applied Physics, 2013. **52**(8S): p. 08JE13.
152. Stocker, D.A., E.F. Schubert, and J.M. Redwing, *Crystallographic wet chemical etching of GaN.* Applied Physics Letters, 1998. **73**(18): p. 2654-2656.
153. Morimichi, I., et al., *Straight and Smooth Etching of GaN (1100) Plane by Combination of Reactive Ion Etching and KOH Wet Etching Techniques.* Japanese Journal of Applied Physics, 2006. **45**(5R): p. 3988.

154. Koblmüller, G., C.S. Gallinat, and J.S. Speck, *Surface kinetics and thermal instability of N-face InN grown by plasma-assisted molecular beam epitaxy.* Journal of Applied Physics, 2007. **101**(8): p. 083516.
155. Gačević, Ž., et al., *A comprehensive diagram to grow (0001)InGaN alloys by molecular beam epitaxy.* Journal of Crystal Growth, 2013. **364**: p. 123-127.
156. Jindal, V. and F. Shahedipour-Sandvik, *Theoretical prediction of GaN nanostructure equilibrium and nonequilibrium shapes.* Journal of Applied Physics, 2009. **106**(8): p. 083115.
157. Lundskog, A., et al., *Morphology Control of Hot-Wall MOCVD Selective Area Grown Hexagonal GaN Pyramids.* Crystal Growth & Design, 2012. **12**(11): p. 5491-5496.
158. Gacevic, Z., D. Gomez Sanchez, and E. Calleja, *Formation mechanisms of GaN nanowires grown by selective area growth homoepitaxy.* Nano Lett, 2015. **15**(2): p. 1117-21.
159. Urban, A., et al., *Corrigendum: Ga-polar GaN nanocolumn arrays with semipolar faceted tips (2013 New J. Phys. 15 053045).* New Journal of Physics, 2014. **16**(1): p. 019501.
160. Brubaker, M.D., et al., *Polarity-Controlled GaN/AlN Nucleation Layers for Selective-Area Growth of GaN Nanowire Arrays on Si(111) Substrates by Molecular Beam Epitaxy.* Crystal Growth & Design, 2015. **16**(2): p. 596-604.
161. Northrup, J.E. and J. Neugebauer, *Theory of GaN (10-10) and (11-20) surfaces.* Physical Review B, 1996. **53**(16): p. R10477-R10480.
162. Dreyer, C.E., A. Janotti, and C.G. Van de Walle, *Absolute surface energies of polar and nonpolar planes of GaN.* Physical Review B, 2014. **89**(8).
163. Moses, P.G. and C.G. Van de Walle, *Band bowing and band alignment in InGaN alloys.* Applied Physics Letters, 2010. **96**(2): p. 021908.
164. Kuykendall, T., et al., *Complete composition tunability of InGaN nanowires using a combinatorial approach.* Nat Mater, 2007. **6**(12): p. 951-6.
165. Varadhan, P., et al., *Surface Passivation of GaN Nanowires for Enhanced Photoelectrochemical Water-Splitting.* Nano Letters, 2017. **17**(3): p. 1520-1528.
166. Klahr, B., et al., *Water Oxidation at Hematite Photoelectrodes: The Role of Surface States.* Journal of the American Chemical Society, 2012. **134**(9): p. 4294-4302.
167. Tang, J., J.R. Durrant, and D.R. Klug, *Mechanism of Photocatalytic Water Splitting in TiO2. Reaction of Water with Photoholes, Importance of Charge Carrier Dynamics, and Evidence for Four-Hole Chemistry.* Journal of the American Chemical Society, 2008. **130**(42): p. 13885-13891.